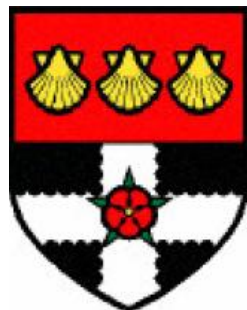


**THE UNIVERSITY OF READING**

Department of Meteorology



The application of  
seasonal rainfall forecasts and  
satellite rainfall estimates to seasonal crop  
yield forecasting for Africa

**HELEN GREATREX**

A thesis submitted for the degree of Doctor of Philosophy

May 2012

---

---

# **DECLARATION**

I confirm that this is all my own work and the use of all material from other sources has been properly and fully acknowledged

Helen Greatrex

---

---

# ABSTRACT

Rain-fed agriculture is extremely important in sub-Saharan Africa, thus the ability to forecast and monitor regional crop yields throughout the growing season would be of enormous benefit to decision makers. Of equal importance to be able to assign a measure of uncertainty to the forecast, especially considering that many predictions are made in the context of a complex climate and sparse meteorological and agricultural observations.

This work investigates these issues in the context of an operational updating regional crop yield forecast, concentrating in particular on a case study forecasting Ethiopian maize. Part 1 of the work presented a detailed discussion of Ethiopia's climate and agricultural systems.

As real-time ground based weather observations are sparse in Africa, Part 2 contains an investigation into remotely sensed satellite rainfall estimates. A daily TAMSAT calibration and the geostatistical process of sequential simulation were used to create a spatially correlated ensemble of Meteosat-derived rainfall estimates. The ensemble mean was evaluated as a daily deterministic rainfall product and was found to be as good as or better than other products applied in the same region. A validation of the full ensemble showed that they realistically estimated Ethiopian rainfall fields that agreed both with observed spatial correlations and input pixel level statistics.

Part 3 of the work includes a discussion on regional crop simulation modelling and presents a new parameterisation of the GLAM crop simulation model for tropical maize. GLAM<sub>MAIZE</sub> was then driven using individual members of the satellite ensemble; this was shown to exhibit the correct sensitivities to climate inputs and performed reasonably against yield observations.

Finally, Part 4 presented a new method of creating stochastic spatially and temporally correlated rainfall fields. This 'regional weather generator' was tested using a case study on Ethiopian April rainfall and a detailed discussion was included about future development plans.

---

---

# ACKNOWLEDGEMENTS

Thank you first and foremost to my supervisors David Grimes and Tim Wheeler; without your support this thesis would not exist! In particular, thank you to Tim for cheerfully introducing me to and guiding me through agricultural research. Thank you to David for your constant encouragement, guidance and humour and for enabling me to visit Africa five times during my project! I could not have imagined a better project or supervisors.

In addition, thank you to the Ethiopian National Meteorological Agency and the Central Statistical Agency for your advice and datasets and for all the support provided by Allard de Wit. I look forward to future collaborations! My work was also made immeasurably easier and more interesting through working with my friends and colleagues in the TAMSAT and ‘Crops and Climate’ research groups.

It has been a fantastic experience to work at the Department of Meteorology, especially due to the friendships I have made along the way. Thank you to all of my past and present housemates and to everyone who worked with me in 1U09 – you made the last few years so much fun! A special thanks must go to Dirk, Keri, David, Rob, Laura, Abi and Dann for always being there, putting up with constant natterings about African crops and Welsh rugby, for helping me overcome a thousand small crises and for always being able to make me see the lighter side of life.

Thank you to my family for providing me with roots, love and a safe haven and to Dave for all the interesting science chats! I would not be where I am now without you. Finally, love and thanks to James for always being there with endless support, encouragement proof-reading and cooking!

# CONTENTS

<b>CHAPTER ONE INTRODUCTION AND AIMS .....</b>	<b>1</b>
1.1    MOTIVATION.....	1
1.1.1. Scarcity of observations .....	4
1.1.2. A question of scale .....	5
1.1.3. Quantifying uncertainty.....	6
1.2    THESIS AIMS.....	7
1.3    THESIS STRUCTURE.....	8
1.4    A GOLDEN BULLET?.....	10

## PART 1: OBSERVATIONS

---

<b>CHAPTER TWO ETHIOPIAN AGRICULTURE &amp; CROP FORECASTING .....</b>	<b>12</b>
2.1    OVERVIEW .....	12
2.2    TOPOGRAPHY AND REGIONS .....	16
2.3    ETHIOPIAN AGRICULTURE .....	18
2.3.1. Background .....	18
2.4    ETHIOPIAN CALENDAR .....	22
2.5    CROP PRODUCTION, YIELD AND AREA PLANTED DATA.....	22
2.5.1. Data collection.....	23
2.5.2. National level data analysis.....	24
2.5.3. Regional level data analysis .....	28
2.6    PLANTING DATES AND SEASON LENGTH .....	30
2.7    CONCLUSION TO CHAPTER TWO.....	32

---

---

<b>CHAPTER THREE ETHIOPIAN CLIMATE AND OBSERVATIONS .....</b>	<b>33</b>
3.1     OVERVIEW .....	33
3.2     CLIMATE DATASETS .....	36
3.2.1. Rain-gauge Data .....	36
3.2.2. Satellite data .....	38
3.2.3. Model data .....	39
3.3     INITIAL ANALYSIS OF GAUGE DATA .....	40
3.4     SPATIAL INTERPOLATION OF THE RAIN-GAUGE DATA .....	42
3.4.1. Geostatistics .....	44
3.5     CONCLUSION TO CHAPTER THREE.....	52
3.6     CONCLUSION TO PART 1 & FINAL DESCRIPTION OF THE CASE STUDY .....	54

---

## PART 2: SATELLITE RAINFALL ESTIMATES

---

<b>CHAPTER FOUR SATELLITE RAINFALL ESTIMATION METHODOLOGY .....</b>	<b>56</b>
4.1     RAINFALL ESTIMATION IN AFRICA .....	56
4.2     RAINFALL ESTIMATION FROM SATELLITES .....	59
4.2.1. Satellite methodologies .....	61
4.2.2. Validation studies over Africa.....	63
4.3     TAMSAT METHODOLOGY FOR RAINFALL ESTIMATES.....	64
4.3.1. Basic approach and validation.....	64
4.3.2. Quantifying the uncertainty in TAMSAT methodology when studying daily data .....	66
4.3.3. Creating daily rainfall estimates from the calibration .....	72
4.3.4. Final calibration equations .....	73
4.4     CONCLUSION TO CHAPTER FOUR .....	74

---

---

<b>CHAPTER FIVE CALIBRATION OF TAMSAT OVER ETHIOPIA .....</b>	<b>75</b>
5.1     OVERVIEW .....	75
5.2     SELECTING ZONE BOUNDARIES.....	76
5.2.1. Example.....	77
5.3     CALIBRATION PROCEDURE .....	79
5.3.1. Overview .....	79
5.3.2. Mean rainfall amount .....	80
5.3.3. Probability of rain.....	83
5.3.4. Error parameters .....	84
5.4     ETHIOPIAN CALIBRATION .....	85
5.4.1. Excluded months .....	85
5.4.2. Zone Choice .....	88
5.4.3. Rainfall amount .....	89
5.4.4. Probability of Rain .....	90
5.4.5. The variance of rainfall amount .....	91
5.5     CONCLUSION TO CHAPTER FIVE.....	92
<b>CHAPTER SIX SEQUENTIAL SIMULATION .....</b>	<b>94</b>
6.1     OVERVIEW .....	94
6.2     METHODS OF CREATING SPATIALLY CORRELATED RAINFALL FIELDS.....	95
6.3     FORMAL DESCRIPTION OF SEQUENTIAL SIMULATION .....	98
6.3.1. Overall method.....	98
6.3.2. Sequential Indicator Simulation .....	99
6.3.3. Sequential Gaussian Simulation .....	101
6.4     PRACTICAL NOTES AND CALIBRATION PARAMETERS.....	102
6.4.1. The structure of rainfall events.....	102

---

---

6.4.2. Random paths.....	103
6.4.3. Variograms.....	104
6.4.4. Number of ensemble members.....	110
6.5 SEQUENTIAL SIMULATION AND TAMSAT RAINFALL ESTIMATES.....	112
6.5.1. Step 1 – Sequential indicator simulation.....	112
6.5.2. Step 2 - Gaussian Sequential simulation.....	116
6.6 CONCLUSION TO CHAPTER SIX.....	121
<b>CHAPTER SEVEN VALIDATION OF THE TAMSAT DAILY SATELLITE RAINFALL ENSEMBLES .....</b>	<b>122</b>
7.1 OVERVIEW .....	122
7.2 VALIDATION OF THE ENSEMBLE MEAN.....	123
7.3 VERIFYING ENSEMBLE PARAMETERS.....	128
7.4 VALIDATION OF THE PROBABILISTIC ENSEMBLE .....	135
7.4.1. Validation of the rainfall distribution.....	135
7.4.2. Spatial correlation.....	140
7.4.3. Time-series .....	143
7.5 MODIFIED TAMSAT ENSEMBLES.....	145
7.6 CONCLUSION TO CHAPTER SEVEN.....	150
7.7 CONCLUSION TO PART 2 .....	152

---

## PART 3: ETHIOPIAN CROP YIELD MONITORING

---

<b>CHAPTER EIGHT CROP YIELD MODELLING .....</b>	<b>154</b>
8.1 PHENOLOGY, GROWTH & CROP-WEATHER RELATIONSHIPS .....	154
8.1.1. Crop development .....	154
8.1.2. Crop growth.....	156
8.1.3. Crop weather relationships .....	157

---

---

8.2	MAIZE .....	158
8.2.1.	Maize phenology and sensitivities .....	159
8.2.2.	Harvest index.....	163
8.2.3.	Yield definitions.....	164
8.3	CROP SIMULATION MODELLING.....	165
8.4	THE GENERAL LARGE AREA MODEL FOR ANNUAL CROPS.....	167
8.4.1.	Intelligent Planting .....	169
8.4.2.	Development and Leaf Area Index.....	169
8.4.3.	Water Balance and Transpiration .....	171
8.4.4.	Biomass and Yield.....	172
8.5	A NEW PARAMETERISATION OF GLAM FOR MAIZE.....	173
8.6	CULTIVAR AND PARAMETER VALUES .....	177
8.7	CONCLUSION TO CHAPTER EIGHT .....	180
	<b>CHAPTER NINE APPLICATION OF SATELLITE RAINFALL ENSEMBLES TO CROP YIELD MONITORING .....</b>	<b>181</b>
9.1	EXPERIMENT SUMMARY .....	182
9.2	ASSESSMENT OF INTERNAL CONSISTENCY & SENSITIVITIES .....	186
9.2.1.	Seasonal time-series .....	187
9.2.2.	Relationship between climate and yield .....	189
9.3	COMPARING MODELLED AND OBSERVED SEASON LENGTH .....	191
9.4	COMPARING ERA-INTERIM AND THE TAMSAT ENSEMBLES .....	194
9.5	ENSEMBLE ANALYSIS .....	197
9.6	REGIONAL LEVEL STATISTICS .....	202
9.7	COMPARING MODELLED YIELDS WITH OBSERVATIONS .....	205
9.8	CONCLUSION TO CHAPTER NINE .....	207

---

---

9.9	CONCLUSION TO PART 3 .....	209
-----	----------------------------	-----

---

## PART 4: SEASONAL FORECASTS & WEATHER GENERATORS

---

### CHAPTER TEN SEASONAL CROP YIELD FORECASTING ..... 211

10.1	INTRODUCTION .....	211
10.2	SEASONAL WEATHER FORECASTS.....	212
10.3	AN UPDATING FORECAST SYSTEM .....	216
10.4	LINKING A SEASONAL WEATHER FORECAST TO A CROP MODEL.....	218
10.5	WEATHER GENERATORS .....	222
10.5.1.	Non-parametric techniques.....	222
10.5.2.	Parametric weather generators .....	222
10.5.3.	Inter-comparison studies .....	224
10.5.4.	Incorporating spatial correlation.....	225
10.6	RAININT .....	226
10.6.1.	Introduction .....	226
10.6.2.	Input parameters .....	228
10.6.3.	RainInt Methodology .....	231
10.6.4.	Internal consistency .....	233
10.6.5.	Characteristics and features.....	237
10.7	FUTURE RESEARCH DIRECTIONS FOR SEASONAL FORECASTING AND WEATHER GENERATORS ....	240
10.8	CONCLUSION OF CHAPTER 10/PART 4 .....	241

---

## CONCLUSIONS, APPENDICES & REFERENCES

---

### CHAPTER ELEVEN CONCLUSION..... 242

11.1	SUMMARY OF MAIN RESULTS .....	242
------	-------------------------------	-----

---

---

11.1.1. An operational crop yield forecast system .....	243
11.1.2. Satellite rainfall estimation for Africa.....	244
11.1.3. Capturing uncertainty in satellite rainfall estimates .....	247
11.1.4. Crop simulation modelling and GLAM <sub>MAIZE</sub> .....	248
11.1.5. Weather generators.....	252
11.2 FUTURE RESEARCH DIRECTIONS.....	253
11.3 FINAL COMMENTS .....	256
<b>APPENDIX ONE TAMSAT CALIBRATION PARAMETERS.....</b>	<b>A1</b>
A1.1. ZONE CHOICE .....	A1
A1.2. CALIBRATION PARAMETERS.....	A3
A1.3. PROBABILITY OF RAIN .....	A7
A1.4. ERROR REGRESSIONS .....	A10
<b>APPENDIX TWO STATISTICAL DEFINITIONS AND TESTS .....</b>	<b>15</b>
A2.1. SKILL SCORES FOR DICHOTOMOUS FORECASTS .....	15
A2.2. OTHER SKILL SCORES .....	17

## **GLOSSARY**

## **REFERENCES**

# CHAPTER ONE

# INTRODUCTION AND AIMS

## 1.1 MOTIVATION

*“The climate has always presented challenges to those who rely on it.”*

Hellmuth *et al.*, 2010

Sub-Saharan Africa contains some of the most food insecure regions in the world. Most of the continent relies on rain-fed agriculture with few coping mechanisms or crop management options, therefore a climate shock such as a drought or flood can have a disproportionately large effect on food security. The severity of the situation for Africa is evident in Figure 1.1, which depicts the current global food security risk index.

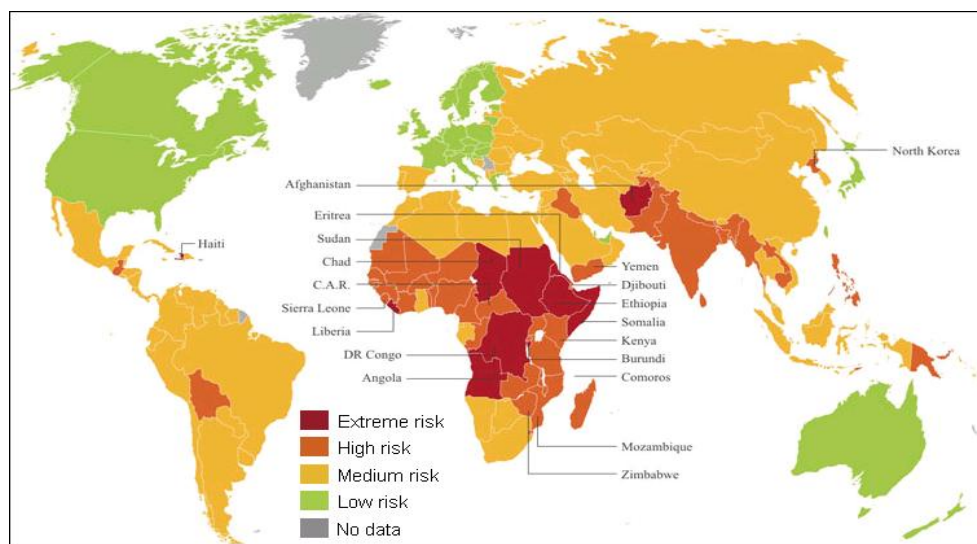


**Figure 1.1. Food security risk index for 2011.** The Food Security Risk Index (FSRI), released by risk analysis and mapping company Maplecroft, is based on the key elements of food security as laid out by the UN's Food and Agriculture Organization (FAO). It is calculated using 12 indicators, measuring the availability, access and stability of food supplies across all countries, as well as the nutritional and health status of populations. Plot taken from Maplecroft (2011).

There are many factors affecting food security in a given location, including conflict, poor access to food, lack of storage facilities and poor market conditions; these are discussed in more detail in Section 1.4 and in Haile (2005). Low agricultural productivity also plays a large role in African food security. This is often due to a lack of management options such as fertilizer, irrigation, pest control, machinery (such as tractors) or seed for modern crop cultivars (Wiebe, 2003; MacAskill, 2006). This means that African crops can be exceptionally vulnerable to their environment, particularly to soil fertility and climate. Whilst soil fertility is a serious issue for African agriculture it varies relatively slowly over time. Weather is therefore often the major determinant of year to year variability in African crop yields.

There are many studies considering the impact of climate change on African agriculture (for recent examples see Thornton *et al.*; 2009; Thow *et al.*, 2010; World Bank, 2010; Lobell *et al.*, 2011; Samson *et al.*, 2011 & Liu *et al.*, 2008). However less work has been done on the impact of current climate variability and weather. As discussed in Cooper *et al* (2008), for the majority of communities in Sub Saharan Africa to adjust to climate change, it would be beneficial for them to learn first how to cope with current climate variability (which generally even swamps a future climate change signal). This can then provide the communities with the skills and knowledge needed to adapt to a future climate.

One method of applying information about the current climate to agriculture is through the use of early warning systems. These can be split into monitoring systems, which provide an estimate of the health of a crop during a season, or forecast systems, which attempt to forecast yield before harvest (normally from just before the time of planting onwards). As described in Chapter Two, many countries in Sub-Saharan Africa currently use highly qualitative methods to estimate crop yields within a season, thus it can be difficult to identify food shortages until well after harvest. The ability to forecast crop yield would be of enormous benefit to decision makers as it could allow a country to shift its food needs assessment to earlier in the growing season. This would allow more time for intervention by external organisations in the event of food shortages, or for governments to plan in the

event of a food surplus (Haile, 2005). It would also provide additional information for policy makers from the many seasonal weather forecasts available for the region. This is important, as “*whether through quantitative methods or a subjective process, raw climate information must be translated into information about impacts and management implications if it is to be used*” (Hansen *et al.*, 2011). In general, a forecast system will link a weather input (such as a seasonal forecast or observations) to a crop simulation model in order to predict the effect of weather and management on yield. Crop simulation models can range from simple empirical relationships between rainfall and crop yield, to complex process based models which dynamically capture the underlying phenological and physiological processes affecting a plant.

There has been a significant amount of research into seasonal crop yield forecasting. Many of these studies are undertaken at a plot or farm level, for instance Hansen and Indeje (2004), Bert *et al.* (2006) and Moeller *et al.* (2008). Although these are valuable in terms of understanding underlying crop processes and for easily testing management questions, they are often less useful at answering regional food security questions. Of interest to this work are plot based studies which test different methods of incorporating climate information into a forecast. For example, Hansen *et al.* (2004) showed that the uncertainty of a seasonal crop yield forecast diminishes as it is updated with observed weather throughout the season, and the studies of Lumsden and Schulze (2007) and Baigorria (2007) suggested how a detailed plot-based crop simulation model could be applied at a larger (but still sub-regional) scale.

There have been less attempts to seasonally forecast crop yield at a regional scale. The research is often linked to an operational forecast to allow users to address food security questions. For example the Government of Queensland issue seasonal wheat forecasts based on ENSO phase and a water stress model, Oz-Wheat (Potgieter *et al.*, 2006; Potgieter, 2011) and the European Union’s MARS-OP project issues forecasts for a range of European crops derived from the WOFOST based Crop Growth Monitoring System (Bettio and Genovese, 2004; Lazar and Genovese, 2004; Micale and Genovese, 2004;

Royer and Genovese, 2004). Finally, an interesting system in development is that presented by Nicklin and Challinor (2011) which is designed to link the GLAM crop simulation model directly to the output from a dynamical seasonal weather forecast. Please note, an overview of forecast products available for the Ethiopian case study discussed in this thesis can be found in Chapter Two.

There are several issues which must be addressed before a crop yield forecasting system can be applied operationally in Sub-Saharan Africa.

### 1.1.1. SCARCITY OF OBSERVATIONS

The first barrier to crop yield forecasting for Africa is the scarcity of climate and agricultural data. Agricultural observations such as planting date, cultivar type and historical yields are essential for the calibration of a crop model, therefore any forecast system can only be run in areas where these are available. Climate observations are also extremely important. If one wishes to forecast the yield at the time of harvest, then weather observations can be used directly as inputs to the system. If one wishes to forecast yield in advance of harvest, weather observations are used indirectly through the calibration and validation of weather forecast inputs. Crop yields normally depend heavily on the intra-seasonal distribution of rainfall; a short dry spell at the wrong time is often able to ruin an entire crop, even in a season where in general, there is enough water. A lack of detailed and timely weather information can therefore have a large impact on a crop yield estimate.

Climate observations are traditionally obtained from weather stations and rain-gauges. As shown in Section 4.1, there is a significant lack of real-time information from weather stations in Africa. There is also a lack of rainfall radars in the continent, which might have provided more detailed rainfall information. As discussed in Section 4.1, it should be noted that there is much more ‘historical’ weather information available in Africa, making it possible to calibrate and validate derived weather products. One potential answer to the lack of climate information from weather stations is to use the large amount of remotely

sensed weather data from satellites which has become available in recent years. There are several studies showing the validity of this approach. For example Thornton *et al.* (1997) successfully used METEOSAT-derived 10-daily rainfall estimates as an input to the CERES crop simulation model to forecast millet, White *et al.* (2008) used remotely sensed estimates of temperature to study the predicted time to anthesis of wheat. Finally, Teo (2006) and De Wit (2007) showed that ensembles of remotely sensed rainfall data could be used to drive the GLAM and WOFOST crop simulation models respectively.

It should be noted that one must be careful to apply satellite weather estimates at the appropriate spatio-temporal scales, an issue explored further in the Section below.

### 1.1.2. A QUESTION OF SCALE

Different types of decision makers require crop yield estimates on a variety of spatial scales. For example, a farmer wishing to test different crop management options will need an estimate of crop yield at a field or plot scale, whilst international organisations such as the UN's Food and Agriculture Organisation (FAO) are more likely to need estimates of crop yield at a regional, national or continental scale. For this reason, it is important to consider end user needs before one designs a crop yield estimation system. In the case of this work, questions about how crop yield fits into food security must be addressed at a regional or national scale.

Crop simulation models and their weather inputs also have varying spatiotemporal scales and fully integrating the two can be difficult. This is discussed in detail for a case study in the Sahel in Baron *et al.* (2005). Weather estimates range from point measurements from weather stations, to pixels of a few kilometres from satellites, to grid squares of a few degrees latitude and longitude from numerical weather models. Crop models are designed to model the response of a plant to weather and management at a certain scale. A detailed process based crop model is designed to simulate the response of weather on an 'average plant' in a field. This means that the model is conditioned to respond to point-based weather inputs, for example, long dry spells and heavy rainfall events. At the other end of

the scale, statistical models of crop yield are often designed to reflect the relationship between weather and yield at a regional or national scale, making the use of point based weather inputs inappropriate. It is easy to see how one might link weather inputs to crop models in the two examples mentioned above, but the situation becomes more complex when one considers ‘intermediate complexity’ crop simulation models. These are relatively new models, such as GLAM (Challinor *et al.*, 2004) and AQUA-CROP (Steduto *et al.*, 2009), which aim to explicitly model crop phenology and physiology, but parameterise any process which does not explicitly relate to yield. The models are designed to work at a regional scale (comparable to the resolution of a numerical weather model) and their ability to capture non-linear interactions between climate and yield makes them valuable for regional studies. These models still contain processes such as soil moisture balance or transpiration suggesting that they still require point level rainfall characteristics such as dry spells. As discussed in Section 3.4, regional averages of rainfall would change these statistics, therefore some care must be taken in selecting appropriate weather inputs. This issue is analysed in more detail for GLAM in Challinor *et al* (2003).

### 1.1.3. QUANTIFYING UNCERTAINTY

A further issue which affects crop yield estimation is that of quantifying uncertainty. This is extremely important because many communities within Africa rely on rain-fed agriculture for their livelihoods, consequently it is important for regional and national level decision makers to know how much they can trust an estimate of crop yield before they act on that information. Seasonal weather forecasts are probabilistic by nature, therefore there will always be uncertainty associated with a corresponding seasonal crop yield forecast. There will also be uncertainty in any weather observations used to monitor crop yield, either due to the sparsity of ‘on the ground’ weather data, or in the algorithms used to create satellite weather estimates. Finally there is uncertainty on the equations and assumptions within the crop simulation model itself. Quantifying the impact of climate uncertainty on crop yield is a non-trivial process, especially when one considers that the relationship between weather and crops is complex and non-linear.

Weather generators have traditionally been used to quantify the uncertainty in weather estimates at a specific site. These are stochastic models which produce an ensemble of potential seasons whose overall statistics agree with the mean climate at that location. Each ensemble member can then be run through a crop simulation model in order to see how that uncertainty in weather affects crop yield. There have been several publications which show that this approach can produce realistic results (Semenov and Doblas-Reyes, 2007; Apipattanavis *et al.*, 2010). However, as discussed in Section 10.5.4, weather generators are point-based; a weather generator run in adjacent locations would not show any spatial correlation, even though it is clearly apparent that these correlations exist in the real world. Therefore the application of weather generators to crop yield estimation at a regional scale is very much a current research question and is considered further in Part 4 of this thesis.

## 1.2 THESIS AIMS

There are two overarching themes in this thesis:

- 1) *Quantifying the uncertainty in rainfall estimates for a complex African climate, focusing in particular on the study of satellite rainfall estimation and seasonal weather forecasts.*
- 2) *Researching how the uncertainty in rainfall estimates propagates through to uncertainty in modelled crop yield.*

Researching these questions will allow a better understanding into how climate affects crop yield and will help enable operational crop yield forecasts to include the effect of climate uncertainty. However it should be noted that creating an operational forecast system for African crop yield is beyond the scope of this thesis. The general themes above can be disaggregated into the following specific aims and questions:

- a) How can satellite rainfall estimates be used as a substitute for ground based weather observations?

- b) How can the uncertainty on satellite rainfall estimates be quantified and taken through to an uncertainty in crop yield estimates?
- c) How can the GLAM crop simulation model be parameterised for tropical maize? This is needed for the case study described below.
- d) How can one create a spatially correlated weather generator which is suitable for input into a regional scale crop simulation model?
- e) How can the crop yield forecast run from observations be linked to one run from a seasonal weather forecast in order to create a system which can update throughout the season?

As it would be difficult to present generalised results for the whole of Africa, Ethiopian maize was chosen as a case study for reasons discussed in Part 1 of the thesis.

### **1.3 THESIS STRUCTURE**

The thesis is split into four sections in order to answer the questions above:

Part 1 is designed to provide an overview of Ethiopia as a case study and also describe any datasets used in the rest of the thesis. It comprises two chapters; one on Ethiopian agriculture (Chapter Two) and one on the Ethiopian climate (Chapter Three). Chapter Three also contains an overview of the geo-statistical processes used to interpolate point-based rain-gauge data to areal estimates.

Part 2 considers the use, calibration and validation of satellite rainfall estimates which can be used to monitor rainfall in the absence of a dense rain-gauge network. This aims to build on previous work by Teo Chee Kiat (Teo, 2006), who developed the methodology to create spatially correlated ensembles of satellite rainfall estimates for The Gambia. The current work aims to investigate how this methodology can be applied to a larger, more climatically complex region of Africa. Chapter Four contains a literature review of different types of satellite rainfall estimate and more detail about the chosen TAMSAT

methodology. Chapter Five contains a calibration of these rainfall estimates for the climatically complex region of Ethiopia. Chapter Six moves on to consider the uncertainty on these estimates and describes a geo-statistical methodology for creating spatially correlated ensembles of rainfall maps on each day of the season. Finally, Chapter Seven contains a validation of the estimates against an independent rain-gauge dataset.

Part 3 then applies these rainfall ensembles to the field of crop simulation modelling. Chapter Eight considers the phenology and physiology of maize plus the different crop simulation models available, before moving on to describe a new parameterisation of the General Large Area Model for annual crops (GLAM) for maize. Chapter Nine contains the results of running GLAM<sub>MAIZE</sub> using both the satellite rainfall ensembles and modelled rainfall from the ERA-INTERIM numerical model (Berrisford *et al.*, 2009). This chapter also compares these results with observations of crop yield.

Part 4 (Chapter 10) considers the application of seasonal forecasting and weather generators to the thesis aims presented in Section 1.2. In particular, the chapter discusses the structure and components of an operational crop yield forecasting system, before focussing on stochastic weather generators as a method of linking a seasonal rainfall forecasts with a crop simulation model. The final part of Chapter 10 introduces RainInt, a new methology of linking output from a point based weather generator to create spatially correlated ensembles of time-series of rainfall maps.

Chapter Eleven then concludes the work with a summary of major findings and an indication of future research directions. The thesis also contains two Appendices; these provide the full calibration for the TAMSAT satellite estimates and the definitions for statistical tests presented within the main body of the text.

## 1.4 A GOLDEN BULLET?

Finally, it would be easy to hold climate shocks responsible for the majority of African food crises. For example, Dilley (2002) notes that all recent famines in Africa requiring large-scale external food aid have been attributed fully or partially to extreme weather events. However, it should be noted that although it is important to be able to forecast and monitor weather and quantify its impact on agriculture, this is not food security's 'golden bullet'. Even a perfect forecast and accurate monitoring of crop yield might not alleviate a food security crisis (Sen, 1983).

For example, the FEWS-NET summary of the 2011 Somalian famine is that "*The eastern Horn of Africa has experienced two consecutive seasons of very poor rainfall, resulting in the worst drought in 60 years. Crops have failed, livestock deaths are widespread, and food prices are very high . . . This is the most severe food security emergency in the world today*" Fews-Net, 2011. When the situation was analysed in more detail, it became apparent that the current failure of the Somalian rains was well forecast in enough time for decision makers to take action (I.R.I., 2011), but compounding political and socio-economic problems have turned a poor harvest into a famine. This view is echoed in a recent article in the Lancet, which suggests that the primary problem is not a lack of food, but high prices, conflict, lack of access and market breakdowns putting food out of reach of poor people (Loewenberg, 2011).

Therefore although the results presented in this thesis are presented in the context of food security and will add to the published body of work on crop yield estimation, it should be kept in mind that even a fully operational, perfectly calibrated system would still have to be implemented alongside other food security measures to have a significant impact on the ground.

---

---

# PART 1

# OBSERVATIONS

This Section of the thesis is designed to provide an overview of Ethiopia as a case study and also describe any datasets used in the rest of the thesis. It is comprised of two chapters:

*Chapter Two* (Ethiopian Agriculture & Crop Forecasting) discusses Ethiopia's socio-economic status, current crop yield forecasting systems, calendar and agronomy. It also describes the yield, area planted, production and planting date datasets.

*Chapter Three* (Ethiopian Climate and Observations) describes Ethiopia's topography and climate. It also discusses rainfall and synoptic meteorology datasets. Finally, geostatistics and kriging are introduced to the reader.

# CHAPTER TWO

# ETHIOPIAN AGRICULTURE

# & CROP FORECASTING

This chapter gives an overview of Ethiopia and its suitability as a case study, before moving on to describe the country's agronomy and any agricultural data-sets that are used in the thesis.

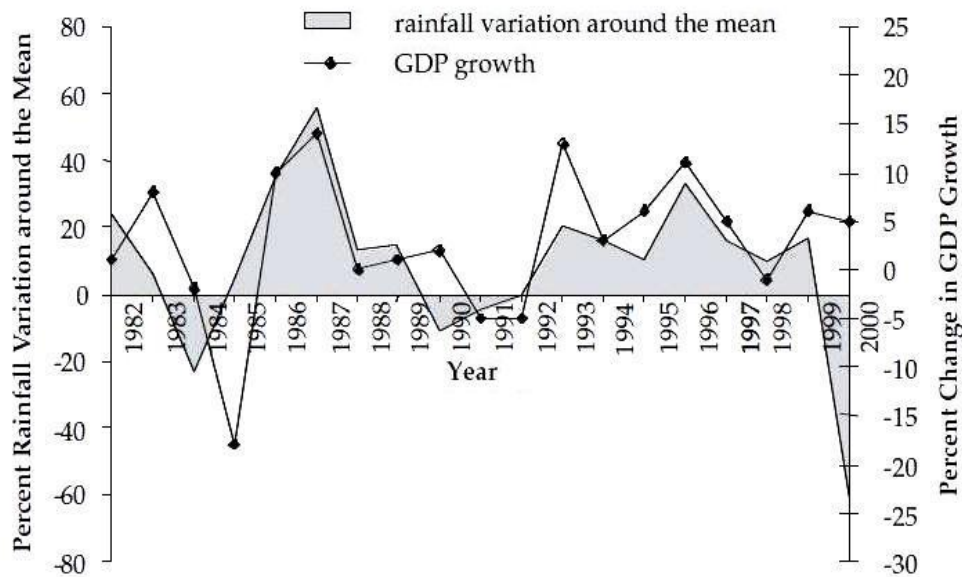
## 2.1 OVERVIEW

*"The agricultural sector remains our Achilles heel and source of vulnerability...  
Nonetheless, we remain convinced that agricultural based development  
remains the only source of hope for Ethiopia."*

Meles Zenawi, Prime Minister of Ethiopia, April 2000 (Devereux, 2000).

Ethiopia is one of the least developed countries in the world; over 77% of its inhabitants rely on less than \$2 per day and much of the population is dependent on climate sensitive activities for income (Kaluski *et al.*, 2002; Regassa *et al.*, 2010). In particular, the economy is strongly reliant on rain fed agriculture. For at least the last 20 years, it is estimated that 80-85% of the population is employed within the sector, which contributes approximately 50% towards Ethiopia's Gross Domestic Product (GDP) (Deressa, 2006, Getahun, 1978; Regassa *et al.*, 2010; Kaluski *et al.*, 2002; Araya and Stroosnijder, 2011). Figure 2.1 shows that the impact of rainfall on the country's GDP and Dercon (2004) independently records a strong link between Ethiopia's economy and rainfall, although it

should be noted that the methodology behind this Figure is somewhat opaque and that it is currently being re-made using an updated dataset.



Source: Compiled from SIMA and African Rainfall and Temperature Evaluation System data.

**Figure 2.1. Rainfall variability and Gross Domestic Product in Ethiopia. Plot taken from World Bank, 2006.**

The result of these links between weather and economy means that a poor harvest can have a significant impact on livelihoods and food security. Factors which lead to a poor harvest include soil fertility (Zelleke *et al.*, 2010), drought (Gebrehiwot *et al.*, 2011 and Araya and Stroosnijder, 2011) and a lack of management options such as fertilizer. In particular, Tilahun (1995) suggests that large scale crop failure can be attributed to water stress incurred when there is a dry spell concurrent with flowering. It should be noted that although there are also well recorded floods in the country, which will undoubtedly have had a large effect on agricultural systems (British Broadcasting Corporation, 2006), there has been little quantitative research into the scale of this impact. Lack of or erratic rain is also regarded as the most important hazard by small holder farmers as seen in Figure 2.2.

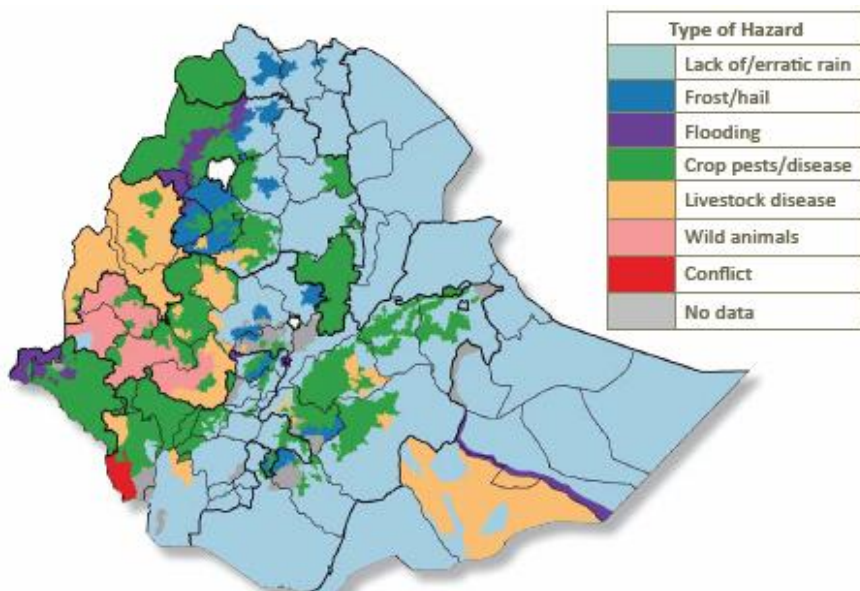


**Figure 2.2. Perception by over 50,000 small holder about the most important hazard affecting their crop. Plot courtesy of the ‘Atlas of Ethiopia Livelihoods’ (Laurence, 2010)**

As considered in the Introduction, the ability to predict crop yields on a time scale of months would be of enormous benefit to users in Sub-Saharan Africa. Kaluski *et al.* (2002) shows in a report on Ethiopian food security, that this is particularly the case in Ethiopia:

*“Food aid can make a meaningful contribution when the presence of famine is identified and reported on time. Expanded and improved early warning systems can predict and direct the preparedness for emergencies. This calls for a centralised data collection with emphasis on early warning indicators supported by effective mapping, rather than on late indicators, such as anthropometric measurements.”*

This capability is only just starting to be present in Ethiopia. The country currently has two methods of monitoring and forecasting crop yield in advance of harvest. The first is an operational Crop Yield Monitoring and Forecasting System (CYMFS), run by the Ethiopian National Meteorological Agency (NMA) in conjunction with the European Union Joint Research Council (JRC) and the Food and Agricultural Organisation (FAO). The system is discussed in detail in Rojas *et al.* (2005), but in short, it combines a Geographical Information System (GIS), the FAO Crop-Specific Water Balance (CSWB) model, the JRC Crop Production System Zones database (CPSZ) and meteorological

information from numerical models provided by the European Centre for Medium-Range Weather Forecasts (ECMWF). Additional and independent real-time Normalised Difference Vegetation Index (NDVI) satellite data from SPOT VEGETATION is also incorporated, using a specific crop mask to concentrate the analysis only on agricultural areas. This crop mask was derived from a static CPSZ database which itself was created using survey data, therefore the NDVI data was simply used to look at plant conditions throughout the season. The technique performed well in trials and is easily applied over Ethiopia (Rojas *et al.*, 2005, Funk *et al.*, 2003), but has several potential shortcomings. The first is its reliance on an empirical CSWB model rather than a process based crop simulation model. As discussed in Challinor *et al.* (2004), empirical crop simulation models are less likely to capture complex non-linear interactions between crop and climate. Teo (2006) also showed that a CSWB model performed less well than a process based model when forecasting groundnut yield over The Gambia. This was because the CSWB model was unable to capture yield loss associated with short duration dry spells that occurred during flowering. The second potential problem is that, as discussed in Section 9.4 and in Maidment *et al.* (*in press*), ECMWF modelled rainfall products such as ERA\_INTERIM and ERA\_40 appear to significantly underestimate or overestimate precipitation over East Africa, which might introduce bias into the CYMFS results.

The second method used by the Ethiopian authorities to monitor crop yield is described below in a personal communication from Mr Habekiristos Beyeyne, the crops team leader at the Central Statistical Agency (CSA). This is the body charged with providing the Ministry of Agriculture and Rural Development (MoARD) with accurate pre-harvest crop yield information.

*“At the time of harvest for either cropping season, the CSA will invite key stakeholders such as farmers unions, NGOs & external organisations (FAO) to a meeting to discuss how the season has developed. These stakeholders are asked to agree a percentage change in perceived crop yield from the previous season. For example, it might be decided that the crop yield in Tigray during 2009 is 80% of the crop yield in Tigray during 2008.*

*This number is then multiplied by the previous year's yield to give a 'pre-harvest estimate'" (Beyeyne, 2009).*

These estimates can be highly subjective and dependent on the agenda of stake-holders but are widely used by Ethiopian decision makers.

Ethiopia was chosen as case study for this thesis because it will allow the results of the work to be applied to help improve current operational systems. In particular, the inclusion of a process based crop simulation model and satellite rainfall estimates is a new approach compared to the current CYMFS. The ability to incorporate uncertainty in the estimates is also novel, as is the ability to link a statistical seasonal forecast to the system to give an estimate of crop yield before the start of the growing season. A second reason for choosing Ethiopia as a case study is because it has a complex climate and agronomy, as discussed in this chapter and the next. Therefore one might expect the process based approach described in this work to have greater skill than the simpler operational methods currently in force. In addition, as described in Section 2.5 and Section 3.2, Ethiopia appears to be one of the few Sub-Saharan countries with enough climate and agricultural data with which to design and test the system.

## **2.2 TOPOGRAPHY AND REGIONS**

Ethiopia is located in Sub-Saharan Africa, between 33 - 48° longitude and 3.5 - 15° latitude. It is a country dominated by a complex topography; the Great Rift Valley stretches from North West to South East, cradled by the butterfly of the Ethiopian Highlands. The lowlands in the west of the country are comprised of the Somali and Danakil Deserts and are widely uninhabited (Laurence, 2010). As shown in Figure 2.3, altitudes range from below sea level to over 4000m within a few hundred kilometres. Topography also appears to be a major factor behind the placement of administrative regions and zones, probably because different ethnic groups would have originally used topography and rivers as tribal boundaries. Ethiopia is split into 9 regions and 2 cities as shown in Figure 2.4. each region is then split into zones and further sub-divided into woredas (equivalent to small districts).

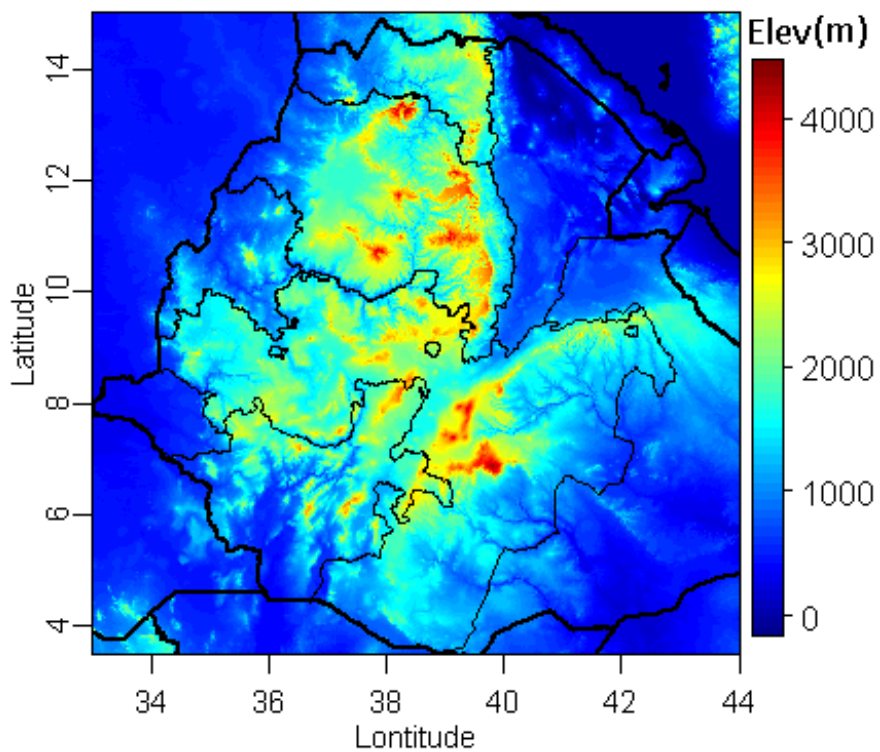


**Figure 2.3. Elevation map of Ethiopia. Country borders are shown as thick lines, whilst regional boundaries are shown as thin lines.**

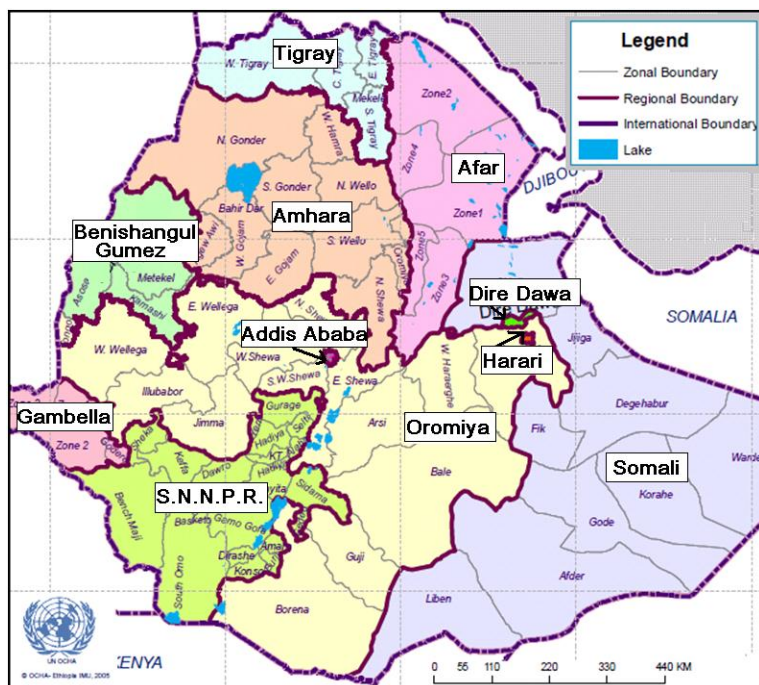


**Figure 2.4. Ethiopian regions. The zones which make up each region can also be seen.**

## 2.3 ETHIOPIAN AGRICULTURE

### 2.3.1. BACKGROUND

Chapter Three describes the complexities of the Ethiopian climate. This diversity in weather and topography leads to an equally diverse cropping system, over 95% of which is inter-cropped and rain-fed (Deressa, 2006). There are six staple crops cultivated in Ethiopia: maize, millet, teff, sorghum, barley and wheat (Rosell, 2011) and the proportion of the total area planted of these (out of all cereals) can be seen in Figure 2.5. Of the staple crops, teff (*Eragrostis tef*), and maize (*Zea Mays*), are considered to be the two most important for food security. Teff is a C4 grass originating from the Ethiopian highlands and is generally regarded as Ethiopia's most important staple food crop (Habtegebrial *et al.*, 2007). However, it is unusual to see the crop grown outside Ethiopia and it has received relatively little attention from developers of crop simulation models. There has recently been an attempt to incorporate the crop into the FAO's AQUACROP model (Araya *et al.*, 2010), but the author of this thesis knows of no parameterisation for any detailed process based crop simulation model. Therefore, it would be extremely difficult to use teff as the basis of this work.

Maize (otherwise known as corn), is now rivalling teff as the main staple food crop in Ethiopia, due to its higher nutritional value and rising teff prices. This shift can be seen particularly in the short spring Belg crop in Figure 2.5. Maize is also important for regional food security, for example Ethiopia produces 44% of maize in the IGAD sub-region (consisting of Ethiopia, Sudan, Somalia, Eritrea, Somalia, Kenya and Uganda). Finally, as detailed in Section 8.2, maize has been exceptionally well studied and modelled. Consequently the crop has been chosen as the primary crop for this body of work.

There are two main agricultural periods in Ethiopia:

***Belg season***

This occurs primarily during February, March and April to correspond with the Belg rains. It generally consists of short season crops and out of the six staple food crops, short cycle maize is considered the most important (Figure 2.5). Although the season is considered important as a hunger breaker (DPPC, 2003), the Belg season accounts for only 3% of total production (Taffesse *et al.*, 2011). Due to this and because it is also difficult to estimate Ethiopian rainfall during January and February (discussed in Section 5.4.1), it was decided to only concentrate on the Meher season in this thesis.

***Meher season***

This is the main agricultural season in Ethiopia and is dominated by teff and maize grown during the summer Kiremt rains. The maize crop includes a mix of long and short cycle crops. Funk *et al.* (2005) describes the system in more detail:

*“Meher crops are typically harvested in September or October. Short cycle maize and sorghum are typically planted between April and July. Long cycle crops are planted during the Belg season and harvested following the Meher in late fall. ... Given sufficient agricultural inputs they are often substantially (1.5-2.5 times) more productive than short cycle varieties planted during the Meher season. Long cycle crops contribute approximately 50% of national production, compared to 40-44% for ‘short-cycle’ (June-September) varieties”.*

Unfortunately the agricultural data provided for this thesis does not distinguish between short cycle and long cycle crops during the Meher season, but the existence of the two cultivars should be born in mind during the analysis. Figure 2.6 shows the number of agricultural seasons across Ethiopia and Figure 2.7 shows the resulting cropping system. Although this seems exceptionally complicated, most maize is grown in the North and Oromiya region, where there is either a short-season Meher crop or a long-season Meher crop (e.g. plant in Belg and harvest in Meher). There is very little cultivation in the West as this is the location of the Somali desert.

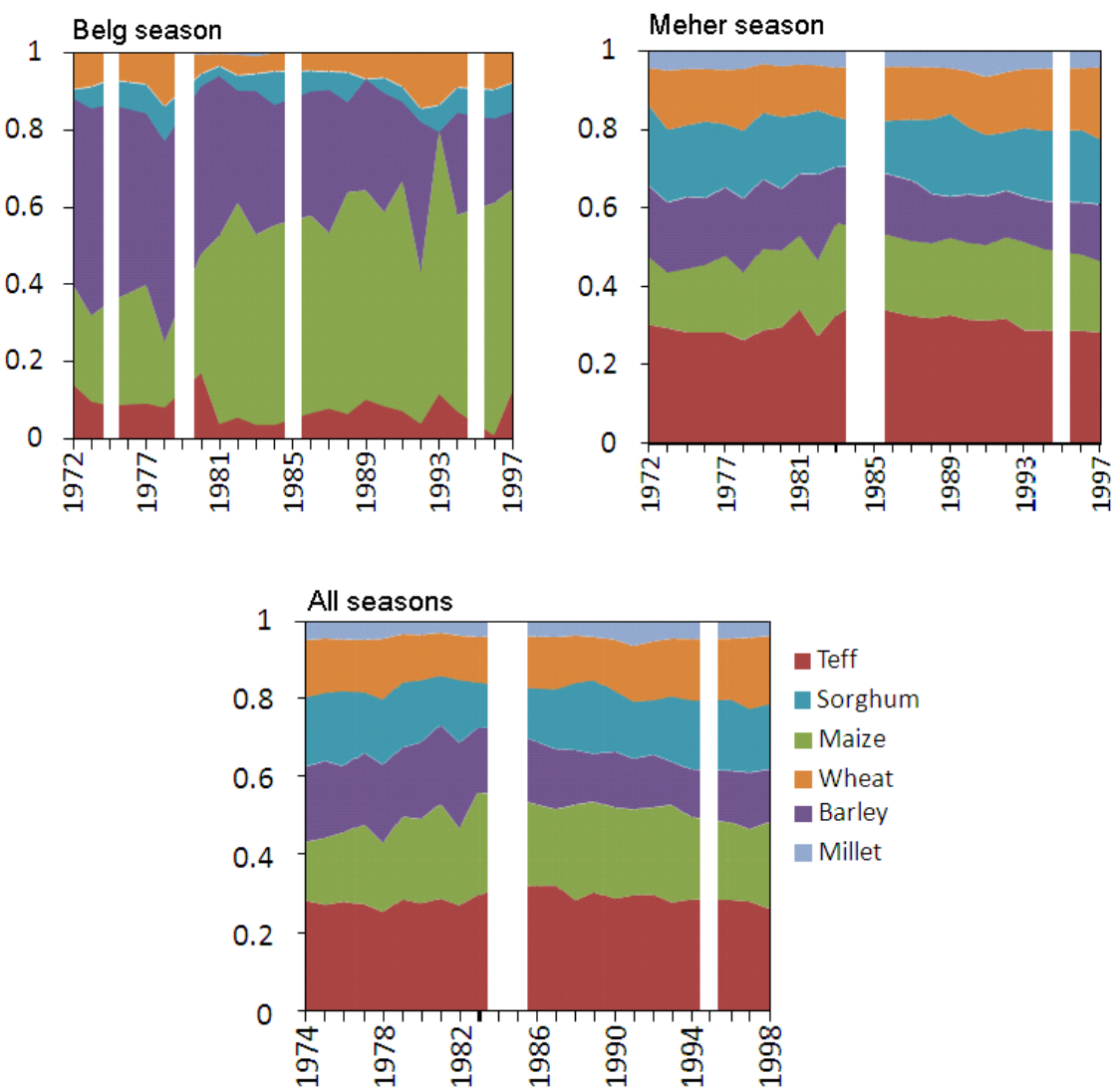


**Figure 2.5.** Time-series of the proportion of the area planted (out of the area dedicated to cereals in Ethiopia), which is assigned to each crop. The year (x-axis) is in the Ethiopian calendar format, discussed in Section 2.4. Data courtesy of the Central Statistical Agency of Ethiopia.

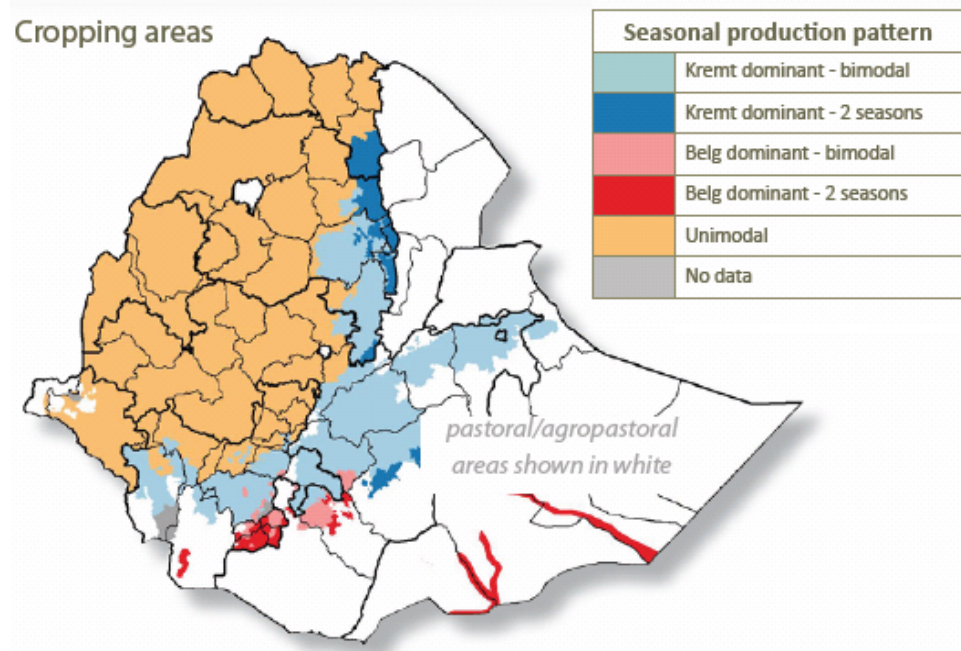


Figure 2.6. Number of planting seasons in Ethiopia. Plot courtesy of the ‘Atlas of Ethiopia Livelihoods’ (Laurence, 2010).

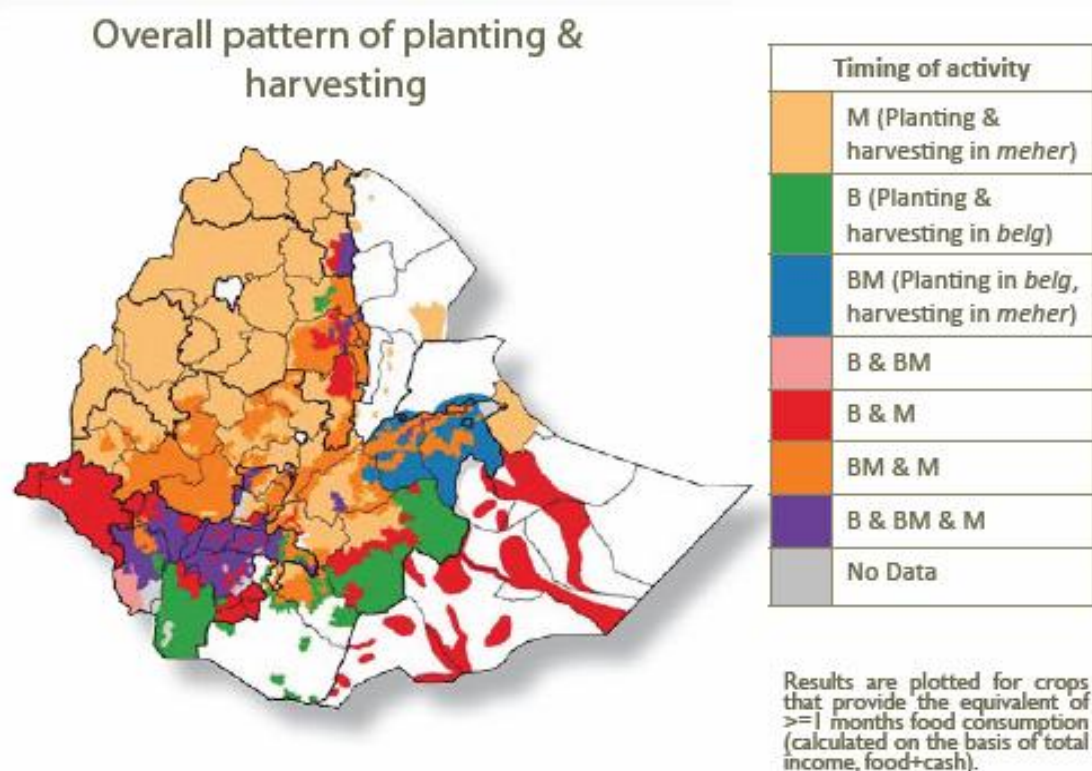


Figure 2.7. Overall pattern of planting and harvesting in Ethiopia. Plot courtesy of the ‘Atlas of Ethiopia Livelihoods’ (Laurence, 2010).

## **2.4 ETHIOPIAN CALENDAR**

In order to avoid confusion when considering observed datasets in Ethiopia, a little must be said about the Ethiopian calendar. The Ge'ez calendar is based on a Coptic system rather than the Gregorian system adopted in most of the world. In Ethiopia the first day of the new year, for years between 1901 and 2099 (inclusive), is usually September 11th, but falls on September 12th in years before a Gregorian leap year. There is also a 7-8 year gap between the Ethiopian and Gregorian calendars due to a different determination of the birth of Jesus. Therefore 01/01/2000 in the Ethiopian calendar falls on the 12/09/2007 in the United Kingdom. Finally, the Ethiopian calendar has 13 months, 12 of which have 30 days and the 13<sup>th</sup> comprising of the extra days in that year.

The use of a different calendar can presents significant confusion when recording observations, especially when considering agricultural statistics. These are normally recorded for the year that the crop was harvested, but as the Ethiopian new year falls in September, the Belg harvest period is March-May and the Meher harvest period October-December, reported statistics can easily become confused. In this thesis, all dates have been converted to the Gregorian calendar.

## **2.5 CROP PRODUCTION, YIELD AND AREA PLANTED DATA**

The Central Statistical Agency of Ethiopia (CSA) have kindly provided national level area planted, production and yield data from 1980–2005 for over 26 crops. They also provided a regional level area planted, production and yield dataset from 1999-2005. In conjunction with these, there is also an FAO national level dataset available from 1960 to the present day. This Section describes the data for maize, plus some initial quality control and data analysis. It should be noted that this thesis has concentrated on the period from 1999-2005 to agree best with both the observed climate datasets discussed in Chapter Three and with the regional yield dataset.

### 2.5.1. DATA COLLECTION

Agricultural data collection is a complex business in Ethiopia. Until recently, the CSA and Ministry of Agriculture (MoARD) have worked independently to produce crop yield and production estimates. Due to their different collection methods, the two sets of results diverged significantly. The CSA collects yield and area planted information each year at a national, regional and zone scale, which is then converted into production statistics. The CSA uses ‘probability agriculture surveys’ to find this information, which involve taking crop cuttings on a sample of approximately 600,000 fields per year. The sample is chosen using rigorous statistical methods which are described in detail in Mottram *et al.* (2005). MoARD directly collects production and area planted estimates at a woreda scale using subjective interviews and local units to create a dataset known as CSFAM. These are then averaged up to zone, region and national level. Yield is estimated from the production and area planted. Although the MoARD dataset includes important information at a woreda scale, they are much more subjective than the CSA estimates. However, they were frequently scaled up to regional and national scales and could differ greatly from CSA figures as shown in Figure 2.8 (Zekaria *et al.*, 2009).

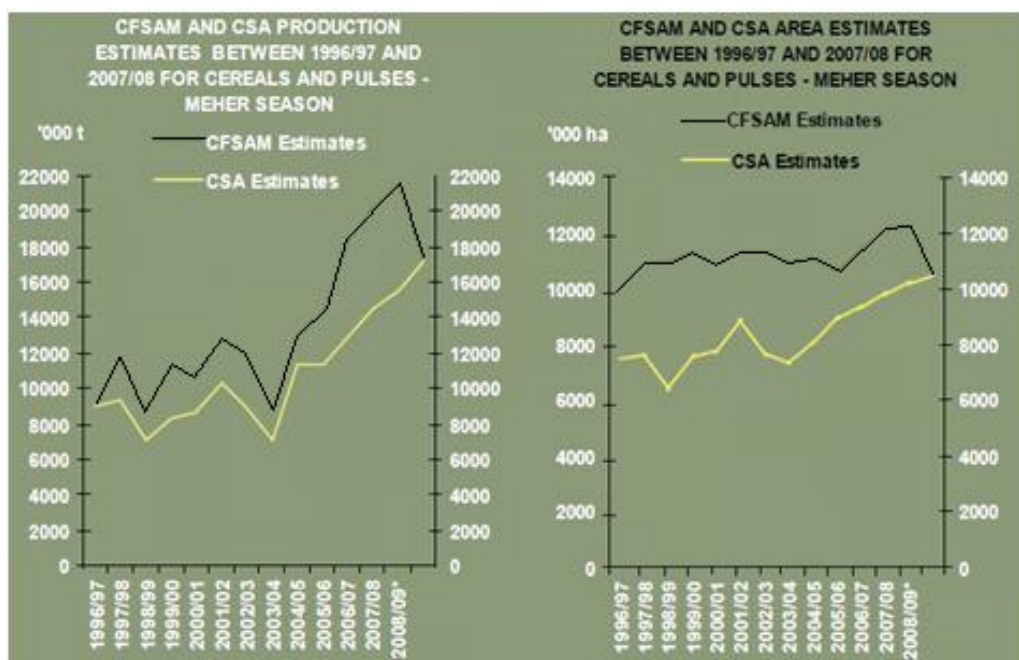
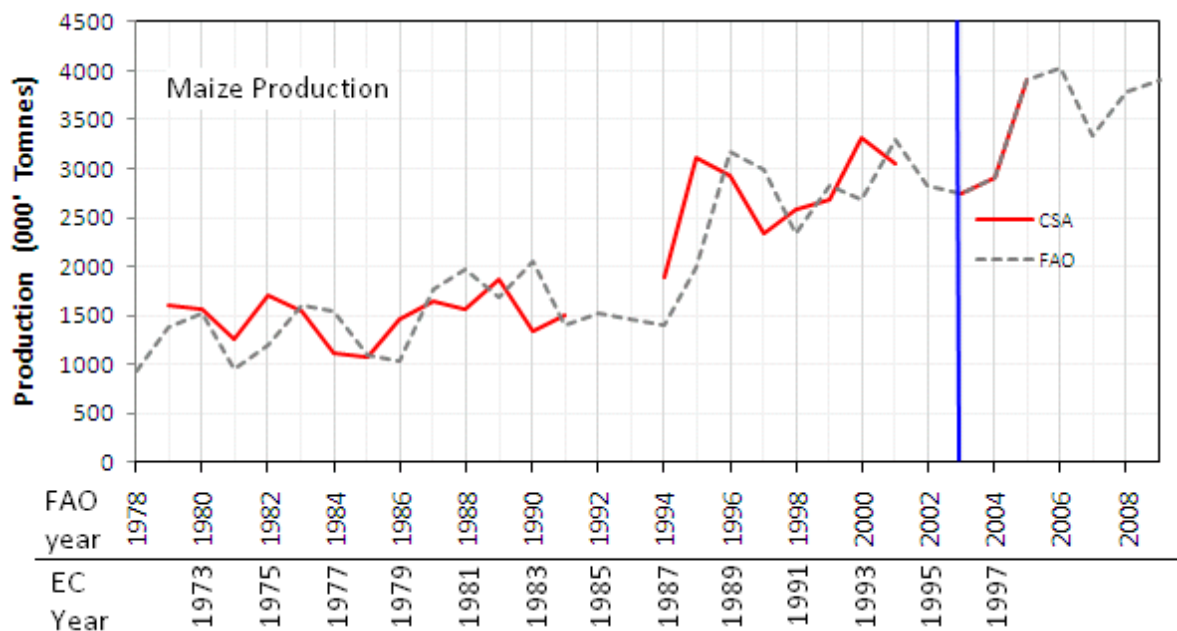


Figure 2.8. CSA and FAO/Ministry of Agriculture production and area planted for cereals and pulses in the Meher season. Plot taken from Zekaria *et al.* (2009).

Before 2008, the FAO used the MoARD dataset for national yield statistics. However there has been a recent European Commission funded project entitled “Support to Food Security Systems in Ethiopia”, which has linked the FAO, CSA and MoARD to create an integrated crop yield estimation system (Zekaria *et al.*, 2009). This applies CSA methodology at large scales and MoARD methodology at the woreda level. The FAO appear to have now recently replaced their archive with the CSA estimates.

### 2.5.2. NATIONAL LEVEL DATA ANALYSIS

When the FAO and CSA national production datasets were first compared, there appeared to be a mis-match in dates before the year 2003 (shown in Figure 2.9). This was echoed in the CSA regional dataset.



**Figure 2.9. Original time-series comparison between the FAO and CSA annual maize production statistics. There appears to be a mismatch in dates before 2003. The FAO year corresponds to the Gregorian calendar used in the UK. EC year corresponds to the Ethiopian year used in the CSA dataset.**

The mismatch in years is undoubtedly due to the Ethiopian calendar conversion, which is especially confusing when Western dates are recorded in the ‘2005-2006 season’ format, because the Ethiopian growing season occurs entirely during one Gregorian year but over two Ethiopian years. The issue is also important to resolve correctly as the aim of this

study is to link the crop yield and climate, so as a result, some time has been spent attributing the correct season to the correct year before 2003.

The first piece of evidence to solve this puzzle comes from the study of Funk *et al.* (2003) which presents a similar time-series for all cereal and pulse crops during the summer Meher season. These are compared with an equivalent dataset provided for this thesis in Figure 2.10, which seems to suggest that it is the original CSA yield time-series which are correct. The argument is particularly convincing because the paper presents evidence to show that these yields could be predicted using a regression against spring rainfall amount. Interestingly, the presented dataset contains a value of crop yield for the year 2002 which was recorded as missing in the dataset obtained for this thesis. If this value of yield also holds for maize, which seems reasonable considering Figure 2.10, then it suggests that 2002 was a particularly bad year for Ethiopian agriculture. The drop in yield in 2002 is also reflected in the final results of this thesis in Section 9.7, which perhaps adds more weight to the argument that the CSA yields are correct.

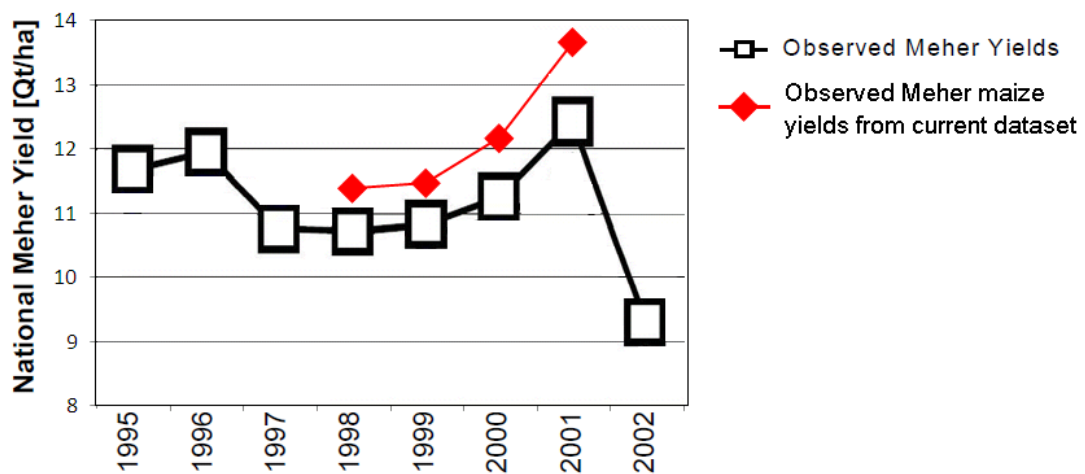


**Figure 2.10.** Meher maize yield obtained from the CSA for this project (red). Meher yield for all cereals and pulses from Funk *et al.*, 2003 (white squares). The source of this yield data was also quoted as the CSA.

In spite of the case presented above, there is a significant amount of evidence to suggest that the FAO have the correct dataset. The maize market assessment and baseline study for Ethiopia (US-AID, 2003) is quoted as saying that:

*“Ethiopia did not take advantage to export large quantities of maize to these regions even when it had production glut in 1995/96, 1996/97”.*

Mariam (2002) also published maize production figures attributed to the CSA where the value for the 1998/1999 season matched up to the 1998 value depicted in Figure 2.9. Finally, it appeared unusual that there were no CSA statistics recorded in 2002, even though it was not a census year (during which all CSA resources are drawn into a household survey), although there is some evidence to suggest that an agricultural census was taken that year in Admass, 2004. Therefore it might be reasonable to assume that before 2003, the CSA had reported the year of planting, whilst after the FAO collaboration, they have reported the year of harvest.

With no additional information, it was decided that the degree of uncertainty about which time-series is correct was too high to choose one decisively over the other. Therefore, for the rest of this Chapter, the CSA yields were changed to match the FAO time-series, but both ‘observed’ time-series are included in the comparisons with modelled yield in Chapter Nine. In light of the discussion presented above, years after 2003 were also checked for consistency. For example 2004-2005 was reported as a ‘bumper year’ for maize, with production estimates up by 21% on the average for the preceding 5 years (Riddle, 2005). This agrees well with the picture presented in Figure 2.9.

National level crop production, yield and area planted for maize are shown in Figure 2.11. These include shifted annual estimates from the CSA, plus those for the Meher and Belg seasons. Annual estimates from the FAO are also shown (red dotted line) and now agree reasonably well with those from the CSA, although in 2002 the FAO estimate seem to include just the Meher production. The largest feature in the plot is Ethiopia’s shift from the People’s Democratic Republic of Ethiopia to a new government in 1991 and the subsequent increase in planting area. Belg maize yields appear to be significantly lower than those in the Meher season. This is because short season maize is grown in the Belg season compared to the mix of long and short season maize in the Meher season, thus Belg plant have less time to develop and so tend to be smaller with lower yields.

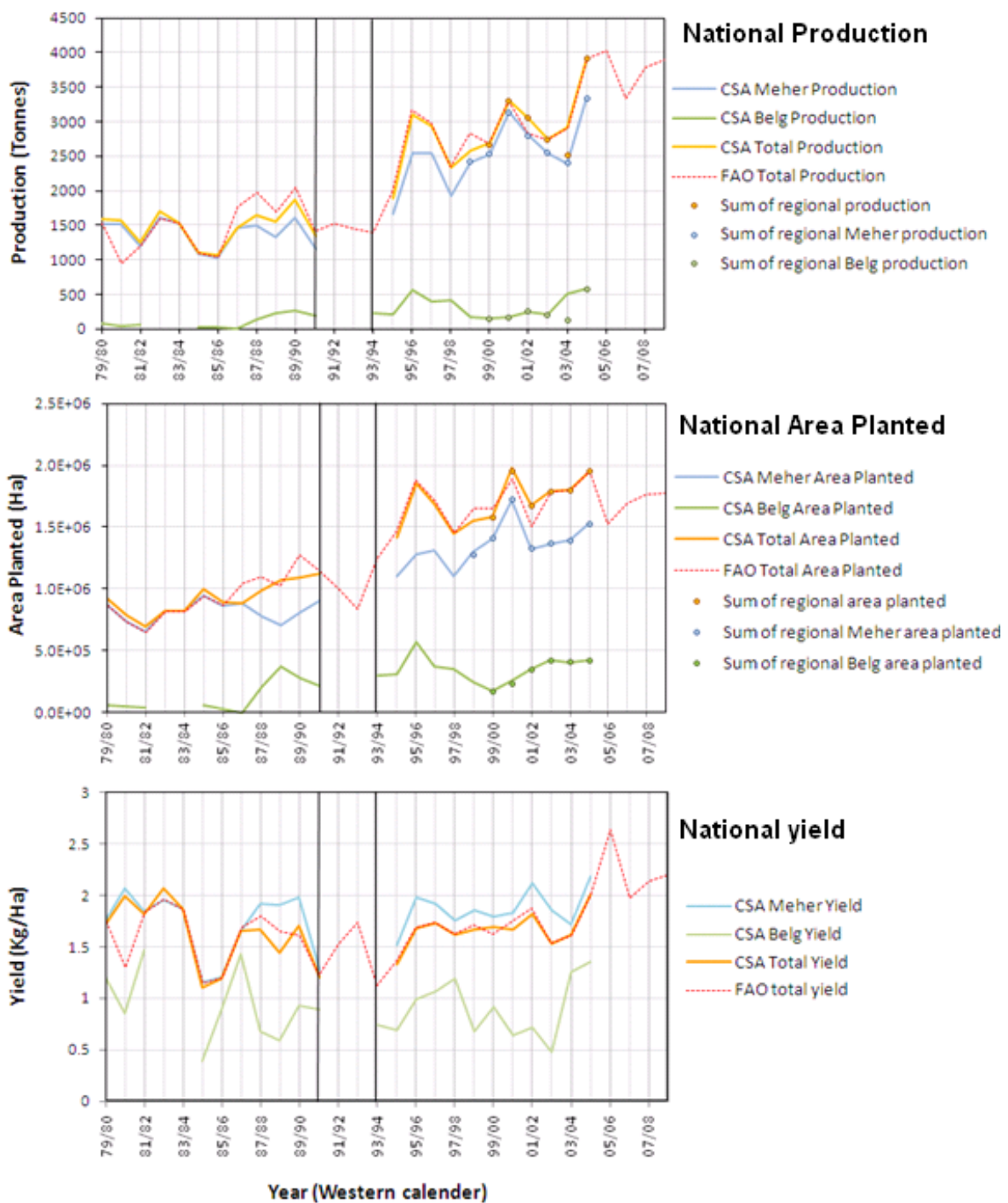


Figure 2.11. Maize production, area planted and yield from the corrected CSA and FAO datasets. The breakdown of the CSA data into Belg and Meher seasons is also included. Prior to 1991, Ethiopia was part of the People's Democratic Republic of Ethiopia. There was then a period of transition before a new government formed in 1994 where it was difficult to collect agronomic data. This is denoted by the black lines on the plot. The dates are from the western calendar and are recorded in the '05/06 season' format, because the Ethiopian growing season entirely occurs during one Gregorian year but over two Ethiopian years, thus it was difficult to assign a year when converting from the Ethiopian calendar as described in Section 2.5.2.

### **2.5.2.1. Technology trends**

The majority of large scale crop simulation models are designed specifically to look at the relationship between climate and crop yield, therefore the observed yield data used to calibrate the models should not include variation from other factors such as politics or technological advance. In general these are filtered out using a linear model to de-trend the dataset (Challinor *et al.*, 2004, Li *et al.*, 2010), however care must be taken to ensure that the long term variability is not due to climate. In the Meher crop yield dataset needed for this thesis, there appear to be three regimes. Before 1991, there is a steady decrease in yield which corresponds to the collapse of the Derg regime. In the period of political transition between 1991 and 1994, there was very little data available and so these years are not available for analysis. Between 1995 and 2004 which is the time-period of interest for this work, there appears to be a small upwards trend in yield, however when a linear model was applied, it was not found to be significant when compared to no trend (an F-test was applied which gave  $p(>F) = 0.16$ ). Therefore for national yields for the Meher season, no trend was applied. The assumption that there is no technology trend in Ethiopia appears to be reasonable as it is still a country dominated by small holder farms with limited access to technology. In addition, there has been very low investment in agricultural development (Laurence, 2010).

### **2.5.3. REGIONAL LEVEL DATA ANALYSIS**

As described at the start of this section, the CSA also provided a regional level dataset from 1999-2005 comprising of area planted, production and yield. This also suffered from the same dating issue discussed in Section 2.5.2 and has been shifted to match the FAO data. The sum of the regional area planted and regional production have also been plotted against the national level statistics in Figure 2.11. These in general show very good agreement, which inspires confidence that the regional data is complete and consistent with the national data. One difference can be seen in 2003/2004 production, which was diagnosed as missing data for the Belg season in the S.N.N.P.R region. As shown in Figure 2.12, only a few of the 11 regions described in Section 2.2 grow maize as a major crop. In particular, Oromiya, Amhara, S.N.N.P.R. and Tigray make up 97% of national production.

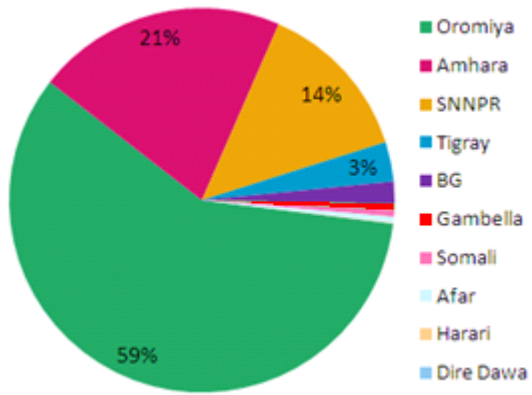


**Figure 2.12. Proportion of average Meher maize production (from 1999-2005) that is attributed to the different regions in Ethiopia.**

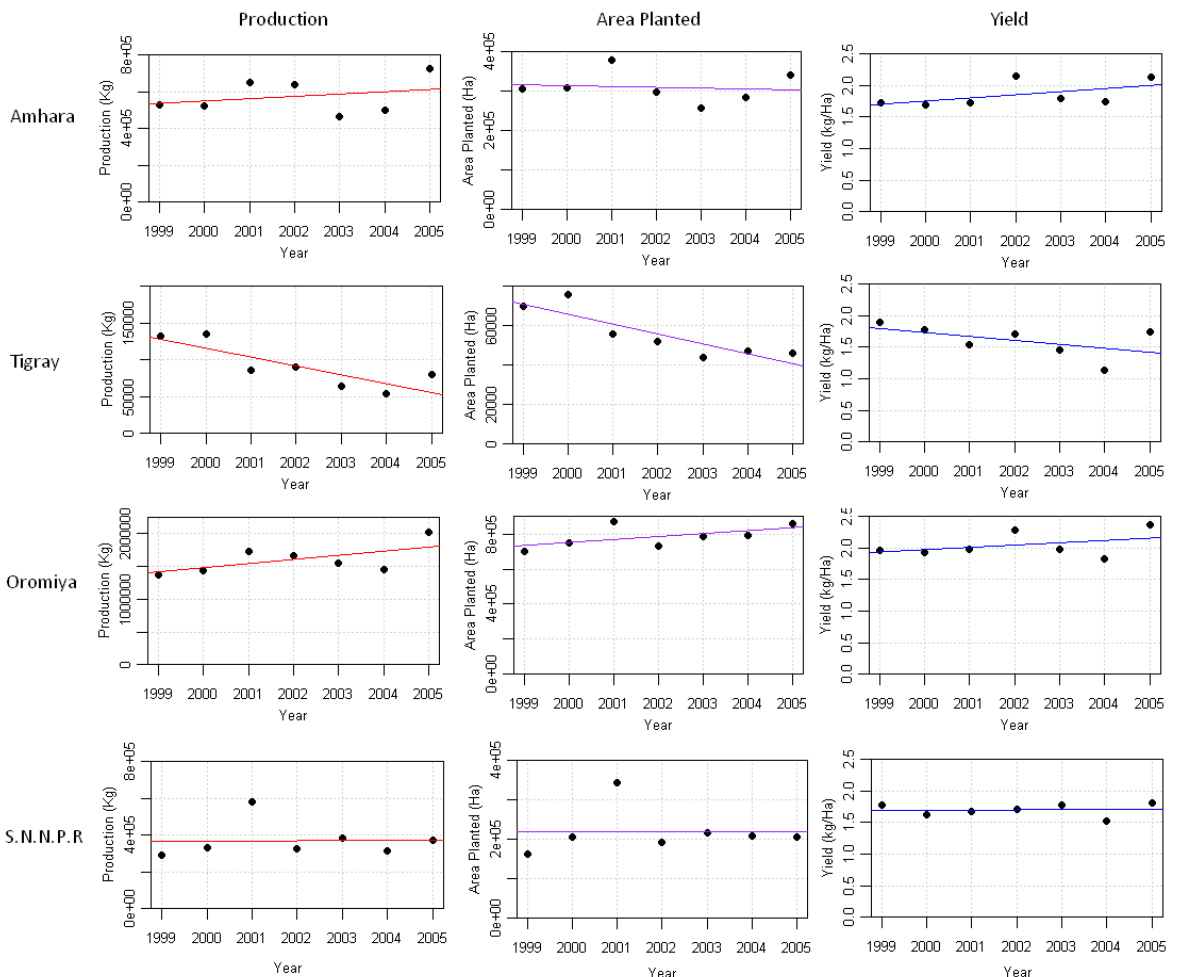


**Figure 2.13. Yield production and area planted for the 4 main maize growing regions. Linear fits are also shown for each case but none was found to be significantly better than a flat line (minimum  $P(>F) = 0.22$ ). Please note the differing scales in the production and area planted plots. The year corresponds to the year of harvest.**

The yield, area planted and production for the four main regions are shown in Figure 2.13. As shown in the overall statistics, there is no apparent technological or socio-economic trend. In addition, the S.N.N.P.R region seems to be resilient to any external factors during this time period including climate, because its yield is constant at 2 kg/Ha. Because of this and because of the complexity of the S.N.N.P.R cropping season shown in Figure 2.7, this region has been excluded from further study.

## **2.6 PLANTING DATES AND SEASON LENGTH**

The complex nature of the agricultural system described above leads to significant differences in planting date and season length across the country. These were defined, along with the exact pixels where maize is grown, using the MoARD Livelihoods Integration Unit (LIU) "Livelihoods of Rural Ethiopia" database (MacAskill, 2006). This assigned a geographical and wealth derived 'livelihood zone' to each farmer in Ethiopia and then surveyed approximately 50,000 farmers sampled from the zones between 2005-2009. The data was then interpolated to a  $0.25^\circ \times 0.25^\circ$  grid. The area planted, planting date and length of season are depicted for maize in the Meher season in Figure 2.14 and Figure 2.15. The detailed socio-economic nature of the dataset means that they are likely to be reasonable and realistic. The plots have also captured the winter maize season in the Somali region which occurs during the late Kiremt (or Deyr) rains in the area. As shown in Figure 2.12, there is also very little maize planted in the Somali region therefore it has been excluded from this study.

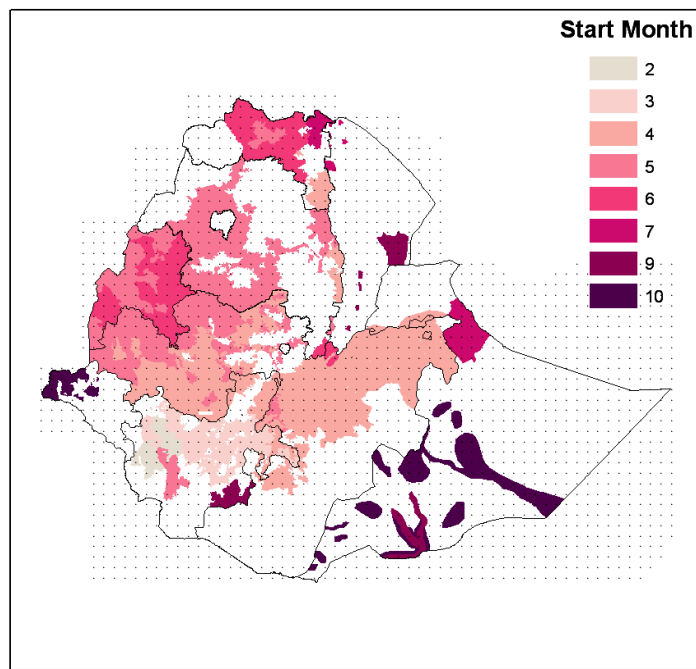


**Figure 2.14.** Planting month and area cultivated for maize in the Meher season. Any areas which are planted after August have been excluded from this study as it would be reasonable to assume that they are a very different cultivar than the longer season crops.

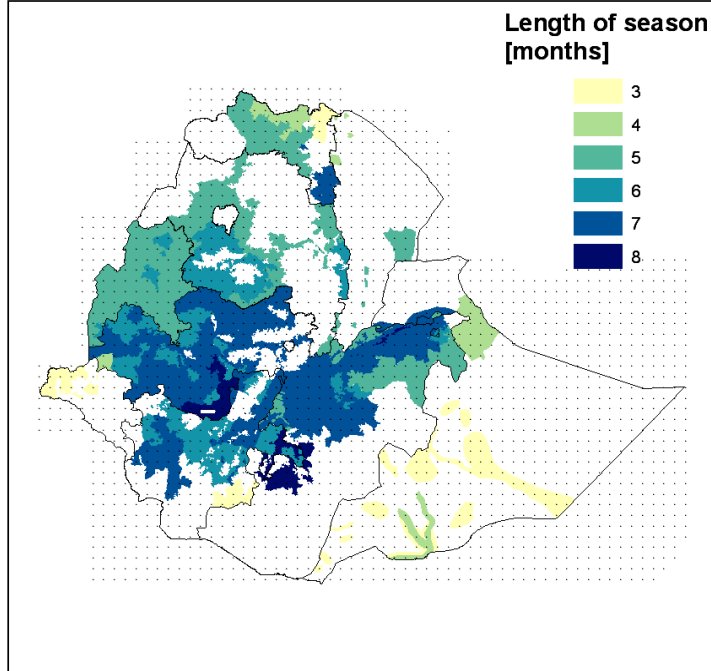


**Figure 2.15.** Season length for maize in the Meher season.

## **2.7 CONCLUSION TO CHAPTER TWO**

The country of Ethiopia is reliant on rain-fed agriculture, therefore the ability to forecast and monitor crop yield would be extremely beneficial. There are two current systems, a process-based crop yield monitoring and forecasting system run by the National Meteorological Agency, plus a more subjective system run by the Central Statistical Agency. Maize and teff are dominant food crops in Ethiopia, thus these are of the most interest in an operational crop yield forecasting system for food security decisions. Due to the rarity of teff on a global scale and the difficulty in parameterising it for crop simulation modelling, maize has been chosen as the main crop in this thesis.

Crop production, area planted and yield data has been made available by the Ethiopian Central Statistics Agency from 1980-2005. This data appears to be robust, although there was a discrepancy between the CSA and the FAO about which year corresponded to each value of yield, probably due to the complexities of calculating the correct year from the Ethiopian calendar. Regional level data was also made available by the CSA between 1997 and 2005. This shows very little year to year variability, even though there is a well documented link between rainfall and Ethiopia's agriculturally-based Gross Domestic Product. Finally, planting date and season length data was presented on a  $0.25^\circ \times 0.25^\circ$  grid.

# CHAPTER THREE

# ETHIOPIAN CLIMATE AND

# OBSERVATIONS

This chapter gives an overview of the Ethiopian climate and describes any climate-related datasets used in this thesis. It also provides an overview of kriging, which is the chosen method of spatial interpolation for the rain-gauge datasets.

## 3.1 OVERVIEW

Ethiopia is one of the most climatically complex countries in Africa. This is in part due to its topography, but also because of the country's placement with respect to large scale weather patterns. There are three seasons which affect the country:

- The dry spell running from October to January is called the Bega season.
- The Belg season is a short rainy period stretching from February to May
- The Kiremt season is the main rainy period which extends from June to September.

As evident in Figure 3.1, there is a large amount of spatio-temporal complexity in Ethiopia's seasonal rainfall cycle, which is in general defined by the progression of the Inter-Tropical Convergence Zone (ITCZ). The North and Mid-West of Ethiopia has a single Kiremt season with its maximum in late July. The rest of the country has a bimodal seasonal distribution made up of the Belg and Kiremt rains. In the South these two seasons become more distinct as the Kiremt rains are shifted from September to November. In this region, the early April-May rains are named the Gu season and the late rainy season is called the Deyr rains.

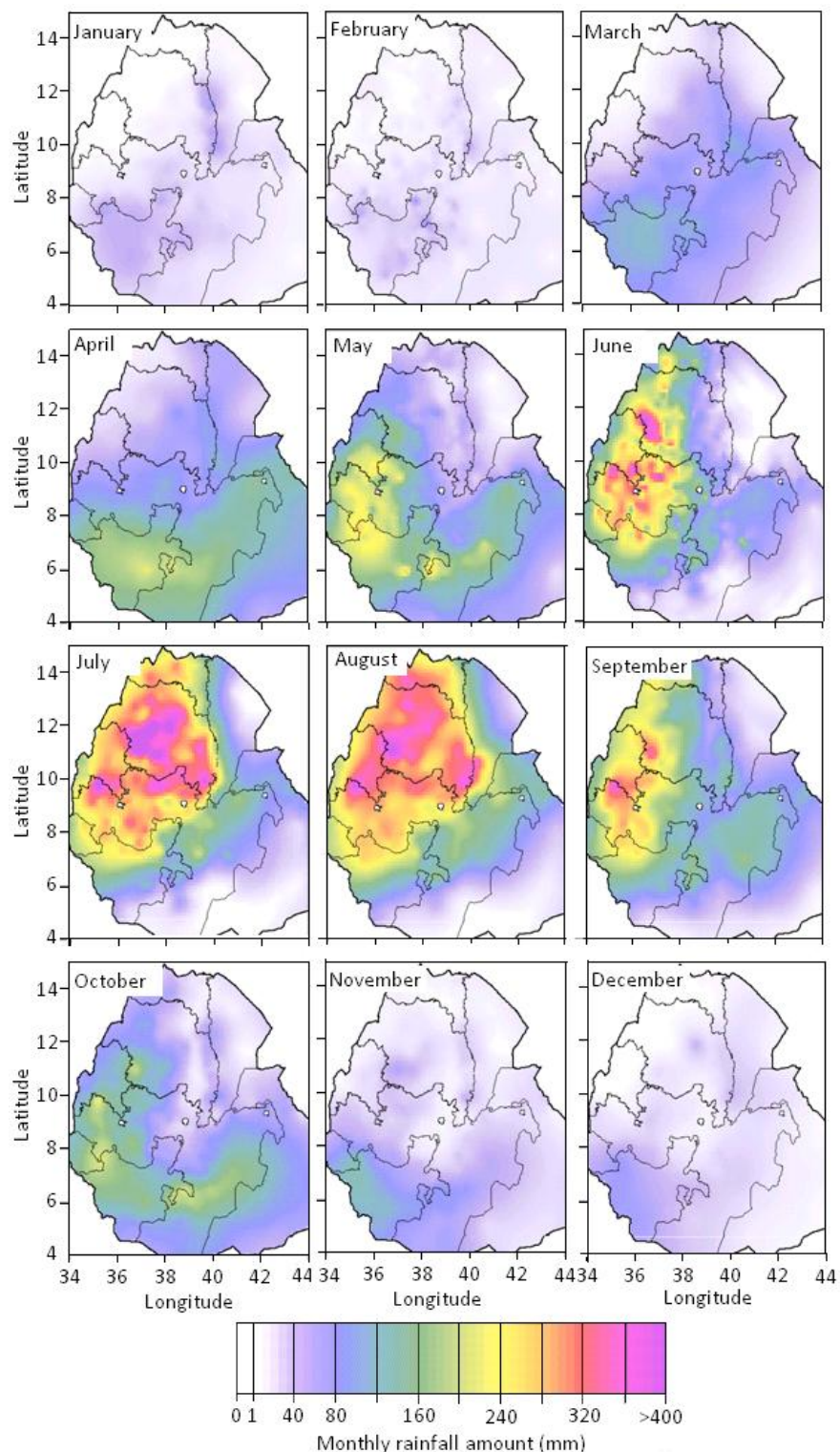


**Figure 3.1.** Monthly total rainfall maps of Ethiopia, giving an indication of the spatiotemporal complexity of rainfall patterns across the country. These were created by kriging a monthly kriged dataset of 610 stations from 1994-2007, provided courtesy of the Ethiopian National Meteorological Agency. There were very few gauges in the Somali desert in the South East of the country, therefore these areas may have less realistic results.

Although the progression of the rainy seasons is primarily determined by the ITCZ, several other large scale weather patterns are known to modulate it. The Belg season occurs due to a meridional arm of the ITCZ (Kassahun, 1987), modulated by moist East and South Easterly winds from the Indian Ocean and the Sub Tropical Westerly Jet (STWJ) (Diro *et al.*, 2008 and Rosell, 2011). Low pressure systems in the Arabian sea and Indian Ocean also have the potential to influence rainfall during this season (Diro *et al.*, 2008 and Bekele, 1997). Rainfall during Kiremt is primarily determined by the movement of the ITCZ, modulated by low level moisture fluxes from the Indian and Atlantic Oceans (Diro *et al.*, 2009). Other large scale forcings in this season include the Tropical Easterly Jet (TEJ) (Segele *et al.*, 2009; Korecha and Barnston, 2007; Endalew, 2007), the African Easterly Jet (AEJ) and the Quasi-Biennial Oscillation (QBO) (Diro *et al.*, 2008, Diro *et al.*, 2010b).

Figure 3.1 also highlights the connection between topography and rainfall in Ethiopia. Although there is some relationship between the two (e.g. the shape of the highlands is evident in many of the monthly rainfall sub-plots), the situation becomes much more complicated at finer scales. For example Beyene and Meissner (2010) report orographic enhancement of rainfall during the Kiremt rains, but Dinku *et al.* (2008) reports that there is a reduction in rainfall amount with elevation in parts of North West Ethiopia due to moisture depletion from rain falling out on nearby mountains. The complicated relationship between topography and rainfall is to be expected considering the complexity of the terrain and the variation in the large scale climate forcings, but it does mean that standard models of orographic rainfall enhancement are inappropriate for use in Ethiopia.

Very little, if any, work has been done on classifying Ethiopian rainfall types, therefore although it can be assumed that the majority of rainfall in Ethiopia comes from convective processes, it is unknown how much non-convective, ‘warm’ rain there is. There is some evidence to suggest that the majority of rainfall comes from small scale convection. The observed spatial correlation of rainfall has been analysed later in this thesis (Section 3.4.1.1, Figure 7.9 and Figure 7.10), where there appears to be strong spatial correlation below 30km in all months. Birhanu and Alamirew (2008) also suggest that shorter

duration rainfall events are more intense, suggesting they are from convective processes. Also there is a lot of anecdotal evidence from farmers in Ethiopia to suggest that rainfall is small scale and convective. For example, Meze-Hausken (2004) reports that a traditional Afar saying is "*while it rains on one horn of the ox, it can be dry on the other*", which was interpreted by the study as showing prevalence and importance of localized rainfall events.

## 3.2 CLIMATE DATASETS

### 3.2.1. RAIN-GAUGE DATA

The Ethiopian NMA have kindly provided access to two rain-gauge datasets.

#### 3.2.1.1. Oromiya dataset overview

This is a daily dataset, comprising of 276 gauges from the Oromiya region of Ethiopia for the years 2002-2006. It has been used as the main calibration dataset in this thesis and the station locations can be seen in Figure 3.2.

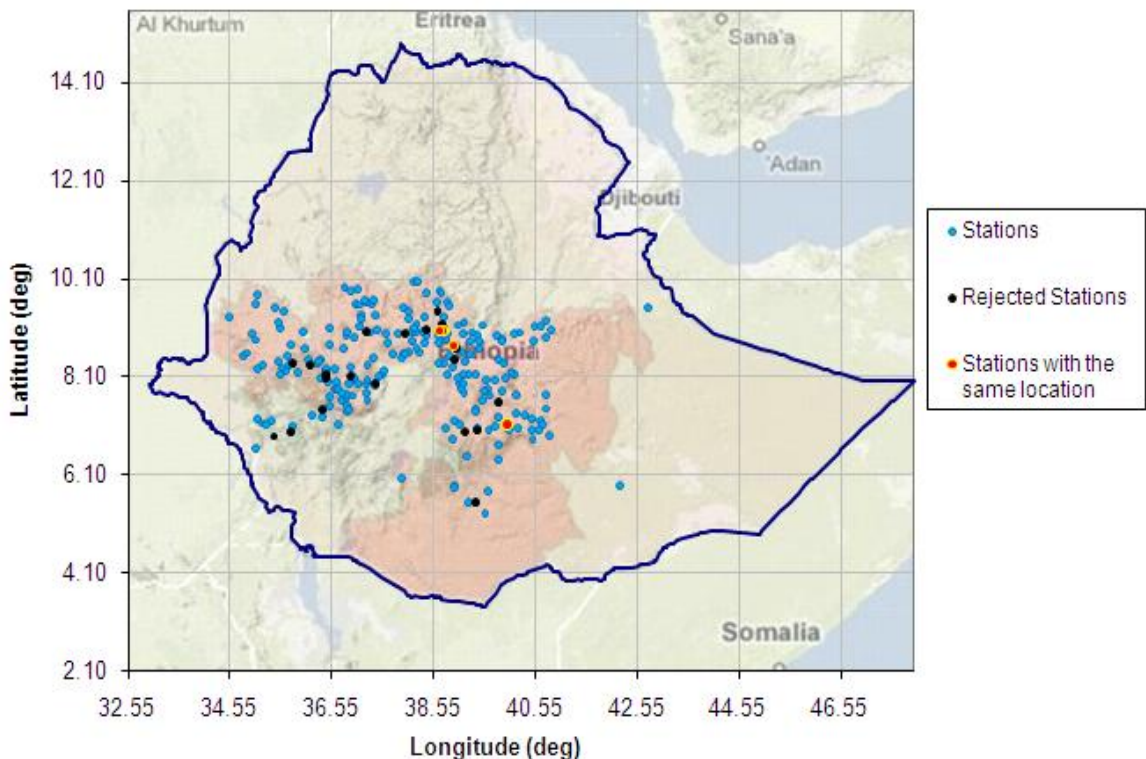


Figure 3.2. Locations of gauges within the Oromiya dataset. Rejected and overlapping stations are also shown.

Due to the large size of the dataset, it was impractical to study each individual station in detail. Therefore 50 stations were randomly selected for a quality control process, in addition to any gauges which warranted further analysis from studies of the overall statistics. These included any gauges where the rainfall record contained outliers, unusual means or that appeared to be in the wrong location. The quality control process for each selected station included a comparison against independent datasets where possible, checking station location data against maps and satellite imagery, then plotting the daily rainfall time-series against nearby stations.

Stations were excluded from the dataset for the following reasons:

- 1- A lack of adequate or accurate location information.
- 2- An unrealistic time-series, especially when compared with nearby stations.
- 3- Less than 6 months of data.

In all, 35 stations were excluded from the dataset; these are shown as black points in Figure 3.2. Unfortunately the locations of the gauges were only provided to an accuracy of degree minutes, therefore there are clusters of stations with the same location in some major cities (shown as red circles in Figure 3.2). As the chosen spatial interpolation method is kriging, this would have an adverse effect on any variograms produced from the data. Consequently any clusters were studied in detail and if possible, stations were given an accurate location determined from Google satellite imagery. Any other stations with the same coordinates were assigned locations a few hundred metres apart.

### ***3.2.1.2. General Gauge Dataset***

This dataset comprises of daily rain-gauge data from 1994-1999, for 20 stations spread over a larger region of Ethiopia. It has been used as the main validation dataset in the thesis. The station locations can be seen in Figure 3.3. The stations have already undergone extensive quality control and have been used as part of a validation dataset for several publications (Diro et al., 2008 , Diro et al., 2009 and Diro *et al.*, 2010b).

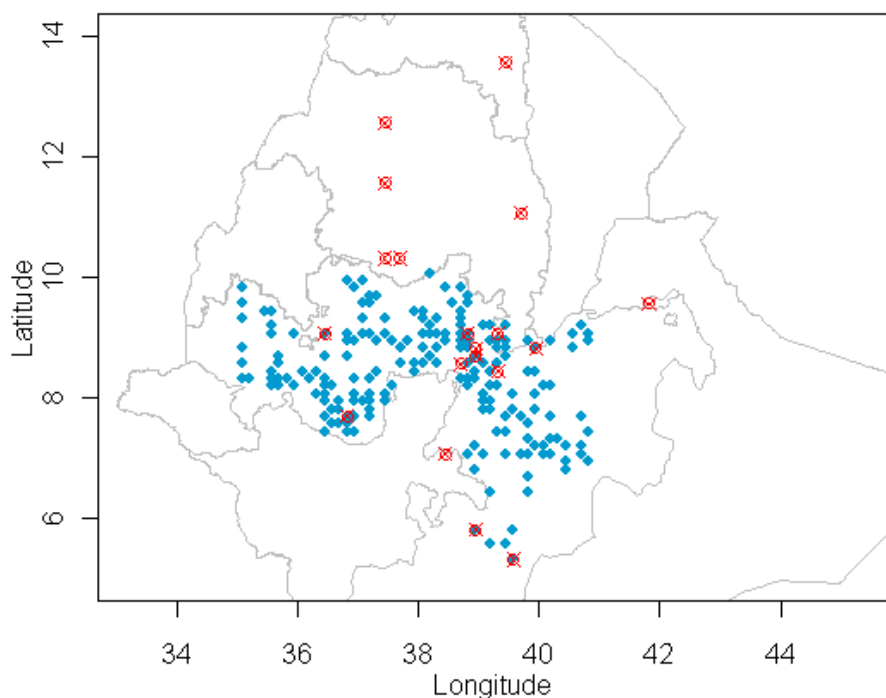


**Figure 3.3.** Locations of the rain-gauges in the General dataset are shown as red crosses. The locations of the Oromiya stations are also shown for reference as blue dots.

### 3.2.2. SATELLITE DATA

One of the stated aims of this thesis is to incorporate satellite rainfall estimates into a crop yield monitoring and forecasting system. These rainfall estimates are discussed at length in Chapter Four to Chapter Seven and are based on infra-red data from METEOSAT 1<sup>st</sup> and 2<sup>nd</sup> generation satellites. Images from the satellite's infra-red 10.8  $\mu\text{m}$  spectral channel were obtained from The European Organisation for the Exploitation of Meteorological Satellites (EUMETSAT). During the time-periods covered by the calibration and validation data-sets i.e. 1994-1999 and 2002-2006, there were very few dates when the satellite data was unavailable. In the case of missing dates, an image was randomly selected from the 10-day period, or dekad, containing the dates. Although this is certainly not the ideal solution to the problem, the infrequency of missing days and the knowledge that the end use of the satellite rainfall data was a crop simulation model (where one day's rainfall would have a limited impact on seasonal crop yields), meant that this was a quick and efficient solution to the problem.

### 3.2.3. MODEL DATA

One of the main aims of this thesis is to consider the uncertainty of rainfall inputs on the output of a crop simulation model. To run such a model, one generally needs rainfall, temperature and solar radiation data, but unfortunately there was no observed synoptic data available for use in this thesis. As the NMA's operational CYMFS in Ethiopia relies on model input from ECMWF, the ECMWF ERA-Interim re-analysis product was chosen for all synoptic data in the study, downscaled to a resolution of  $0.25^\circ \times 0.25^\circ$ . In addition, ERA-Interim rainfall was also used as an alternative input into the system in order to study the difference between modelled and satellite rainfall estimates.

ERA-Interim is ECMWF's most recent global atmospheric re-analysis product which extends from 1989 until the present day (Dee *et al.*, 2011 and Berrisford *et al.*, 2009). It includes 3-hourly estimates of surface parameters at a spatial scale of  $0.7^\circ \times 0.7^\circ$  and is widely used as a proxy for observations. The Alterra research institute in conjunction with the EU Joint Research Council (JRC) and MeteoConsult have created a  $0.25 \times 0.25^\circ$  downscaled version of this dataset using the following method: First, all variables estimated on a 3-hourly basis are converted to daily estimates. Shepard's inverse distance weighting interpolation is then applied (Shepard, 1968). This estimates the value of each weather variable and altitude at an unsampled location as the weighted average of the variable at the 4 surrounding ERA-Interim grid points. For example for the variable F,

$$F(x, y) = \sum_{i=1}^n w_i f_i \quad 3.1$$

where  $n$  is the number of surrounding grid points (in this case this is set to 4),  $f_i$  is the value of  $F$  at each of these grid points, and  $w_i$  is the weight function assigned to each point:

$$w_i = \frac{h_i^{-p}}{\sum_{j=1}^n h_j^{-p}} \quad 3.2$$

Here,  $h_i$  is the distance from the surrounding grid point to the interpolation point and  $p$  is an empirical number called the power parameter, which in this case is set to 2.

Finally, a bias was found when comparing downscaled minimum temperature, maximum temperature and wind speed with observed values. This was assigned to a mismatch in altitudes between the downscaled dataset and observation, which could be over 200m at altitudes above 1600m. Therefore, independent variable specific corrections were applied to the relevant parameters of the downscaled dataset ('Method D'). These were derived from statistical regression between time-series of interpolated variables and observed variables at weather stations over Europe. The bias correction was then applied to the global ERA-Interim dataset. Note, rainfall and solar radiation were not corrected using this method. Details about the downscaling process were gathered from Kerdiles, 2011 and are also included in De Wit *et al.*, 2010.

### 3.3 INITIAL ANALYSIS OF GAUGE DATA

#### 3.3.1.1. Seasonal cycles

When plotting the monthly mean over all the stations, one can easily pick out the seasonal cycle and climatological events. Although one must take into account the limited number of years that went into the analysis, it is interesting to note that there is very little interannual variability after the peak of the rainy season in August and before the peak of the Belg season in mid March.

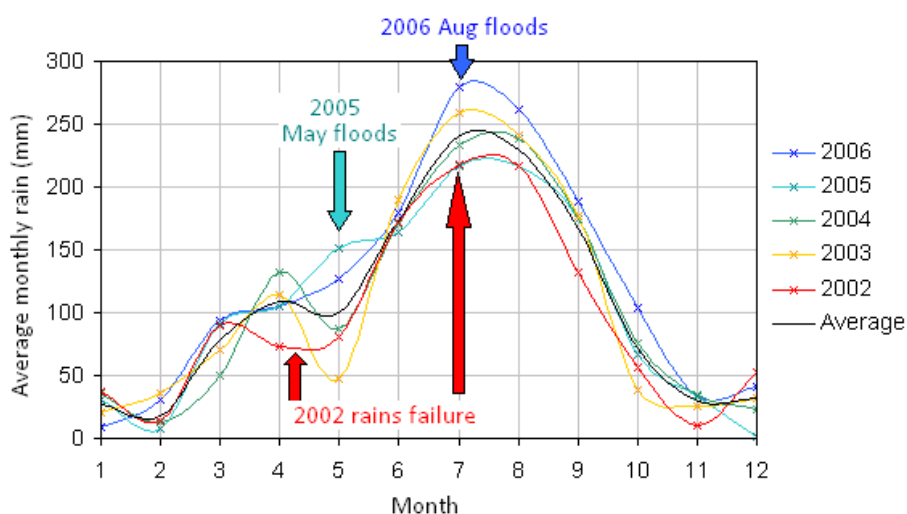
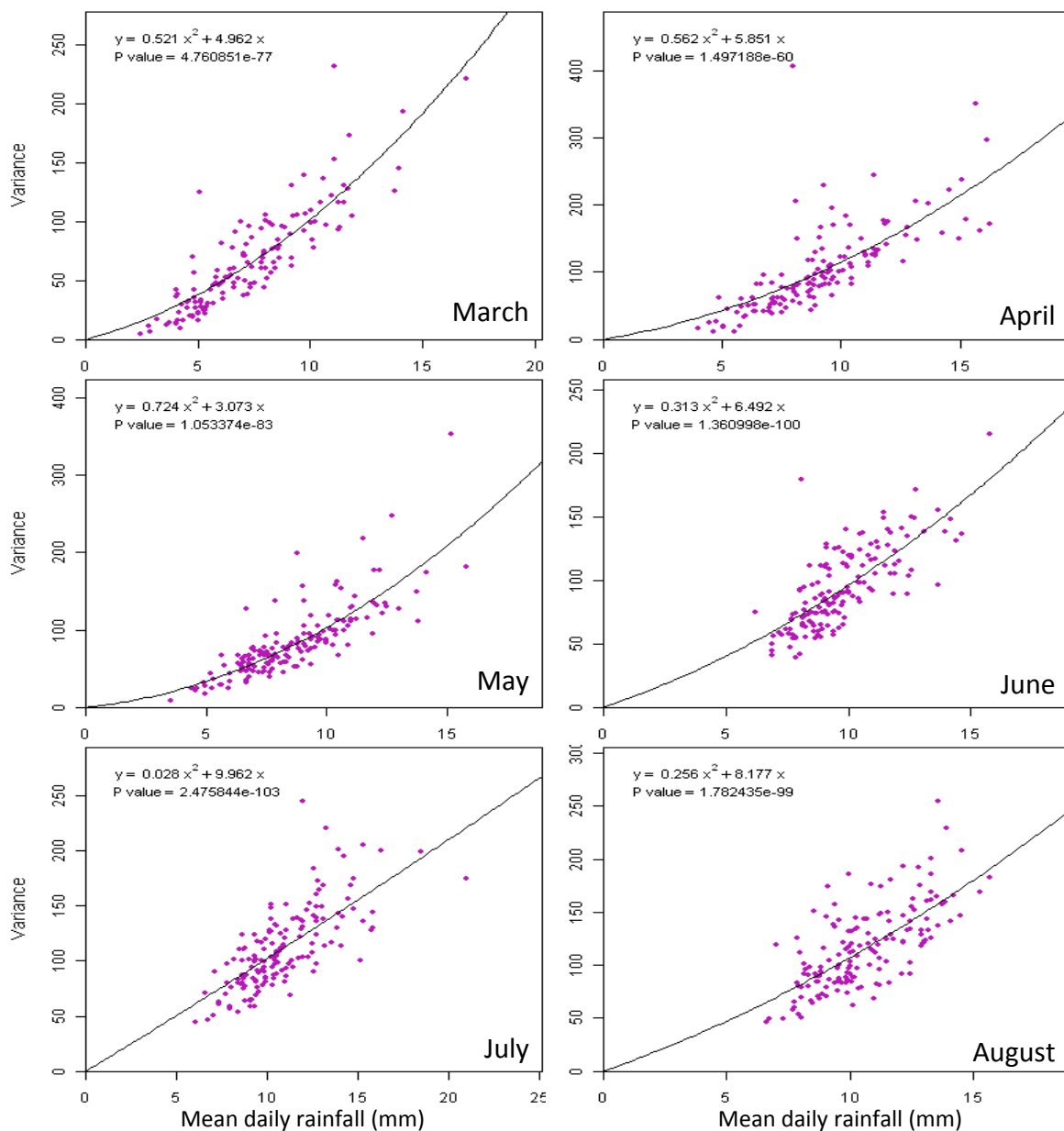


**Figure 3.4.**  
Time-series of the mean of the Oromiya dataset. The Belg and Kiremt seasons and extreme events are easily observed.

### 3.3.1.2. Mean-variance parameters

Because rainfall is heteroscedastic (i.e. its variance depends on rainfall amount), one might expect a relationship between the mean and variance of daily rainfall amounts (Grimes *et al.*, 1999). This can be seen in the Oromiya dataset in Figure 3.5. It is important to quantify the heteroscedasticity in the data, as the relationship is used in the kriging process described in Section 3.4.



Plot continued on the next page

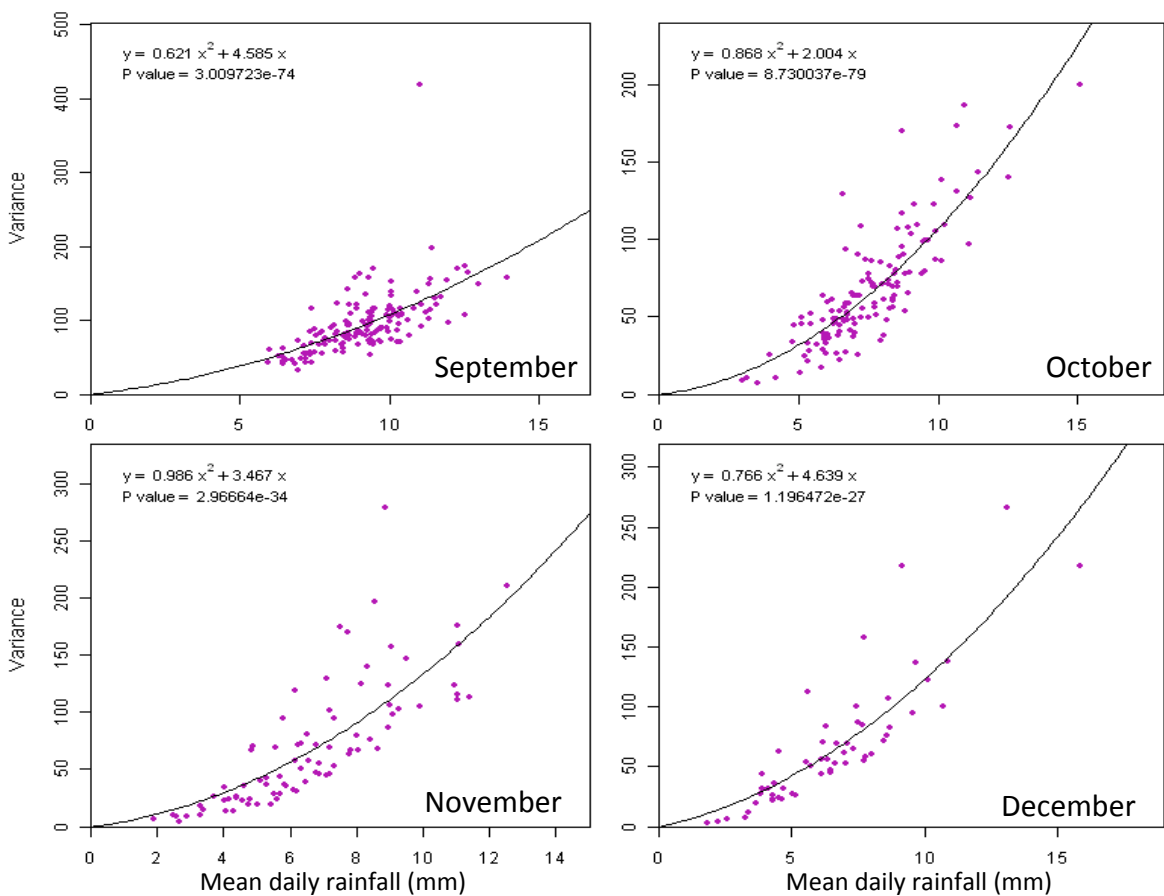


**Figure 3.5.** Plots of daily mean vs variance of rainfall amount for each month in the Oromiya rain-gauge dataset. A good polynomial relationship can be seen for all months. Dry days have been excluded from the analysis.

### 3.4 SPATIAL INTERPOLATION OF THE RAIN-GAUGE DATA

The main intended use of the rain-gauge datasets presented above is to calibrate and validate satellite derived rainfall estimates. The satellite values are estimates of areal averaged rainfall, for example the daily ensembles product discussed in Chapters 4-7 have a minimum resolution of  $0.125^\circ$ . However the values provided in the rain-gauge datasets are point measurements which might be expected to have very different statistics compared to an areal average. This can be seen in Figure 3.6 where a time-series of rainfall (for April 2003) for 5 gauges within Addis Ababa are compared with their mean. The gauges are all located within one ensemble pixel. Although the time-series for individual gauges are comparable, they are not similar enough to justify using one particular gauge as a proxy for pixel rainfall. The mean of the gauges also has different statistics, for example there

are fewer days with zero rainfall and fewer days with extremely high rainfall amounts. This makes physical sense as there is more chance of a rain storm passing over some point of the pixel compared to one specific location within it (hence less zeros), but it is unlikely for the heaviest rainfall to fall over the entire pixel (hence lower pixel rainfall amounts). Consequently, rainfall observations spatially interpolated to the scale of the model they are being compared against often compare more closely than when using raw point rainfall (Grimes, 2006).

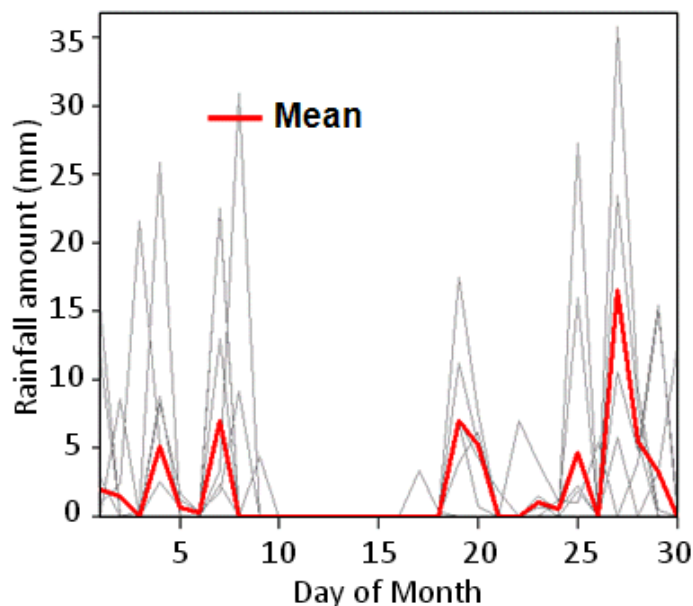


**Figure 3.6.** Plot of individual gauge values (grey) vs. their mean (red) for April 2003. All of the gauges are within Addis Ababa.

There are several spatial interpolation methods available to convert gauge measurements to areal averages, for example inverse distance weighting (described in Section 3.2.3) and spline fits. However these are less appropriate when interpolating sparse rain-gauge datasets because they do not provide an estimate of the error on the interpolation at each location. It can also be difficult to modify the methods to take into account the local nature of rainfall e.g. convective rainfall has a very different spatial structure to frontal rainfall and so perhaps should be treated differently. In this thesis, the geo-statistical approach of kriging has been selected. This is often labelled optimal prediction because the approach seeks to minimise an error function derived from the spatial covariance of the dataset (Ali

*et al.*, 2005), thus providing the user with an estimate of the error on the interpolation at each location. Numerous studies show that kriging gives better results than other methods providing basic assumptions are correct and representative variograms can be constructed (Grimes and Pardo Igúzquiza, 2010, Lebel *et al.*, 1987). The next Section shows how this might best be achieved.

### 3.4.1. GEOSTATISTICS

Geostatistics was originally developed by Georges Matheron in 1968 as a tool to estimate the concentration of iron ore within a mine (Matheron, 1968). It was named in honour of Daniel Krige after his empirical work on estimating the concentration of iron ore in the 1950s. In order to convert this to a tool able to estimate rainfall, the following properties must be taken into account:

- 1 – Rainfall occurrence and amount have very different statistical properties (which are normally modelled as a Dirac and Gamma function respectively). These must be taken into account, either by treating the system as a mixed distribution or by assuming that the two processes can be modelled independently.
- 2 – The spatial structure of rainfall must be modelled locally as it is highly dependent on the geography and climate of the region of interest.
- 3 – Unlike ore samples, the location of rain gauges are generally determined using socio-economic factors rather than a specifically designed sampling system. Therefore rain gauges tend to be clustered in population centres or along valleys, rivers or roads. There tend to be very few gauges located at the tops of mountains, where the rainfall distribution might look quite different.
- 4 – Rainfall varies over time, whilst ore tends to remain constant. Therefore, rainfall measurements for one particular event must be taken over the space of a few hours, whilst many measurements can be built up over time about an unchanging variable.

5 – When one takes into account points 3 and 4 and the fact that rain-gauges are extremely sparse over Africa (Figure 4.1), it is evident that it can be difficult to gain sufficient measurements about one particular rainfall event. Also, rainfall information is often collected over days, dekads (10 days) or months, thus the value recorded will probably include information about the sum over many rainfall events rather than for just one storm.

Geostatistics is the name for a family of techniques developed in order to study and interpolate auto-correlated or regionalised data i.e. data that has a spatial correlation which varies with distance. The techniques are based on the concept that at a location,  $\mathbf{x}$ , a dataset  $Z$ , can be modelled as a slowly varying mean background,  $m$ , plus a random fluctuation,  $R$

$$Z(\mathbf{x}) = m(\mathbf{x}) + R(\mathbf{x}) \quad 3.3$$

The following sub-sections aim to explain some of the more important geo-statistical concepts and show how they can be modified to take into account the additional requirements of modelling rainfall. The topic is explored further in Grimes and Pardo Igúzquiza (2010), which offers a detailed review of the geostatistical analysis of rainfall.

### **3.4.1.1. The variogram**

Imagine there is a set of observations of  $Z$ . For each pair of points within this set, the distance between them can be recorded. Now for a given distance,  $\mathbf{h}$ , a subset of the sample can be defined as  $n(\mathbf{h})$  chosen so that the distance between the pairs in the subset equals  $\mathbf{h}$ . The spatial dependence of the subset can then be determined by calculating the variance of the difference between each pair.

$$\eta(\mathbf{h}) = \frac{1}{n(\mathbf{h})} \sum_i^{m(\mathbf{h})} [Z(\mathbf{x}_i) - Z(\mathbf{x}_i + \mathbf{h})]^2 \quad 3.4$$

If  $\eta$  is plotted against  $\mathbf{h}$ , the resulting plot is called an experimental variogram, which is simply the inverse of the more common correlogram. It should be noted that the differences between the pair must obey second order stationarity for this analysis to be

appropriate. For mathematical convenience, the experimental semi-variogram,  $\gamma^*$ , is more often calculated:

$$\gamma^* \text{ } \mathbf{h} = \frac{\eta}{2} = \frac{1}{2n \text{ } \mathbf{h}} \sum_i^{m \text{ } \mathbf{h}} [Z \text{ } x_i - Z \text{ } x_i + \mathbf{h}]^2 \quad 3.5$$

The semi-variogram is defined as experimental (and the semi-variance denoted by  $\gamma^*$  instead of  $\gamma$ ), because it is created using an observed sample rather than modelling the true underlying distribution. Therefore it has the same relationship to a semi-variogram that a histogram does to a probability distribution (Clark, 1979). As there are often limited numbers of points, rather than splitting the data into subsets for each value of  $\mathbf{h}$ , the data are often instead split into contiguous bins of width  $2\delta$ . In this case, the semi-variogram is created by plotting  $\gamma^*$  against the mean distance,  $\bar{\mathbf{h}}$ . As shown in Figure 3.7, the semi-variogram has several clearly defined characteristics:

- The *nugget* is the variance as distance approaches zero. This might correspond to sampling error or the intrinsic uncertainty in a variable. In the case of rainfall, one might expect the nugget to equal zero because rainfall is highly spatially correlated at the scale of a few metres.
- It is expected that as  $\mathbf{h}$  increases, two samples of  $Z$  that are distance  $\mathbf{h}$  apart would become less spatially correlated. The distance at which the two samples become independent of each other is defined as the *range* of the variogram.
- The statement above means that at the range distance, the variogram will level off. The value of the semi-variance at this point is denoted as the *sill*.

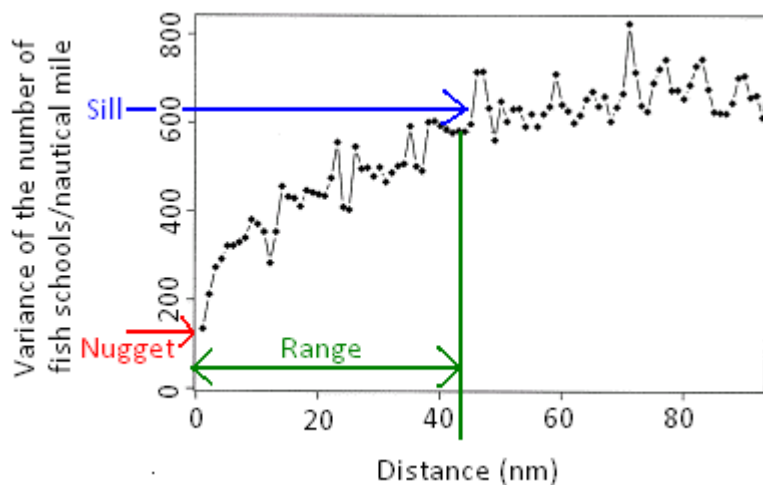


**Figure 3.7.** An example of an experimental variogram. This particular example is taken from a case study modelling fish stocks (Petitgas *et al.*, 2003). The nugget, sill and range have all been marked.

As discussed in the previous section, modelling rainfall differs from modelling ore reserves because there can be several rainfall events at one given location. Although it would be desirable to create a variogram for each individual rainfall event, this is unfeasible in areas where there are sparse gauge measurements. In addition, rainfall information is also often collected over a longer time-scale than one particular event. In this case a climatological variogram can be calculated, as described in Grimes and Pardo Igúzquiza (2010). The method assumes that the spatial correlation of rainfall remains constant for a given region and time-period. For example, all the rainfall which falls in Oromiya during March can be assumed to be convective with a spatial correlation of approximately 20km. If the requirement is satisfied, then a climatological experimental semi-variogram,  $\gamma_c^*$ , can be calculated by building up variograms from several time-periods (each scaled by dividing by the time-period's total variance):

$$\gamma_c^* \mathbf{h} = \frac{1}{K} \sum_{k=1}^K \frac{1}{\sigma_k^2} \frac{1}{2n} \sum_{i=1}^{m \mathbf{h}} [Z(x_i) - Z(x_i + \mathbf{h})]^2 \quad 3.6$$

For events with very few observations, it is often inappropriate to divide the event by its variance because the variance itself will not be robust. In these cases, the relationship between the mean and variance illustrated in Figure 3.5 can be used instead. The impact of

using a climatological variogram rather than modelling individual rainfall events can be seen in Figure 3.8.

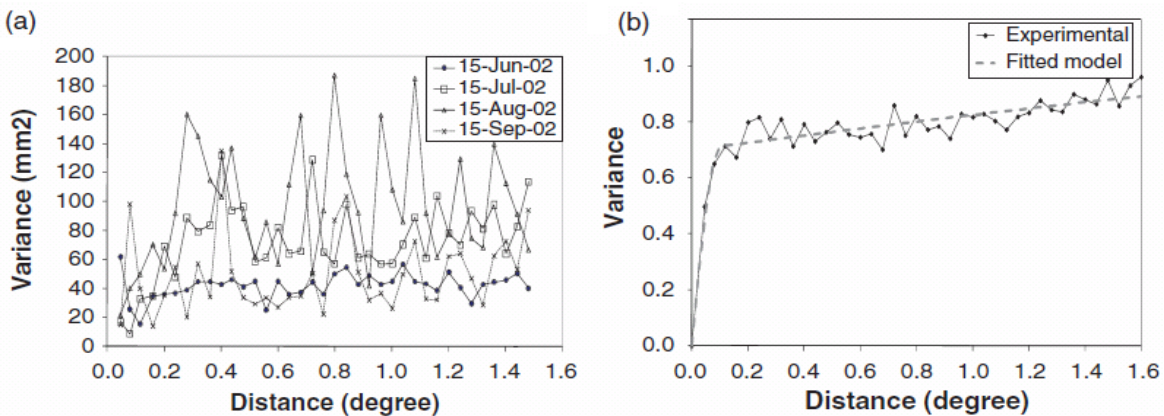


Figure 3.8. Plot taken from Grimes and Pardo Igúzquiza, 2010. Figure 3.8a shows variograms calculated from four individual days for the Oromiya dataset described in Section 3.2.1.1. Although the individual curves are noisy, they all appear to have similar range. Figure 3.8b shows a climatological variogram calculated for rainfall events in May-September, 2002-2006.

The next stage in the geo-statistical process is to fit a model to the experimental variogram to estimate the underlying spatial correlation in the data. Such a model needs to satisfy several criteria, for example it must be non-negative and continuous. These conditions are discussed further in Webster and Oliver (2007), but here it is sufficient to list the most commonly used models for rainfall analysis:

$$\text{Nugget: } Z(\mathbf{h}) = \begin{cases} 0 & |\mathbf{h}| = 0 \\ c & |\mathbf{h}| > 0 \end{cases} \quad 3.7$$

$$\text{Spherical: } Z(\mathbf{h}) = \begin{cases} c \left( \frac{1.5\mathbf{h}}{a} - \frac{1.5\mathbf{h}^3}{a^3} \right) & |\mathbf{h}| \leq a \\ c & |\mathbf{h}| > a \end{cases} \quad 3.8$$

$$\text{Exponential: } Z(\mathbf{h}) = c \left( 1 - e^{\left( \frac{-3a}{\mathbf{h}} \right)} \right) \quad 3.9$$

In these models,  $a$  equals the range of the variogram and  $c$  is the nugget. One of the advantages of using this set of models is that linear, or ‘nested’ combinations are allowed. For example one might make a model constructed out of a nugget plus an exponential model (this combination is often just called an exponential fit). Nested models are often important when considering climatological variograms, because rainfall frequently includes different scales of variation from individual events and large scale climate related features. An example of an experimental climatological variogram modelled by four models is shown in Figure 3.9. In these variograms, the spatial scale of convective rainfall can be seen in the ‘inner range’ of approximately 20km, but the large scale correlation of the ITCZ can be seen with an ‘outer range’ of approximately 500km.

Finally, the variograms described above are anisotropic e.g. it is assumed that the direction of the separation vector  $\mathbf{h}$  will not affect the spatial correlation of rainfall. In some locations, this assumption is clearly inappropriate. For example frontal rain might have a spatial correlation of a few hundred kilometres when looking along a front, but only a few tens of km when looking across it. In this study, it is assumed that Ethiopian rainfall originates from anisotropic convective systems.

### **3.4.1.2. Kriging**

Once a variogram model has been created, rainfall amounts at new un-sampled locations can be determined through the process of kriging. This is simply a weighted interpolation of the sample points, where the weights are derived from the variogram. The advantage of kriging is that it provides an unbiased linear combination of the samples, which is optimised by minimising the variance of an error function derived from the variogram. The method also provides an estimate of the error on the kriged value, known as the kriging variance.

Using the framework of Equation 3.3, the kriging equation can be written as follows:

$$Z^* \mathbf{h} - m \mathbf{h} = \sum_{\alpha=1}^n \lambda_\alpha [Z \mathbf{h}_\alpha - m \mathbf{h}_\alpha] \quad 3.10$$

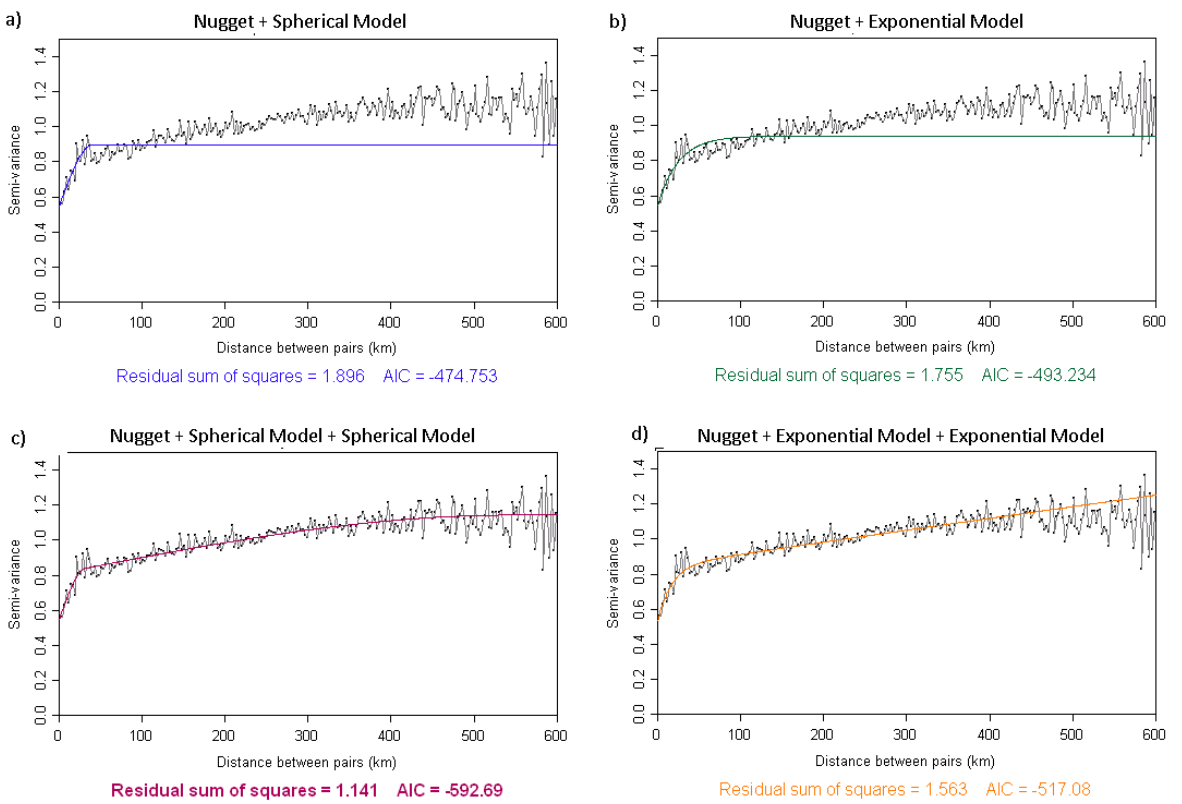


**Figure 3.9. Climatological variogram for March using the Oromiya dataset. Each sub-plot shows a different nested variogram model. The simpler nested models in plots a) and b) often capture the short scale variation in the variogram, but the more complex nested models in plots c) and d) are often more appropriate. Note the statistics in each sub-plot are explained in more detail in Appendix A2.2.**

Here,  $\mathbf{h}$  and  $\mathbf{h}_\alpha$  are location vectors for estimation point and the neighbouring data points (indexed by  $\alpha$ ).  $Z(\mathbf{h})$  is treated as a random field, with a trend  $m(\mathbf{u})$ , and a residual component,  $R(\mathbf{h}) = Z(\mathbf{h}) - m(\mathbf{h})$ . Kriging estimates the residual at  $\mathbf{h}$  as a weighted sum of the residuals at  $n$  surrounding data points. Kriging weights at each surrounding point,  $\lambda_\alpha$ , are derived from the semi-variogram (Bohling, 2005). This equation can then be used to give a final estimate of  $Z(\mathbf{h})$  by minimising the variance of the estimator in a process described in detail in Goovaerts (1997). If a climatological variogram has been used, the final kriging variance must also be re-scaled by multiplying the result from each event by its variance.

Although the kriging process does not mathematically require normality, if the input data has a very skewed distribution then the kriging variance is extremely difficult to interpret. Therefore the data is often converted to a Gaussian distribution using methods such as log-

normal, Box-Cox or normal scores transformations. The normal scores transform is regarded as the most robust of these approaches and is described in more detail in Section 6.5.2 and Figure 6.10.

There are several kriging methods used for different situations. Simple kriging assumes that the trend component is a constant over the entire domain i.e.  $m_h = m$ . Ordinary kriging assumes that the trend component is constant in the local domain of the point being estimated i.e. the data has a stationary variance but non-stationary mean. Kriging with external drift, or Universal kriging, caters for datasets which have an underlying trend in the mean.

So far, all of these methods currently estimate  $Z$  at an unsampled point. It is computationally expensive to calculate this over many points and take an average if one wishes to know the value of  $Z$  at a pixel. Instead, the process of block kriging can be used. This simply applies the kriging methodology described above to find the average expected value in an area around an un-sampled point, rather than the value at the point itself.

### **3.4.1.3. Double kriging**

As described in Section 3.4, it might be expected that the spatial correlation associated with rainfall occurrence will be different to the one associated with rainfall amount. In addition, as rainfall is a positive quantity, estimated rainfall values at an unsampled location will never equal zero and will approach the mean of the observations when estimating at large distances from a gauge. This is not ideal if it is important to accurately capture rainfall occurrence.

The issue can be addressed through the approach of Barancourt *et al.* (1992), who suggested that rainfall at a location  $i$  can be seen as the product of amount,  $F$  and occurrence,  $I$  which can be calculated individually from the dataset

$$Z_i = I_i F_i$$

3.11

Rainfall occurrence is calculated through the use of indicator kriging, where the data at each pixel and day has been converted into a binary value (1 if rainy and 0 if dry). Examples of indicator variograms can be seen in Figure 6.2, Figure 7.4 and Figure 7.9. The result of the process is a kriged map of the probability of rainfall. A threshold probability can then be selected in order to convert the probability map into a rain/no rain mask. In this work, the threshold for each day was selected as equivalent to the proportion of gauges which recorded rain on that day. Rainfall amount is then derived by applying the variogram/kriging process to just the observed positive rainfall amount i.e. ignoring zero-rainfall values in the observations. This also has the advantage of making the observed distribution more Gaussian and a normal scores transformation is rarely needed in this case.

The concepts behind geostatistics and kriging appear throughout this thesis, especially in the process of sequential simulation discussed in Chapter Six. Therefore further issues associated with geostatistical analysis are also discussed at appropriate points throughout the body of work.

### **3.5 CONCLUSION TO CHAPTER THREE**

This chapter discussed Ethiopia's climate, the observations available to measure it and how to interpolate these to a spatial scale useful for regional crop yield forecasts. Ethiopia has a complex bimodal climate due to its topography and placement with respect to large scale weather systems. These features also result in a non-trivial relationship between rainfall and orography and a climate dominated by convective anisotropic weather systems.

Several climate datasets were kindly provided for use in this thesis. The Ethiopian National Meteorological Agency provided:

- A dense daily rain-gauge dataset of 250 stations over the Oromiya region of Ethiopia from 2002–2006. This has been used as the primary calibration dataset in this work.
- A separate daily rain-gauge dataset for 20 stations from 1994–1999. This has been used as the primary validation dataset in this work.

As there was no observed synoptic data available for the project, the Alterra research institute kindly provided access to a downscaled model based reanalysis product based on ERA-Interim. Finally, EUMETSAT in conjunction with the University of Reading's TAMSAT research group, provided access to an archive of infra-red satellite images (at 10.8  $\mu\text{m}$ ) to allow daily satellite derived rainfall estimates to be investigated.

The final part of Chapter Three discussed how the point based rainfall data might be interpolated to areal averages. In particular the geostatistical technique of kriging was examined. This was selected because numerous studies show that kriging gives better results than other interpolation methods, providing that basic assumptions are correct and representative variograms can be constructed (Grimes and Pardo Igúzquiza, 2010, Lebel *et al.*, 1987). The technique of double kriging was concentrated on in particular detail as this has been shown to generate realistic maps of daily rainfall.

### **3.6 CONCLUSION TO PART 1 & FINAL DESCRIPTION OF THE CASE STUDY**

In the preceding Chapters, it has been shown that Ethiopia has an extremely complex climate and topography. This results in an equally complex agronomy, reflected in the country's planting date, area planted, production and yield data-sets.

The rest of this thesis attempts to use the datasets presented in Chapters Two and Three to investigate the impact of climate uncertainty on crop yield estimates as discussed in the Introduction. In order to provide consistency throughout the rest of this work, a case study has been chosen focussing on Ethiopian maize. The selected area for this study has been defined as the red box in Figure 3.10. This has the advantage of containing the main calibration rain-gauge dataset, (shown as blue dots), and the main maize growing area (shown as green shading).

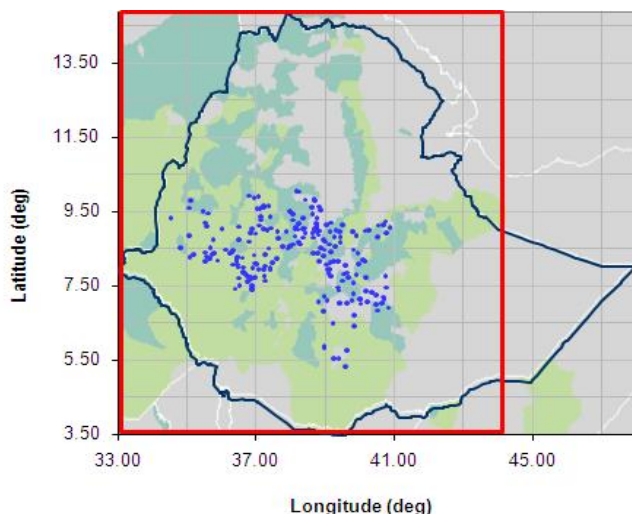


**Figure 3.10.** The location of the study area for this work. The light green areas correspond to locations where maize is grown as a primary crop and dark green areas correspond to locations where maize is grown to a secondary crop. Grey areas correspond to places where maize is not grown. The location of the Oromiya rain-gauges are shown by blue dots.

---

---

# PART 2

# SATELLITE RAINFALL ESTIMATES

This part of the thesis describes the creation, calibration and validation of daily satellite rainfall estimates.

*Chapter Four* (Satellite Rainfall Estimation Methodology) discusses the motivation behind rainfall estimates, contains a literature review of daily satellite rainfall estimates over Africa. It then moves on to consider the University of Reading's TAMSAT approach in more detail.

*Chapter Five* (Calibration of TAMSAT over Ethiopia) applies the methods discussed in the previous chapter to the case study in Ethiopia. The full set of parameters for this calibration are included in Appendix One.

*Chapter Six* (Sequential simulation) describes how the geo-statistical approach of sequential simulation can be used in conjunction with the TAMSAT rainfall estimates to give spatially correlated ensemble maps of rainfall over Ethiopia.

Finally, *Chapter Seven* (Validation of the TAMSAT daily satellite rainfall ensembles) discusses the validation of the satellite ensembles against observations.

## CHAPTER FOUR

# SATELLITE RAINFALL ESTIMATION METHODOLOGY

This chapter aims to provide both a literature review of daily satellite rainfall products over Africa and to provide a detailed explanation of the TAMSAT approach at a 10-day and daily timescale.

### 4.1 RAINFALL ESTIMATION IN AFRICA

As discussed in earlier chapters, timely and accurate rainfall information is of great importance when forecasting crop yields and real-time rainfall observations form an important part of the ‘updating forecast system’ envisaged in Chapter One. Rain-gauge networks have traditionally provided a simple and inexpensive method for daily and dekadal rainfall estimation. In more recent years, these have been complemented by the development of precipitation radar networks, satellite rainfall estimates (SRFEs) and output from Numerical Weather Prediction (NWP) models, which have been particularly successful in increasing the temporal and spatial resolution of the estimates.

However, estimating real-time rainfall amounts over Africa is subject to significant challenges. Precipitation radar networks are rare or non-existent and NWP model outputs are still relatively inaccurate, especially at a daily time-scale (Diro, Grimes *et al.* 2009). The inaccuracy in NWP output is in part due to the fact that rain-gauge networks, vital for calibration and validation, are often sparse and poorly maintained (Washington *et al.*, 2004; Chadwick *et al.*, 2010). This can clearly be seen from information provided by the World Meteorological Organisation’s (WMO) World Weather Watch (WWW)

programme. This collates real-time meteorological information in a Global Observing System (GOS), then disseminates it to users across the world using a global telecommunications system. One of the main components of GOS is its network of rain-gauges, the current state of which can be seen in Figure 4.1.

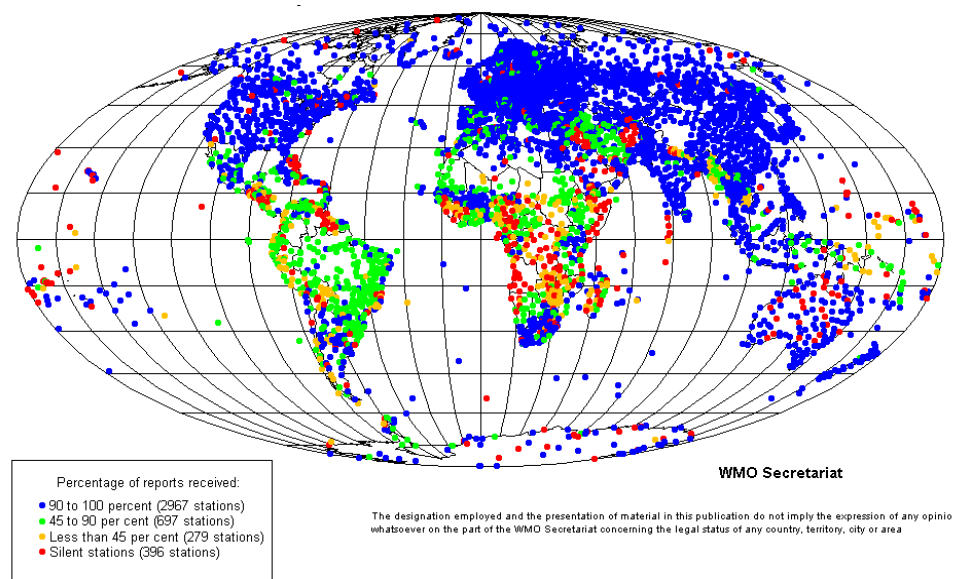


**Figure 4.1.** The distribution of the WMO WWW Regional Basic Synoptic network in October 2009. Each dot signifies a rain-gauge. When compared to Figure 4.2, the effect of the 2002-2008 AMMA observational campaign (which significantly increased the number and reliability of Sahelian rain-gauges) can be seen (WMO, 2010).

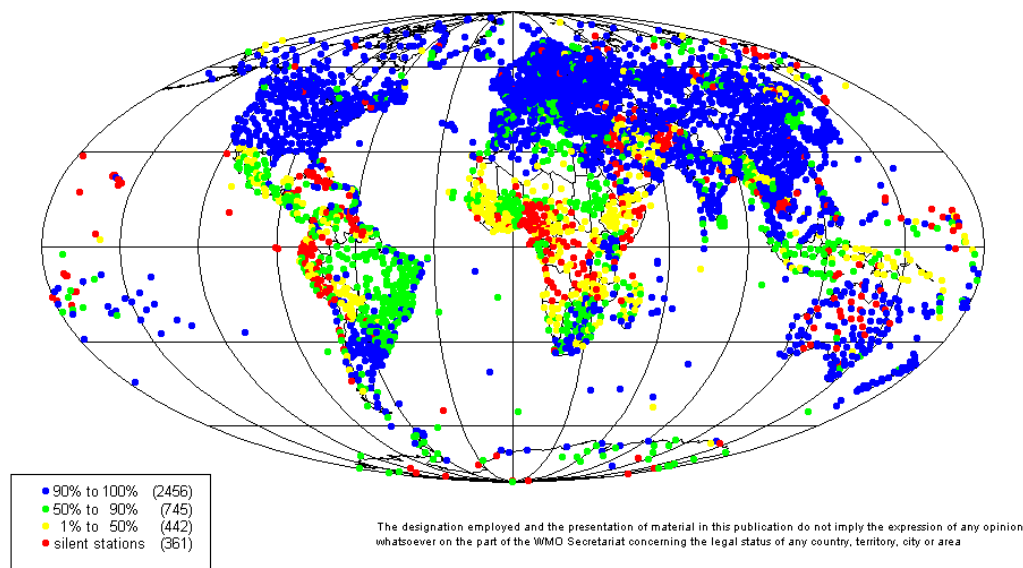


**Figure 4.2.** Distribution of the WMO WWW Regional Basic Synoptic network, 2003 (Washington *et al.*, 2006).

Two conclusions can be drawn from Figure 4.1. First, it can be seen that there is a general lack of rain-gauges in Sub-Saharan Africa, with some studies estimating that the gauge density is 8 times less than the one recommended by the WMO (Washington *et al.*, 2006). The second conclusion is that many of the rain-gauges over Africa fail to report, making the network much less reliable than it first appears. The plot shows that the situation is also very country specific, with country borders easily visible. On a given day, the situation can often be much worse. For example, Figure 4.3 shows the available rain-gauges on the 21<sup>st</sup> February 2012.

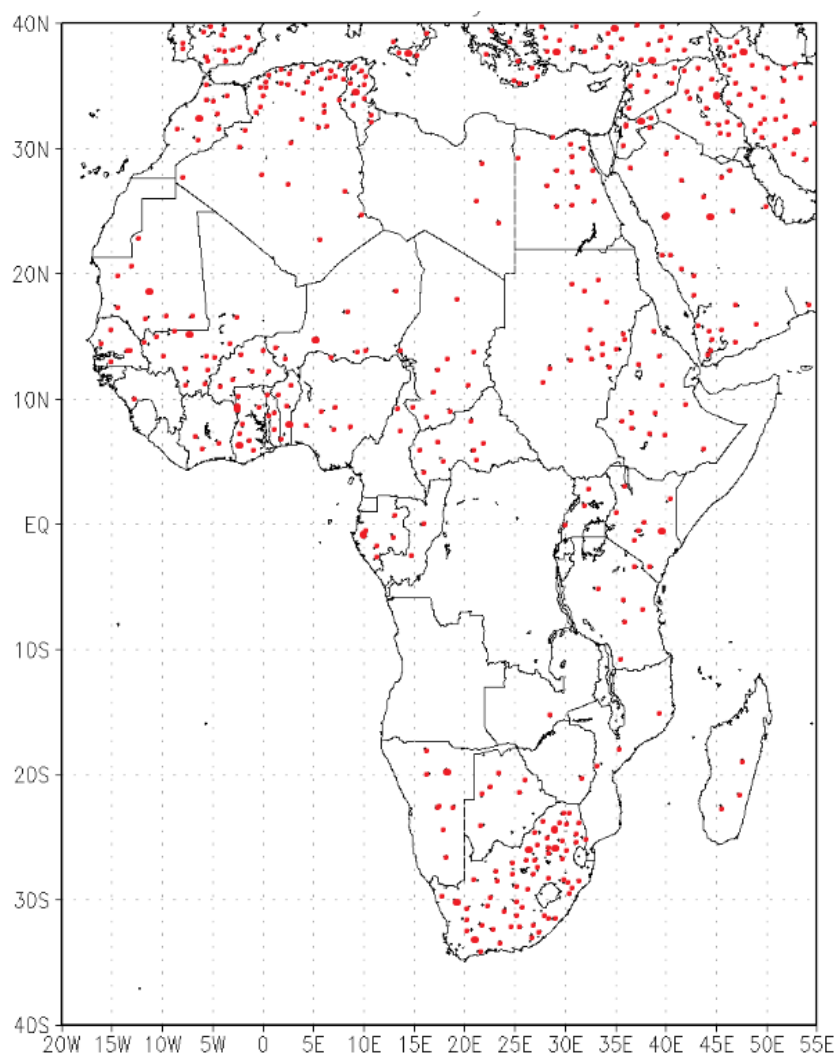


**Figure 4.3. Available rain-gauges from the GTS network on the 21<sup>st</sup> February 2012. Each gauge is depicted as a red dot.**

Sub-Saharan Africa is distinct in comparison to other developing regions in that the situation has deteriorated in recent decades (Ali *et al.*, 2005). Although a comparison of the network in 2009 (Figure 4.1) and in 2003 (Figure 4.2) suggests that the situation may now slowly be improving, the gauge network is still far from a state which could support regional scale crop yield forecasting.

It should be noted that individual countries and regional organisations often have access to denser rain-gauge networks than those mentioned above. For example the Ethiopian National Metrological Agency (NMA) has a daily rain-gauge network of over 1,000 stations, a subset of which is detailed in Section 3.2.1 (Beyene and Meissner, 2010). However, due to logistical and political constraints, these datasets are rarely available in real-time, especially to international and external organisations. Therefore, in this study we refer to such datasets as historical rain gauge data, which is specifically defined as datasets which are not available in real-time to international organisations. As the data are often available retrospectively, historical gauge data can be used for calibration and validation. The existence of these secondary rain-gauge networks does mean that if the crop yield forecasting system was to be run operationally by an African national meteorological agency, then it is likely that there will be a much better calibration dataset available than the one used in this study.

## **4.2 RAINFALL ESTIMATION FROM SATELLITES**

As discussed above, rain gauge, radar and NWP networks are inadequate and insufficient for use in crop yield forecasting, therefore this work concentrates on the use of satellite rainfall estimation. The era of precipitation remote sensing began in the 1960s with the creation of the WMO World Weather Watch mentioned in Section 4.1 and the launch of the first weather satellite, TIROS 1 (Television and Infrared Observation Satellite). There are currently over 8 families of meteorological satellites in orbit (W.M.O., 2010), measuring upwelling radiation at a range of electromagnetic wavelengths, in particular the infra-red (8  $\mu\text{m}$  - 12.5  $\mu\text{m}$ ), visible (500 nm – 700 nm) and passive microwave (PM) channels. Rainfall can be estimated from infra-red (IR) radiation through the premise that

the brightness temperature measured is a proxy for cloud top temperature and hence cloud top height. Visible channels give information about cloud albedo and hence the areal density of cloud droplets found in a cloud. PM channels directly measure both long-wave radiation re-emitted from raindrops and shortwave radiation scattered from ice-crystals. Precipitation estimates can be derived from one or a combination of these sensors. Meteorological satellites are generally classed as the one of two types: polar orbiting satellites which have a low altitude orbit and track over the Earth's surface from North to South, and geostationary satellites which are fixed at an orbit of 35,789km over the Equator. This gives them an orbital period of exactly 24 hours, causing them to remain fixed over one particular location. The altitude of polar orbiting satellites means that they often have a high spatial resolution, however the fact their field of view moves over the Earth's surface means that the temporal resolution can be poor. Geo-stationary satellites on the other hand, have a much better field of view but spatial resolution can be limited by the distance from Earth.

The remainder of this Section reviews available remotely-sensed precipitation algorithms. There are several products currently available, but for the case of this study only ones which have been used, or have the potential to be used in crop yield monitoring in Africa will be discussed. This means rainfall estimates must have a daily temporal resolution, a reasonably high spatial resolution and must be available in real-time. Estimates of the exact spatial resolution needed vary depending on the crop simulation model, however in the case of the model used in this study (GLAM), the estimates should have a resolution coarser than 25 km<sup>2</sup>.

#### **4.2.1. SATELLITE METHODOLOGIES**

##### ***The Tropical Rainfall Measuring Mission (TRMM)’s 3B42-RealTime product (Huffman et al., 2009)***

TRMM is a polar orbiting satellite launched in 1997. It is unique in that contains a precipitation radar along with IR, visible and PM sensors, thus it has the potential to produce high resolution rainfall estimates. Several TRMM daily products exist, however most of these become available at the end of each month due to the complexities of merging IR, PM and visible channels with real-time rain-gauge data. 3B42-RT is a real-time combined IR-PM product, with a 3-hour/0.25° spatio-temporal resolution. The product is created as follows. The TMI instrument on the satellite is first used to make an estimate of precipitation from passive microwave data. Infra-red estimates are also created and calibrated against historical rain gauge data. The IR and PM estimates are then combined, scaled to a monthly product (MS) and calibrated against a historical gauge-satellite dataset (GS). Finally, the GS/MS ratio is used to scale the individual 3-hourly MS estimates. Estimates are available from 2002 until present day. 3B42-RT has been linked with the TOPKAPI land surface model to provide soil moisture estimates (Sinclair and Pegram, 2009), however the 3B42-RT product is rarely used in operational crop yield modelling.

##### ***The National Oceanographic and Atmosphere Administration centre Climate Prediction Centre (NOAA-CPC) African rainfall estimation algorithm, RFE 2 (NOAA, 2010)***

RFE estimates are produced specifically with the aim of monitoring African drought and rainfall. The algorithm uses a mix of PM and IR sensors plus daily rainfall observations to produce daily rainfall estimates at a scale of 0.1°. The product is produced as a weighted average of AMSU microwave satellite rainfall estimates, Special Sensor Microwave/Imager rainfall estimates and IR rainfall estimates (created using the GOES Precipitation Index, GPI). The weighted average is then merged with real-time rain-gauge data to make the final product. RFE 2 is used extensively by the US-AID Famine Early Warning NETwork (FEWSNET) for drought monitoring and to drive simple water balance crop models (Brown, 2008).

***The NOAA-CPC morphing technique, CMORPH (Joyce et al., 2004),***

The motivation for CMORPH comes from the fact that PM sensors provide an instantaneous estimate of rainfall, whilst IR sensors provide better temporal resolution. Infra-red cloud top temperatures are used to define a ‘cloud system advection vector’, which is used to spatially propagate PM estimates forward in time by 30 minutes. This is then repeated until the next PM estimate is available for comparison. Therefore, the algorithm exclusively uses data from PM sensors and only uses IR data at a high temporal resolution to temporally interpolate the passive microwave estimates. As discussed by Joyce, in effect the IR data is used to propagate microwave derived rainfall features when the microwave data itself is not available.

The product has a high spatio-temporal resolution (8km every 30 minutes) and is available from 2002 until the present day. Similar to the TRMM products, CMORPH has been utilised in soil-moisture or available crop water models (Romaguera *et al.*, 2010), but is not widely used in crop yield forecasting.

***Precipitation Estimation from Remotely Sensed Information using Neural Networks, PERSIANN (Hsu *et al.*, 1999)***

This uses infra red and rain-gauge data as input to an artificial neural network and is available at  $0.25^\circ$  and a 3-hourly resolution. Originally in 1997, long wave and IR radiation was used as an input to a neural network, where the mean and variance of cloud top temperatures was classified, propagated and converted to rainfall estimates. More recently, PM data has also been incorporated into the inputs. Again, PERSIANN has been used in soil moisture modelling rather than crop yield forecasting (Juglea *et al.*, 2010).

***Tropical Applications of Meteorology from SATellites, TAMSAT’s dekadal and daily estimates (Dugdale *et al.*, 1991)***

The University of Reading’s TAMSAT group has been producing 10-day operational rainfall estimates for Sub-Saharan Africa since the late 1980s. It uses a simple linear, locally based algorithm based on the 10-12  $\mu\text{m}$  thermal infra-red channel of Meteosat. More recently, Teo and Grimes, 2007, produced ensembles of daily rainfall estimates

designed to incorporate the uncertainty associated with the algorithm. As TAMSAT was selected for use in this project, its algorithms are discussed in detail in Section 4.3.

#### 4.2.2. VALIDATION STUDIES OVER AFRICA

There have been limited attempts to validate or compare satellite products over Africa with particularly little at daily time-scales. Jobard *et al.*, 2011, compared and validated all of the satellite products discussed above at a 10-day timescale over the Sahel and found that the regionally calibrated TAMSAT and RFE 2 had higher skill than global products (CMORPH and PERSIANN). Thorne *et al.*, 2001, compared TAMSAT against a merged satellite/gauge 10-day product (CPC) and kriged rain-gauge data from 800 stations in South Africa. TAMSAT was found to perform better over plateaus whilst CPC performed better over the mountains (although both underestimated within this region). Dinku *et al.*, 2007 also found that TAMSAT underestimated high rainfall amounts over the Ethiopian highlands, but that it performed well in a comparison with other 10-daily resolution satellite products including TRMM 3B42, CMORPH and RFE 2. In this region, TRMM and CMORPH also performed well, but RFE 2 showed less skill. A similar study was also undertaken at daily time-scales over the Ethiopian Highlands (Dinku *et al.*, 2008), where RFE 2, PERSIANN, CMORPH and TRMM 3B42-RT were validated against kriged rain-gauge data. As might be expected from the previous study, TRMM and CMORPH had the highest skill whilst PERSIANN consistently underestimated daily rainfall amounts. Finally, Chadwick, 2010 performed a brief validation of a basic TAMSAT daily product over the Ethiopian Highlands, calibrated using the Oromiya gauge dataset discussed in 3.2.1.1. This was found to have limited skill.

It should be noted that in all of the studies above, the TAMSAT product performed as well or better than other real-time algorithms, despite the fact that these incorporate real-time gauge data into their products (TAMSAT only uses historical rain-gauge data). This performance can be attributed to TAMSAT's local calibration, which is discussed in the following section.

## 4.3 TAMSAT METHODOLOGY FOR RAINFALL ESTIMATES

### 4.3.1. BASIC APPROACH AND VALIDATION

The TAMSAT approach is described as follows. First, Meteosat infrared images are converted to a brightness temperature. The assumption is then made that all rainfall falls from convective clouds and that all cold clouds are convective (thus TAMSAT works well in areas such as the Sahel, but less well in regions where other rainfall regimes dominate). A temperature threshold,  $T$ , can be chosen whereby it is assumed that a pixel with a cloud top temperature colder than the threshold corresponds to a raining cloud and the length of time any pixel spends below the threshold is denoted as Cold Cloud Duration ( $CCD$  or  $D_T$ ). This approach can be seen in Figure 4.4.

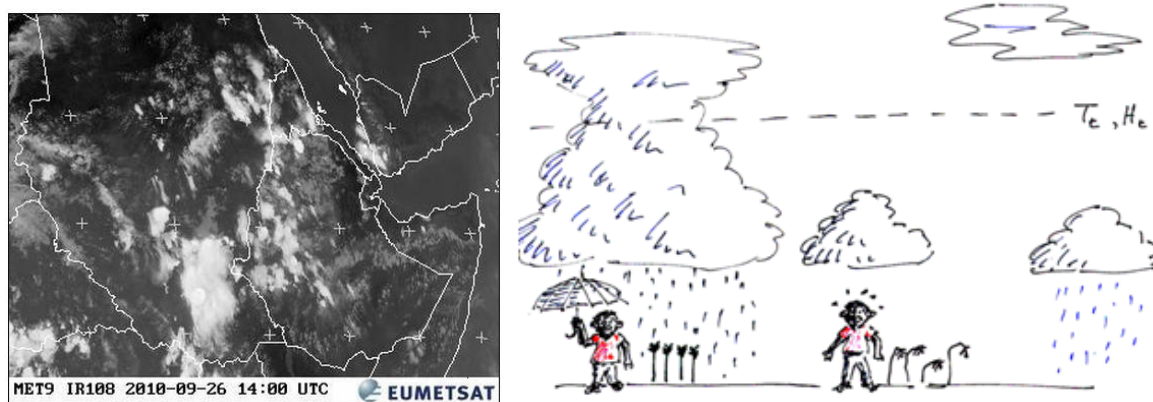


**Figure 4.4.** *Left hand side:* METEOSAT image of East Africa using the  $10.8\mu\text{m}$  channel. The whiter the image, the colder the cloud. *Right hand side:* Schematic showing the TAMSAT methodology. A temperature threshold is defined through local calibration. If a cloud has a cloud top temperature below this threshold then it is designated to be raining. If the cloud has a cloud top temperature above the threshold then it is designated to be dry. The method only works where the majority of rain falls from convective clouds as cirrus and warm rain will cause errors. This is a common issue with IR based satellite rainfall estimates (Tadesse and Anagnostou, 2009) Cartoon used with permission of David Grimes, University of Reading.

For simplicity, only specific CCD temperature thresholds are considered. These are  $-30^\circ\text{C}$ ,  $-40^\circ\text{C}$ ,  $-50^\circ\text{C}$  and  $-60^\circ\text{C}$ , hence  $CCD_{30}$  or  $D_{30}$  corresponds to Cold Cloud Duration created using a temperature threshold of  $-30^\circ\text{C}$ .

The dekadal or 10-day rainfall amount,  $R_{10}$ , can be modelled using a simple linear relationship with CCD, described in equation 4.1.

$$R_{10} = \begin{cases} a_0 + a_1 D_T & D_T > 0 \\ 0 & D_T = 0 \end{cases} \quad 4.1$$

As a simple linear model is used to fit the data, it is assumed that the errors are normally distributed:

$$\sigma_{R_{10}}^2 \sim N(0, 1) \quad 4.2$$

The temperature threshold and parameters  $a_0$  and  $a_1$  are derived locally (for climatologically homogeneous regions) using historical rain gauge data. This follows a 2 stage process – first rain/no rain contingency tables are created to find a temperature threshold with the best agreement against observations. Raw gauge rainfall amounts are then regressed against CCD for this temperature threshold to give the values of  $a_0$  and  $a_1$ .

An example of the dekadal calibration for June over Oromiya can be seen below:

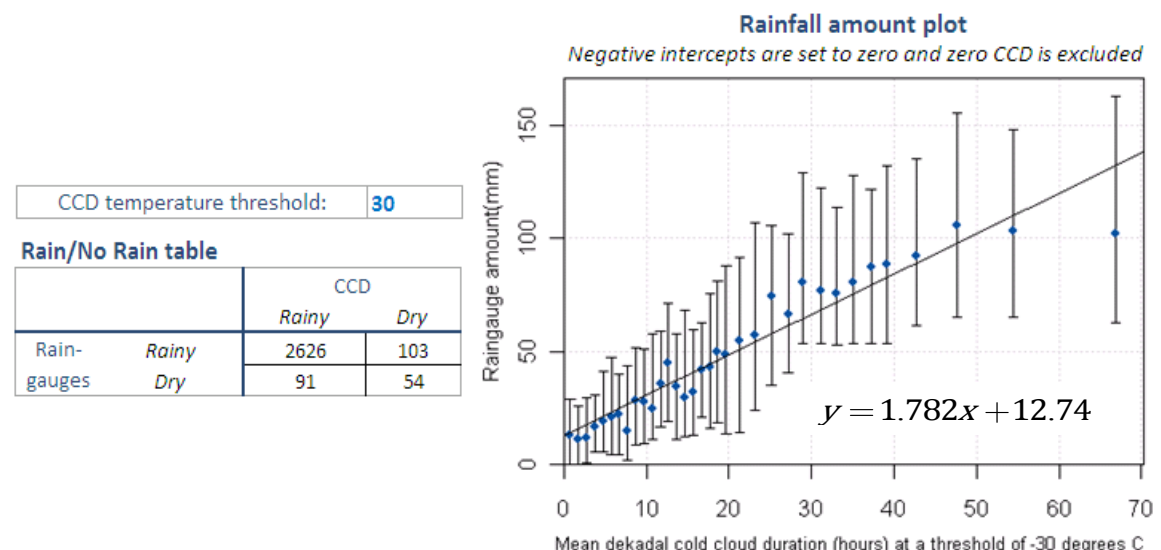
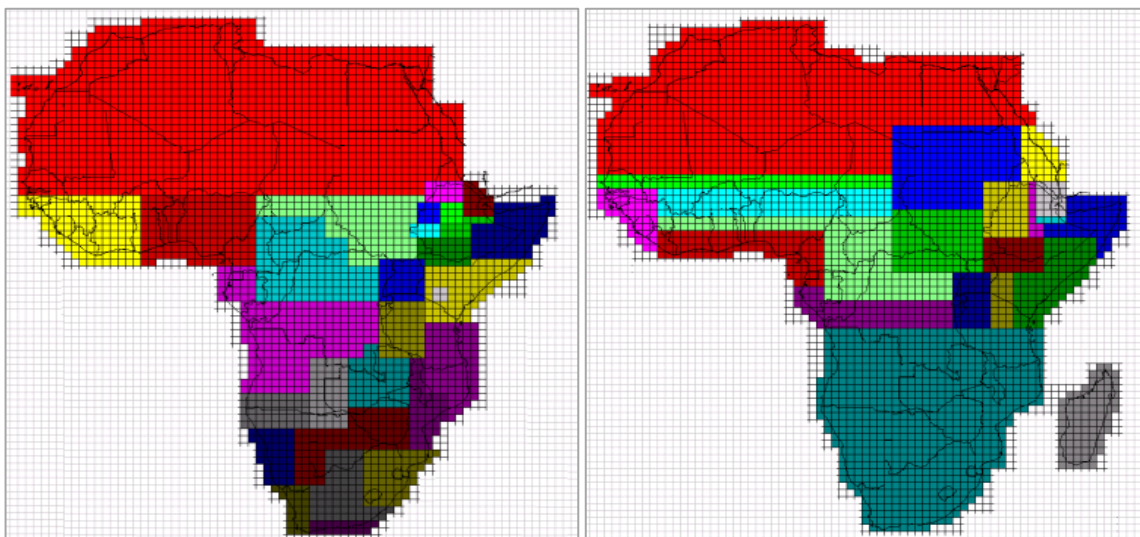


Figure 4.5. A contingency table and rainfall amount calibration plot for the Oromiya gauges during June. The contingency table is ‘balanced’ i.e. most of the values fall into the Rain/Rain category or the Dry/Dry category, with little systematic bias if the forecast was wrong. The rainfall amount table also shows a robust linear fit, although there is an underestimation of high rainfall amounts. This is a typical characteristic of the TAMSAT fit.

Normally a different calibration is performed for each climatological month because it is reasonable to assume the rainfall-CCD relationship might change during the different seasons of the year. A different calibration will also be performed for different climatological ‘zones’ or regions as it is also reasonable to assume that there will be a different CCD-rainfall relationship in different places (e.g. mountains vs plains). These regions are decided by studying both the local climate and maps of the dichotomous bias at different CCD thresholds. This process is often performed by local meteorological agencies during calibration workshops. An example of current calibration regions and parameters for the operational dekadal product can be seen in Figure 4.6.



**Figure 4.6. Current calibration regions for February (left) and July (Right) for the 10-day TAMSAT rainfall estimate.** Each colour corresponds to a different region which will have its own unique value of threshold temperature,  $a_0$  and  $a_1$ . Currently, region boundaries are chosen arbitrarily, where it is believed a different rainfall regime may dominate. Therefore more detailed regions are found in climatologically rainy areas or areas with detailed or varied topography and climate.

#### **4.3.2. QUANTIFYING THE UNCERTAINTY IN TAMSAT METHODOLOGY WHEN STUDYING DAILY DATA**

It is important to quantify the error on satellite rainfall estimates, especially when linking them to an end user application such as a crop model. This non-trivial process must include the difference in spatial scale between observed calibration data and the areal satellite estimates, the statistics of the rainfall data, the uncertainties present in all datasets

and the observed spatial correlation of rainfall. The situation also becomes more complicated when considering daily rainfall. This is highly intermittent, hence in contrast to parameters such as temperature and solar radiation, rainfall on a smaller spatio-temporal scale will be more variable than rainfall averaged over a larger region or time-period. The statistics of daily rainfall are complex, highly skewed and in general are modelled using a gamma distribution. In addition, the statistics of whether it has rained or not also become important, as daily rainfall maps are much more likely to include large regions where it does not rain. Finally, daily rainfall estimates are heteroscedastic (i.e. the variance of the gamma distribution varies for different values of CCD). As shown in Figure 4.7, these factors lead daily rainfall estimates to have a proportionally larger uncertainty than their dekadai counterparts. The following sections describe how the basic TAMSAT algorithm can be modified both to take into account the more complex statistics of daily rainfall and to quantify the error on the estimate.

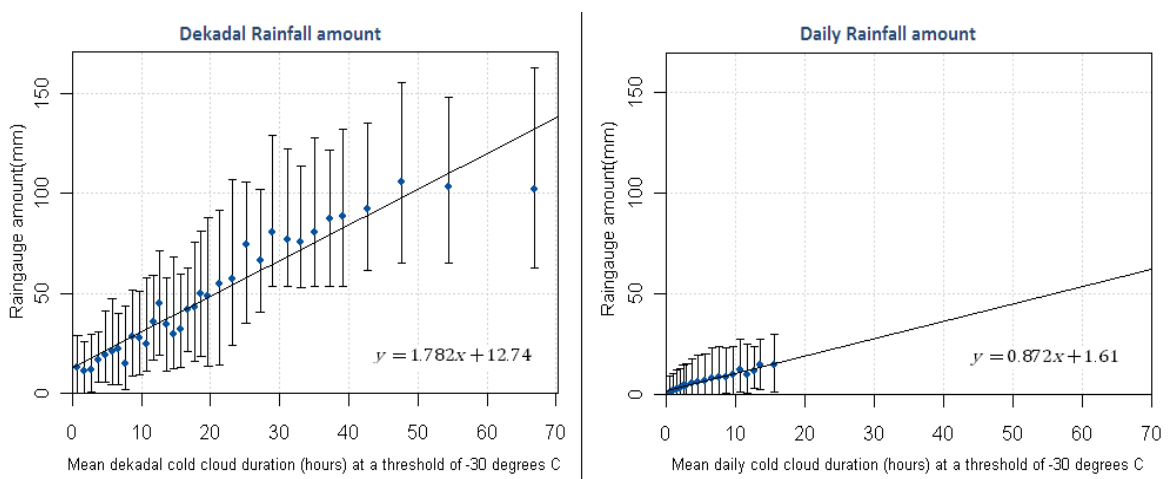


**Figure 4.7. A comparison of a dekadal and a daily calibration using the same input dataset (Oromiya gauges during June, from 2002-2006). Although the daily rainfall fit looks robust, the error bars are proportionally larger.**

#### 4.3.2.1. A modified TAMSAT algorithm

In order to address the issues discussed above, Teo and Grimes (2007) developed an extension of the TAMSAT algorithm using a mixed distribution model. This was shown to out-perform the traditional TAMSAT algorithm for a case study creating daily rainfall

estimates for The Gambia and is discussed briefly below. For a given value of  $CCD$ , daily rainfall,  $Z$ , can be modelled as:

$$P(Z > 0 | CCD = D_T) = p = \begin{cases} \frac{1}{e^{-b_0 + b_1 D_T}} & D_T > 0 \\ p_0 & D_T = 0 \end{cases} \quad 4.3$$

$$f(Z | Z > 0, CCD = D_T) = g(\mu, D_T, \sigma) \quad 4.4$$

$$\mu = a_0 + a_1 D_T \quad 4.5$$

$$\sigma^2 = \kappa \mu^\theta \quad 4.6$$

These equations state that the probability,  $p$ , of rainfall can be modelled as a logistic regression of  $CCD$  at a given temperature threshold ( $D_T$ ). If the  $CCD$  at that threshold is equal to zero, then the probability of rain is simply a fixed probability,  $p_0$ . In those instances where it is raining, the rainfall amount for a given  $CCD$  can be modelled as a gamma distribution with shape and scale parameters  $\mu$  and  $\sigma$  respectively. These parameters are drawn from a generalised linear regression between  $D_T$  and kriged rainfall amount, with the variance modelled by equation 4.6, rather than as a normal distribution (thus taking into account the skewed nature of daily rainfall estimates). The parameters for equation 4.6 are found by an iterative least squares approach to model variance as a parameter of the mean rainfall for a given  $CCD$ . It should be noted that this model is subtly different from a gamma generalised linear model (GLM), as in that case the variance would be modelled as  $\sigma = \kappa \mu^2$ . As with the dekad calibration, any parameters are locally calibrated using observed rain-gauge data. A schematic of the calibration can be seen in the following diagram.

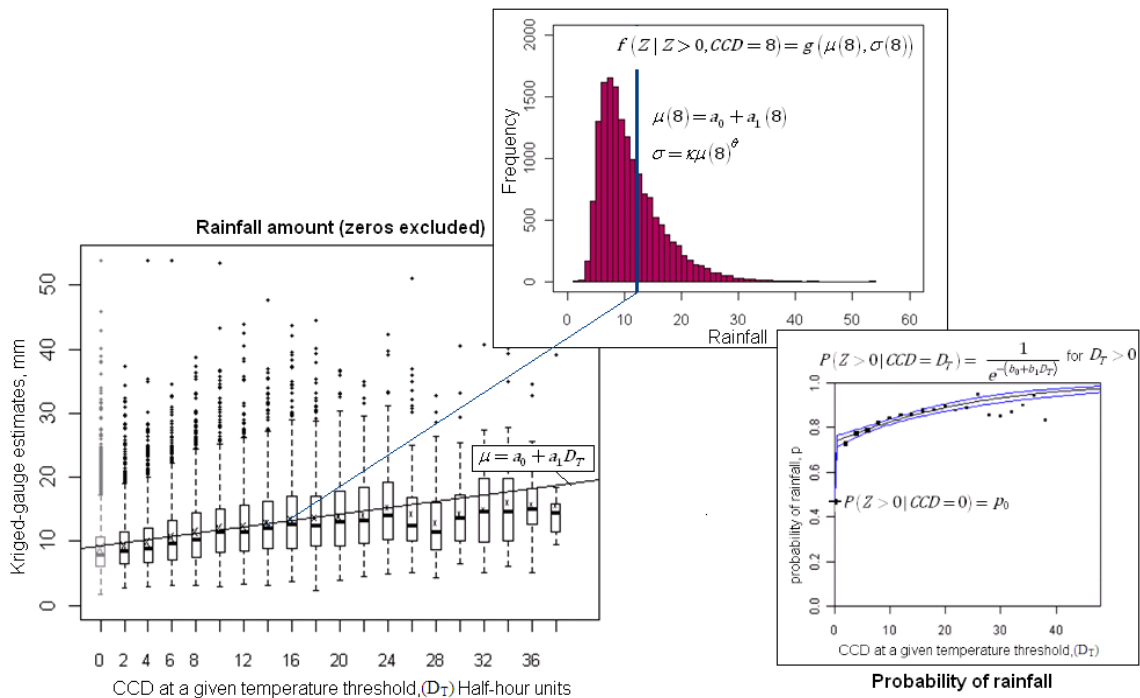


**Figure 4.8.** Schematic of the daily TAMSAT calibration process. Historical rain gauge data can be used to plot the probability of rain and the rainfall amount (if raining) against CCD at different temperature thresholds. The probability of rain is then modelled as a logistic regression and a generalised linear fit is then applied to the rainfall amount. For any value of  $D_T$ , rainfall can then be modelled as a gamma distribution with its mean and variance derived from the linear fit. An example is given for 8 hours of CCD.

#### 4.3.2.2. Multiple CCD thresholds

So far, the calibration equations described above have assumed that only one temperature threshold of CCD is used in each zone. This is a longstanding assumption for the dekadal TAMSAT calibration. However, Grimes *et al.* (2003) showed that using CCD at multiple thresholds in a dekadcal calibration for Zambia provided some additional information about whether a cloud was raining or not, but not enough to warrant the additional complexity of the method.

The structure of rainfall on a daily scale is very different to dekadal averages. For example, a daily infra-red image is much more likely to correspond to one particular rainfall event or storm, therefore there is potentially more of a problem with cirrus contamination. This is where the cold, high, non-rainy cirrus cloud in the anvil of a storm is detected as raining by TAMSAT. For daily estimates, a large proportion of a pixel

might be covered by non-rainy cirrus, but in the case of a 10-day estimate, a storm is more likely to have tracked over a greater proportion of a pixel. Also, as the 10-day estimate is likely to be the sum of several convective events, there is likely to be a smaller proportion of high cloud corresponding to cirrus. Consequently, this thesis has re-investigated the ‘single threshold’ assumption and so the linear relationship for mean rainfall given in equation 4.5 can be written as:

$$\mu = a_0 + a_1 D_{30} + a_2 D_{40} + a_3 D_{50} + a_4 D_{60} \quad 4.7$$

#### **4.3.2.3. Detailed error analysis of the TAMSAT algorithm**

The basic TAMSAT error estimate (equation 4.2), is simply a normal distribution around the basic linear fit. The error estimate for the new TAMSAT algorithm (equation 4.6) modifies this for daily rainfall, taking into account the heteroscedasticity and skewed nature of the dataset. However equation 4.6 simply gives the variance of the regression from the calibration graph and thus tells us little about the true underlying stochastic relationship between rainfall and *CCD*,  $\sigma_F^2$ . Grimes and Pardo Igúzquiza (2010) postulated that this relationship could be described as:

$$\sigma_F^2 = \sigma_C^2 - \sigma_G^2 + \bar{\sigma}_l^2 + \varepsilon^2 \quad 4.8$$

where  $\sigma_C^2$  is the total regression variance from the calibration graph,  $\sigma_G^2$  is the variance from kriging the rain gauge data,  $\bar{\sigma}_l^2$  is the variance on the location of the satellite pixel and  $\varepsilon$  are unknown and hopefully negligible errors (therefore  $\varepsilon^2$  will be excluded from this point on). The components are all independent and are discussed in more detail below.

First and most simply, the regression error from the graph,  $\sigma_C^2$ , has been described in equation 4.6. This is simply the error from the linear fit on the calibration graph. In order to describe  $\sigma_G^2$ , attention must be paid to the calibration dataset itself, which originates from point-source rain-gauges. Interpolating the point gauge values to give areal estimates

entails an uncertainty which can be quantified using the kriging paradigm. As we are interested in the underlying uncertainty between rainfall and *CCD*, this error can then be subtracted from the total error represented in equation 4.8. It has been shown that the kriging error is also heteroscedastic and can be modelled in a similar way to equation 4.6 (Teo and Grimes, 2007), where its parameters are found from plotting the mean kriging error at a given *CCD* against the mean satellite rainfall estimate at that *CCD*. Therefore, equation 4.8 now becomes:

$$\sigma_F^2 = \kappa_c \mu^{\theta_c} - \kappa_G \mu^{\theta_G} + \sigma_I^2 + \varepsilon^2 \quad 4.9$$

where  $\kappa_c \mu^{\theta_c}$  is the modelled total error from the regression graph above and  $\kappa_G \mu^{\theta_G}$  is the error from observations.

This relationship breaks down for low rainfall amounts, where often the kriging variance will be larger than the regression variance. This is clearly unrealistic, thus a lower limit to  $\sigma_G^2$  has been derived from considering the error in knowing the location of the satellite pixel,  $\bar{\sigma}_I^2$ . This depends on several factors and also includes parameters such as the leakage of radiance between pixels. The error is small and difficult to calculate analytically and has thus rather arbitrarily been defined as equivalent to the variance associated with an uncertainty in pixel location of plus or minus one pixel:

$$\sigma_I^2 = \frac{1}{n} \sum_{j=1}^n (CCD_i - CCD_j)^2 \quad 4.10$$

Here, n is the number of surrounding pixels and the subscript *j* refers to an individual nearest neighbour around the *i*th pixel. The location error is independent of *CCD* and for this study was found to be 2.5 mm for the study region. The final error estimate can now be written as:

$$\sigma_F^2 = \begin{cases} \sigma_c^2 - \sigma_G^2 + \bar{\sigma}_I^2 & \sigma_G^2 + \sigma_I^2 \leq \sigma_c^2 \\ \bar{\sigma}_I^2 & \sigma_G^2 + \sigma_I^2 > \sigma_c^2 \end{cases} \quad 4.11$$

This equation is now a complete treatment of satellite errors and will be used in replacement of equation 4.6.

#### 4.3.3. CREATING DAILY RAINFALL ESTIMATES FROM THE CALIBRATION

It should be noted that unlike the dekadal calibration discussed in Section 4.3.1, the new TAMSAT calibration described by equations 4.3, 4.4, 4.5 and 4.11 does not lead directly to a rainfall estimate. Instead, the equations describe the statistical properties of the relationship between CCD and rainfall, for example the probability of rain or the shape of the rainfall amount distribution. In order to use the equations to predict rainfall occurrence and amount, either a deterministic or probabilistic approach can be taken. Both of these methods use the assumption discussed in Section 3.4.1.3, that rainfall at a pixel  $j$  can be expressed as the product of rainfall and occurrence.

If one is to make a deterministic estimate of rainfall, this relationship can be written as:

$$Z_j = p_j \mu_j \quad 4.12$$

where  $p_j$  is the probability of rain at a location  $j$  and  $\mu_j$  is the modelled mean rainfall amount if raining. The probability of rain is found from equation 4.3 and the rainfall amount from equation 4.4., therefore in full:

$$Z_j = \begin{cases} \frac{1}{e^{-b_0 + b_1 D_T}} a_0 + a_1 D_T & D_T > 0 \\ p_0 a_0 + a_1 D_T & D_T = 0 \end{cases} \quad 4.13$$

For rainfall amounts, this is the equivalent to simply taking the linear fit of the amount plot in Figure 4.8. Therefore the disadvantage of using this approach above is that the variance of the rainfall distribution is not exploited. In addition, because the probability of rain is positive even for zero CCD, there will be no dry pixels in the estimate.

One of the stated aims of this thesis is to model the uncertainty associated with rainfall estimates when applied to crop yield modelling. Several studies have shown that including

this uncertainty is important in impacts models such as hydrological or crop simulation models (Tsonis *et al.*, 1996, Tsintikidis *et al.*, 1999, Nikolopoulos *et al.*, 2010, Teo, 2006). Therefore rather than applying the deterministic approach above, some thought has been given to a probabilistic satellite rainfall estimate. In this case, a large ensemble of potential rainfall values can be created for a given *CCD* using the relationship:

$$Z_j = I_j F_j \quad 4.14$$

where  $I_j$  is a binary variable representing whether it is raining or not at pixel  $j$  and  $F_j$  represents rainfall amount at the pixel. For each ensemble member and pixel,  $I_j$  can be found using a Bernoulli trial with its probability set to that described in equation 4.3.  $F_j$  is found by randomly selecting from the gamma distribution described in equation 4.4. The calibration process for the variables in these equations is described in the next chapter. This approach also needs to be extended because the observed spatial correlation of rainfall at a given location is not taken into account. In order to create spatially correlated maps of rainfall suitable for use in a crop model, one must apply stochastic methods such as sequential simulation. The methods for doing this are discussed in detail in Chapter Six and validated in Chapter Seven.

#### 4.3.4. FINAL CALIBRATION EQUATIONS

For easy reference, the final calibration for daily TAMSAT rainfall estimates has been summarised below. In future Chapters, these equations will be referred to as ‘Daily Calibration Equations’ and the reader referred back to this Section.

##### ***Probability of rain:***

This is a logistic regression between the probability of rain and *CCD* defined as:

$$P(Z > 0 | CCD = D_T) = p = \begin{cases} \frac{1}{e^{-b_0 + b_1 D_T}} & D_T > 0 \\ p_0 & D_T = 0 \end{cases} \quad 4.15$$

The relationship is originally described in Equation 4.3.

### Rainfall amount

The positive rainfall amount,  $F$ , can be described by a gamma Generalised Linear Model as originally described in Equation 4.4:

$$f(Z|Z>0) = F = g(\mu_F, \sigma_F) \quad 4.16$$

The mean of the calibration model,  $\mu_F$ , is calculated using the multiple linear regression discussed in Section 4.3.2.2:

$$\mu_F = a_0 + a_1 D_{30} + a_2 D_{40} + a_3 D_{50} + a_4 D_{60} \quad 4.17$$

Finally the error on the calibration model,  $\sigma_F$ , is described by the relationship discussed in Section 4.3.2.3 and Equation 4.11:

$$\sigma_F^2 = \begin{cases} \sigma_C^2 - \sigma_G^2 + \bar{\sigma}_I^2 & \sigma_G^2 + \sigma_I^2 \leq \sigma_C^2 \\ \bar{\sigma}_I^2 & \sigma_G^2 + \sigma_I^2 > \sigma_C^2 \end{cases} \quad 4.18$$

The individual terms in all of the summary equations are fully described at the point they are first mentioned in the text.

## 4.4 CONCLUSION TO CHAPTER FOUR

This chapter considered how remote sensing can be used to create daily rainfall estimates over Africa. Satellite rainfall estimation is a rapidly growing research field, therefore the initial part of the chapter contained a review of different approaches which are currently available. The chapter then focused on Meteosat-derived TAMSAT rainfall estimates due to their good performance in intercomparisons studies and use in previous studies on crop yield forecasting. The operational 10-day TAMSAT calibration procedure was first described to provide an overview of the approach. The approach of Teo and Grimes (2007) was then used to describe a daily TAMSAT calibration procedure which allows the uncertainty in the estimate to be accounted for. New features of the calibration include a gamma generalised linear model and the capability to include multiple CCD thresholds.

# CHAPTER FIVE

# CALIBRATION OF TAMSAT OVER

# ETHIOPIA

## 5.1 OVERVIEW

As described in the previous chapter and summarised in Section 4.3.4, there are several parameters which must be calibrated to create ensembles of daily TAMSAT estimates. These include the probability of rain,  $p$ , plus the mean rainfall amount,  $\mu_F$ , and variance,  $\sigma_F$ , at a given value and temperature threshold of CCD. As discussed in Section 4.3.1, each of these parameters is assumed to be constant within regions that have a homogeneous climate, but may differ between different regions. For example they would be expected to differ between a mountainous region and a plateau. The regional boundaries and calibration parameters would also be expected to vary from month to month.

The aim of this chapter is to apply the daily TAMSAT calibration derived in the previous chapter to the Ethiopian case study. Firstly the choice of the homogeneous climate zones is considered. Parameters are then derived for the probability of rainfall, the rainfall amount and the rainfall variance. Finally, some analysis of the daily TAMSAT satellite estimates is described.

## 5.2 SELECTING ZONE BOUNDARIES

The aim of this chapter is to apply the calibration described in Chapter Four to the Ethiopian case study discussed in Section 3.6. As shown in below in Figure 5.1, there is a dense rain-gauge dataset available for calibration, but these gauges are situated in a small proportion of the total area for which satellite estimates are needed. An added complication is that the area containing the gauges is exclusively within Ethiopia's highlands, thus the gauges do not cover all of Ethiopia's diverse landscapes and micro-climates.

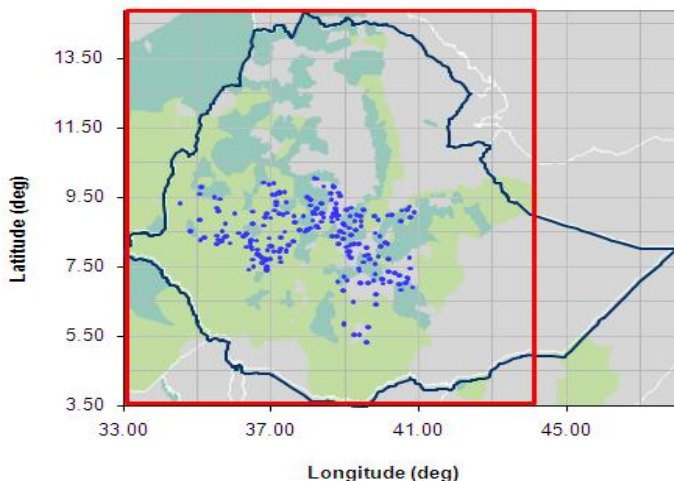


**Figure 5.1.** The study region. Rain-gauges used in the calibration are shown as blue dots. These are taken from the Oromiya dataset and are discussed in Section 3.2.1.1. The red line is the region for which crop yield estimates and so satellite estimates are needed.

The daily methodology described in Section 4.3.2 is relatively new and has previously only been applied in one small region which did not need multiple calibration zones (Teo and Grimes, 2007). In addition, past dekadal TAMSAT calibrations have been performed in areas where the calibration rain-gauges have been scattered more uniformly over the area required for satellite estimates. Consequently, some thought must be given to the delineation of calibration zones in areas which do not contain gauges. The complexity of the Ethiopian climate and topography suggest that this task is not trivial and must be completed with care, hence five potential methods of creating calibration zones have been selected for comparison:

**ONE-ZONE:** The entire region should be left as one zone.

*ISOHYET*: The region could be split using a monthly rainfall contour, as it is reasonable to expect that monthly rainfall amounts might give a clear indication of climatologically homogeneous regions. For simplicity the region has been split into a maximum of 2 zones.

*ELEVATION*: The region could be split using an elevation contour. Ethiopia's rainfall is highly dependent on its topography therefore an elevation contour may provide a good estimate of climatologically homogeneous areas. For simplicity the region has been split into a maximum of 2 zones.

*DEKDAL*: The TAMSAT dekadal calibration zones could be used for the daily Ethiopian calibration. These are a subjective fit, but created using a much wider network of rain-gauges. It is reasonable to assume that daily and dekadal rainfall may have the same climatological structure, thus a dekadal calibration might be able to incorporate additional relevant information from the extra gauges.

*MANUAL*: A similar fit to the one above could be subjectively created using the daily rain-gauge data.

Although the process of choosing and comparing zones was designed to be as automatic as possible, some of the zonal boundaries had to be manually fitted for the ISOHYET, ELEVATION and MANUAL cases. This is described further below.

### **5.2.1. EXAMPLE**

The boundary selection process involved plotting dichotomous (rain/no rain) statistics created from the calibration dataset and CCD at different thresholds onto maps overlaid with monthly rainfall and elevation contours. Thresholds of elevation and monthly rainfall were then chosen that best seemed to split the region into climatologically homogeneous zones. The statistics used are the dichotomous bias, probability of detection and Pierce's skill score; all are explained further in appendix A2.1. In some cases, no clear split can be seen between different calibration regions hence the threshold choice was somewhat arbitrary. For the MANUAL fit, the region was subjectively split into zones using the plots as a guide.

Figure 5.2 shows an example of the June calibration plots. Here, the dichotomous bias (defined in Appendix A2.1) was plotted for each rain-gauge and zone boundaries were selected using the method discussed above. In this case, a monthly rainfall contour of 160mm seemed to be the most appropriate, splitting the gauges into a region of high bias to the East and a low bias to the West (Figure 5.2a). However, there was no obvious choice of elevation contour for this month that would split the region into 2 separate climatic zones (Figure 5.2b), so in this month a boundary of 2,300m was arbitrarily chosen. Figure 5.2d shows the manual zone choice. The small region of high bias in the Eastern mountains was selected as a separate zone, because that area's climate is recognised to be different to that in the lowlands and it appeared to have a different relationship with CCD. The case is somewhat different for October in Figure 5.3, where it was difficult to split the region into zones using mean monthly rainfall or elevation contours. The zone boundaries for the ISOHYET, ELEVATION and MANUAL fits were chosen in a similar fashion for all other months and are included in Appendix A1.1.

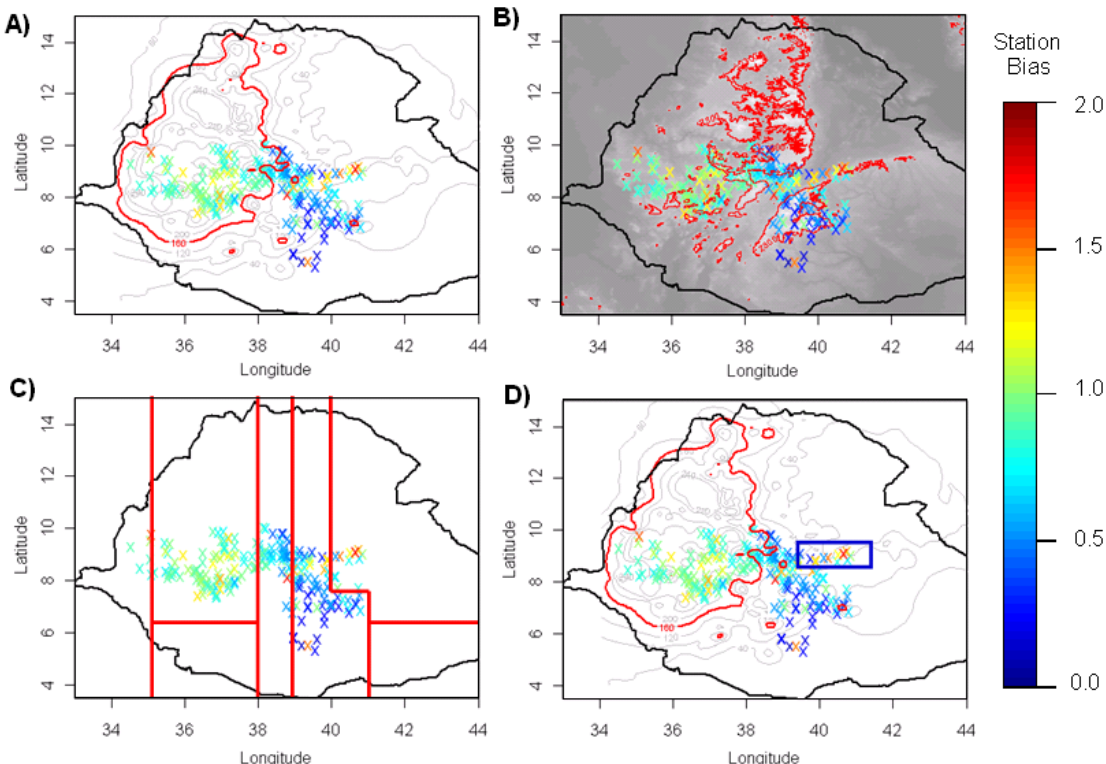


**Figure 5.2. Different zone thresholds for June.** The coloured crosses in each sub-plot show the statistical bias of the rain/no rain parameter for each rain-gauge at a CCD threshold of 40°C. Plot A shows the region split using a rainfall contour of 160mm (ISOHYET method). Plot B shows the study area split using an elevation contour of 2300m (ELEVATION method). Plot C shows the DEKADAL fit - this consists of 7 zones, but zones containing no gauges are merged with their neighbours. Plot D shows the MANUAL fit.

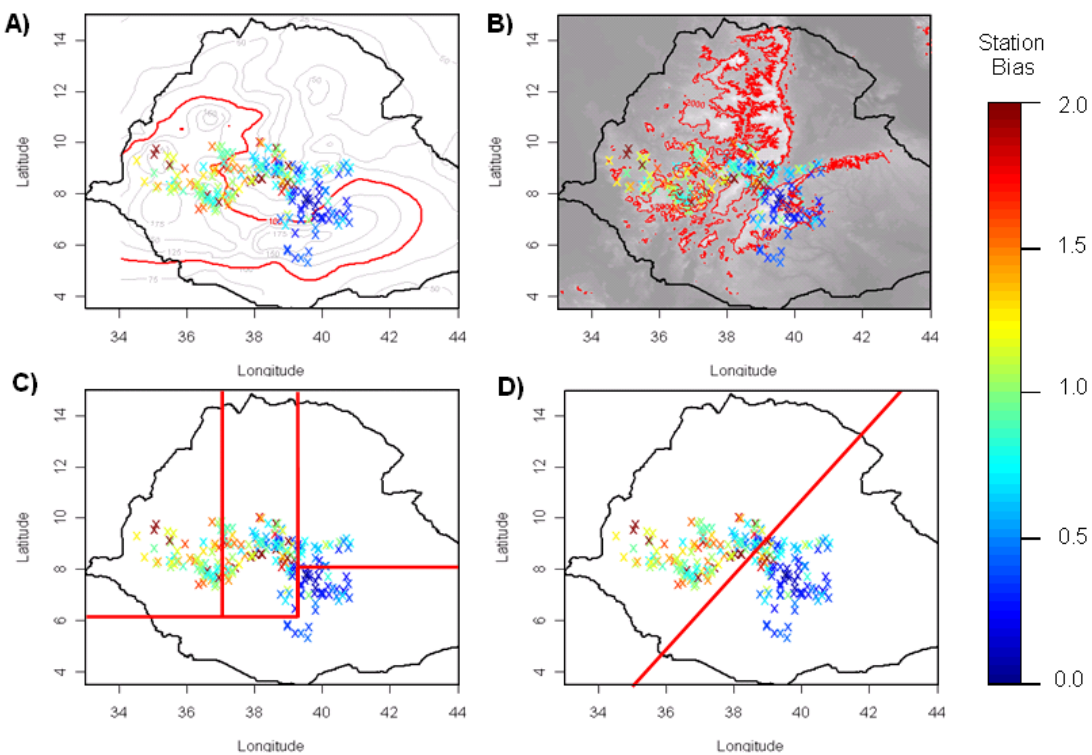


**Figure 5.3.** Different zone thresholds for October. The coloured crosses in each sub-plot show the bias of the rain/no rain parameter for each rain-gauge at a CCD threshold of 40°C. Plot A shows the study area split using a rainfall contour of 100mm (ISOHYET method). Plot B shows the study area split using an elevation contour of 2,000m (ELEVATION method). Plot C shows a 4 zone DEKADAL split and plot D shows the MANUAL fit.

The process of selecting the ‘best’ zone type for each month is discussed later in the chapter.

## 5.3 CALIBRATION PROCEDURE

### 5.3.1. OVERVIEW

The aim of the calibration process is to select parameters for the daily calibration equations described in Section 4.3.4 for each month. Therefore, for each month, the Daily Calibration Equations were applied to every combination of zone choice and CCD threshold. There are 4 temperature thresholds (-30°C, -40°C, -50°C and -60°C) and 5 potential zone choices. This corresponds to 15 potential calibration for each zone choice and so 75 for each month, e.g. one calibration would comprise of the ONE-ZONE choice, plus just using CCD<sub>40</sub> and CCD<sub>50</sub>. The results were then compared statistically and

subjectively and the best option selected as the calibration for that month. The following sub-sections detail this process for mean rainfall amount, the probability of rain and rainfall variance.

### 5.3.2. MEAN RAINFALL AMOUNT

As described above, the multiple regression between positive rainfall amount and CCD detailed in Equation 4.17, was applied to each combination of zone choice and CCD threshold. The goodness of fit of each combination were then compared using Akaike's Information Criterion skill score (AIC) and ANOVA tables, which are discussed in more detail in Appendix A2.2. An example of the rainfall amount calibration procedure is described below for the month of March. For reference, the chosen zone boundaries for this month are shown in Figure 5.4. The multiple regression results for all other month are included in Appendix A1.2.

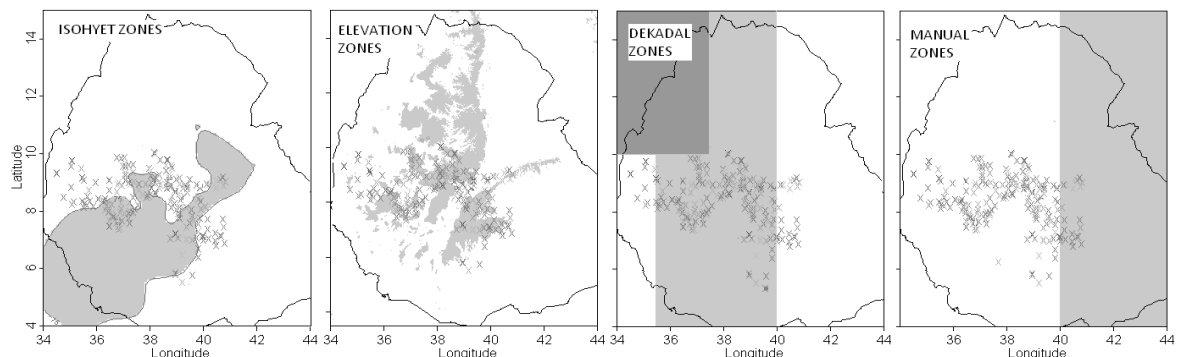


**Figure 5.4.** Boundaries selected for the ISOHYET, ELEVATION, DEKDAL and MANUAL zones for March. The Oromiya gauge dataset can also be seen as crosses on the plot.

First, values of AIC for each zone choice and a single temperature threshold were calculated and are shown in Table 5.1, where lower values of AIC indicate a better fit.

Zone hypothesis	Temperature Threshold			
	30°C	40°C	50°C	60°C
1: all one zone	37919	38142	38582	39117
2: Rainfall contour	37905	38125	38553	39094
3: Elevation contour	37897	38133	38575	39120
4: Dekadal zones	37847	38067	38505	39065
5: Manual fit	37849	38069	38507	39070

**Table 5.1.** AIC values for a single temperature threshold and different zone hypotheses for March. Lower values of AIC indicate a better fit (three lowest values are highlighted).

The fits with lower values of AIC shown in Table 5.1 all include  $CCD_{30}$  and multiple zones. Therefore the results of the multiple regression fits including  $CCD_{30}$  were selected for study and are included in Table 5.2.

Zone hypothesis	Temperature Threshold						
	30 & 40°C	30 & 50°C	30 & 60°C	30,40 & 50°C	30,40 & 60°C	30,50 & 60°C	All thresholds
1: all one zone	37904	37893	37900	37895	37895	37893	37894
2: Rainfall	37890	37875	37876	37878	37874	37868	37871
3: Elevation	37879	37868	37875	37870	37870	37869	37871
4: Dekadal	37831	37817	37828	37822	37825	37821	37825
5: Manual fit	37831	37817	37827	37820	37823	37818	37821

**Table 5.2.** AIC values for multiple temperature thresholds and different zone hypotheses for March. Lower values of AIC indicate a better fit (the three lowest values are highlighted blue and the 5 lowest values after that are highlighted purple).

The fits with lower values of AIC all use the MANUAL or DEKADAL zone choices. The results in Table 5.2 also seems to suggest that including multiple thresholds might give a better calibration than simply using  $CCD_{30}$ , because the AIC values for these fits is much lower than the corresponding  $CCD_{30}$  fit in Table 5.1. In particular, the results in Table 5.2 suggests that the 30°C threshold is required for the calibration, plus either a 50°C or a 60°C threshold. This makes physical sense, as March falls at the beginning of the rainy season where rainfall is much more likely to come from isolated convection, thus including

information from colder temperature threshold may indicate a method of removing cirrus contamination from the anvil of thunderclouds. It is unsurprising that the MANUAL and DEKADAL fits seem to produce similar calibration statistics, as Figure 5.4 shows that they are very similar. It is probable that the MANUAL fit has lower values of the AIC statistic, because there are less zones and AIC penalises model complexity. The results suggest that there is not enough data to justify using the DEKADAL fit, plus the MANUAL and DEKADAL fits are very similar as shown in Appendix 1. Therefore the MANUAL model was chosen as the zone boundaries for March.

Finally, ANOVA tables and F-tests were used to compare the calibrations with the MANUAL fit and the with lowest values of AIC:

#### **MANUAL FIT, Zone 1 (West zone):**

$$\text{Model 1: } \mu_F = a_0 + a_1 CCD_{30} \quad 5.1$$

$$\text{Model 2: } \mu_F = a_0 + a_1 CCD_{30} + a_2 CCD_{50} \quad 5.2$$

$$\text{Model 3: } \mu_F = a_0 + a_1 CCD_{30} + a_2 CCD_{50} + a_3 CCD_{60} \quad 5.3$$

Model	AIC	Residual degrees of freedom	Residual deviance	Model degrees of freedom	Deviance degrees of freedom	F-value	P(> F)	Significant to
1	34264	6410	1591.94					
2	34230	6409	1583.38	1	8.56	29.70	5.24e-8	< 0.001
3	34230	6408	1582.83	1	0.56	1.93	0.16	< 0.05

**Table 5.3. ANOVA and AIC table for the 3 best fits for zone 1.**

Therefore in this case, model 2 fits the data best:

$$\mu_{F Zone1} = a_0 + a_1 CCD_{30} + a_2 CCD_{50} \quad 5.4$$

where  $a_0 = 6.24$ ,  $a_1 = 0.33$  and  $a_2 = 0.21$

**MANUAL FIT, Zone 2 (East zone):**

$$\text{Model 1: } \mu_F = a_0 + a_1 \text{CCD}_{30} \quad 5.5$$

$$\text{Model 2: } \mu_F = a_0 + a_1 \text{CCD}_{30} + a_2 \text{CCD}_{50} \quad 5.6$$

$$\text{Model 3: } \mu_F = a_0 + a_1 \text{CCD}_{30} + a_2 \text{CCD}_{50} + a_3 \text{CCD}_{60} \quad 5.7$$

Model	AIC	Residual degrees of freedom	Residual deviance	Model degrees of freedom	Deviance degrees of freedom	F-value	P(> F)	Significant to
1	3585	628	170.04					
2	3586	627	169.84	1	0.196	0.60	0.440	< 0.05
3	3588	626	169.84	1	0.006	0.02	0.894	< 0.1

**Table 5.4. ANOVA and AIC table for the 3 best fits for zone 2.**

In this case, the addition of either the 50°C or 60°C thresholds do not add extra value to the fit, so Model 1 is best for this zone:

$$\mu_{F \text{ Zone2}} = a_0 + a_1 \text{CCD}_{30} \quad 5.8$$

where  $a_0 = 7.64$  and  $a_1 = 0.37$ .

### 5.3.3. PROBABILITY OF RAIN

The method described in Section 5.3.2 allows selection of both the zone choice and the parameters needed to derive mean rainfall amount (if raining) at a given pixel. Attention must now be paid to the probability of rain. This can be modelled as a weighted logarithmic regression between rainfall and CCD, described in Equation 4.15 in the Daily Calibration Equations. In order to avoid over-fitting, only the dominant CCD temperature threshold was used in this fit i.e. for the March example above, this would be CCD<sub>30</sub>.

In order to calculate the parameters for this statistic, the rain-gauge values in each zone and month were first grouped according to CCD at the appropriate temperature threshold. The proportion of rainy gauges in each bin was then plotted against CCD and modelled using the weighted logistic regression. An example is shown below for March, where as

described in the previous section, the zone choice was the MANUAL East/West split and the dominant CCD temperature threshold was -30 °C.

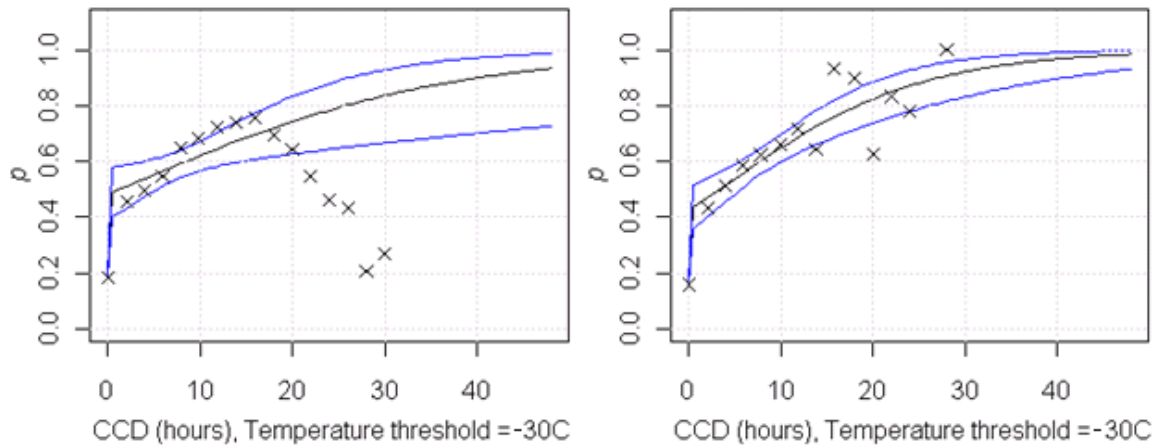


**Figure 5.5.** Parameters for the probability of rain during March for the West zone (left hand plot) and East zone (right hand plot). The logistic regression is plotted as the central black line, whilst the 90% confidence intervals are shown as blue lines.

Interestingly, Figure 5.5 indicates that rainfall frequency is suppressed at high CCD in the West zone, however the rainfall amount statistics in the previous Section showed less of a signal. This suggests that there are occasional large convective storms which are associated with a lot of cold cloud but that also high values of CCD are found on cloudy dry days, thus there is more uncertainty in the probability of rain at high CCD. This is compounded by the fact that there are very few days recording high CCD values in March. The multiple regression results for each month are included in Appendix A1.3 and are discussed in detail in Section 5.4.4.

#### 5.3.4. ERROR PARAMETERS

Finally, the parameters relating to variance described in Equation 4.18 were calculated by plotting the kriging and regression variances against mean rainfall amount which was then modelled using an iterative least squares approach. The error plots for each zone are shown in Figure 5.6. The importance of the satellite location error as a lower limit of the total variance can be seen, as otherwise the satellite variance would become negative for

small amounts of rainfall (this is discussed further in Section 4.3.2.3). For March, the final error relationship was found to be as follows for each zone:

$$\text{Zone 1 (West)} : \sigma_{SZ1}^2 = 0.75\mu^{0.77} - 3.72\mu^{0.34} \quad 5.9$$

$$\text{Zone 2 (East)} : \sigma_{SZ2}^2 = 0.54\mu^{0.88} - 2.67\mu^{0.43} \quad 5.10$$

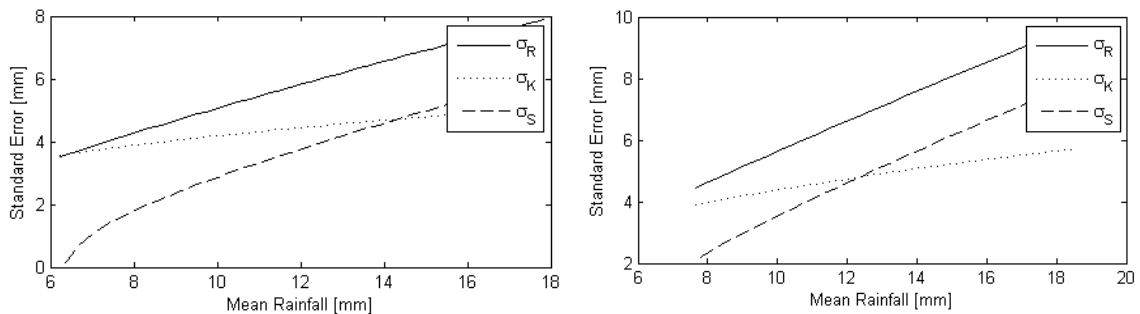


**Figure 5.6.** Error plots for the West zone (top) and East zone (right) in March. The regression variance is given by  $\sigma_R$ , the kriging variance by  $\sigma_K$  and the difference by  $\sigma_S$ .

## 5.4 ETHIOPIAN CALIBRATION

The process described above was then applied to every month and the full results are included in Appendix One. This Section considers how the calibration parameters vary from month to month and also discusses why January and February were excluded from the calibration.

### 5.4.1. EXCLUDED MONTHS

January and February fall at the heart of Ethiopia's dry season and are not part of the cropping calendar, thus it was decided to exclude these months from the study. However, it is interesting to examine some basic calibration plots for these months.

Figure 5.7 depicts the monthly rainfall totals in January and February and Figure 5.8 and Figure 5.9 shows plots of rainfall amount vs CCD at different temperature thresholds for each month (pixels with zero recorded rainfall were excluded). As only approximately

15% of daily pixels were rainy, there was not enough data to consider using different regions or multiple thresholds, therefore the study region is considered as one zone and each sub-plot shows a single temperature threshold.

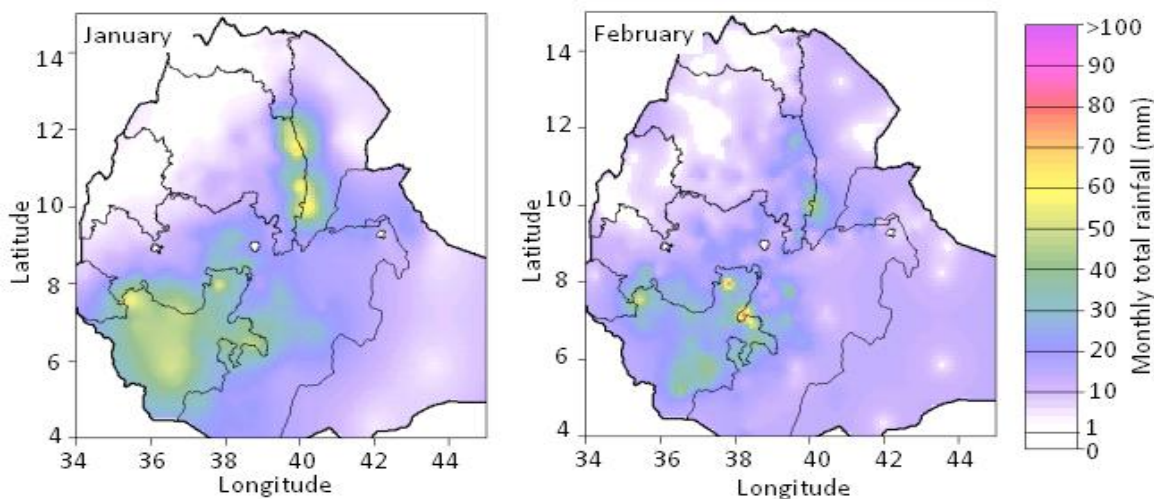


**Figure 5.7. January and February monthly rainfall totals.** These plots were created through kriging a monthly kriged dataset of over 600 stations provided courtesy of the Ethiopian National Meteorological Agency. There were very few gauges in the Somali desert in the South East of the country, therefore these areas may have less realistic results. This can particularly be seen in February, where there stations were dry, but as the range of the variogram was 300km, they appear as white ‘bulls eyes’ on the plot.

The calibration plot for January (Figure 5.8) shows the importance of considering different temperature thresholds. If  $CCD_{60}$  was considered independently, one might come to the conclusion that there was a simple linear relationship between  $CCD$  and rainfall, whilst the  $CCD_{30}$  plot implies a reduction of rainfall amount at high values of  $CCD$ . This is similar to the picture for March in Section 5.3.3.. The effect could either be due to lack of data, or because Figure 5.7 suggests that rainfall in January appears to fall in lowland areas to the South West of the gauge dataset. Therefore it could be envisioned that cloud from these rainfall systems spreads across Oromiya but that rainfall is suppressed, perhaps due to lack of moisture. This argument is supported by Admass (2004), who suggests that the North Easterly winds customary to the Bega season can be interrupted by migratory low pressure systems originating from the East. These can then interact with the ITCZ, resulting in cloud and rain which extends into Southern Ethiopia and occasionally into central regions.

The same effect can be seen when studying the February calibration (Figure 5.9). Although the calibration plots look much more reasonable in terms of fit, there are still only a few events recording high CCD, therefore more data would be needed for a robust calibration. There were only 6 days where pixels corresponding to gauges in the Oromiya dataset recorded rain. Three of these days formed one event (from the 26-28<sup>th</sup> February 2003) which could reasonably be classified as a slightly early start to the Belg rains.

The calibration plots show the importance of only applying TAMSAT estimates to regions and months where one is certain that rain falls from convective systems. Finally, Figure 5.8 also highlights the danger of calibrating TAMSAT with a spatially limited dataset. The plot shows that rainfall is very variable over Ethiopian in January and February, thus applying a calibration over the entire country using gauges based just in Oromiya is clearly inappropriate as the calibration might be expected to overestimate precipitation in the wet region to the South West of Oromiya (S.N.N.P.R) or overestimate rainfall in dry regions to the North.

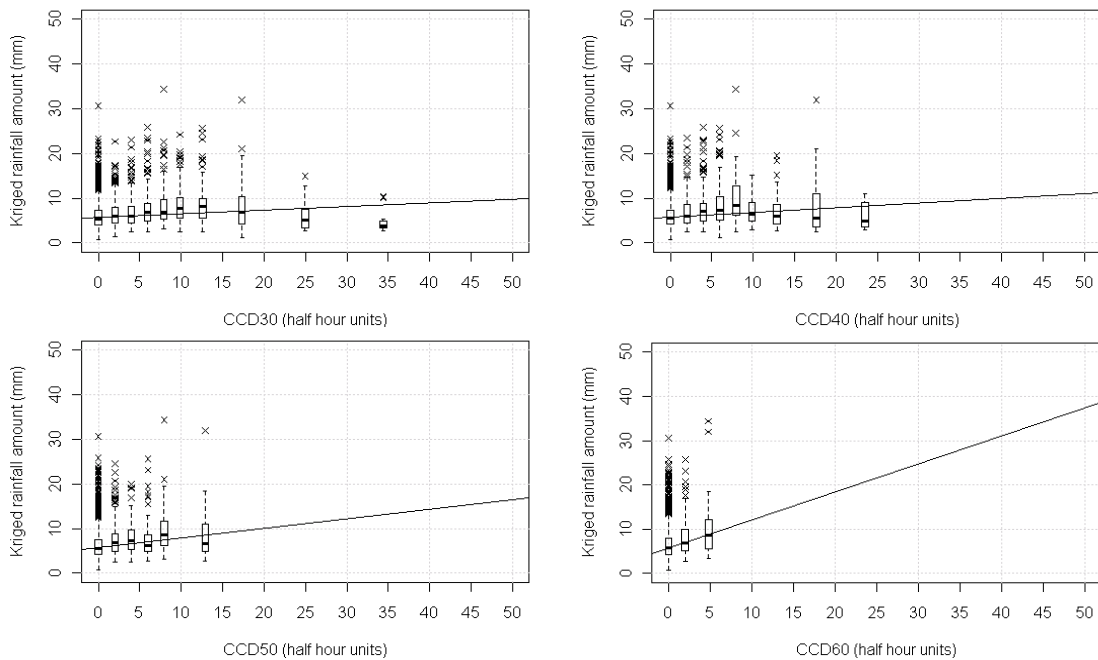


**Figure 5.8. January calibration plots. Each sub-plot shows CCD at a different temperature threshold plotted against kriged rainfall amount from 2002-2006.**

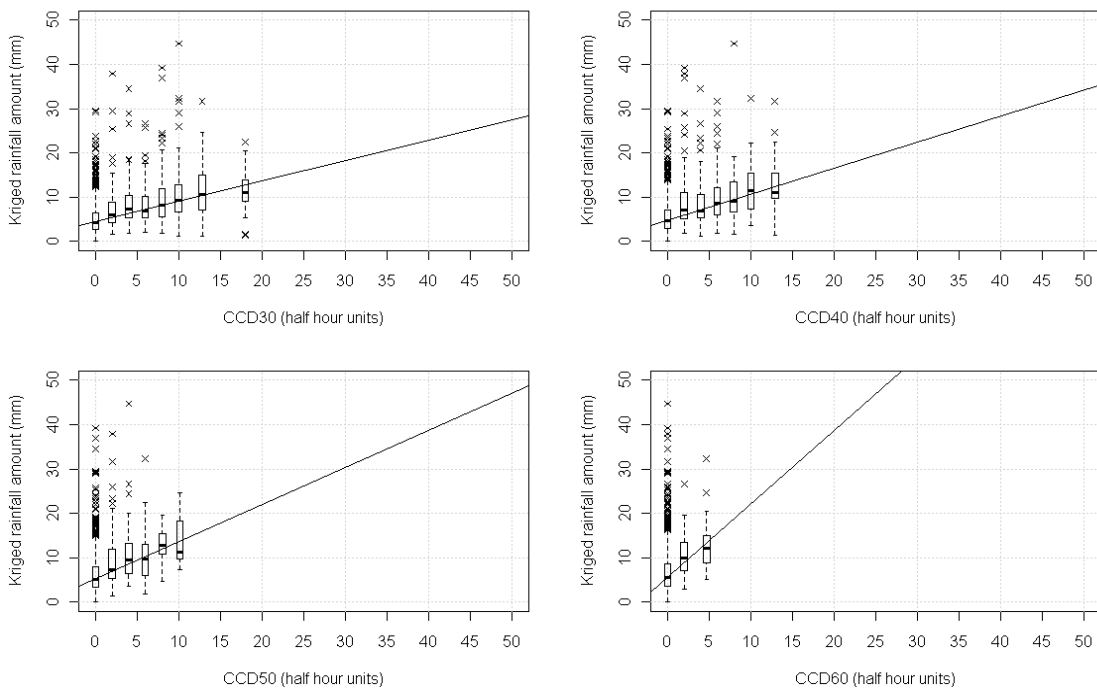


**Figure 5.9. February calibration plots. Each sub-plot shows CCD at a different temperature threshold plotted against kriged rainfall amount from 2002-2006.**

#### 5.4.2. ZONE CHOICE

Please note that plots of zone choices for all months are contained in Appendix 1.

The final zone hypothesis for each month, which were chosen using the process discussed in Section 5.3.2, shows a progression throughout the year linked to the seasonal rainfall cycle. At the height of the main rainy season in July and August, the simple ‘one zone’ hypothesis outperformed the others. This is probably because of the limited distribution of the rain-gauges. Figure 3.1 indicates that the monthly rainfall amount over the region in these two months was relatively stable and heavy ( $> 200\text{mm per month}$ ), therefore all of the calibration gauges fell into one homogeneous climate zone, making it difficult to determine any others. This idea is confirmed by the fact that in the other main rainy season months (May, June and September), the chosen zone hypothesis was the monthly rainfall contour, which picked out these regions of higher rainfall. The picture was slightly different during the Belg rains (April) and at the end of the main rainy season (October), where the monthly rainfall total was below 200mm/month over the whole region. Here,

the more complex ‘dekadal’ hypothesis had the best fit, suggesting that the situation was complicated enough to need the extra information included in the dekadal fit. Finally, in the dry months (March, November and December), there was less consistency in the zone choice apart from a general wet West/dry East divide, which again follows the main rainfall progression, but is perhaps indicative of a lack of information.

#### **5.4.3. RAINFALL AMOUNT**

Please note that full calibration coefficients and plots are contained in Appendix 1.

The variation in the parameters described in Equation 4.17 over the calibration months is shown in Figure 5.10 and Figure 5.11. Figure 5.10 describes the intercept of the equation (parameter  $a_0$ ) whilst Figure 5.11 describes the parameters  $a_1$ ,  $a_2$ ,  $a_3$  and  $a_4$  (which correspond to  $CCD_{30}$  to  $CCD_{60}$ ). A noticeable seasonal cycle can be seen in the intercept parameter, with both the Belg and Kiremt rains noticeable. A slight seasonal cycle can also be seen in Figure 5.11, but in general, most of the difference in the rainfall amount between months is driven by the intercept parameter. The higher intercept in wetter months could be either assigned to heavy rain from short duration convective events or rain from warm cloud. As discussed in Section 3.1, there is very little literature into rainfall types in Ethiopia, so it would be difficult to comment on the second hypothesis. However, Birhanu and Alamirew, suggest that rainfall has a higher intensity during short convective events of 1-2hrs, which perhaps adds to the argument that the high intercept is due to these events.

Figure 5.11 also indicates that  $CCD_{30}$  is important in nearly every month in the calibration, but that apart from in the wettest months, a colder temperature threshold is needed to supplement the  $CCD_{30}$  fit. This may be because in these months rainfall is much more likely to come from less organised convection, thus as discussed in Section 5.3.2, including information from colder temperature threshold may indicate a method of removing cirrus contamination from the anvil of thunderclouds. The full figures for the calibration amount can be found in Appendix A1.2.

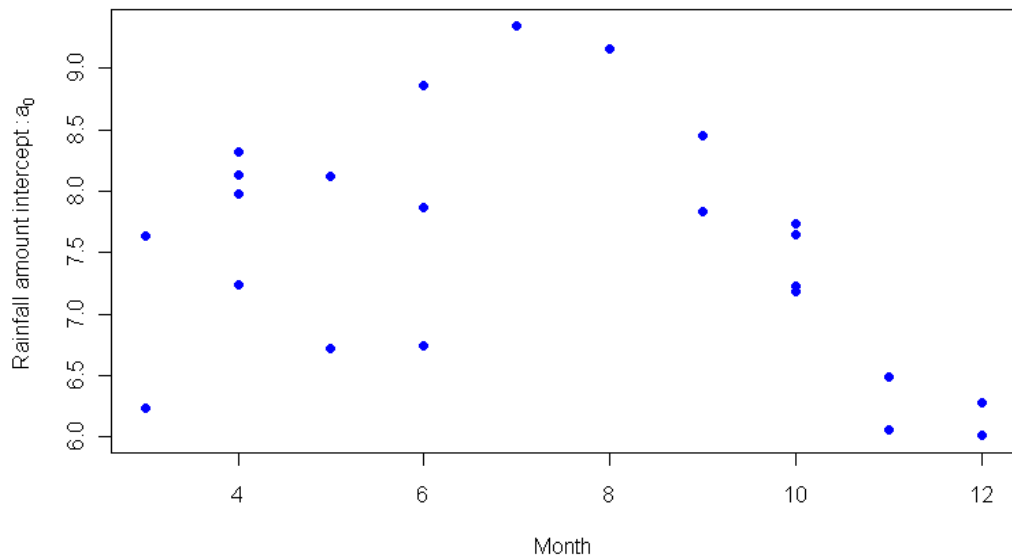


**Figure 5.10.** Parameter  $a_0$  in equation 4.7, which corresponds to the intercept of the multiple linear regression of rainfall amount for each month. Each point corresponds to the fit in one zone in one month.

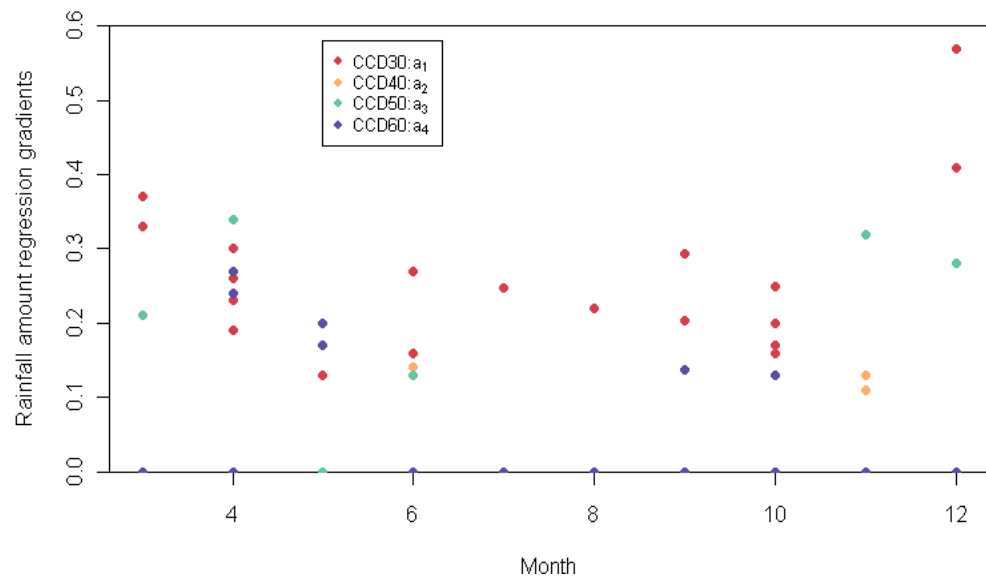


**Figure 5.11.** Parameters  $a_1$ ,  $a_2$ ,  $a_3$  and  $a_4$ , in equation 4.7, affecting  $CCD_{30}$ ,  $CCD_{40}$ ,  $CCD_{50}$  and  $CCD_{60}$  respectively. Each point corresponds to the fit in one zone in one month. The full parameters for each month are specified in Appendix A1.2.

#### 5.4.4. PROBABILITY OF RAIN

The probability of rain was determined by a logistic regression between CCD and observed probabilities described in Section 4.3.4. Plots of this fit for each month and calibration zone can be seen in Appendix A1.3. The majority of zones and months showed a

reasonably good fit using the logistic regression. However as discussed in Section 5.3.3, zone 1 in March showed a suppression of the probability of rain at high CCD. This agrees with the story found in January and February and suggests that at this time of year, there are large scale cloudy (non rainy) systems present over Ethiopia which render the TAMSAT approach less effective.

The main monthly variation in the parameters of Equation 4.15 is from the probability of rain at zero CCD (or the intercept of the logistic regression). This progression can be seen in Figure 5.12, where a higher monthly rainfall amount in the summer corresponds to a higher probability of rain at zero CCD. This again could be because of more short duration convective events in wetter months or because of rainfall from warm clouds.

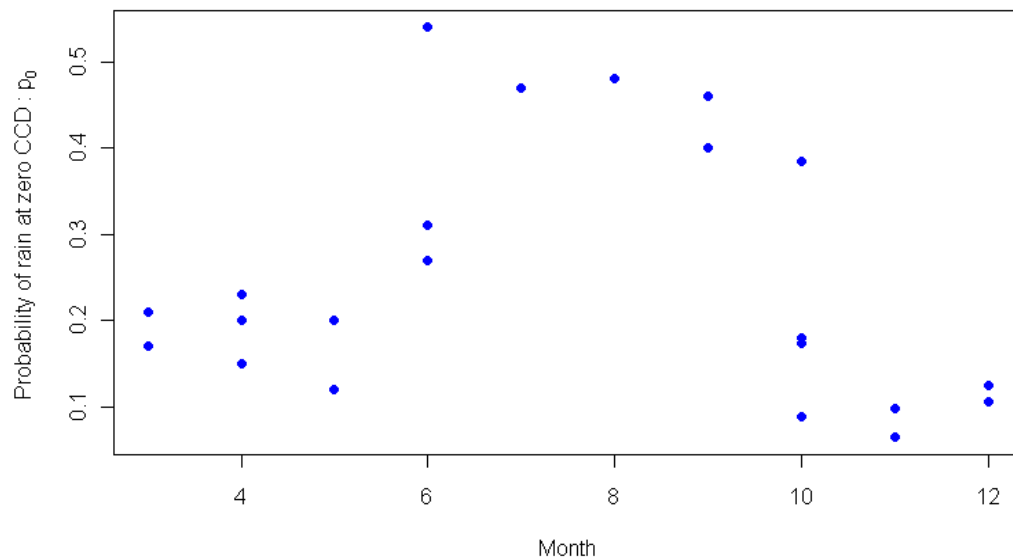


**Figure 5.12.** The probability of rain given zero CCD for the calibration months. Each point corresponds to the value in one calibration zone.

#### 5.4.5. THE VARIANCE OF RAINFALL AMOUNT

As shown in Figure 5.13, the parameters of the variance equations discussed in Section 4.3.4 show very little dependence on season. A higher dependence was expected considering that there is a good relationship between the observed mean and variance of rainfall described in Figure 3.5. There is no obvious reason behind the lack of dependence.

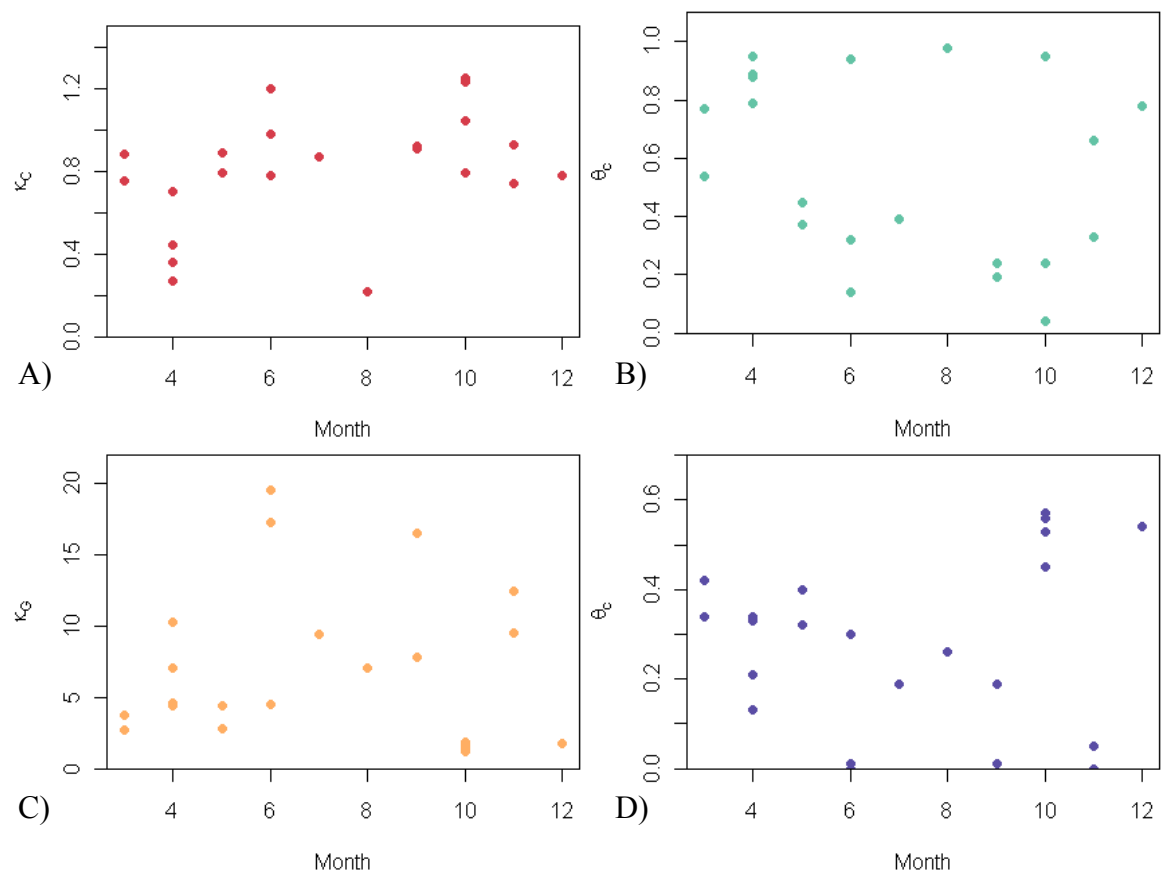


**Figure 5.13.** The different variance parameters over the calibration months. **Figure A** shows  $\kappa_c$ , **figure B** shows  $\theta_c$ , **figure C** shows  $K_G$  and **figure D** shows  $\theta_G$ .

## 5.5 CONCLUSION TO CHAPTER FIVE

This chapter presented how the TAMSAT calibration procedure described in Chapter Four was applied to the Ethiopian case study. The situation was complicated due to the fact that the calibration gauge dataset had limited spatial coverage. Specifically, all the gauge data came from the relatively wet Oromiya region of Ethiopia, thus it was difficult to extend the calibration to the drier regions in the North and East. Therefore alongside an example of the calibration process for March, the chapter contained a comparison of five different theories for delineating calibration zones. Finally, the chapter contained a discussion of major results from the calibration process (the calibration values themselves can be found in Appendix One).

The results of the calibration process show that there is a strong dependence of the optimum zone choice on the seasonal cycle. The results also show that the multiple calibration approach was justified, with many months requiring one cold temperature threshold with one warm threshold. This warrants future research as it might provide a method for cirrus identification (i.e. cold cloud that does not rain). Finally, it should be noted that January and February were excluded from future study due to a poor calibration attributed to non-convective rainfall.

# CHAPTER SIX

# SEQUENTIAL SIMULATION

## 6.1 OVERVIEW

Chapter Four and Chapter Five discussed a methodology and calibration to allow the production of daily TAMSAT satellite rainfall estimates for the Ethiopian case study outlined in Section 3.6. This calibration was designed to best capture the uncertainty associated with daily rainfall in Ethiopia. As discussed in Section 4.3.3, if one wishes to incorporate this uncertainty into rainfall estimates, a probabilistic ensemble approach must be taken. For each ensemble member and pixel, a Bernoulli trial can be conducted to decide if it is raining or not, then if the pixel is raining, the rainfall amount can be randomly selected from the appropriate Gamma distribution. The properties of the Gamma distribution and the probability of rain distribution are discussed in Section 4.3.4, whilst the parameters which go into these equations are derived in Chapter Five.

The process outlined above means that an ensemble of rainfall estimates generated for any given pixel will have the correct temporal distribution and statistics. However it also implies that rainfall fields as a whole will have no spatial correlation because each pixel has no relationship with its neighbours. As mentioned in Section 3.4.1, rainfall has a well documented spatial correlation but the simulated rainfall fields derived above will not reflect this. This means that unrealistically, simulated rainfall fields will never contain large dry areas on a given day.

The issue presents a significant difficulty when using the results in a large scale impact model such as a hydrological or crop simulation model, as crop simulation models in

particular are sensitive to dry spells. Instead a better route would be to create ensembles of spatially correlated maps of rainfall with the following characteristics:

- 1) The field must have a realistic spatial correlation derived from observations.
- 2) Rainfall statistics at any pixel within the field (e.g. mean rainfall or the probability of rain) must agree with observed rainfall statistics at that location. Therefore the simulation method must take into account the non-Gaussian nature of rainfall.
- 3) Each ensemble member must be an equally probable and realistic estimate of rainfall over the region.

This chapter describes how the satellite calibration illustrated in Chapter Four and Chapter Five can be modified to create ensembles of spatially correlated rainfall fields which correspond to these criteria, whilst Chapter Seven illustrates a validation against an independent gauge dataset. Section 6.2 considers different methods of creating spatially correlated fields, Section 6.3 contains a formal description of one particular method, sequential simulation. Calibration parameters are discussed in Section 6.4, whilst Section 6.5 describes the process in detail for one particular case study on the 1<sup>st</sup> July 2002.

## **6.2 METHODS OF CREATING SPATIALLY CORRELATED RAINFALL FIELDS**

There are several methods used by statisticians to create spatially correlated fields of a variable, however only a few have been applied to rainfall estimation. These include conditional methods such as LU decomposition (Davis, 1987), sequential simulation (Deutsch and Journel, 1998) and simulated annealing (Deutsch and Journel, 1998), plus non-conditional methods such as turning bands (Journel and Huijbregts, 1978 and Tompson *et al.*, 1989; Bellerby and Sun, 2005) and the spectral method (Borgman *et al.*, 1984). In this context, the word conditional is defined as a method which produces an estimate that agrees with observations at a specific location.

As described in Germann *et al.* (2009), LU decomposition works on the assumption that rainfall estimates are generated as error perturbation fields superimposed onto a deterministic field:

$$\Phi_{t,i} = R_t + \delta_{t,i} \quad 6.1$$

Here,  $R_t$  is the deterministic field at time  $t$ ,  $\delta_{t,i}$  is the perturbation at time  $t$  and location  $i$  and  $\Phi_{t,i}$  is the final probabilistic rainfall field. As described in Germann *et al.*, 2006, these perturbations can be represented as mean plus a spatially correlated random noise factor. This can then be solved to give the final rainfall estimate. The approach does not assume second order stationarity of residual uncertainties and is an exact method in that it does not require any approximations in the input parameters. However it can be computationally expensive. Germann *et al.*, 2009 have successfully applied the method to make spatially correlated fields of radar precipitation datasets in the Alps, thus it has been tested in a mountainous region. Bouvier *et al.*, 2003 also showed that the method works well when applied in Mexico.

Simulated annealing is described in Haberlandt and Gattke, 2004,

*“Simulated annealing can be considered as a discrete optimisation technique in which an initial image is gradually perturbed long enough to match a set of constraints such as the reproduction of the probability distribution and the spatial covariance estimated from the observed sample data”.*

The process is flexible and can include a variety of different factors. It also preserves initial statistics such as the rainfall histogram and has been shown to work for rainfall in Pardo-Igúzquiza (1998) and Haberlandt and Gattke (2004). However it is again computationally expensive.

As described in Bellerby and Sun (2005), turning bands works by transforming a multi-dimensional question into the sum of a finite series of one dimensional problems. As the method requires a Gaussian field, the data is first corrected using a normal scores transform, then back transformed at the end of the process (hence its non-conditionality).

Bellerby and Sun (2005), used this process to create a rainfall ensembles using 200 lines randomly distributed on the unit sphere based on rainfall estimates from TRMM.

The spectral or fast Fourier transform method first creates a ‘white noise’ perturbation field. A low pass filter is then applied to impose a spatio-temporal correlation structure. This is then back-transformed and the mean and variance of the underlying field added to make a deterministic field. This method is computationally efficient but again assumes second order stationarity of the covariance matrix. This is a relatively new approach to rainfall estimation, with De Michele and Bernardara, 2004 testing the method successfully on the Global Atmospheric Research Program (GARP) Atlantic Tropical Experiment (GATE) rainfall data set.

Finally, sequential simulation is another geostatistical approach which is described fully in the following sections and in Teo and Grimes (2007). This has been shown by Teo and Grimes (2007) and De Wit and De Bruin (2006) to be a robust method for creating rainfall ensembles in areas with sparse calibration data. It is also easily adapted to take into account the mixed distribution of rainfall occurrence and amount. For these reasons, sequential simulation was chosen for use in this thesis. A more detailed review of the different method for creating spatially correlated rainfall fields is given in Grimes and Pardo Igúzquiza, 2010.

## 6.3 FORMAL DESCRIPTION OF SEQUENTIAL SIMULATION

This Section contains a formal mathematical description of the sequential simulation process. For a full mathematical derivation for any rainfall input, please refer to Teo, 2006; and Teo and Grimes, 2007.

### 6.3.1. OVERALL METHOD

As examined in Section 3.4.1.3 and Section 4.3.3, it is advantageous to consider generating rainfall estimates as a two stage process:

- 1) *Is it raining or not?* The probability of rainfall can be modelled as a logistic regression against CCD. The occurrence of rainfall also tends to have a large scale spatial dependence on rainfall in climatological variograms.
- 2) *If raining, what is the rainfall amount?* The rainfall amount can be modelled as a gamma distribution at a given CCD. In convective regimes, rainfall amount will also have a relatively small scale spatial correlation, because it is more dependent on the micro-physics within one particular convective cell.

Therefore, as for double kriging, it is reasonable for the ensemble generation process to treat the two quantities independently. This can be done within the sequential simulation framework, therefore at a given pixel,  $j$ , and for a given ensemble member,  $m$ , rainfall,  $Z$ , can be modelled as:

$$Z_{jm} = I_{jm} F_{jm} \quad 6.2$$

where  $I_{jm}$  is a binary number indicating if it is raining or not and  $F_{jm}$  is the rainfall amount. In practice, this method is applied by first creating an ensemble of spatially correlated binary rain/no-rain indicator masks, then separately creating an ensemble of spatially correlated rainfall amount fields. The final rainfall field is created for each ensemble member by multiplying them both together.

The description of sequential simulation is now split into two sections, one considering the binary indicator ensemble and the other considering the rainfall amount ensemble.

### 6.3.2. SEQUENTIAL INDICATOR SIMULATION

The main aim of sequential indicator simulation is to create an ensemble which captures the uncertainty associated with satellite rainfall occurrence, but to preserve the observed spatial correlation of the field for each ensemble member. At the root of the process is the concept that the probability of rainfall,  $P$ , for pixel  $j$ , and ensemble member  $m$  can be represented as:

$$P_{jm} = p_j^0 + R_{jm} \quad 6.3$$

where  $p_j^0$  is the ‘best-guess’ of the rainfall probability at  $j$ , fixed across all ensemble members and  $R_{jm}$  is a small residual randomly sampled from the uncertainty on this guess.

In this case,  $p^0$  is taken as the probability defined in Equation 4.15 in the Daily Calibration Equations, although as discussed in Teo and Grimes (2007), any method could have been used to determine it. The parameter  $p^0$  is defined as the prior probability of rainfall. The word prior should be taken in its Bayesian sense, as the most likely probability of rain (according to the calibration) for a particular value of CCD. When a large ensemble of rainfall estimates is created according to Equation 4.15, the proportion of rainy ensemble values at pixel  $j$  should equal  $p_j^0$ .

In order to preserve the spatial correlation present in  $p^0$ , the residuals described in Equation 6.3 must be spatially correlated, hence the following process is used to create each individual ensemble member,  $m$ :

- 1) We start by randomly selecting a set of seed pixels, within the total domain,  $U$ . These pixels should be far enough apart to be independent of each other and there can be any number,  $n$ , of the pixels as long as they conform to the above criteria. The locations of the seed pixels is expressed as:

$$\mathbf{u}_s | s = 1, \dots, n \quad 6.4$$

- 2) For each seed pixel,  $s$ , we assign 1 if it is raining and 0 if dry using a Bernoulli trial with probability  $p_s^0$ . A set of indicator residuals for ensemble member,  $S_{Rm}$ , can now be written as:

$$S_{Rm} = r_{sm} = i_{sm} - p_j^0 \mid \mathbf{u}_s \in U \quad 6.5$$

where  $i_{sm}$  represents binary rainfall occurrence at the seed (i.e. it can be 0 for dry or 1 for raining) and  $r_{sm}$  represents the residual probability.

- 3) We now randomly choose a new pixel in the domain and call it the target pixel,  $t$ . We wish to select a residual probability for this pixel which takes into account the already determined occurrence of rainfall at the set of seed pixels (thus including the observed spatial correlation of rainfall occurrence). This is done by calculating the residual at the target,  $r_{tm}$ , as a weighted linear combination of the seed residuals using simple kriging:

$$r_{tm}^{SK} = \sum_{s=1}^n \lambda_{tm} r_{sm} \quad 6.6$$

Here,  $\lambda_{tm}$  represents the kriging weight for the target pixel associated with the seed pixels.

- 4) The full probability of rainfall at the target pixel, is calculated from the relationship expressed in Equation 6.3, as the sum of the prior and residual probability:

$$P_{tm} = p_t^0 + r_{tm}^{SK} \quad 6.7$$

Finally, the rainfall occurrence is then allocated using a Bernoulli trial and the target pixel added to the collection of seeds.

- 5) A new target pixel is chosen and the process repeated until all pixels have been assigned as raining or dry.

The result of this process will be a spatially correlated mask of rain/no-rain values conditioned on the prior probability of rain at each point.

### 6.3.3. SEQUENTIAL GAUSSIAN SIMULATION

A similar process is used to create the rainfall amount ensemble fields. In this case, the rainfall amount,  $F_{jm}$ , for pixel  $j$  and ensemble member  $m$  can be represented as:

$$F_{jm} = \mu_j + W_{jm} \quad 6.8$$

where  $\mu_j$  is the mean estimated rainfall and  $W_{jm}$  a spatially correlated residual at pixel  $j$ , selected from a Gamma distribution with mean  $\mu_j$ . In our case, the mean estimated rainfall is obtained from the Daily Calibration Equations in Section 4.3.4. In particular, the mean is taken from the multiple regression outlined in Equation 4.17 and the variance of the gamma distribution is defined in Equation 4.18. To stay in line with these equations, from this point onwards the mean rainfall at  $j$  is given by  $\mu_{Fj}$  and the variance of the gamma distribution by  $\sigma_{Fj}^2$ .

In order to create ensembles from this field, the following process is followed:

- 1) Use the same collection of seed pixels,  $U$ , as defined in Section 6.3.2 at locations  $u_s | s = 1, \dots, n$  .
- 2) Assign a rainfall amount to each seed pixel from the gamma distribution defined in Equation 4.16. A set of residuals for pixel  $s$  and ensemble member  $m$ ,  $S_{Rm}$ , can now be written as:

$$S_{Rm} = w_{sm} = f_{sm} - \mu_{Fs} | u_s \in U \quad 6.9$$

where  $\mu_{Fs}$  is the rainfall at seed pixel  $s$  and  $f_{sm}$  is the value randomly selected from the gamma distribution at that location for ensemble member  $m$ .

- 3) A requirement of sequential Gaussian simulation is that the sampled distribution is Gaussian, otherwise the kriging error is difficult to interpret correctly. In our case the distribution is gamma, a reversible normal scores transform must be applied to the set of residuals (discussed further in Section 6.5.2):

$$S_{Ym} = \phi S_{Rm} \quad 6.10$$

- 4) Similar to sequential indicator simulation, a target pixel,  $t$  is then selected and simple kriging used to find the kriging estimate,  $y_t^{SK}$  and its associated kriging error  $\sigma_t^{SK}$ . These are effectively the parameters of the modified normal residual distribution at the target location.
- 5) A value is then randomly selected from the normal distribution at  $t$  and the pixel added to the set of seeds. Steps 4 and 5 are then repeated until the grid has been filled
- 6) In order to create the final grid, the residuals are back transformed to the Gamma distribution, then the mean prior rainfall is added at each location to make the rainfall estimate.

The final realisation of the rainfall field for ensemble member  $m$  is then calculated using Equation 6.3. In order to create new ensemble members, the entire process is repeated with a new set of seed pixels.

## 6.4 PRACTICAL NOTES AND CALIBRATION PARAMETERS

### 6.4.1. THE STRUCTURE OF RAINFALL EVENTS

A potential criticism of a method which generates rainfall amount and occurrence independently is that rainfall fields may have sharp ‘cut offs’ at rain/no rain boundaries, therefore the detailed synoptic structure of rainfall may not be correctly represented in the ensembles. Several papers also cite that a better approach is to use mixed models or multivariate Gaussian (Dunn, 2004, Cannon, 2008). An example of an observed convective system (from radar) and a simulated rainfall field can be seen in Figure 6.1.

This example shows that, although the ensemble members do indeed sometimes have sharp cut offs of rainfall, the observed rainfall amount pattern is far from easily modelled. When considering that the process is being applied to Ethiopia, for which very little is known about the structure of rainfall events, it would be very difficult to impose a rainfall structure on the ensembles. For example, the Figure shows that it is unreasonable to assume that there is always low rainfall at the edge of a rainfall event. Therefore Equation 6.2 was used to create rainfall fields without imposing extra information about rainfall structure.

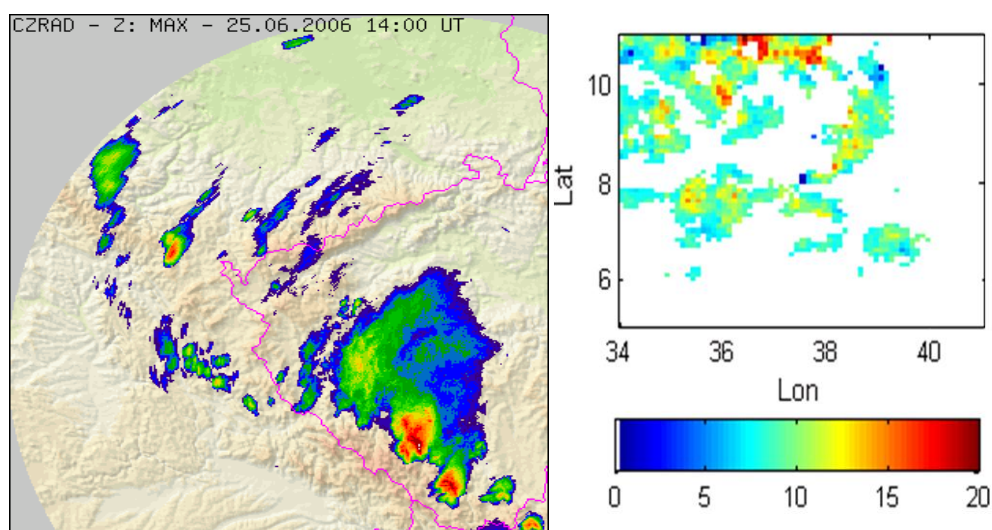


**Figure 6.1.** A comparison between a radar image of a convective storm in Hungary on the left (Setvak, 2006), and one of the outputs from sequential simulation. As there is no radar in Ethiopia, the two pictures above are not meant to be a direct comparison and show different places on different days; they are simply examples of convective systems.

#### 6.4.2. RANDOM PATHS

It is computationally expensive to generate a new random path through the pixels for each ensemble member as new kriging weights would be needed each time. As discussed in Teo, 2006, the random path is fixed at the beginning of the process for all ensemble members.

### 6.4.3. VARIOGRAMS

The variograms used for the simple kriging process are subtly different to those described in Section 3.4, as they are the variograms of the indicator and amount residuals rather than of the parameters themselves. For each gauge,  $g$ , and on a given day,  $d$ , the indicator residuals were calculated as:

$$r_{gd} = i_{gd} - p_g \quad 6.11$$

where  $i_g$  is a binary value showing if there is rain recorded on day,  $d$ , and  $p_g$  is the sample proportion of rainy day having the same value of CCD within the same month. Similarly the rainfall amount residuals for a given day and gauge,  $w_{gd}$ , were calculated as:

$$w_{gd} = f_{gd} - m_g \quad 6.12$$

where  $f_{gd}$  is the rainfall amount at that gauge and day and  $m_g$  is the average of non-zero rainfall at gauges within pixels having the same value of CCD within that month. The final rainfall amount residuals were then transformed to a normal distribution as:

$$Y_{gd} = \phi(w_{gd}) \quad 6.13$$

In each case, the final semi-variance,  $\gamma_c$  was then calculated using:

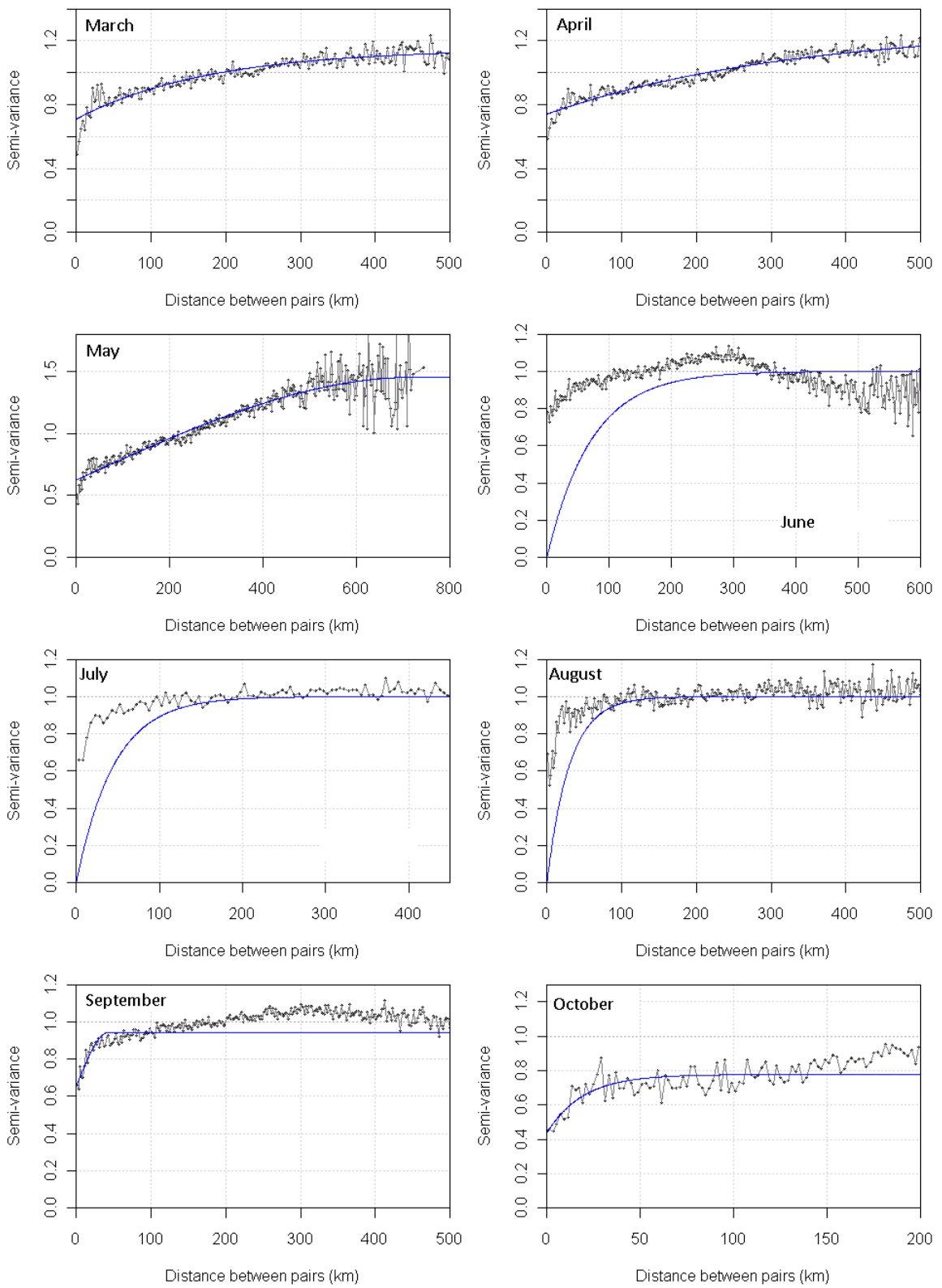
$$\gamma_c(h) = \frac{1}{M} \sum_{k=1}^M \frac{E[(z_k(u) - z_k(u+h))^2]}{\sigma_k^2} \quad 6.14$$

where the value  $z_k$  is either  $r_{gd}$  or  $Y_{gd}$  depending on the case,  $h$  is the separation between stations,  $k$  refers to the day of the month,  $M$  is the number of days in the month and  $\sigma_k^2$  is the variance on day  $k$ .

---

## Chapter Six Sequential simulation

---



**Plot continued on the next page**

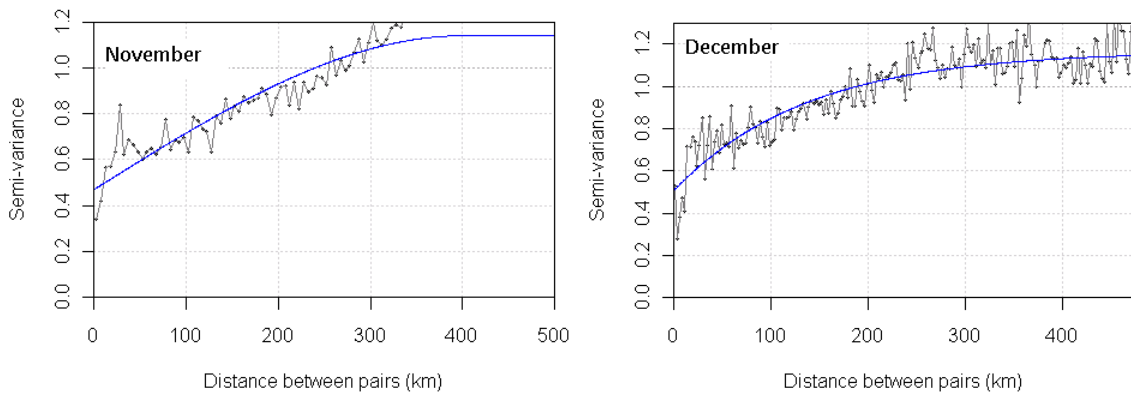


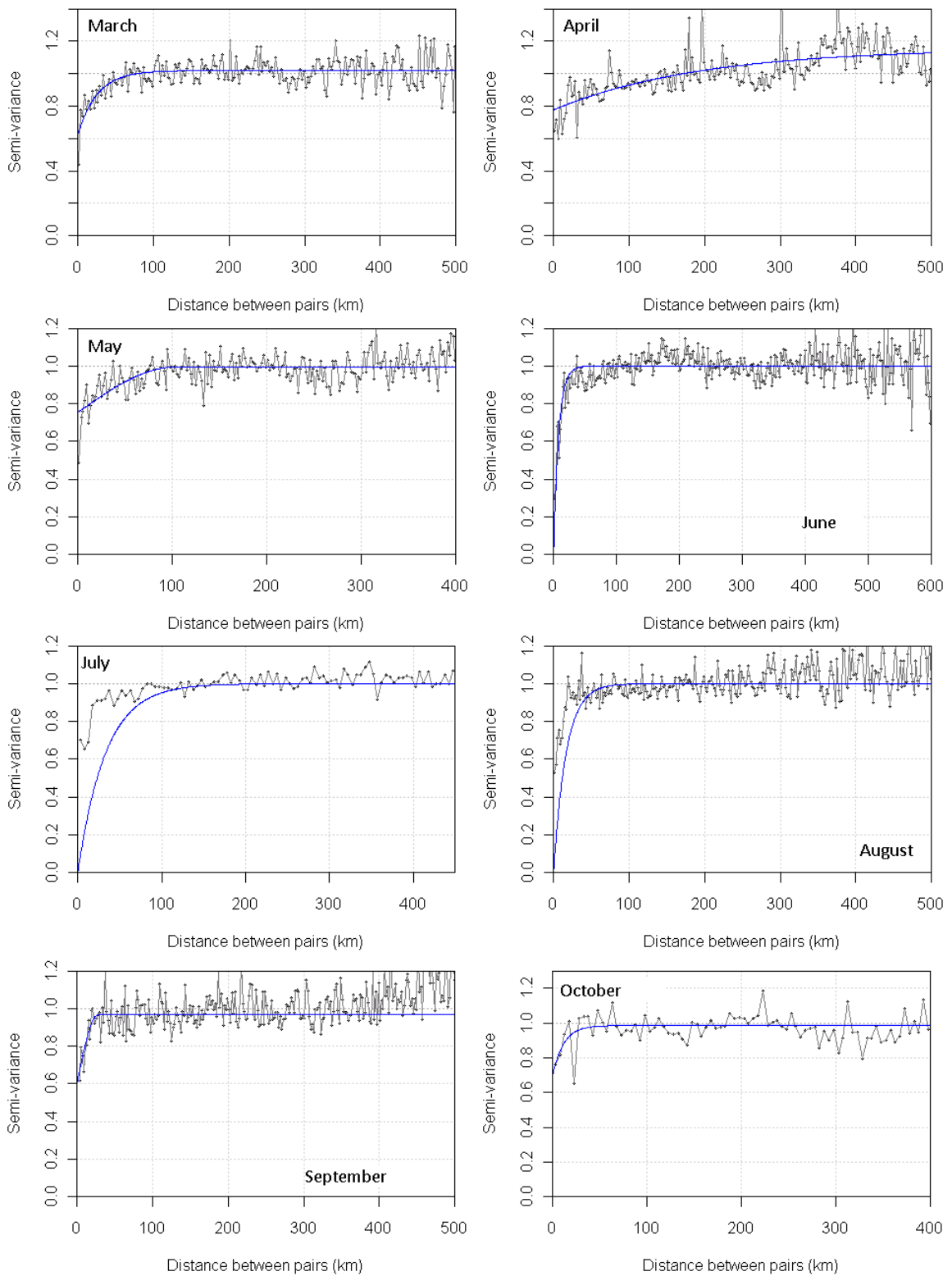
**Figure 6.2. Indicator residual variograms used in sequential simulation.**

The indicator and amount residual variograms are shown in Figure 6.2 and Figure 6.3. The variograms were generated using gauge data from the Oromiya dataset and show climatology of the region, especially in the indicator residual variograms. The range of these is shorter during the height of the rainy season (June, July and August) as the entire Oromiya region is covered by the ITCZ rains during these months and so the spatial correlation of rainfall in the region is dominated by the scale of convective cells (< 100km). During the other months, only part of the Oromiya region is inside the rainy area, therefore large scale gradients in rainfall occurrence can be observed in the data. As discussed in Section 5.1, the satellite rainfall estimates are being applied over a much larger region than the Oromiya calibration dataset. Variograms created using a dataset spread over the entire region might appear substantially different and would affect the sequential simulation results. However, as the study is limited by available rain-gauges, this observation cannot be verified or corrected.

---

## Chapter Six Sequential simulation

---



**Plot continued on the next page**

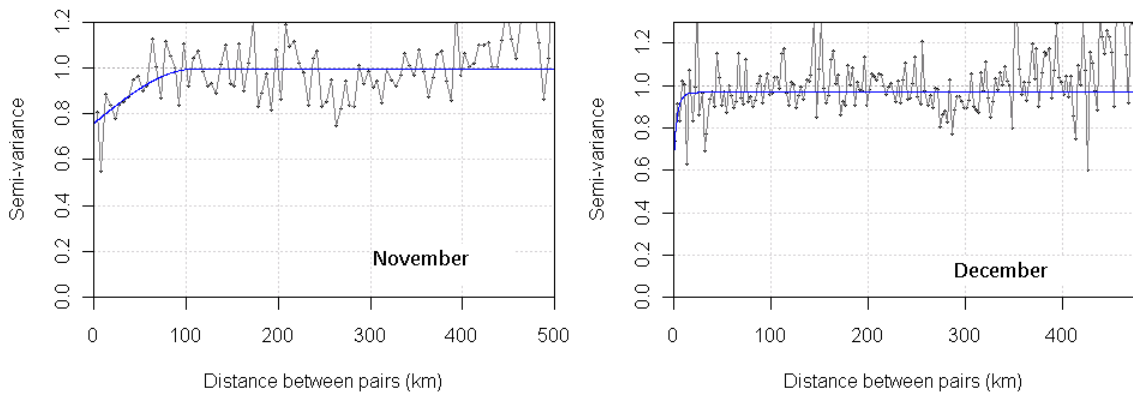


**Figure 6.3. Residual amount variograms used in sequential simulation.**

There are several features of the fits which can be discussed in Figure 6.2 and Figure 6.3.

- ◆ *The fit in June, July and August appears to be poor, with the modelled fit going through the origin, but the experimental variogram having a nugget of greater than 0.5.* This is because these months were modelled using the original incarnation of the sequential simulation code which only contained an exponential model with zero nugget. These were not re-run because it might be considered unrealistic that summer rainfall occurrence has such a high nugget, in particular that observed rainfall June has a nugget of 0.8. This is more likely caused by location or measurement error. As variograms with zero nugget have been used successfully in previous studies (Teo and Grimes, 2007), it was decided to keep a zero nugget in lieu of new information. For months outside June, July and August, the code has been updated to include an ‘nugget + exponential’ and ‘nugget + spherical’ model discussed in Section 3.4.1.1.
- ◆ *In some cases, the model fit of the variogram appears poor, especially in months such as March, April and May where both convective processes and large scale synoptic variations appear to have an impact on the range of the variogram.* This is due to the fact that the variogram model in the sequential simulation code still could not take into account any complex nested variogram structures. For example in March, there appears to be a mixture of ranges at approximately 30 km and 400km (Note, this agrees with the theory presented in this Chapter, that rainfall occurrence in March was affected by small scale convection and large-scale rainfall events). The sequential simulation code

was not developed further at this point as it seemed reasonable to assume that the strong spatial correlation of the daily Cold Cloud Duration field will make the variogram range choice less significant.

- ♦ *There is less month to month variation in the variograms of normalised residual amount in Figure 6.3 compared to the variation in the residual individual variogram presented in Figure 6.2.* This might be expected because rainfall amount is more dominated by micro-physical processes within a convective cell which are less likely to change over the course of the year. The variogram range for all months is less than 100km supporting this theory, thus one could envision that month-to month differences in the normalised amount variogram range are more likely to be from a lack of data or a poor variogram model fit. However, there could still be nested rainfall gradients across the region, especially in months such as April when only part of the country is covered by the Belg rains.

Section 10.6 presents the results of a modification of the sequential simulation process for a large scale weather generator which allows nested variograms. The results show a much better correlation than those presented here and in Chapter 7.

#### 6.4.4. NUMBER OF ENSEMBLE MEMBERS

As discussed at the beginning of Section 6.3, one of the requirements of sequential simulation is that at each pixel, ensemble statistics such the mean, variance and probability of rain should be conditioned on and matched to input statistics from observations. Therefore, it was important to determine the number of realisations needed in an ensemble for its statistics to be considered robust. In order to investigate this, a large ensemble of rainfall maps was created for one particular case study, the 1<sup>st</sup> July 2002.

For a given pixel in the map and for  $N$  ensemble members in total, a sub-set of  $n$  ensemble members was selected. For these ensemble members and that pixel, the proportion of rainy ensemble members, mean and variance of rainfall amount was calculated. The mean, variance and probability of rain from the input data was then subtracted from the ensemble statistics at that pixel to give the residual mean, variance and probability of rain. This process was then repeated for different values of  $n$ . The entire process was then repeated for each pixel.

For example for  $n=30$ , pixel  $j$  and mean rainfall amount :

- a) Randomly select thirty maps from the ensemble and select pixel  $j$  in each one.
- b) Calculate the mean rainfall amount from these thirty points.
- c) Subtract the prior mean rainfall amount at pixel  $j$ .
- d) Plot against the ensemble subset size,  $n$ .

Formally, for the mean rainfall amount statistic, plot  $n$  against  $H$  where:

$$H = \frac{\sum_{x=1}^n R_{jx}}{n} \quad 6.15$$

Here  $R_{jx}$  is the rainfall value (if raining) at pixel  $j$  and ensemble member  $x$ . The rainfall amount fields were used rather than the final rainfall ensembles, therefore all pixels were rainy. A similar equation can be written for the probability and variance of rainfall

amount. The order in which the ensemble members were chosen was random for each statistic, but remained fixed for any one pixel.

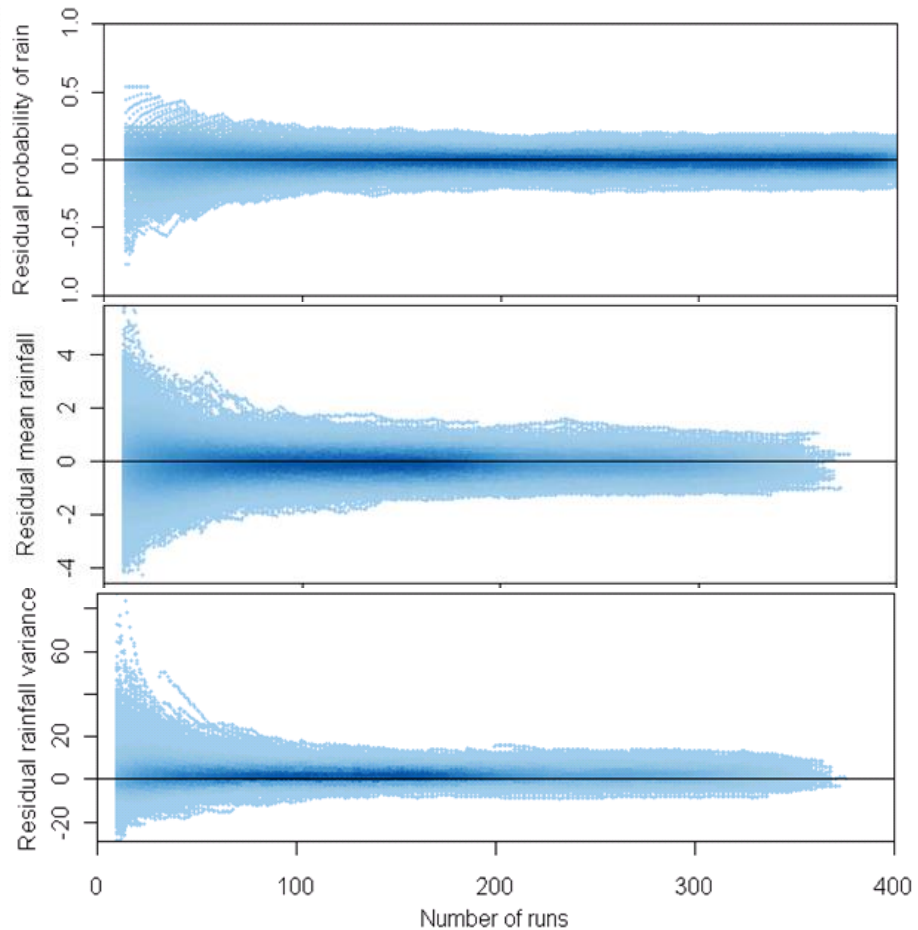


**Figure 6.4.** These plots compare the ensemble residual probability of rain, mean rainfall and rainfall variance for July 1<sup>st</sup> 2002 compared to ensemble size. Each individual blue line represents one pixel and the darker the blue, the denser the dataset. It is interesting to see that there are some pixels where the ensemble statistics never falls to zero, even though the majority of the pixels show the correct behaviour.

If the assumption is correct that statistics created from a large ensemble would perfectly equal the input statistics, one might expect the residual values to decrease to zero as  $n$  increases. The results of this study can be seen in Figure 6.4. This process was only carried out for one day due to the complexity of creating a large ensemble and because it confirms the results of past studies (Teo and Grimes, 2007; De Wit *et al.*, 2009). From this small sensitivity study, it was decided that an ensemble size of 200 is large enough to capture the input statistics but small enough to be computationally manageable.

## 6.5 SEQUENTIAL SIMULATION AND TAMSAT RAINFALL ESTIMATES

This part of the chapter is designed to illustrate sequential simulation more graphically than the previous Section and show how it has been used in conjunction with the TAMSAT calibration described in Chapter Four and Chapter Five. As the calibration changes for each month, for simplicity the Section considers a case study of the 1<sup>st</sup> July 2002.

### 6.5.1. STEP 1 – SEQUENTIAL INDICATOR SIMULATION

#### *Create an ensemble of Rain/No-Rain masks*

Firstly, as described in Chapter Four, thermal infra-red images recorded by Meteosat for the day are converted to CCD using the appropriate temperature threshold required by the calibration. The statistical relationship derived between CCD and the probability of rain (Equation 4.15) can then be used to convert the CCD into the prior probability of rainfall at each pixel,  $p_j^0$ . For each ensemble member, seed pixels are then chosen at random locations which are far enough apart to be spatially independent. This is defined as far enough apart that the distance between the seed pixels is beyond the range of the residual variogram. The probability of rain at the seeds is then input into a Bernoulli trial to decide whether it is raining or not for this ensemble member. A Bernoulli trial is one with a fixed probability and only 2 outcomes, for example tossing a coin is a Bernoulli trial with a probability of 0.5. These steps are illustrated in Figure 6.5. For the case study day, 9 pixels were chosen as seeds (their locations can be seen as white circles on Figure 6.5.).

The sequential simulation process is then used to fill the rest of the grid. As discussed in Section 6.3.2, the method relies on the concept that the probability of rain can be considered as the sum of a fixed underlying prior probability and spatially correlated random fluctuations. The physical meaning of these fluctuations or residuals is ‘how likely is it that that the pixel is raining after considering the prior probability of rain’. Thus the residual probability at the seed pixels,  $p_{r\_seed}$  is calculated by subtracting the prior probability from 1 if the pixel is rainy, or from 0 if it is dry:

$$p_{seed} = p_{0\_seed} + p_{r\_seed}$$

6.16

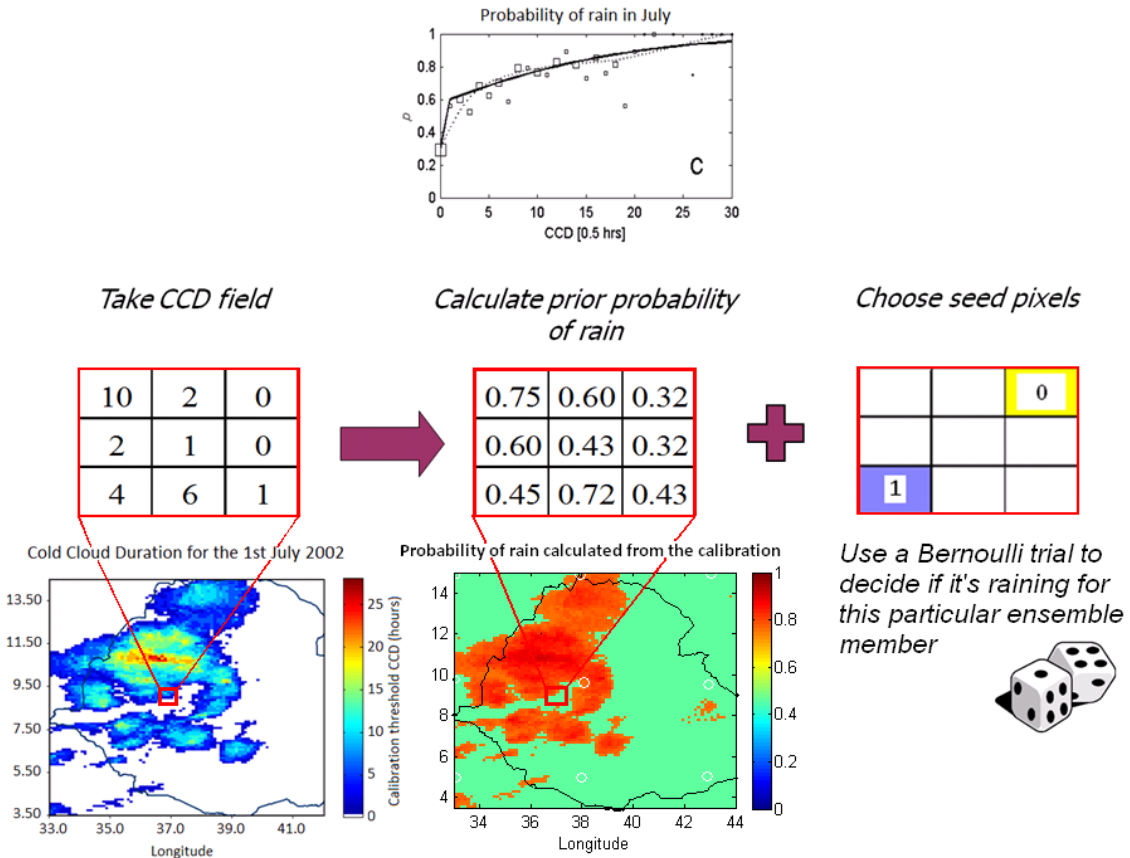


**Figure 6.5.** The first indicator sequential simulation steps for 1 ensemble member. The 3x3 grids represent a small subset of the main region and used as a schematic to explain the method. The seed pixels selected to make the actual ensemble members for the day are shown as white circles on the probability of rain plot.

First, the CCD at each pixel is determined and the prior probability of rain is calculated using the TAMSAT calibration derived in Chapter Four and Chapter Five. Seed pixels are then selected and a Bernoulli trial run for each seed to determine if they are raining or not. This trial uses the prior probability at each seed as its input. Here, rainy pixels are coloured blue whilst dry pixels are coloured yellow.

If this value is near one, it means that it was very unlikely that the seed pixel was chosen to be rainy (as there was a low probability of rain and a rainy pixel). If the value is near minus one, it suggests that it was very unlikely that the pixel was chosen to be dry (as there is a high probability of rain and a dry pixel). If the residual probability is near zero, it means that the result was likely.

A new target pixel is randomly chosen, pixel  $t$ . Simple kriging is then used to calculate this residual probability at the target pixel, thus taking into account the observed spatial correlation of rainfall. In order to calculate the final probability of rain at the pixel, this

value is then added to the prior probability of rain at that location. Finally, another Bernoulli trial is conducted to decide if this pixel is raining or not and pixel  $t$  added to the collection of seeds. A new target pixel is then selected and the process repeated until the grid has been filled. These steps are shown in Figure 6.6.

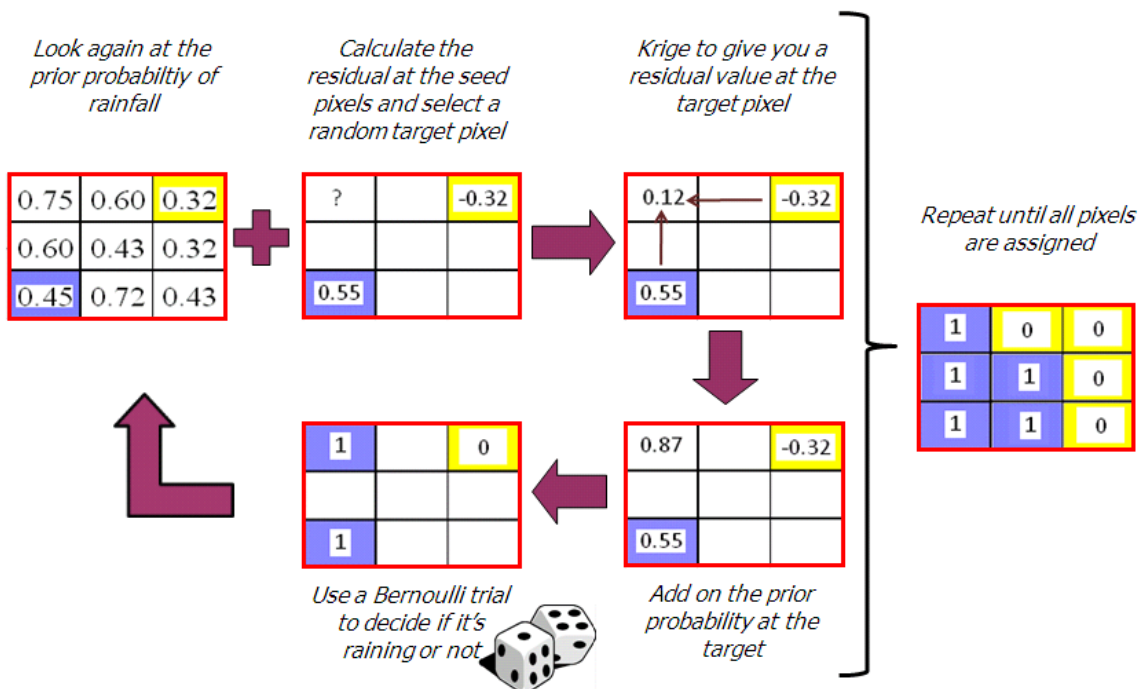


Figure 6.6. Part 2 of the schematic of indicator sequential simulation for one ensemble member. The 3x3 grids represent a subset of the overall region and blue pixels have been selected as rainy, whilst yellow pixels have been selected as dry. The residual probability of rain is first calculated for the seed pixels. In this case, the lower left pixel is raining, thus the residual probability is  $1 - 0.45 = 0.55$ . The top right pixel is dry, so the residual probability is  $0 - 0.32 = -0.32$ . Simple kriging is then used to calculate the residual probability at the target pixel, the full probability of rain calculated and a Bernoulli trial conducted to decide if the pixel is raining or not. The process is then repeated until the grid has been filled.

The process is then repeated for other ensemble members, creating an ensemble of spatially correlated rain/no rain masks. As the residual probabilities are symmetrically distributed about the prior probability, the mean of the ensemble members should equal the prior probability. This is shown in Figure 6.7 for the 1<sup>st</sup> July 2002 case study. It is reasonable to assume that the slight inconsistencies between the bottom two sub-plots are because the ensemble size is too small to give a perfect representation of the input parameters. Although the ensembles look internally consistent in that the ensemble mean equals the input probability of rain, there appears to be too many rainy pixels in areas which are observed to be dry (e.g. to the right of the red box). This is discussed further in

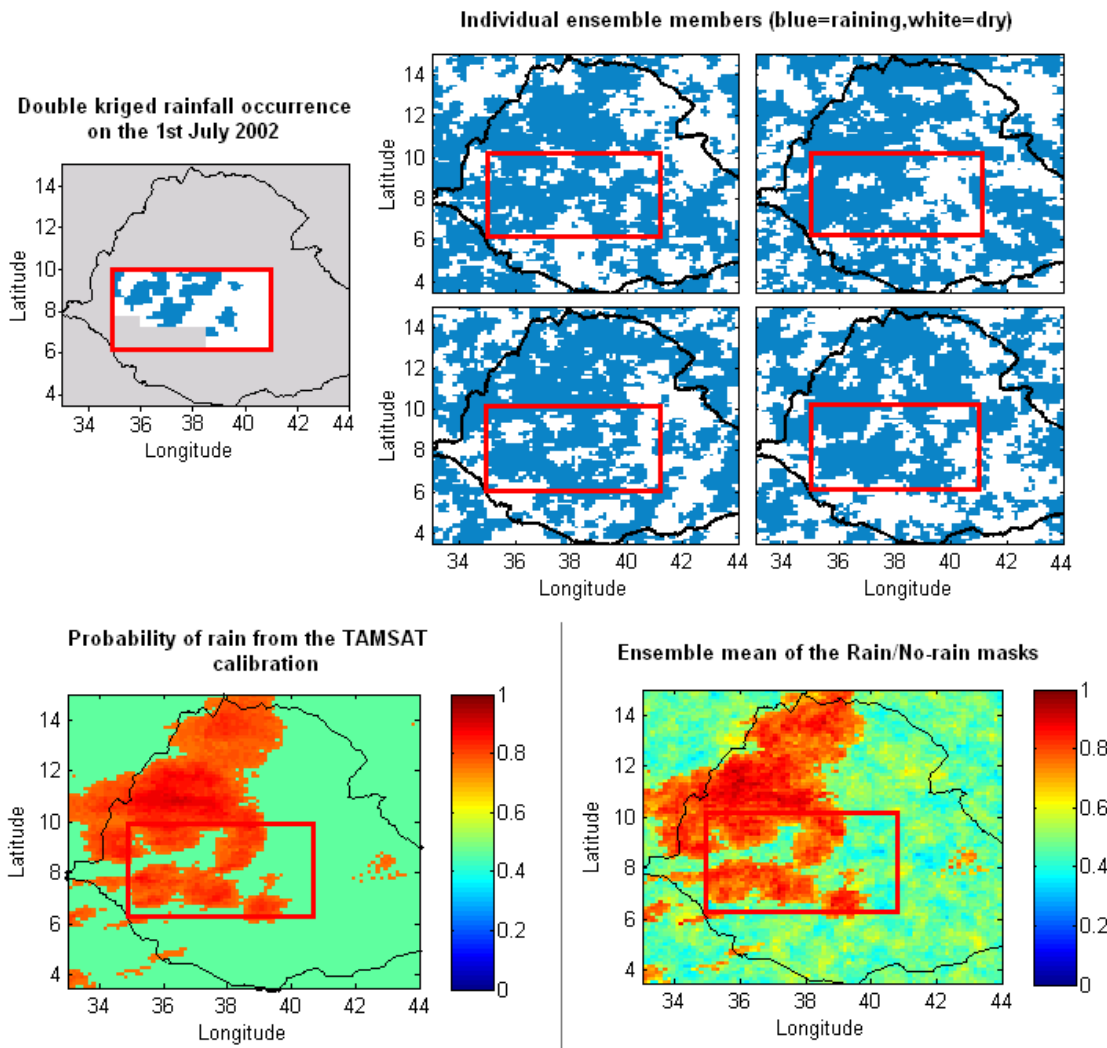


Figure 6.7. The top left sub-plot shows the kriged rainfall occurrence for the 1<sup>st</sup> July 2002, where blue denotes a raining pixel and white denotes a dry one. The grey areas show areas with no gauge data and in all plots, the red box denotes the region containing gauge data. The top right plot shows 4 individual ensemble members. These illustrate 4 simulations of potential rainfall occurrence on the 1<sup>st</sup> July 2002. The two plots of probability of rain in the centre show that the process is internally consistent, in that the ensemble mean (right) resembles the input prior probability of rain (left).

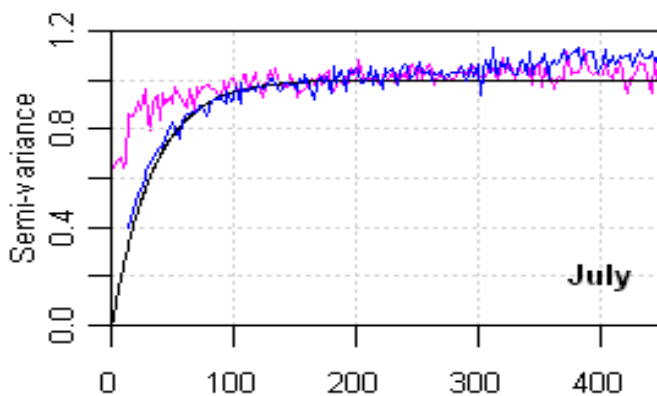


Figure 6.8. Validation of the indicator experimental variogram from the ensemble (blue). This shows a good fit to the input variogram (black), although there are some differences with observed values (pink) as discussed in Section 6.4.3. The x axis corresponds to the distance between any two data points.

Section 7.5. Finally, a variogram created from the ensemble is depicted in

Figure 6.8. This shows a good fit to the input variogram (black), although there are some differences with observed values (pink) as discussed in Section 6.4.3

### **6.5.2. STEP 2 - GAUSSIAN SEQUENTIAL SIMULATION**

#### *Selecting rainfall amounts*

Using a similar process to the one described in Section 6.5.1, rainfall amounts now need to be selected for the rainy pixels in each ensemble member. In this case, rather than using a prior probability of rain as the input statistic, the rainfall amount can be represented as a gamma distribution with its mean  $\mu$  and variance  $\sigma^2$  generated from the CCD/Rainfall relationship described in Equation 4.5 and Equation 4.11. For each ensemble member, seed pixels are again chosen at random (rainy) locations which are far enough apart to be spatially independent. The rainfall amount at these seeds is then selected from the gamma distribution at that point. These steps are illustrated in Figure 6.9:

Similar to indicator sequential simulation, Gaussian sequential simulation is dependent on the concept that a field can be treated as a combination of a fixed and random component. In this case, the fixed component is the mean rainfall as calculated from the TAMSAT calibration, whilst the random components are spatially correlated residuals selected from the gamma distribution of rainfall at that point. As discussed in the Section above, the mean of the ensembles should equal the input mean from the gamma distribution, therefore it is important that for any distribution selected, the residuals are symmetric about the mean. As the gamma distribution is usually skewed, the data must first be transformed to a Gaussian distribution before residuals are selected. The method for doing this is now outlined below:

- 1) Take the residual rainfall amount from the seed pixels:

$$res_{seed} = R_{seed} - \mu_{seed}$$

6.17

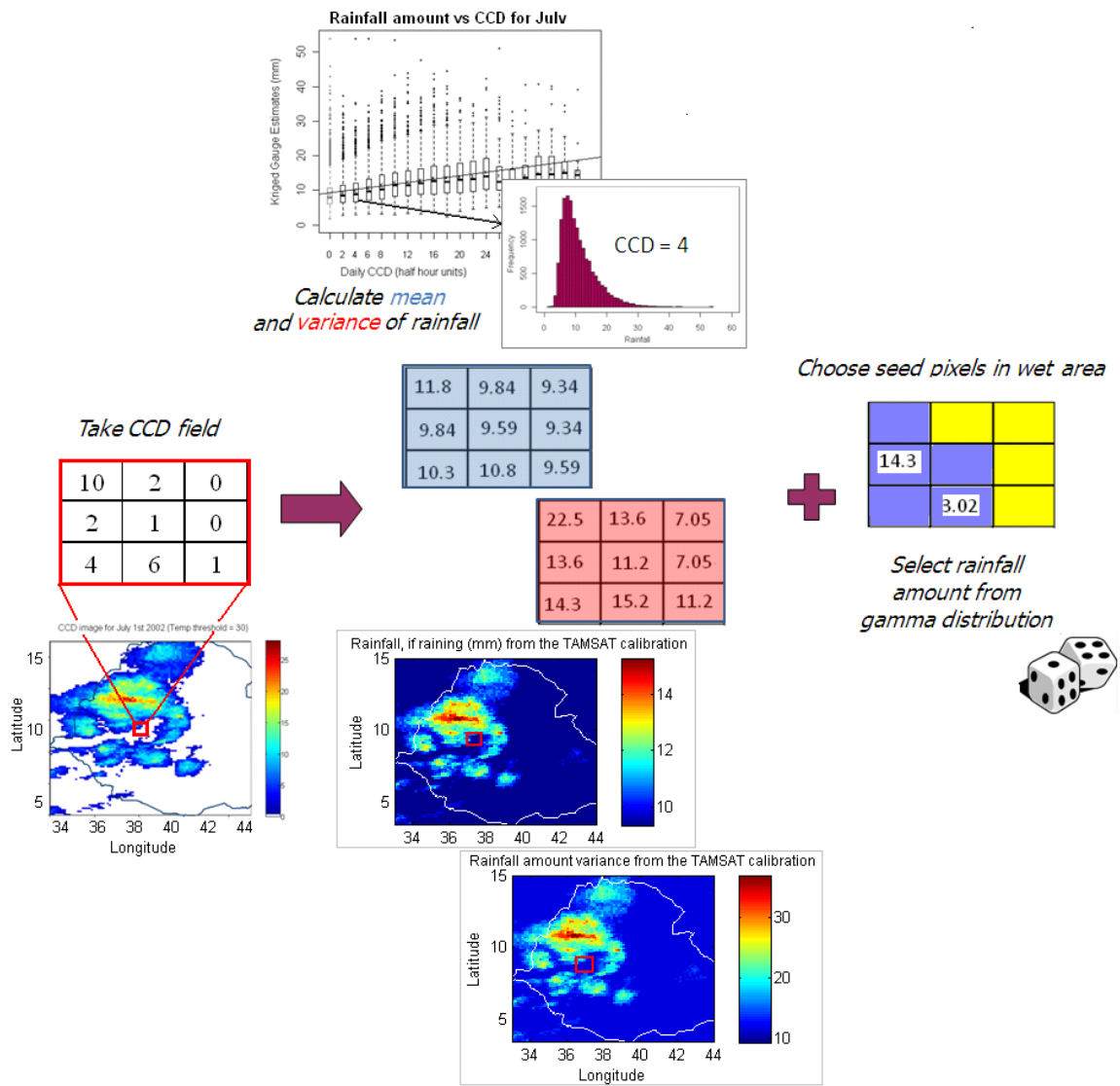


**Figure 6.9.** Schematic showing how the rainfall amount fields are set up for Gaussian sequential simulation. The 3x3 grids represent a subset of the overall region. Rainy (blue) and dry (yellow) areas have already been selected for this ensemble member using sequential indicator simulation.

First, the CCD and calibration parameters were used to create maps of the mean and variance of rainfall (if raining). Seed pixels are then chosen and rainfall amounts selected out of a gamma distribution with mean and variance determined by the calibration maps.

- 2) As these residuals have come from a gamma distribution and will be skewed, use a normal scores transformation to create normalised residuals. A normal scores transformation involves ranking and sorting the original residuals into a cumulative distribution, finding an equivalent rank from a Gaussian distribution, then using the Gaussian values associated with those ranks as the transformed residuals. The process can be seen in Figure 6.10.

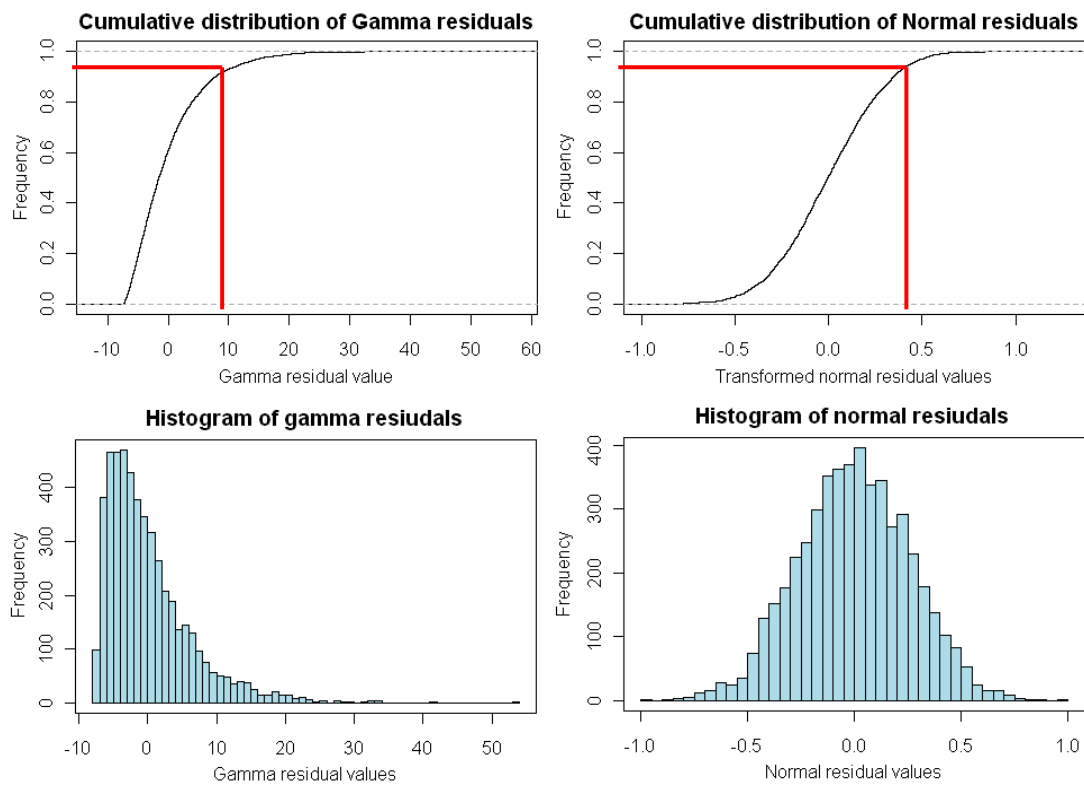


**Figure 6.10.** An example of the normal scores transformation process. The left hand plots show the cumulative distribution and histogram of a selection of gamma residuals, similar to those found at the seed pixels. The cumulative distribution function is then used to transform the residuals to a Gaussian distribution. For example, the red lines show that a Gamma residual of 9mm is ranked 0.9 in its cumulative distribution functions, leading to a transformed value of 0.4.

- 3) Randomly select a target seed pixel, pixel  $t$ .
- 4) Use simple kriging to find quantitative influence of the seed pixels on the rainfall distribution at the target. This is expressed as the mean and variance of the residual normal distribution at that point.
- 5) Randomly select a value from this distribution.
- 6) Repeat steps 3 to 6 until the entire grid has been filled.
- 7) Use the mean and variance from the calibration to back-transform the residuals to the gamma distribution and re-add the mean to give rainfall values.

All of these steps are shown graphically in Figure 6.11. The process is then repeated for other ensemble members, creating the final ensemble of spatially correlated rainfall fields. As the residuals were forced to be distributed symmetrically about the mean rainfall amount, the mean of the ensemble members (excluding zeros) should equal the mean of the rainfall amount distribution. This is shown in for the 1<sup>st</sup> July 2002 case study in Figure 6.12. Figure 6.13 shows a comparison between a rainfall amount residual variogram derived from the ensemble with the variogram input into the model. As for the indicator variogram, this shows a reasonable fit.

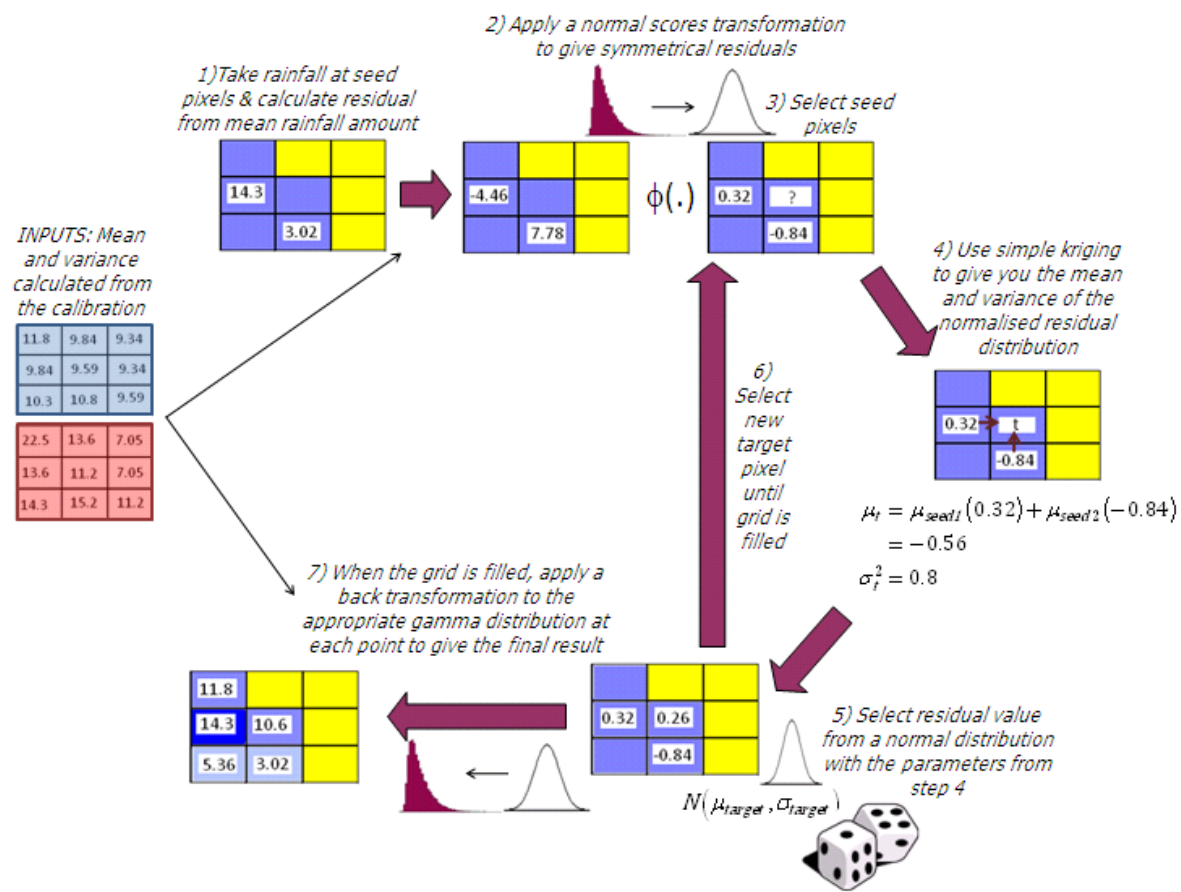
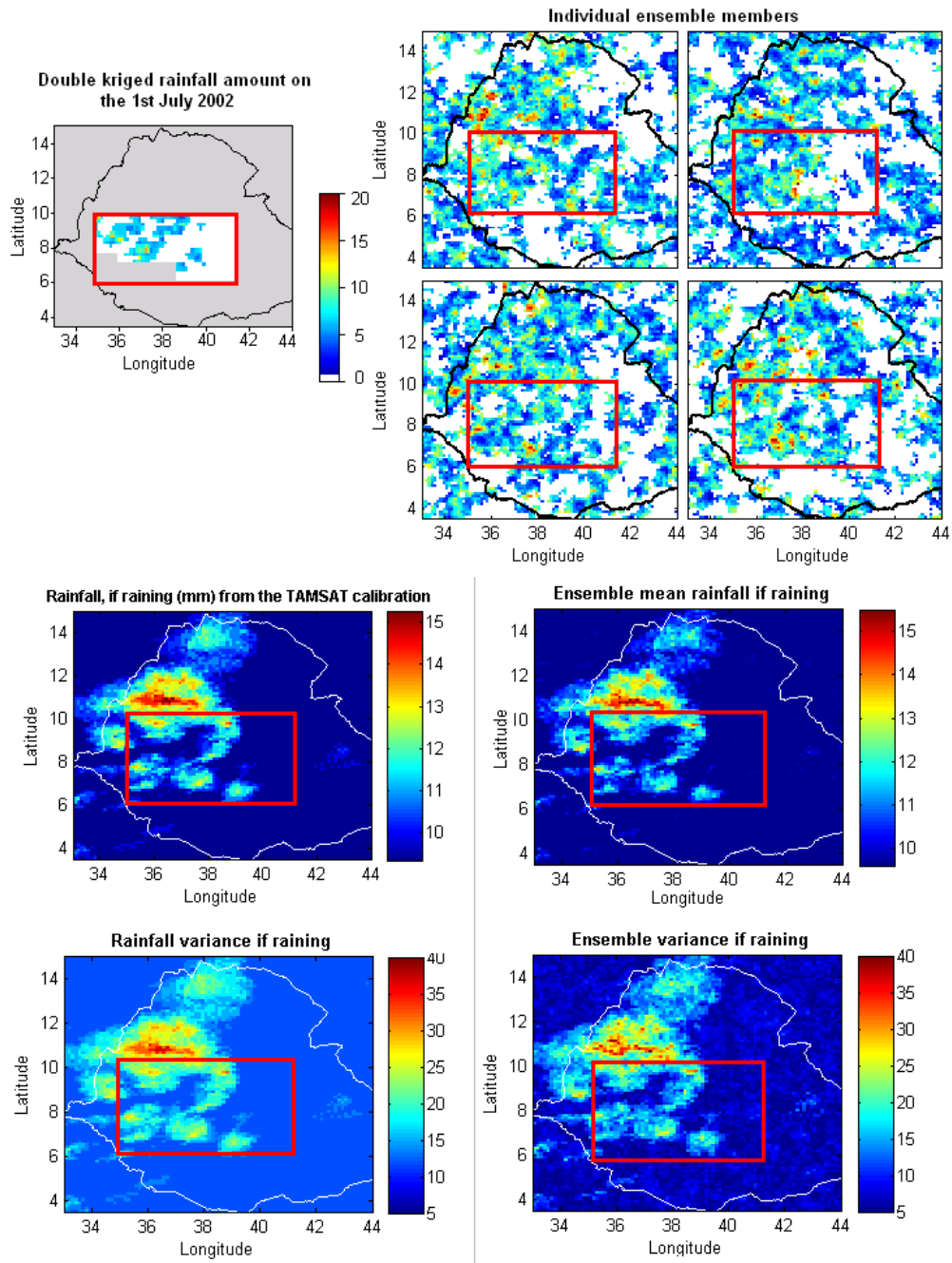


Figure 6.11. Part 2 of the schematic showing Gaussian sequential simulation. The 3x3 grids represent a subset of the overall region. Rainy (blue) and dry (yellow) areas have already been selected for this ensemble member using sequential indicator simulation and the rainfall amounts at seed pixels were selected in Figure 6.9. First, the rainfall residuals are calculated. These are transformed to a normal distribution so that residuals can be evenly selected. A target pixel,  $t$ , is chosen and simple kriging used to find what a the mean and variance of a normal distribution at that point might be. A random residual value is then chosen from this distribution. A new target pixel is then chosen and the process repeated until the grid comprises of a spatially correlated normal field. Finally, the prior mean and variance at each pixel is used to back transform the values to rainfall amounts.



**Figure 6.12.** The top left sub-plot shows the final kriged rainfall field for the 1<sup>st</sup> July 2002. The grey areas show areas with no gauge data and in all sub-plots, the red box denotes the region containing the calibration gauges.

The top right plot shows 4 individual ensemble members. These illustrate 4 simulations of potential rainfall on the 1<sup>st</sup> July 2002. These appear to present a realistic simulation of the pattern of rain.

The two plots at the bottom show that the process is internally consistent, in that the ensemble mean excluding zero rainfall (right) and variance resembles the input mean and variance (left). The slight inconsistencies are because ensemble size is too small to give a perfect representation of the input parameters.

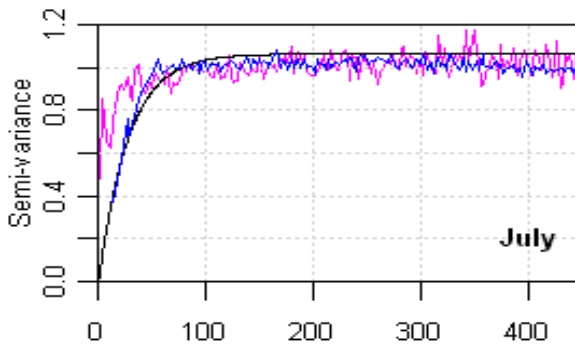


**Figure 6.13. Validation of the normalised rainfall amount experimental variogram from the ensemble (blue). This shows a good fit to the input variogram (black), although there are some differences with observed values (pink) as discussed in Section 6.4.3**

## 6.6 CONCLUSION TO CHAPTER SIX

The daily TAMSAT calibration presented in Chapter Four and Chapter Five was designed to best stochastically capture the uncertainty associated with daily rainfall in Ethiopia. As this calibration was point specific, this chapter discussed how to incorporate spatial correlation into the method. To do this, the work focused on the geostatistical method of sequential simulation which enabled the creation of ensembles of spatially correlated maps of rainfall with the following characteristics:

- 1) The field had a realistic spatial correlation derived from observations.
- 2) Rainfall statistics at any pixel within the field (e.g. mean rainfall or the probability of rain) agreed with observed rainfall statistics at that location and the simulation method took into account the non-Gaussian nature of rainfall.
- 3) Each ensemble member was an equally probable and realistic estimate of rainfall over the region.

The aim of this chapter was to conceptually explain the detailed methodology behind sequential simulation. Chapter Seven then uses this method to create and validate rainfall ensembles for the Ethiopian case study. One of the initial results discussed in this Chapter was that the ensembles appeared to over predict low rainfall amounts. This issue is discussed in detail in Section 7.5.

# **CHAPTER SEVEN**

# **VALIDATION OF THE TAMSAT**

## **DAILY SATELLITE RAINFALL**

## **ENSEMBLES**

### **7.1 OVERVIEW**

As discussed in previous chapters, the TAMSAT stochastic daily rainfall ensembles described in Chapter Four, Chapter Five and Chapter Six (hereafter referred to as TAMSAT ensembles) were calibrated on a daily rain-gauge dataset of approximately 250 stations in Oromiya for the years 2002-2006. To validate these estimates, a set of TAMSAT ensembles was created from 1994-1999 in order to match a smaller daily rain-gauge dataset of 20 stations, which covers a larger proportion of Ethiopia. The station locations can be seen in Figure 6.1 and more details about the dataset can be found in Section 3.2.1.2. Although the number of gauges is relatively small in the dataset, the reason for using it for validation was to test the performance of the ensemble in pixels outside the calibration region and time period.

This chapter considers a comparison and validation of the TAMSAT ensemble against observations and other satellite rainfall estimates. It first considers a validation of the ensemble mean, then examines the properties of the ensemble and finally describes a validation of the full ensemble dataset.

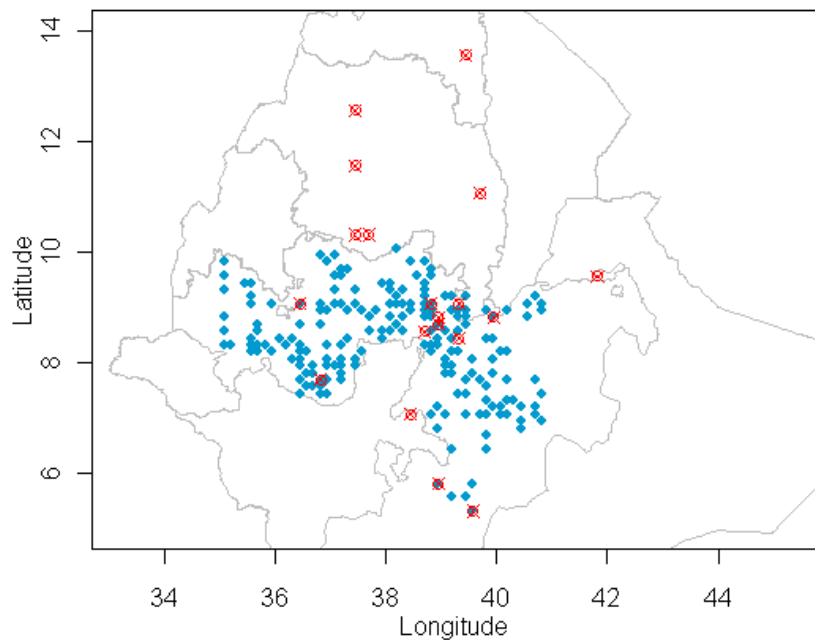


**Figure 7.1. RED:** Location of the rain-gauges in the validation dataset. These have a daily resolution from 1994-1999. **BLUE:** Location of the rain-gauges in the calibration dataset. These stations have a daily resolution from 2002-2004.

## 7.2 VALIDATION OF THE ENSEMBLE MEAN

As discussed in Chapter Four and Chapter Six, the mean of the TAMSAT ensembles corresponds to the ‘best guess’ of the method i.e. to the rainfall amount described in Equation 4.13. This is effectively the deterministic estimate of rainfall from the method, therefore it is interesting to compare it to observations and other satellite estimates. This is especially the case because as discussed in Chapter Four, two additional studies have described a validation of daily satellite rainfall estimates over the Ethiopian Highlands:

- Chadwick (2010) applied the standard dekadal TAMSAT calibration (described in Section 4.3.1) to make daily rainfall estimates using the same Oromiya dataset used for the ensembles.
- Dinku *et al.* (2008) compared RFE2, TRMM 3B42, CMORPH and PERSIANN against a kriged dataset of 187 gauges at a resolution of  $0.25^\circ$ .

The validation described in this Section aims to use similar statistics to these papers so that the ensemble mean can be compared against the other deterministic products. A TAMSAT ensemble was created at a resolution of  $0.125^\circ$  for the years 1994-1999 and its daily mean compared to the validation gauge data-set (which was also kriged to a resolution of  $0.125^\circ$ ). For each day in the validation dataset, 200 realisations of rainfall maps were created using sequential indicator simulation and sequential Gaussian simulation. As discussed in Section 6.4, it is expected that an ensemble size of 200 is large enough for any associated statistics to converge, thus it is assumed that the ensemble mean is a true representation of the rainfall amount described in Equation 4.13. It should be noted that in general, a higher degree of averaging will result in a better skill score, thus the finer spatial resolution of the ensembles must be taken into account when comparing the statistics to those from Dinku *et al.* (2008).

A comparison between the ensemble mean and kriged gauge rainfall was first completed at a daily  $0.125^\circ$  scale. This is shown in Figure 7.2 and the parameters of the fit for each case recorded in Table 7.1. For ease of comparison, the statistics used for evaluation match those described in Dinku *et al.* (2008) and Chadwick (2010). These comprise of the correlation coefficient ( $R^2$ ), root mean squared error (RMSE), relative root mean squared error (RMS) and the multiplicative bias (BIAS2). All of these statistics are described in full in Appendix Two.

Although each month exhibits a relatively poor fit on a daily basis, the estimates have a low bias and compare comparably or better than the results found in the external validation studies. This is especially good because as mentioned above, the estimates are being compared at a resolution of  $0.125^\circ$  rather than the  $0.25^\circ$  resolution used in Dinku *et al.* (2008). It is difficult to directly compare the results presented here with those described in Chadwick (2010) as those were validated at Meteosat pixel scale ( $\sim 4\text{km}$ ).

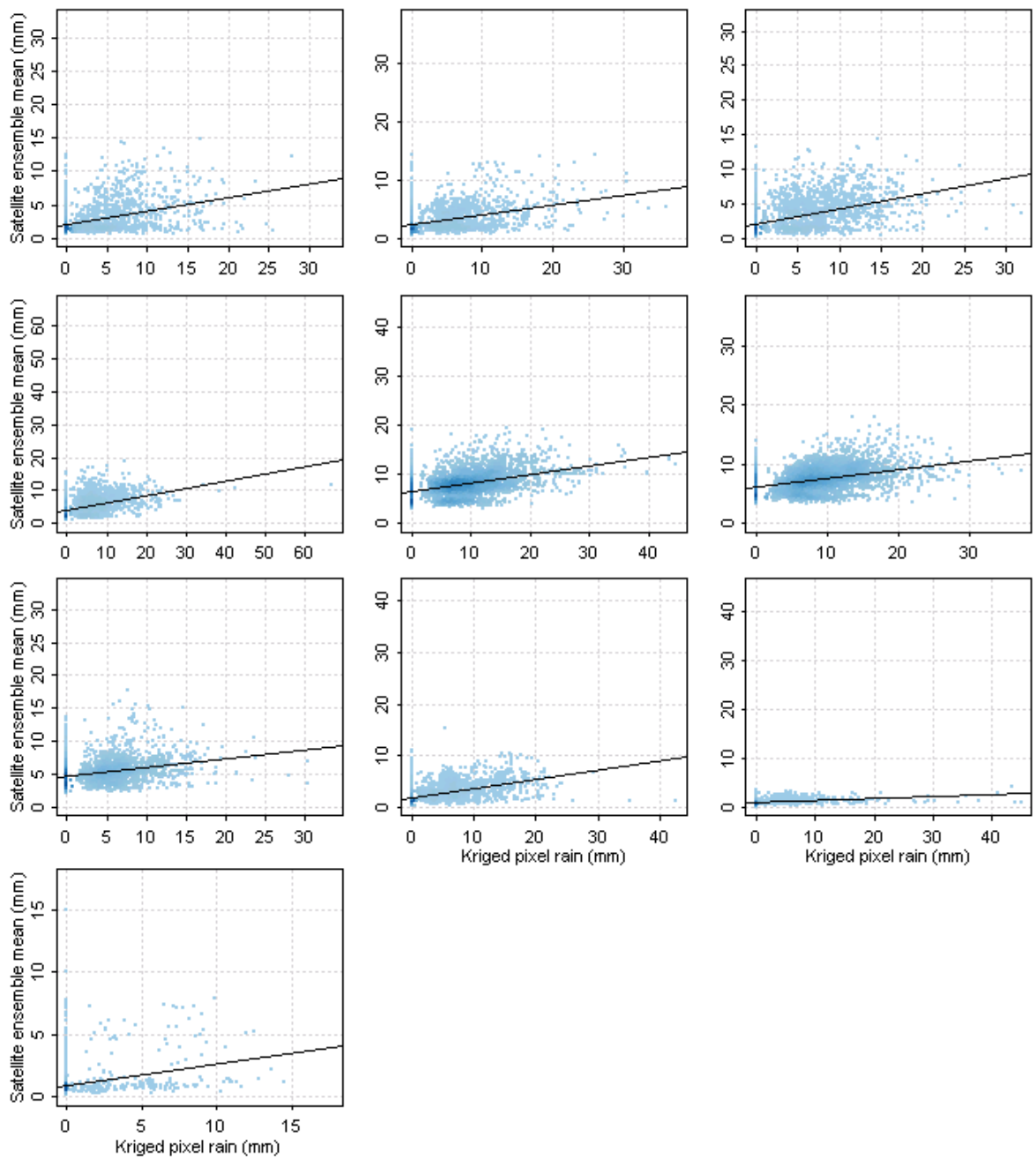


**Figure 7.2** Scatter plots of daily kriged rainfall amount at a given pixel vs the satellite ensemble mean at that pixel. As expected a validation at a daily pixel scale gives relatively poor results. A darker blue colour represents a higher density of points.

Month	Intercept (s.e.)	Gradient (s.e.)	p-value	Adj. $R^2$	RMSE	RMS	Bias2
<i>Range of the statistic</i>	-	-	-	0 - 1	0 - $\infty$	0 - $\infty$	$-\infty - \infty$
'Perfect value'	-	-	-	1	0	0	1
<i>March</i>	2.06 (0.03)	0.20 (0.01)	< 0.001	0.17	2.00	1.48	1.23
<i>April</i>	2.37 (0.03)	0.16 (0.01)	< 0.001	0.16	2.13	1.58	1.07
<i>May</i>	2.13 (0.04)	0.22 (0.01)	< 0.001	0.23	1.98	1.61	0.93
<i>June</i>	4.19 (0.06)	0.22 (0.01)	< 0.001	0.18	2.56	1.08	1.37
<i>July</i>	<b>6.56 (0.06)</b>	<b>0.17 (0.01)</b>	<b>&lt; 0.001</b>	<b>0.19</b>	<b>2.72</b>	<b>0.74</b>	<b>0.98</b>
<i>August</i>	<b>6.21 (0.05)</b>	<b>0.15 (0.01)</b>	<b>&lt; 0.001</b>	<b>0.17</b>	<b>2.33</b>	<b>0.76</b>	<b>0.96</b>
<i>Sept</i>	<b>4.75 (0.05)</b>	<b>0.13 (0.01)</b>	<b>&lt; 0.001</b>	<b>0.09</b>	<b>2.39</b>	<b>0.85</b>	<b>1.39</b>
<i>October</i>	1.85 (0.03)	0.18 (0.01)	< 0.001	0.27	2.00	1.96	0.84
<i>November</i>	0.85 (0.01)	0.04 (< 0.01)	< 0.001	0.09	0.50	3.86	0.92
<i>December</i>	0.86 (0.01)	0.16 (0.01)	< 0.001	0.10	0.90	1.79	3.03
<i>Range from satellite products discussed in Dinku et al. (for July-Sept)</i>		-	<b>0.1-0.2</b>	-	<b>1.5-2.6</b>	<b>0.7-1.6</b>	

**Table 7.1.** Statistics of the linear fits shown in Figure 7.2. These have also been compared with the same statistics taken from a range of products in Dinku *et al.*, 2008. The statistics in the Dinku validation were for July-September, thus these months have been highlighted in the table. The TAMSAT ensemble mean shows a low bias in comparison to the other estimates.

In Figure 7.2, the ensemble mean has a worse fit in the two dry months, November and December. This might be due to less calibration data being available (as there were fewer rain days), but this result is less important than earlier months when considering that the end use of the product is for crop simulation modelling and that November and December fall at the end of the growing season when maize is less sensitive to rainfall.

No dichotomous statistics were included in the validation because by its nature, an ensemble mean of 200 rainfall pixels will almost always be rainy (as discussed in Section 4.3.3). Consequently the ensemble mean by itself can never be considered as a deterministic estimate of daily rainfall if one is interested in rainfall occurrence. However, its promise and comparative skill in predicting rainfall amount suggests that it may be

worth future studies modifying the approach described in Equation 4.13 to create such a product. The lack of systematic bias in the product can be clearly seen in Figure 7.3, where as the amount of averaging increases, the linear relationship between the ensemble mean and kriged gauge improves. This supports the result found by Coppola *et al.*, 2006 in a similar study and is encouraging because the output in this case is large scale crop simulation modelling, thus the results will be averaged, albeit non-linearly within the crop model. It should be noted that averaging over widely spaced pixels tends to mean that high rainfall amounts are excluded from the analysis (as they are relatively rare), hence it is probable that Figure 7.3 does not validate the ensemble for high rainfall amounts.

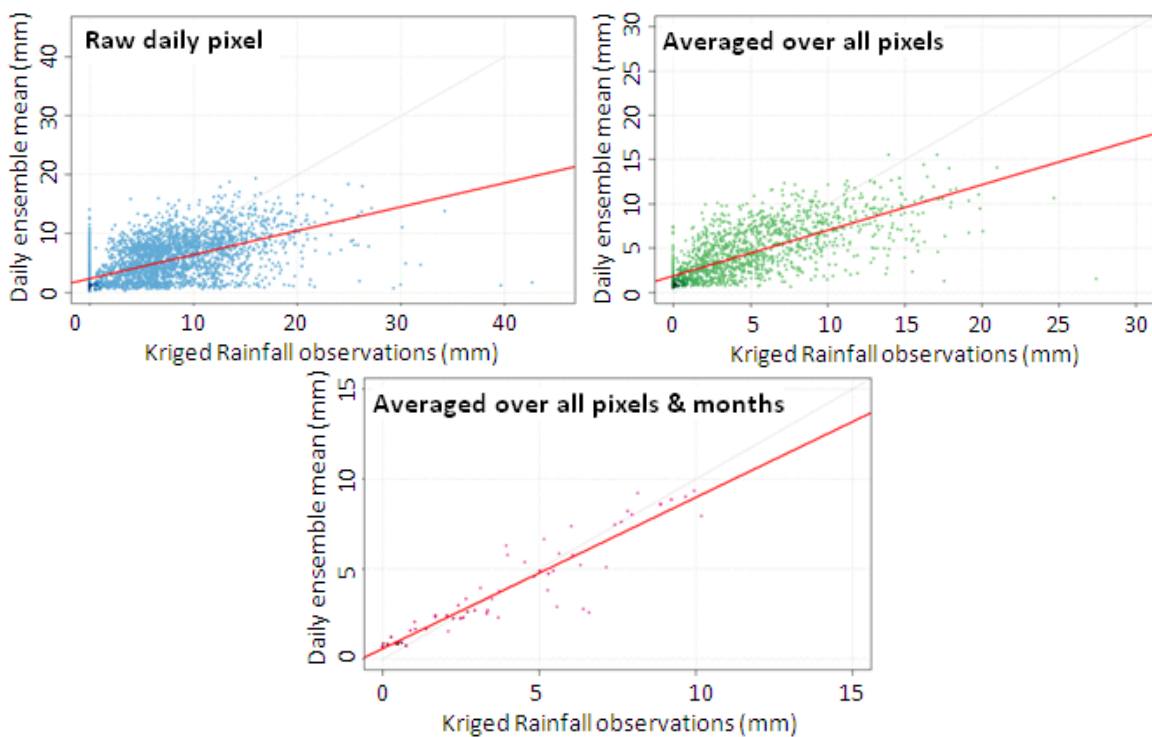


**Figure 7.3.** Scatter plot of kriged rainfall amount vs ensemble mean for all months. Plot A (top left) includes one point for each day and  $0.125^\circ$  pixel and as expected, is similar to the linear fits in Figure 7.2. Each point in Plot B includes the mean of all locations for each day. Each point in Plot C (bottom) represents the mean of all locations for each month & year i.e. there are 72 points, one for each month and year.

### 7.3 VERIFYING ENSEMBLE PARAMETERS

Before any validation study, it is first sensible to explore if the TAMSAT ensemble is faithfully reproducing input statistics from the calibration dataset. It should be noted that the ensemble generation method should constrain the ensembles into reproducing these statistics. Consequently this Section aims to show that the TAMSAT ensemble has been made correctly and is internally consistent. This process was first started in Figure 6.7 and Figure 6.9 which showed that on a given day, ensemble members appear to be realistic and that the probability of rain and rainfall distribution statistics are preserved in the daily ensemble mean.

In order to inspect the spatial correlation of the ensemble, indicator and normalised amount residual variograms have been computed from the ensembles for the same pixels and dates found in the Oromiya calibration dataset. These have then been plotted (in blue) against the variogram models used in the ensemble generation process (black solid line) and the observed residual variograms (pink). The indicator residual variograms can be seen in Figure 7.4 and the normalised amount residual variograms in Figure 7.5.

It is apparent that in most cases the residual indicator variograms calculated from the ensembles agree well with their input models, even in June, July and August where the model itself does not fit the observations well (this is discussed in Section 6.4.3). The agreement is worst in October, which is the only month to have a modelled range of less than 50 km. This effect can also be seen in the normalised residual variograms in Figure 7.5, which tend to have smaller modelled ranges and where the agreement between model and ensemble is comparatively worse than in their indicator counterparts. In particular, the ensemble seems to overestimate the range of the normalised amount variogram during the climatologically complex Belg rainy season of March, April and May. It is interesting to note that at long ranges, the ensemble variograms seem to agree with the observed variograms better than with the model. This might be due to the spatial correlation of the CCD field which was input each day.

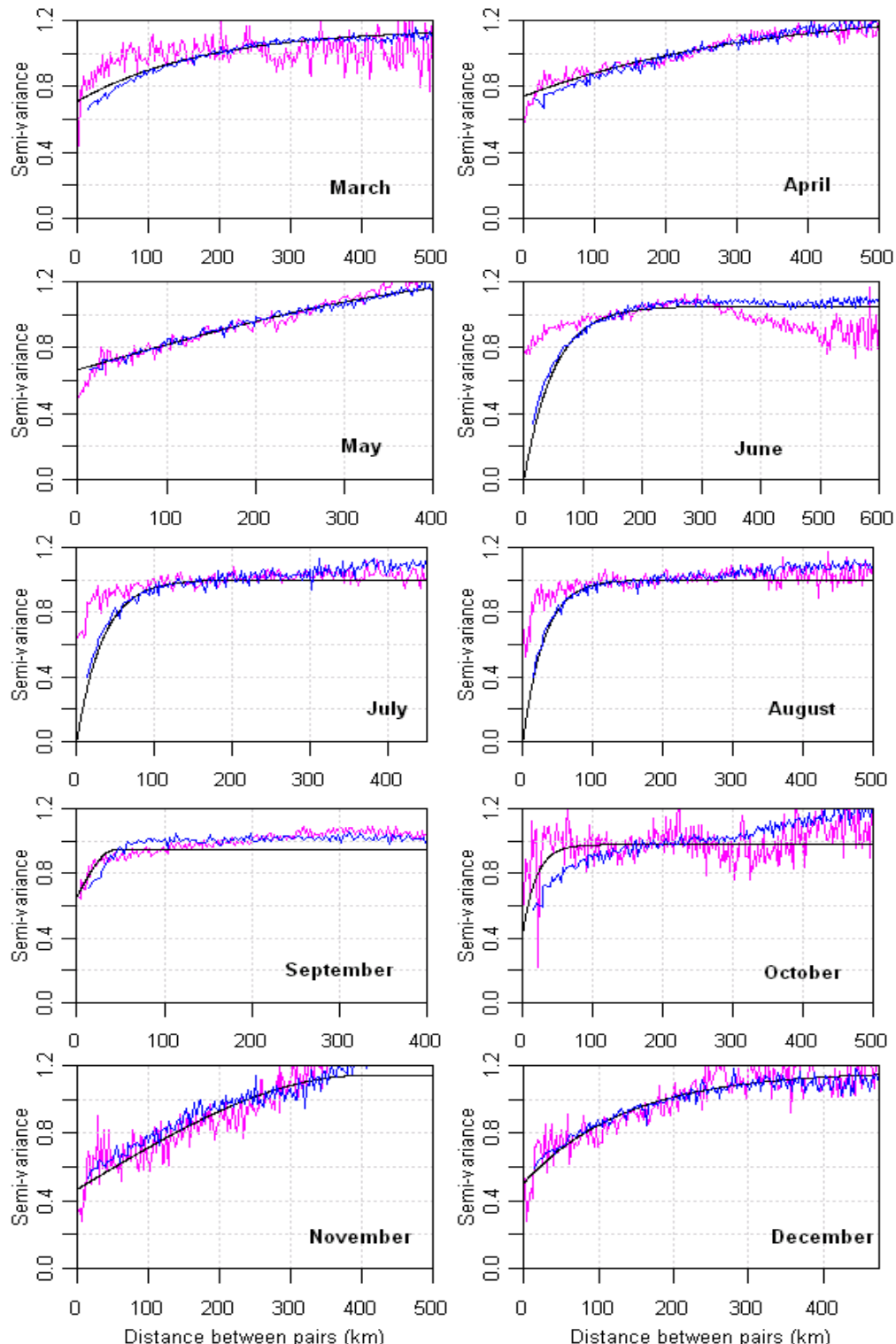


**Figure 7.4.** Residual Indicator variograms for each month. The pink line shows the residual variogram calculate from observations, the black solid line is the model input into the sequential simulation process and the blue line is the residual variogram calculated from ensemble members. These are sampled at the same pixels and dates as the observations.

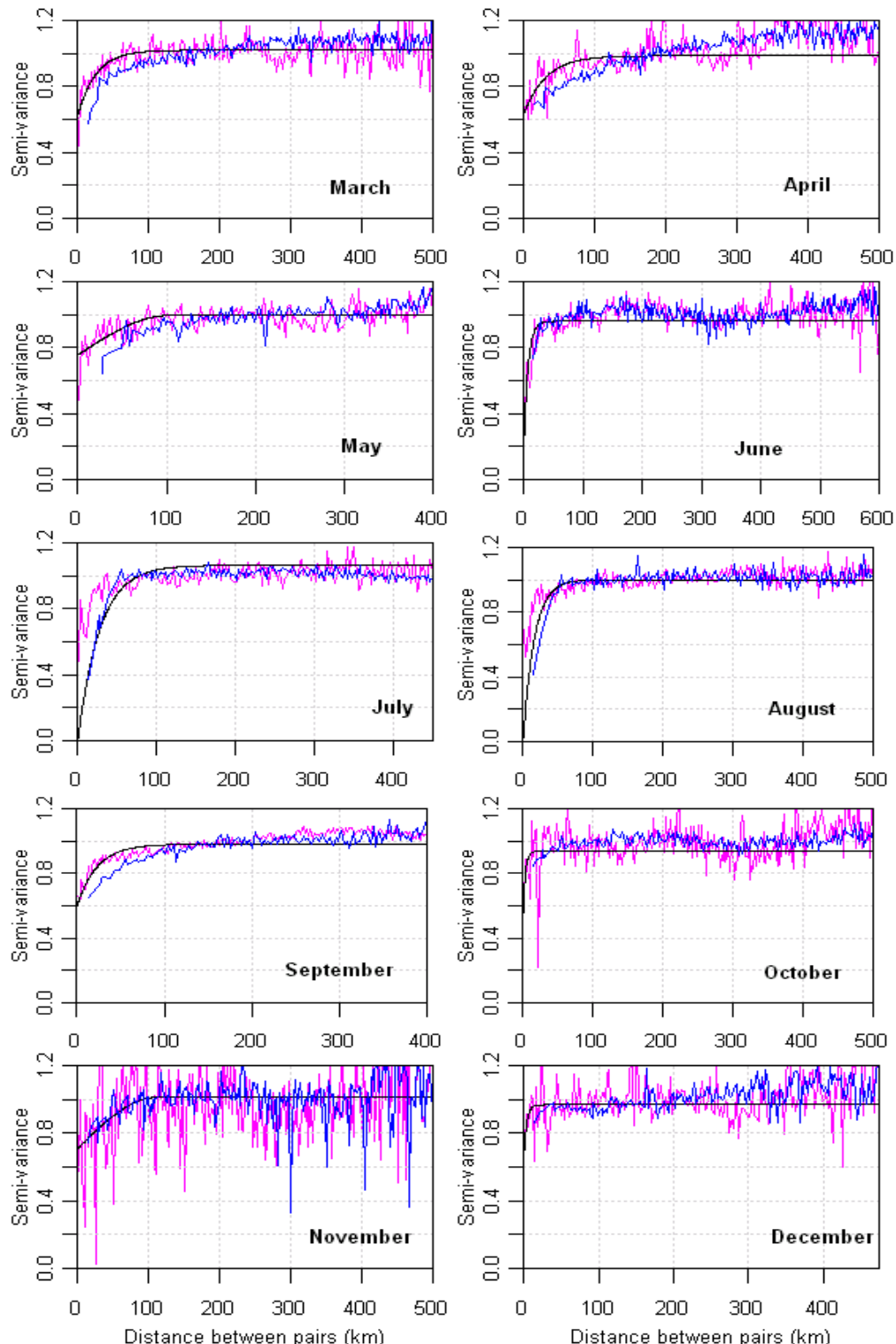


**Figure 7.5.** Normalised residual amount variograms for each month. The pink line shows the residual variogram calculate from observations, the black solid line is the model input into the sequential simulation process and the blue line is the residual variogram calculated from ensemble members. These are sampled at the same pixels and dates as the observations.

A possible reason for the difficulties in modelling spatial correlation is that the modelled range is approaching the pixel resolution of the ensemble ( $0.125^\circ$ ), therefore it is more difficult for the ensemble to respond both to sharp gradients in CCD and preserve spatial correlation. In addition, a more complex nested modelled variogram structure might have been more appropriate for some months, especially during the Belg season, however the version of the sequential simulation software used did not allow this. The spatial correlation of the ensembles is also forced by the structure of the Cold Cloud Duration field of each day, thus if the experimental variogram was not modelled accurately, then this might have produced a conflict within the ensemble. An advancement in the sequential simulation software to counteract this effect is described in Section 10.6.

In order to study the distribution of rainfall amounts in the TAMSAT ensemble on a given day, one must compare it to a corresponding distribution from observed rainfall. This process is non-trivial because there can only be one observed value of rainfall for a given location and day, or pixel-day. Therefore, the following method was employed to study the rainfall amount distribution at pixel scale for each month. For ease of comprehension, this explanation also includes a small example for three gauges situated in West Ethiopia for two days during March. As discussed in Section 5.3.2, the rainfall amount was calibrated as:

$$\mu_{F\text{ Zone}1} = 6.24 + 0.33CCD_{30} + 0.21CCD_{50} \quad 7.1$$

Firstly, for each day in the month and for each rain-gauge recording rain, the kriged gauge rainfall amount was recorded alongside its contemporaneous Cold Cloud Duration value at appropriate threshold temperatures for its calibration zone. This is shown below for the test dataset:

Gauge Name	Date	Rainfall Value	CCD30	CCD50
Addis_Ababa1	1/3/2002	2	0	0
Bedele	1/3/2002	8.2	4	2
Nekemte	1/3/2002	3.8	16	9
Addis_Ababa1	2/3/2002	14.1	4	2
Bedele	2/3/2002	1.3	3	1
Nekemte	2/3/2002	9.3	0	0

The rain-gauge values were then grouped into ‘bins’ according to their value of CCD and the bins were ranked according to generated rainfall amount:

**Bin 1:** 0 hrs  $CCD_{30}$ , 0 hrs  $CCD_{50}$ , mean rainfall amount from Eqn 7.1 = 6.24 mm

Contains

Gauge Name	Date	Gauge-value	$CCD_{30}$	$CCD_{50}$
Addis_Ababa1	1/3/2002	2	0	0
Nekemte	2/3/2002	9.3	0	0

**Bin 2:** 3 hrs  $CCD_{30}$ , 1 hr  $CCD_{50}$ , mean rainfall amount from Eqn 7.1 = 7.44 mm

Contains

Bedele	2/3/2002	1.3	3	1
--------	----------	-----	---	---

**Bin 3:** 4 hrs  $CCD_{30}$ , 2 hrs  $CCD_{50}$ , mean rainfall amount from Eqn 7.1 = 7.98 mm

Contains

Bedele	1/3/2002	8.2	4	2
Addis_Ababa1	2/3/2002	14.1	4	2

**Bin 4:** 16 hrs  $CCD_{30}$ , 9 hr  $CCD_{50}$ , mean rainfall amount from Eqn 7.1 = 13.41mm

Contains

Addis_Ababa1	2/3/2002	14.1	4	2
--------------	----------	------	---	---

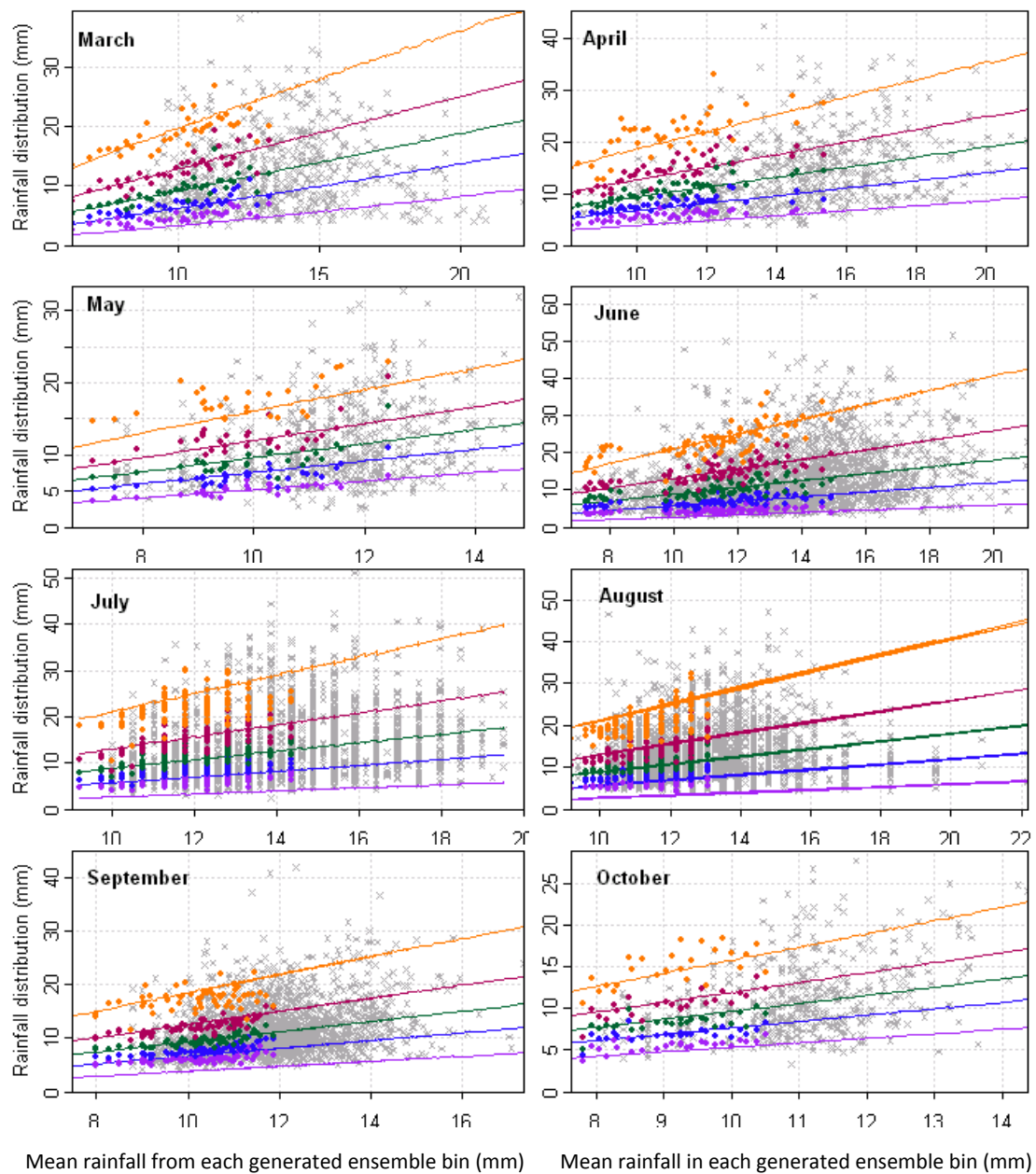
If there were more than 20 gauge values inside a bin, then the 90<sup>th</sup> percentile, 75<sup>th</sup> percentile, median, 25<sup>th</sup> percentile and 5<sup>th</sup> percentile values were calculated for the kriged rainfall amount.

Then for each CCD bin, a large ensemble of rainfall amounts (> 10000 members) was created using the gamma distribution described in Equation 4.16. The 90<sup>th</sup> percentile, 75<sup>th</sup> percentile, median, 25<sup>th</sup> percentile and 5<sup>th</sup> percentile values were calculated from the distribution. The entire method was then repeated then for each zone (so in our case study, it would be repeated for the Eastern zone). Finally, the gauge and satellite statistics were plotted against the mean predicted rainfall for that CCD bin. For bins containing less than 20 gauges, the raw gauge values were plotted to give an idea of where they fell in the distribution.

Figure 7.6 shows the results calculated from the Oromiya calibration dataset and the corresponding TAMSAT ensemble. In the plots, lines represent statistics from the ensemble rainfall distribution, whilst coloured points indicate the observed kriged gauge statistics for the corresponding CCD bin. From top to bottom (gold, pink, green, blue, purple), the plotted statistics are the 95% percentile of values in that bin, the 75% percentile, the median, the 25% percentile and the 5% percentile. Grey crosses indicate the rainfall observations in bins with less than 20 gauge-values, these bins were judged to have too few values to generate robust statistics. They were included in the plot as in general, the appropriate percentiles should fall within the modelled rainfall amount distribution. An indication of a good fit is where the coloured gauge statistics (points) lie close to the coloured ensemble statistics (lines). As the rain-gauge data were only used indirectly to choose the calibration parameters, these results fall somewhere in-between a validation and a check for internal consistency. The study cannot be repeated for the validation dataset as 20 pixels are too few for the method to be useful.

It should be noted that the method does not take into account the spatial correlation of the ensembles. However, they do prove a useful check on rainfall amount distributions. Overall, a good fit can be seen between the rainfall distribution of the Oromiya dataset and the modelled ensemble distribution. However, with the exception of May and October, all months show that for low values of predicted rainfall, the 5<sup>th</sup> percentile line from the ensemble is lower than the respective 5<sup>th</sup> percentile points from the gauge. This suggests that the ensemble distribution will generate excess low rainfall amounts, a feature discussed in Section 7.5. In the Belg season of April and May, the plots also show that the ensemble struggles to capture the higher rainfall amounts in each distribution, especially for low values of CCD. Overall, this suggests that the relationship between the mean and variance of rainfall has not been modelled precisely; this is perhaps unsurprising considering that an approximation is made for the rainfall variance at low CCD (discussed further in Section 4.3.2.3). It should be noted that this plot does not show the response of the ensemble to high rainfall amounts overall, just the statistics of a distribution for a given value of CCD.

An interesting result can be seen in March, where for CCD above 16 hours, all observed rainfall values fell below the ensemble median value. Although there is too little gauge data at high CCD for this to be a robust observation, it appears that observed rainfall is suppressed at high CCD during March. This is similar to the case discussed in Section 5.4.1 for January and February and suggests that the current TAMSAT calibration might be unreliable for high CCD values during the Bega dry season.



**Plot continued on the next page.**

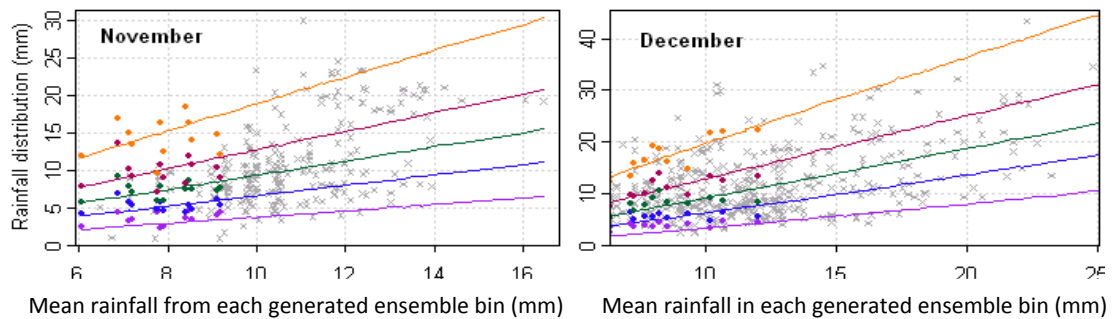


**Figure 7.6.** Analysis of forecast rainfall amount for each month. July and August have ‘neater’ distributions because the calibrations in those months only include one zone and one CCD threshold, consequently there are fewer possible CCD bins for the rainfall to be classed in.

## 7.4 VALIDATION OF THE PROBABILISTIC ENSEMBLE

The remainder of this chapter now analyses the properties of the rainfall ensemble and validates it against the gauge dataset shown in Figure 7.1. For each day in the validation dataset from 1994-1999, 200 realisations of rainfall maps were created using sequential indicator simulation and sequential Gaussian simulation.

### 7.4.1. VALIDATION OF THE RAINFALL DISTRIBUTION

The distribution of daily rainfall from the ensemble was first assessed by cumulative frequency analysis. This approach can also be seen in Bellerby and Sun (2005) and Teo and Grimes (2007). Here, simulated and observed probabilities of rainfall exceedance were compared for different rainfall thresholds. The method of creating the plot from experimental data is as follows:

For each day and pixel containing a rain-gauge, or pixel-day, the *simulated exceedance probability* was calculated, that is the proportion of ensemble members which exceed a threshold of rainfall amount. The ensemble values are then grouped into bins according to this measure. For example one bin might include all locations and dates where the proportion of members with  $> 2\text{mm}$  rain was between 0.4-0.5. The observed kriged rainfall for the pixel-days within each bin was then used to calculate the *observed exceedance probability*, or the proportion of gauges with rainfall above the threshold.

Finally, the observed exceedance probability was plotted against the simulated exceedance probability for each bin, as shown in Figure 7.7. If the ensemble was perfectly representing the probability of exceeding a rainfall threshold, the values should fall on the one-to-one line.

The plot shows that distribution of rainfall from the kriged gauge values is extremely well replicated by the ensemble. This is particularly encouraging for the  $P(Z = 0)$  plot on the top left as it shows that the ensemble is correctly replicating the occurrence of dry days. The fit appears to be slightly less sound at high rainfall thresholds, where there are more points with a high simulated rainfall probability compared to observed (suggesting that the ensemble distribution has a longer tail). However, very little data went into the majority of these points because high rainfall is a relatively rare event. When a weighted linear fit as applied the results appear to be unbiased, as shown by the red line on the graph. Finally, there were more pixel-days where observations suggest that there was a small chance of less than 10mm of rainfall, than compared to the ensemble.

This can be explained when studying the monthly distributions of observed and forecast rainfall. This analysis is shown in Figure 7.8, where each row comprises of the histogram of observed kriged rainfall amount, the histogram of ensemble rainfall amount, plus a Quantile-Quantile, or Q-Q plot of the two distributions. A Q-Q plot is created by plotting the values of the quantiles of one data set against the values of the quantiles in another set, in order to determine if both come from the same population. A quantile is defined as the point below which a given fraction of points lies. If both distributions come from the same distribution, they should lie on the 1:1 line.

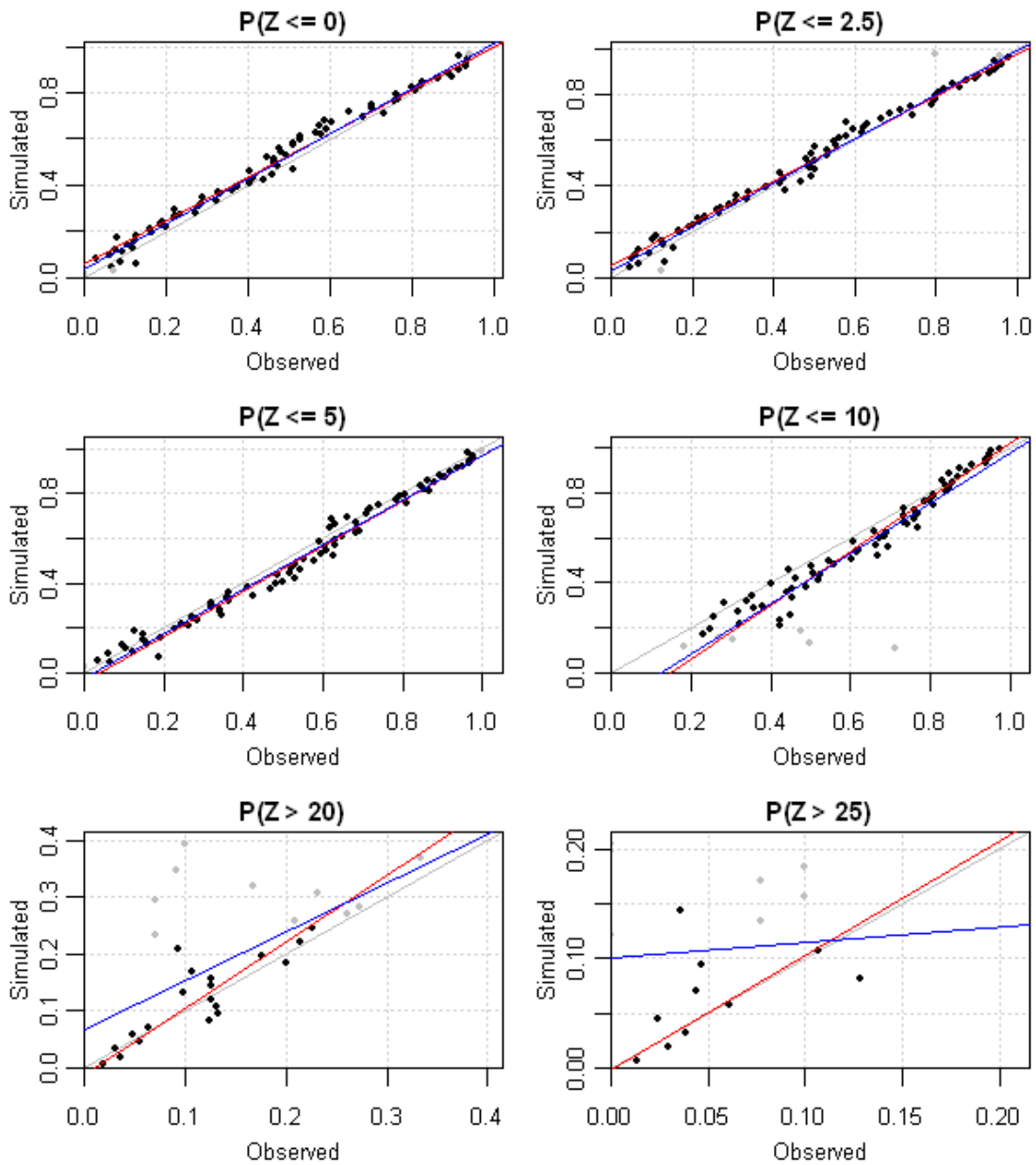
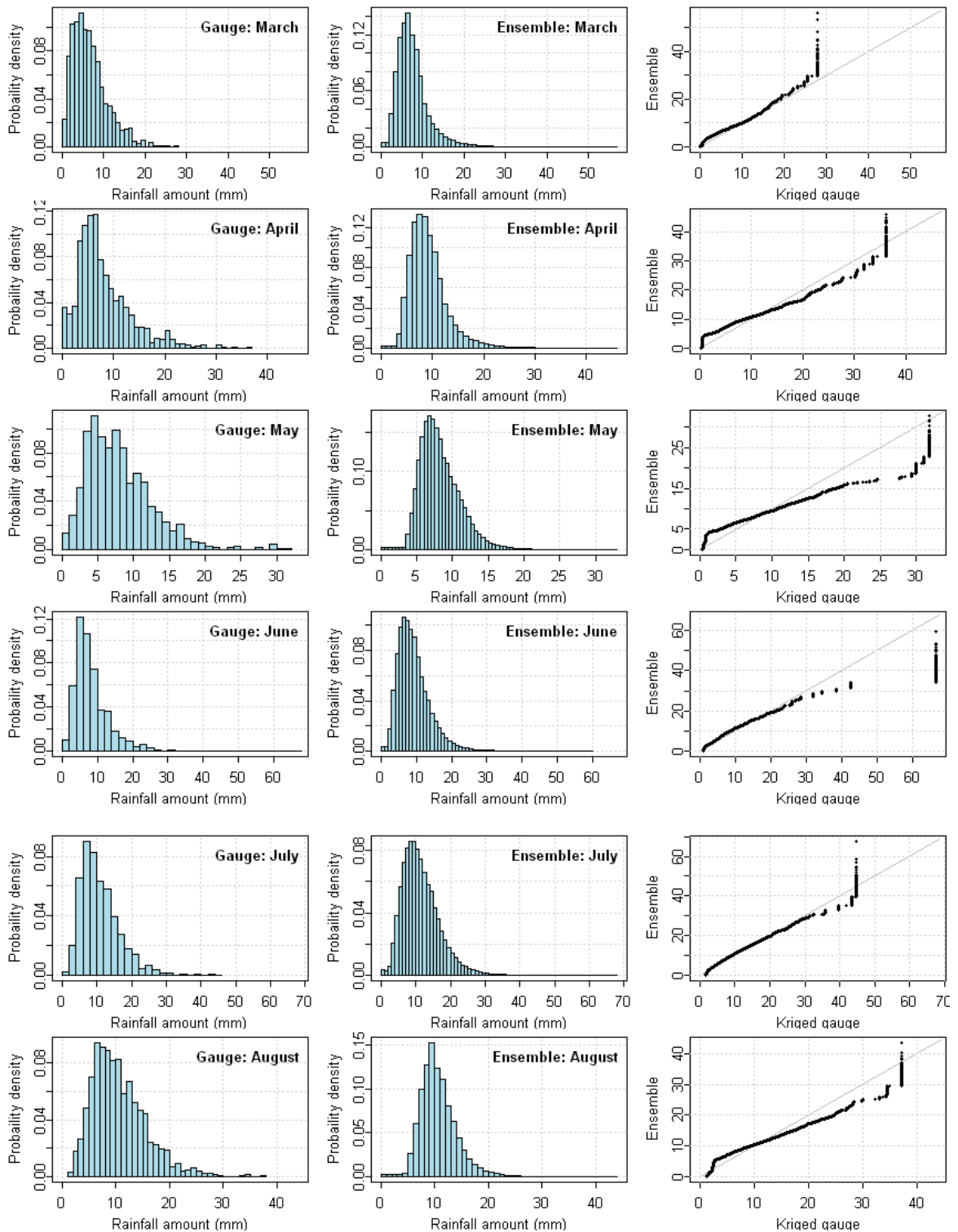
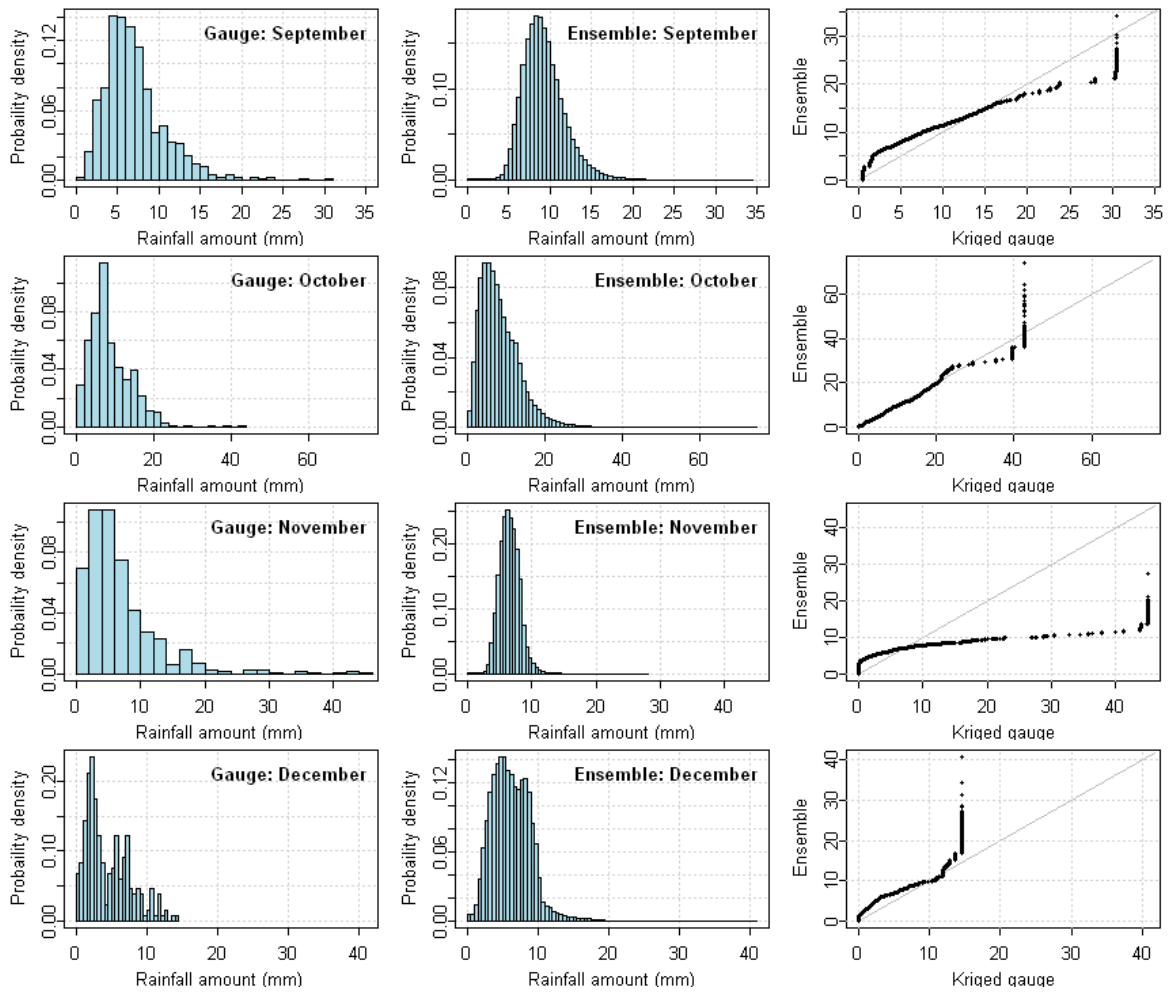


Figure 7.7. Probability of exceedance graphs. Comparison between simulations and the corresponding gauge-pixel data of rainfall exceedance probabilities at various thresholds, where all datasets have been scaled to  $0.125^\circ$ .

The solid grey line is the ‘one-to-one’ line, the blue line is a linear fit of the data and the red line is a linear fit weighted using the number of values which went into each bin.

Probability bins with less than 5 observed gauge estimates have been omitted and less than 25 have been marked in grey. Note, the top 4 plots show the probability of having less than or equal to the rainfall threshold, whilst the bottom two plots show the probability of receiving greater rainfall than the threshold.





**Figure 7.8.** Comparison of the rainfall amount distribution from gauge and from the ensembles. The left hand plots show histograms created from kriged gauge data at  $0.125^\circ$ , the central plots show histograms created from the ensemble values and the right hand graphs are QQ-plots of the differences between the distributions. A vertical line in the QQ-plot, normally seen for high rainfall amounts, is because there are 200 ensemble members for each gauge value, therefore the full set of ensemble members can sometimes be seen for isolated gauge values.

Most months show an overestimation of low rainfall (especially during drier months) and an underestimation of high rainfall (especially during wetter months). They also show that in general the peak of the gamma distribution is approximately 10mm. Therefore values of rainfall amount of approximately 10mm are much more likely to be randomly selected by the ensemble which perhaps explains why the selection of medium rainfall amounts is slightly overestimated in Figure 7.7. In addition, the plots show that the fit is particularly poor in November, where the ensemble variance appears to be underestimated. This poor fit can also be seen in the mean rainfall plot in Figure 7.2. However, as the calibration

parameters in Appendix A1.2 , the rainfall distribution in Figure 7.6 and the residual variograms in Figure 7.4 and Figure 7.5 all look reasonable, it is difficult to ascertain a reason for the poor fit, apart from to comment on the fact that there was very little observed rainfall amount data, plus that the TAMSAT calibration process struggled to capture the correct rainfall distribution in other dry months, January and February. As the fit looks reasonable in December, and November and December seem to have similar spatial characteristics in the variograms, there is perhaps a case for merging the calibration in the two months.

#### **7.4.2. SPATIAL CORRELATION**

Experimental indicator and positive rainfall amount variograms were calculated from the Oromiya dataset and from a selection of ensemble members for the same time and pixels. Please see Section 3.4.1.1 for a description of variogram terminology. These are different from the residual variograms discussed in Section 7.4.2 (which illustrate the internal consistency of the ensembles), as they describe the observed correlation of rainfall occurrence and amount directly. This is something which was not included in the sequential simulation calibration. The validation dataset was deemed to be too small to use in the variogram analysis, however because the raw Oromiya gauge data was only used indirectly in the calibration process through the derivation of calibration parameters and residual variograms, it was felt to be suitable for use in the validation. Indicator variograms can be seen in Figure 7.9 and positive rainfall amount in Figure 7.10.

In general, the ensembles show a good fit to the data, although the effect of forcing the nugget to zero for June, July and August is reflected in the appropriate plots. Months which have an observed nested distribution were also modelled less well, although contrary to Teo and Grimes, 2007, the variogram sills are modelled well. Additionally, long range behaviour of the ensembles matches observations.

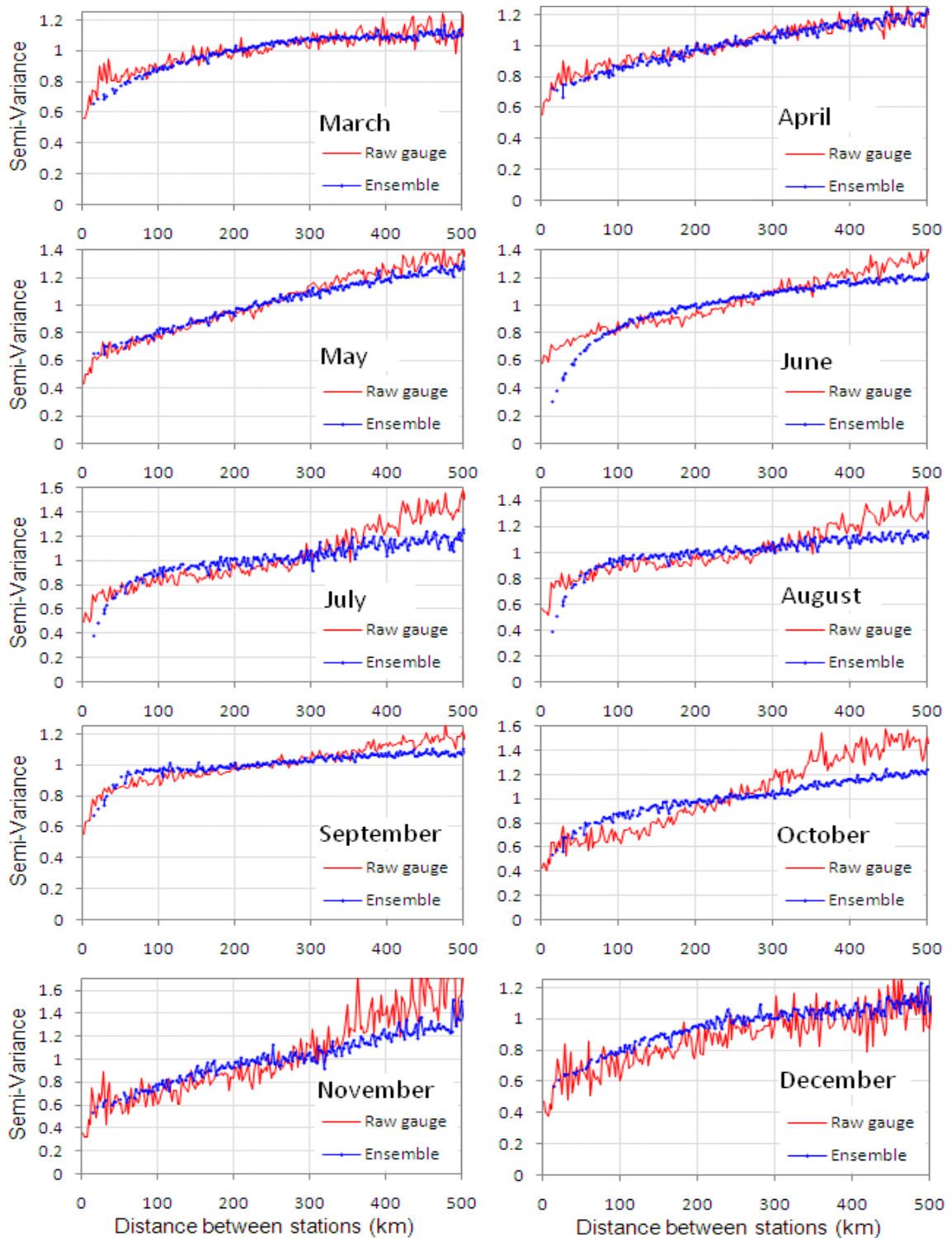


**Figure 7.9.** Indicator variograms of rainfall occurrence for each month. The red line corresponds to the variogram generated by the raw gauge dataset and the blue line from the ensembles. A good comparison can be seen for most months.

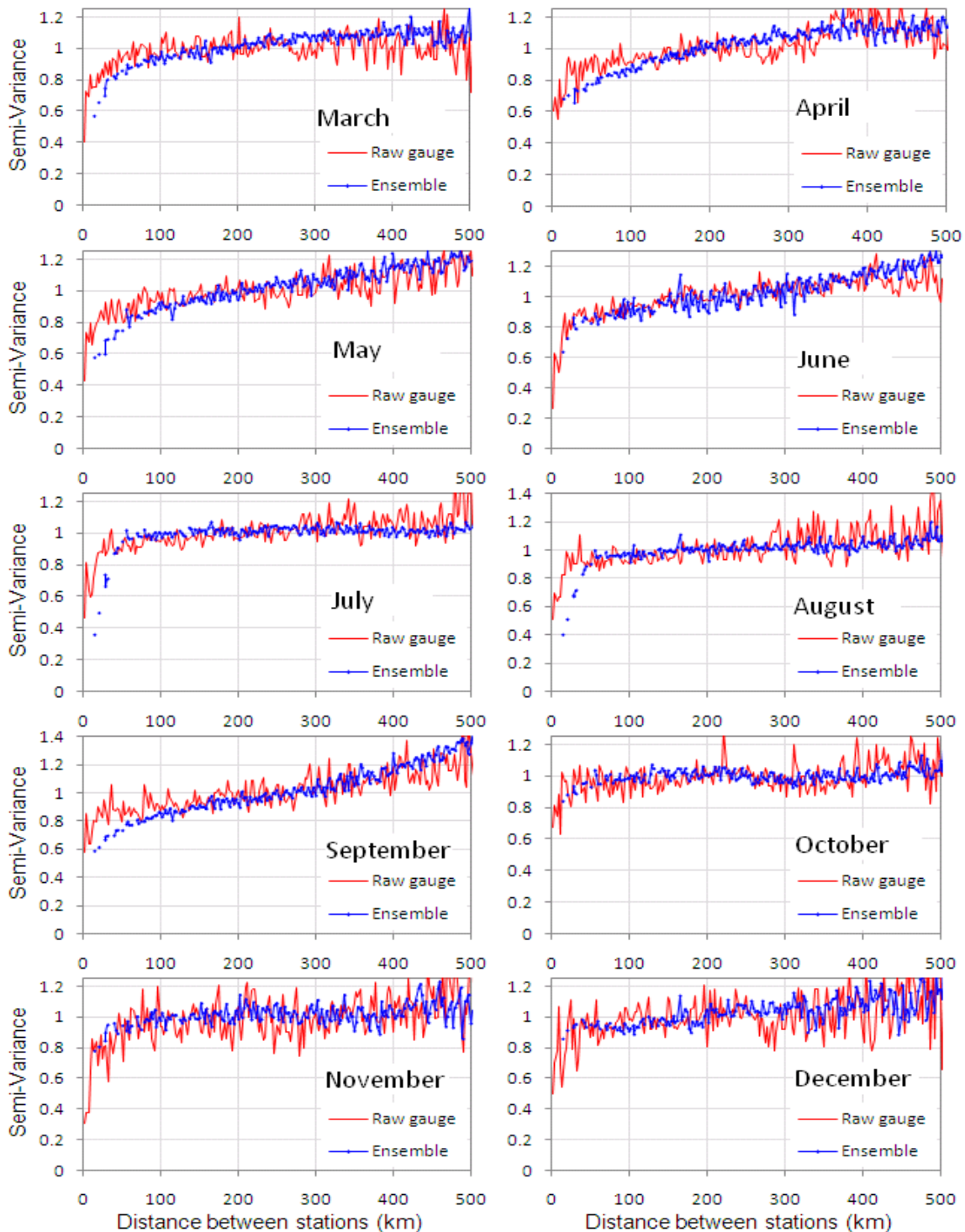


**Figure 7.10.** Variograms of positive rainfall occurrence for each month. The red line corresponds to the variogram generated by the raw gauge dataset and the blue line from the ensembles. A good comparison can be seen for most months.

### 7.4.3. TIME-SERIES

Finally, daily time-series were plotted over the entire validation time-period (1994-1999) and the ensemble values compared with gauge data in Figure 7.11 and Figure 7.12. The two statistics chosen for the time-series were the daily mean over the validation pixels and the proportion of rainy validation pixels each day. The results show that the ensemble is capturing the seasonal cycle and that in general, the ensemble is suggesting a reasonable range of values on a given day. There are very few days when at least one ensemble member does not capture the observed rainfall.

However, the ensemble does show a slight overestimating of low rainfall amounts during the dry months, a feature which is discussed in the next section. The ensemble also has less year-to-year variability than the gauges, which is an issue if one is attempting to use the satellite to make climatologies of ‘wet’ or ‘dry’ years.

The analysis was repeated at a 10-day scale in Figure 7.13. This was so that the ensembles could be compared against the TAMSAT 30-year rainfall climatology (TARCAT), which has calibrated on an extensive gauge dataset of 700 stations throughout Ethiopia spanning 30 years and has been comprehensively validated Maidment *et al.*, 2012. It is encouraging to see that the time-series from the ensembles closely resembles the one produced by TARCAT, although both struggle to capture the Belg rainfall season accurately. The ensemble cloud is also capturing the observed rainfall in nearly every dekad.

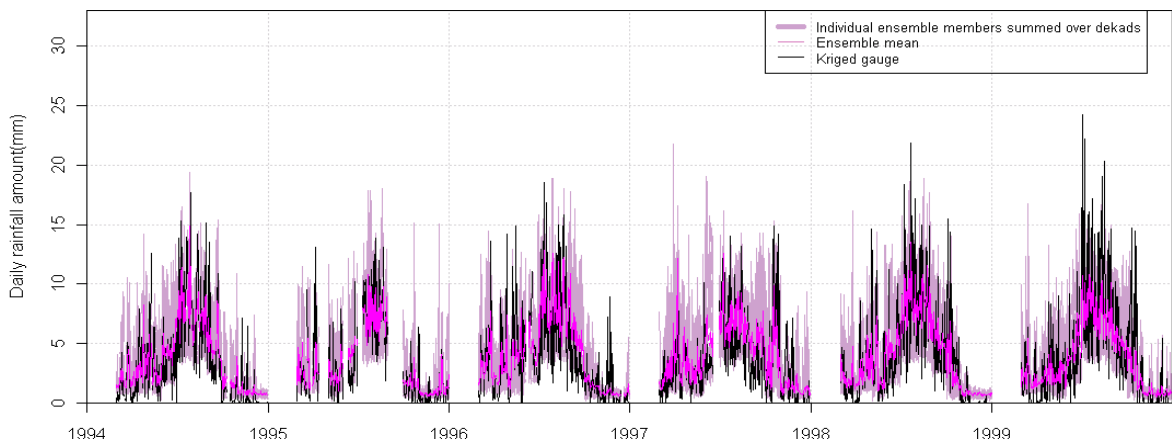


**Figure 7.11.** Mean kriged rainfall over the 20 validation stations (black), plotted against daily rainfall averaged over the same 20 pixels for each ensemble member (light purple cloud) and the ensemble mean (pink). Values were only plotted for days containing gauge data.

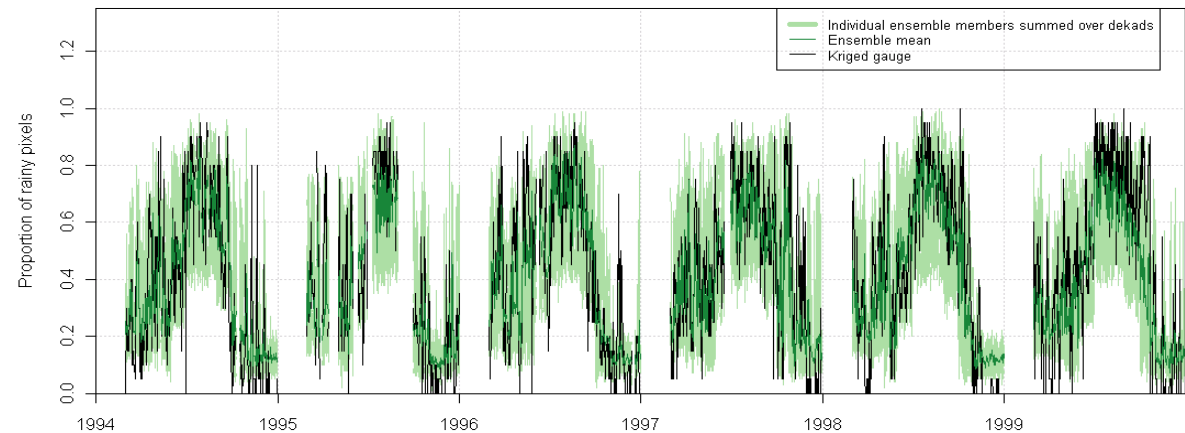


**Figure 7.12** The proportion of rainy gauges over the 20 validation stations (black), plotted against proportion of rainy pixels for each ensemble member (light green cloud) and the ensemble mean (green). Values were only plotted for days containing gauge data.

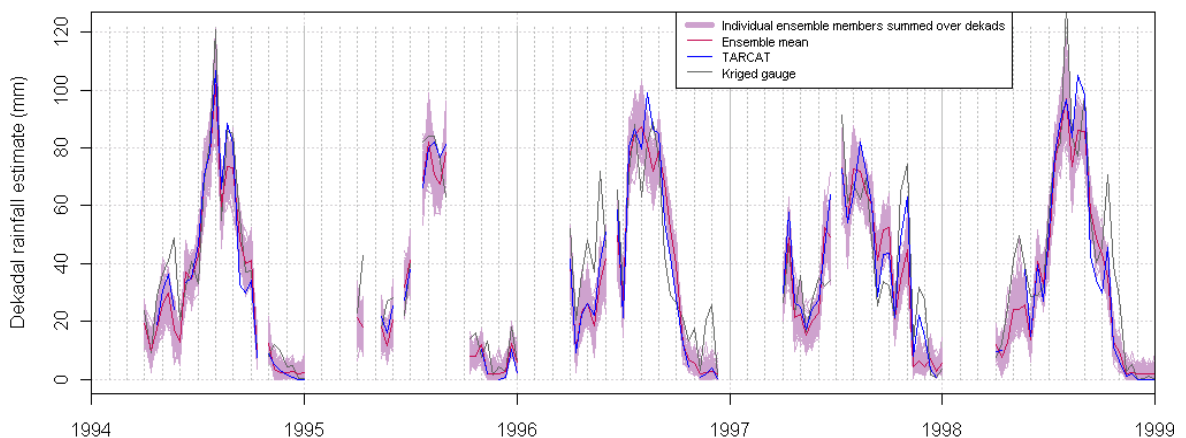


**Figure 7.13.** Time-series of the mean dekalad rainfall from the average of the 20 validation stations from kriged gauge data (black), the TARCAT rainfall climatology (blue), the ensemble mean (red) and the 200 individual ensemble members (purple cloud). Values were only plotted for dekads where all the data was present.

## **7.5 MODIFIED TAMSAT ENSEMBLES**

Several of the analyses and plots in this chapter and in Chapter Six have suggested that the ensembles overestimate the occurrence of low rainfall. In particular

- 1) Visually, the ensemble realisations depicted in Figure 6.7 and Figure 6.12 appear to overestimate rainfall occurrence and obscure the overall rainfall picture. Previous sequential simulation studies have noted that the ‘general rainfall picture’ is preserved in ensemble members, even if the detail in each one is unique (Teo and Grimes, 2007).
- 2) The rainfall amount analyses in Figure 7.6 show that the 5<sup>th</sup> percentile of rainfall is lower than observations in the majority of months.
- 3) The histogram and Q-Q plot comparison of rainfall amounts in Figure 7.8 show excess low rainfall in the majority of months.
- 4) The time-series of mean rainfall in Figure 7.11 shows excess low rainfall in dry months, when one might expect there to be no rainfall.
- 5) A similar issue was discovered in the ensembles produced in Teo and Grimes, 2007

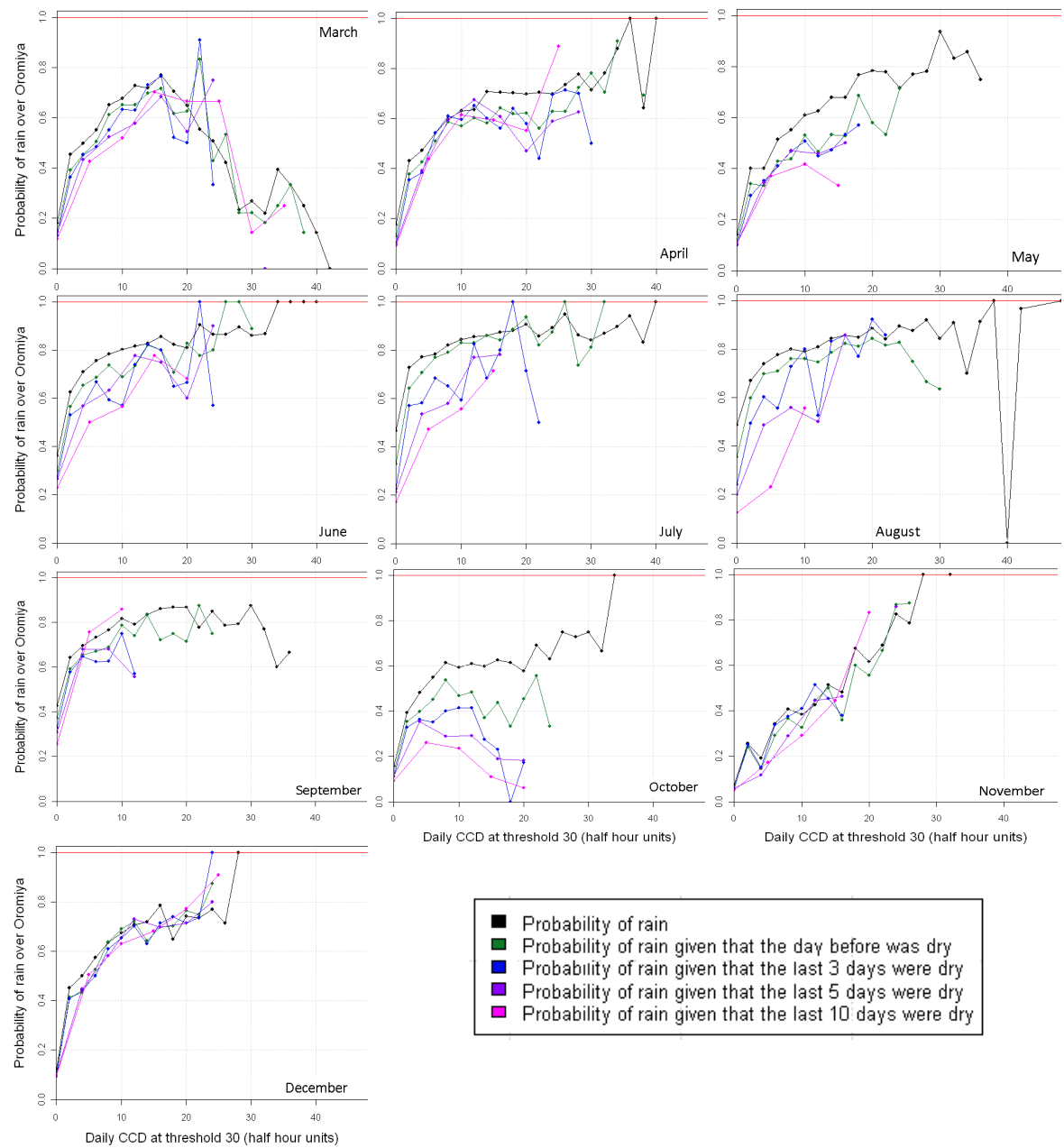
There are two main hypotheses which might explain the poor distribution:

The first is that the time-series of rainfall occurrence in Figure 7.12 show that the cause of this excess rainfall is probably an overestimation of rainfall occurrence. The problem is also more apparent in dry months, therefore it is proposed that the excess rainfall might be caused by an incorrect parameterisation of the relationship between the probability of rain and Cold Cloud Distribution. In particular, it would be reasonable to expect that the probability of rain for a given value of CCD would be lower during a dry spell than a day falling in a rainy period. Therefore, Figure 7.14 shows a Markov analysis of the probability of rain against CCD for different dry spell lengths. These plots show that although the situation is complicated and varies from month to month, there is no significant Markov effect at low CCD, especially during dry months. The plot also shows

that there is suppression of rain at high CCD in March which adds to the body of evidence that not all the rainfall in March is from convective systems.

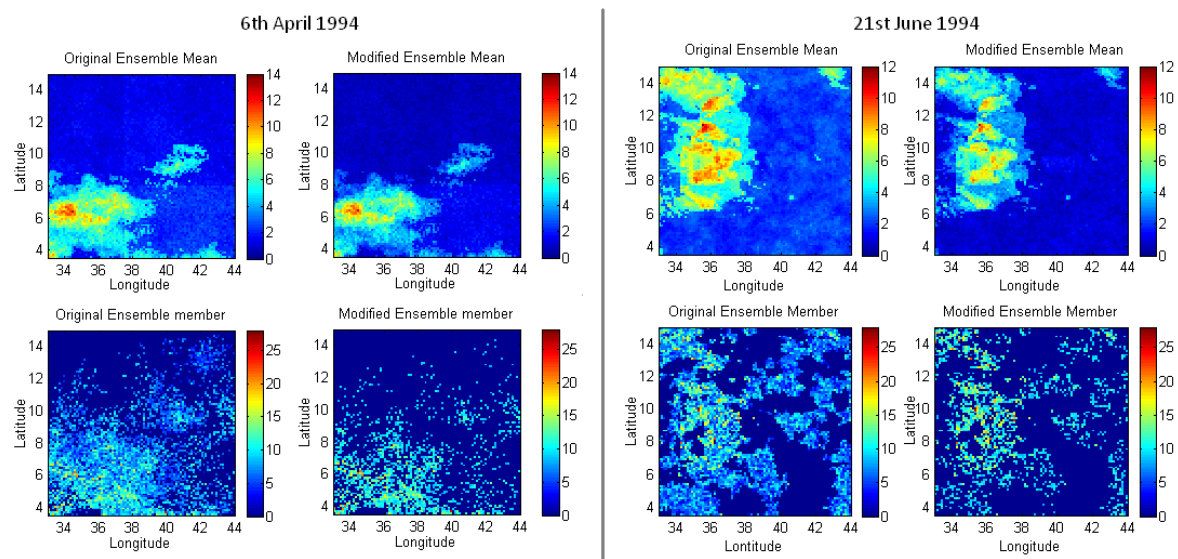
The second hypothesis regarding the excess low rainfall is that the error distribution for rainfall amount discussed in Section 4.3.2.3 contains a simple approximation at low CCD, where the traditional error analysis breaks down. It is reasonable to assume that this approximation needs more careful analysis in dry months where it is often applied.

The exact reason behind the overestimation of low rainfall amounts is likely to be a combination of these and other factors and in order to address it properly, a significant amount of time would have to be spent re-investigating the calibration procedure. This was inappropriate to do within the time-span of this thesis, especially as although the issue is important with respect to crop simulation modelling (because a constant drizzle is a perfect condition for plants to grow, thus plants could grow in desert conditions), regional scale crop simulation models are less sensitive to daily pixel scale rainfall amounts. Consequently, a correction was made to the existing ensembles dataset. Two methods were investigated. Method 1 removed all pixels containing less than 8 mm of rain. Method 2 set 75% of ensemble members to zero for any pixel-day with an ensemble mean of less than 2.5mm. The 8 mm, 75% and 2.5 mm thresholds were determined empirically, although it should be noted that the 8mm threshold was selected to be high enough to capture the ensemble mean for all months at 0 hours of CCD, otherwise no discernable effect would be seen.



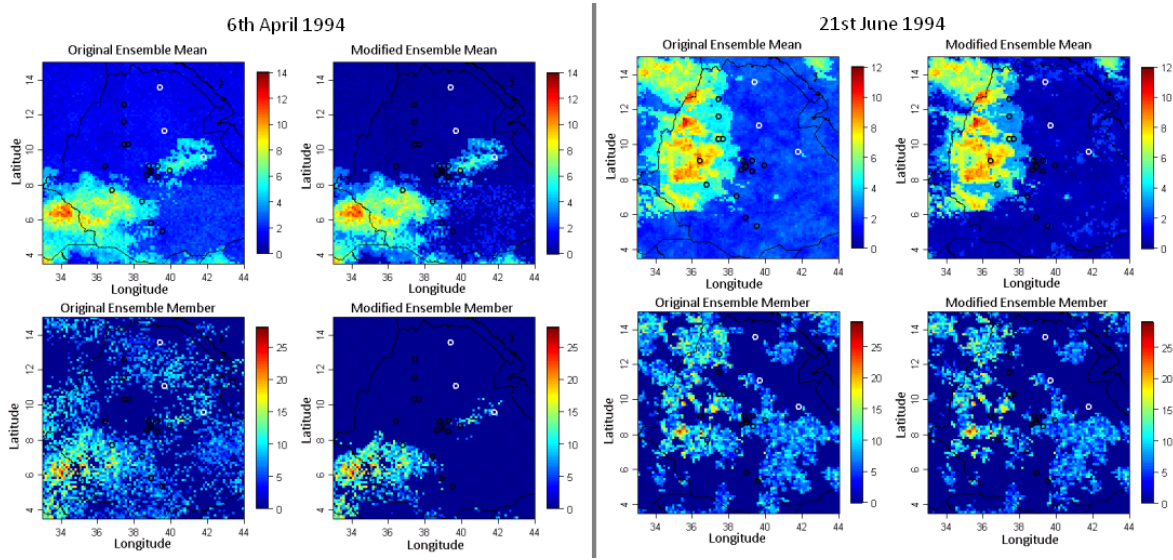
**Figure 7.14. A Markov analysis of Ethiopian rainfall. The probability of rain is plotted against CCD for different lead times.**

Figure 7.15. shows the effect of correction method 1 for two case studies; one for a dry day and one in the height of the main rainy season. The threshold technique works well at removing the background field of rainfall in the ensemble mean. However, it is clearly apparent that the method is destroying the spatial correlation of the ensembles and targeting ensemble members in the rainy season (which do not appear to have a problem from excess low rainfall).



**Figure 7.15.** Case studies for the 6<sup>th</sup> April 1994 and the 21<sup>st</sup> June 1994. The left hand side of each case study shows the original ensemble mean and an original ensemble member. The right hand side shows ensemble members which have had Method 1 applied. This causes significant changes to the spatial correlation of the ensembles.

Method 2 seems to have much better results, as it is keeping much of the spatial detail which would have been lost by the Method 1's 8mm threshold, but removing excess low rainfall amounts in dry areas. This can be seen in particular in Figure 7.16, where the modified ensemble mean and individual ensemble members look more realistic.



**Figure 7.16.** Case studies for the 6<sup>th</sup> April 1994 and the 21<sup>st</sup> June 1994. The left hand side of each case study shows the original ensemble mean and an original ensemble member. The right hand side shows ensemble members which have had the method 2 applied. The method appears to be much more efficient at targeting areas of superfluous drizzle.

Finally, time-series of the modified proportion of rainy pixels and the ensemble mean are shown in Figure 7.17 and Figure 7.18. These show that the rainfall in dry months now more closely resembles observations, especially when considering the probability of rain.

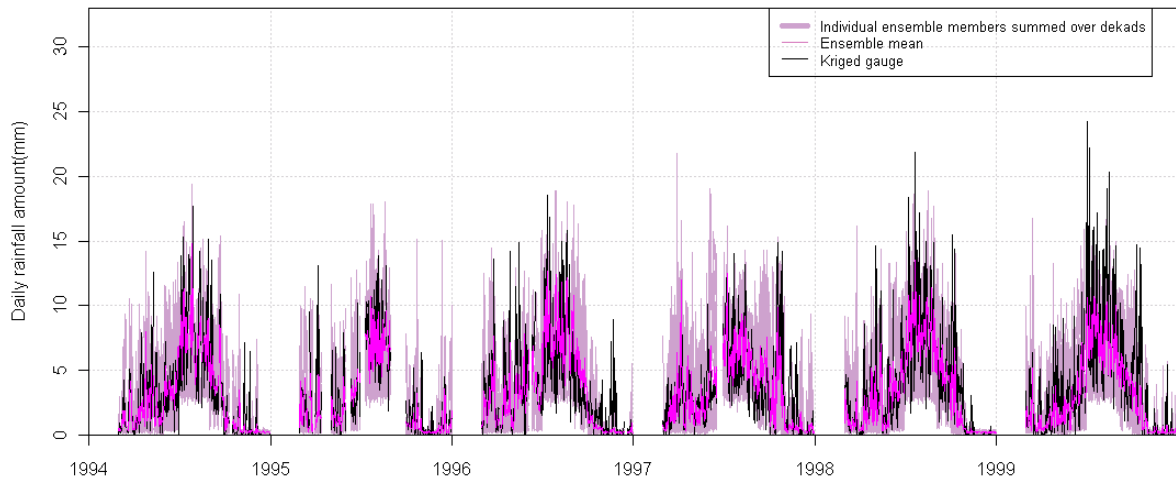


**Figure 7.17.** Time-series of the mean rainfall from gauge (black), the modified ensemble members (purple cloud) and the modified ensemble mean (pink).

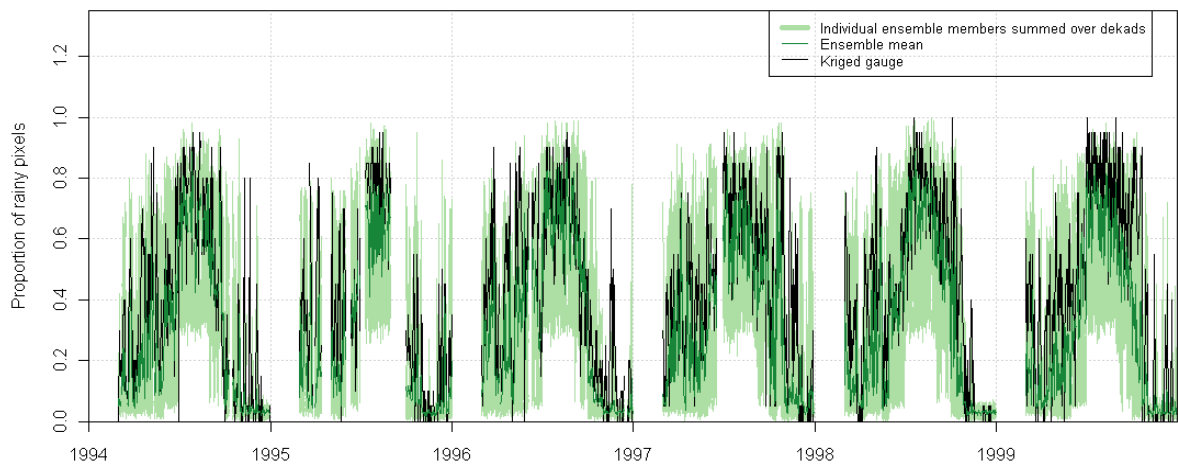


**Figure 7.18 Time-series of the proportion of rainy pixels from gauge (black), the modified ensemble members (green cloud) and the modified ensemble mean (green).**

## 7.6 CONCLUSION TO CHAPTER SEVEN

This chapter considered a comparison and validation of the TAMSAT ensemble against observations and other satellite rainfall estimates. Section 7.2 first considered the ensemble mean and compared it against similar statistics obtained for other daily satellite estimates over Ethiopia. It was found that the estimates have a low bias and compare comparably or better than the results found in the external validation studies. The ensemble mean could not be used directly as a deterministic rainfall estimate as the calibration process means that it cannot model zero rainfall amounts. Therefore a promising avenue for future research might be to investigate how a daily deterministic TAMSAT estimate could be created from the calibration. Initial ideas include setting the rainfall value for zero CCD to zero (as employed in dekadial TAMSAT estimates), or using the threshold approach employed in double kriging to define masks of rainfall occurrence (an approach is discussed further in Section 3.4.1.3).

Section 7.3 studied the properties of the TAMSAT ensemble to check for internal consistency. The results showed that the ensemble reproduced the spatial correlation and CCD/rainfall relationship input into the model, although the process occasionally failed to capture high rainfall amounts at pixels which had a low value of CCD.

The properties of the ensemble were then validated against an independent gauge dataset in Section 7.4. The ensembles were found to reproduce observed rainfall statistics extremely well in most months, with an under-performance in November and December attributed to a lack of data and the fact that the TAMSAT calibration was less appropriate in Ethiopia's dry season (as there is a higher probability of non-convective rain and high non-raining clouds). Finally, an empirical improvement to the ensemble was suggested in Section 7.5 to reduce an overestimation of low-rainfall amounts.

## **7.7 CONCLUSION TO PART 2**

Satellite rainfall estimates have great potential for use in regional crop yield modelling, especially in areas with sparse rain gauge data, because they have full spatial coverage and are available in real-time. TAMSAT satellite estimates have been proven to be robust and reliable in the context of African rainfall estimation (Grimes *et al.*, 1999) , however it is important to quantify the uncertainty in the estimates. Therefore the geostatistical process of sequential simulation was used to generate ensembles of daily rainfall maps, where the statistics at any one pixel agree with the input statistics, but each individual ensemble member is unique with a spatial correlation derived from observations.

The methodology was developed further from previous work discussed in Teo and Grimes (2007) in that multiple calibration zones and CCD temperature thresholds were explored. A calibration was then performed for each month for the Ethiopian case study and validated in Chapter Seven. This showed that in general the ensembles captured daily rainfall distributions well, especially in the Belg and Kiremt wet seasons which are important for maize growth. However, the original ensembles slightly overestimated the occurrence of low rainfall amounts which could potentially affect modelled maize yield. Therefore these low rainfall amounts were empirically removed and the ensemble revalidated.

---

---

# PART 3

# ETHIOPIAN CROP

# YIELD MONITORING

This Section of the thesis applies the satellite rainfall ensembles described in Part 2 and the synoptic and agronomic observations discussed in Part 1, to regional scale crop yield forecasts for Ethiopian maize,

*Chapter Eight* (Crop yield modelling) begins with a literature review of crop models. It then discusses the physiology and phenology of tropical maize before applying these to a calibration of the GLAM maize crop model.

*Chapter Nine* (The application of satellite rainfall ensembles to crop yield monitoring) links GLAM<sub>MAIZE</sub> to both satellite rainfall ensembles and modelled rainfall to see how the uncertainty in weather inputs reflects in modelled crop yield. Modelled yield is also compared against observations.

## CHAPTER EIGHT

# CROP YIELD MODELLING

Crops are inherently sensitive to changes in their environment, in particular to weather and climate. Many advances have been made in understanding these interactions in the last century, both through experiment and numerical modelling. This chapter illustrates some of the most important interactions between crops and climate, particularly those pertaining to tropical maize. It then moves on to discuss crop simulation modelling and the General Large Area Model for annual crops (GLAM).

## 8.1 PHENOLOGY, GROWTH & CROP-WEATHER RELATIONSHIPS

The state of a plant at any one time reflects on two distinct processes, growth and development. Growth refers to an increase in a plant's dry matter or size, whilst development denotes progression through its life cycle. Both processes are sensitive to weather and climate:

### 8.1.1. CROP DEVELOPMENT

The rate of plant development is closely linked with temperature, although the relationship is sometimes complicated through an additional correlation with photoperiod, or day length. This is because in order to obtain the best chance of survival and propagation, a plant must align itself to seasonal variations in climate, thus reducing the possibility of stress at key points in its life cycle. For example, to avoid water stress, plants in the tropics have evolved so that flowering occurs during the rainy season, whilst plants in the mid-latitudes have evolved so that vulnerable development periods occur after the winter in order to avoid frost damage.

A development stage is defined as the length of time that elapses between any two significant points in a plant's life cycle. For example, the vegetative development stage is often defined as the time between emergence and flowering. Instead of measuring the length of development stages directly, it has proven profitable to analyse developmental rates e.g. for the example above, the rate of progress towards flowering. As shown in Roberts and Summerfield (1987) and depicted in Figure 8.1, the rate of development has a relatively simple relationship with temperature, defined by three cardinal temperatures:

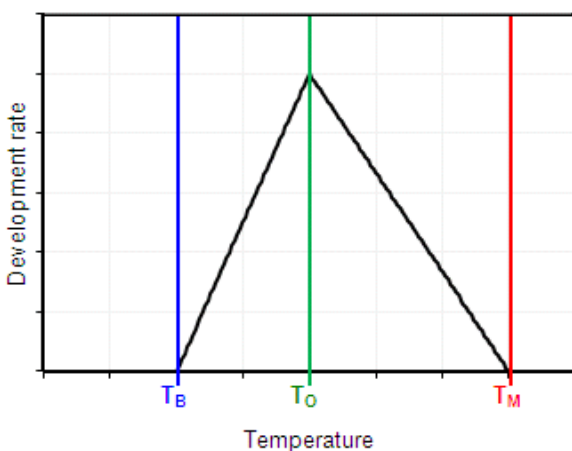


**Figure 8.1. Relationship between temperature and development rate, with the three cardinal temperatures marked as coloured lines.  $T_B$  indicates the base temperature,  $T_O$  indicates the optimum temperature and  $T_M$ , the maximum temperature.**

Development rate is fastest at the optimum temperature,  $T_O$ , and decreases to zero at and below a base temperature,  $T_B$ , and at and above a maximum temperature,  $T_M$ . If the temperature is fixed near the optimum, the plant will develop quickly and so provide little time for growth to occur. As there are often specific heat stress effects present when the temperature approaches  $T_M$  (Prasad *et al.*, 2000; Wheeler *et al.*, 2000; Challinor *et al.*, 2005b), the highest yields tend to be recorded when the plant is grown at temperatures near the base temperature. The values for the cardinal temperatures are found experimentally and vary between crop, cultivar and development stage. Due to the difficulty in growing crops at a fixed temperature, the shape of the relationship described in Figure 8.1 is still being established and is sometimes defined with a flat top, enabling development at a maximum rate for a range of temperatures above  $T_O$  (Craufurd and Wheeler, 2009). Using

the relationship above, developmental stages are often described in thermal time units. For example, if the temperature on day  $i$ ,  $T_i$ , fell between  $T_B$  and  $T_O$ , the amount of thermal time needed to complete a development stage would be described as,

$$\Theta = \sum_{i=1}^f T_i - T_b = \frac{1}{m} \text{ } ^\circ\text{C day} \quad 8.1$$

where  $m$  is the gradient of the curve depicted in Figure 8.1.

For photoperiod insensitive plants, the relatively simple relationship between development rate and temperature is adequate to explain the bulk of their development. However, many crops are sensitive to day length in the developmental stage before flowering in order to avoid potential climate stresses. Short-day plants require shortening day lengths before flowering is triggered, whereas long-day plants require lengthening days. As one might expect, short-day plants tend to be found in the tropics. This is because they are often limited by a lack of water rather than the amount of solar radiation present, therefore in order to avoid water stress, the plant aim to flower in conjunction with the ITCZ which in general follows the sun's zenith point.

### **8.1.2. CROP GROWTH**

Crop growth is simply an increase in a plant's biomass or size, achieved by converting solar energy and nutrients to dry matter. This is done using the process of photosynthesis, which is defined as the method by which carbon dioxide and water are converted to simple carbohydrates and oxygen through the use of solar energy. Photosynthesis is generally limited by water or solar radiation. There are two main photosynthetic pathways, C3 and C4. Most plants follow the C3 pathway, which converts CO<sub>2</sub> to carbohydrates via the Calvin cycle. However a significant minority of tropical plants (including maize and sugar cane) use the C4 pathway. This is much more efficient in dry, arid conditions as it allows the plant to have a better water efficiency. More detail about photosynthesis can be found in Hay and Porter (2006) and Ehleringer and Cerling (2002).

### 8.1.3. CROP WEATHER RELATIONSHIPS

The most important weather variables affecting crop yield are solar radiation, temperature and rainfall, although as these weather phenomena are inextricably interlinked, it is often difficult to observe individual effects in the field.

**Solar radiation** is used directly by a crop in photosynthesis. In the tropics, if a crop is not water limited, yields will be higher in cloudless seasons than in wet seasons (excluding temperature effects). Solar radiation is more of a limiting factor in the mid-latitudes due to short day lengths during winter. The effect of **temperature** is primarily on the development of the crop; as described in Section 8.1.1. In addition, plants are often sensitive to heat stress during certain development stages, a topic which is discussed in more detail for maize in Section 8.2. Finally **rainfall** is experienced by a crop as a slower frequency variation in soil moisture (Osborne, 2004). At leaf level, a crop loses water through the process of evapo-transpiration, which is also affected by relative humidity and ambient temperature. If a plant is water stressed, then it will limit transpiration through restricting photosynthesis, resulting in less growth and smaller yields. Although rainfall is generally beneficial, high intensity rainfall can negatively affect a crop through erosive run-off or flooding. Finally, as with high temperature stress, a crop can be particularly sensitive to water stress at specific points during its development cycle (discussed in more detail for maize in Section 8.2). More attention will now be paid to the main crop of interest for this thesis, maize.

## 8.2 MAIZE

The “strange and marvellous plant”, maize (*Zea mays*), has long been a part of agricultural systems (Smith *et al.*, 2004). It was first documented in 7000 B.C. in the Andean region of central America and now, along with wheat and rice, forms one of the world’s most important staple crops (Norman *et al.*, 1995). Maize is one of the world’s most robust crops to environment and is therefore extremely widely grown. It is found from 55°N to 40°S and at elevations ranging from sea level to over 3500m (Goldsworthy and Fisher, 1984).

Currently, maize is the preferred staple for over 900 million poor consumers and is widely regarded as the most important staple food crop in Africa. The importance of maize in developing countries can be seen clearly in Figure 8.2, which depicts analysis by the International maize and wheat improvement centre (CIMMYT) for the MAIZE global mega programme. As discussed in Section 2.3, maize is one of the most important crops in Ethiopia and is widely grown across the Highlands.

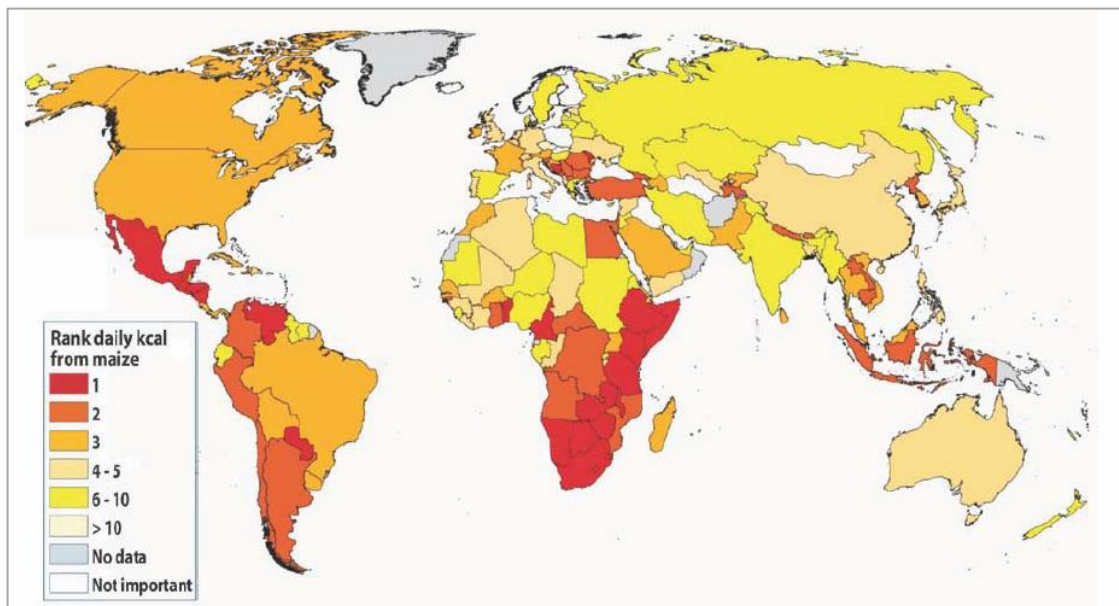


Figure 8.2. Relative rank of maize as a food crop in 2010. Figure taken from Cimmyt (2010)

Although all cultivars of maize have a similar phenology and physiology, the ability of the plant to adapt to different environments means that different genotypes can have very different characteristics, for example in the response to photoperiod or in the interactions between climate and harvest index. Therefore only tropical maize is examined here.

### 8.2.1. MAIZE PHENOLOGY AND SENSITIVITIES

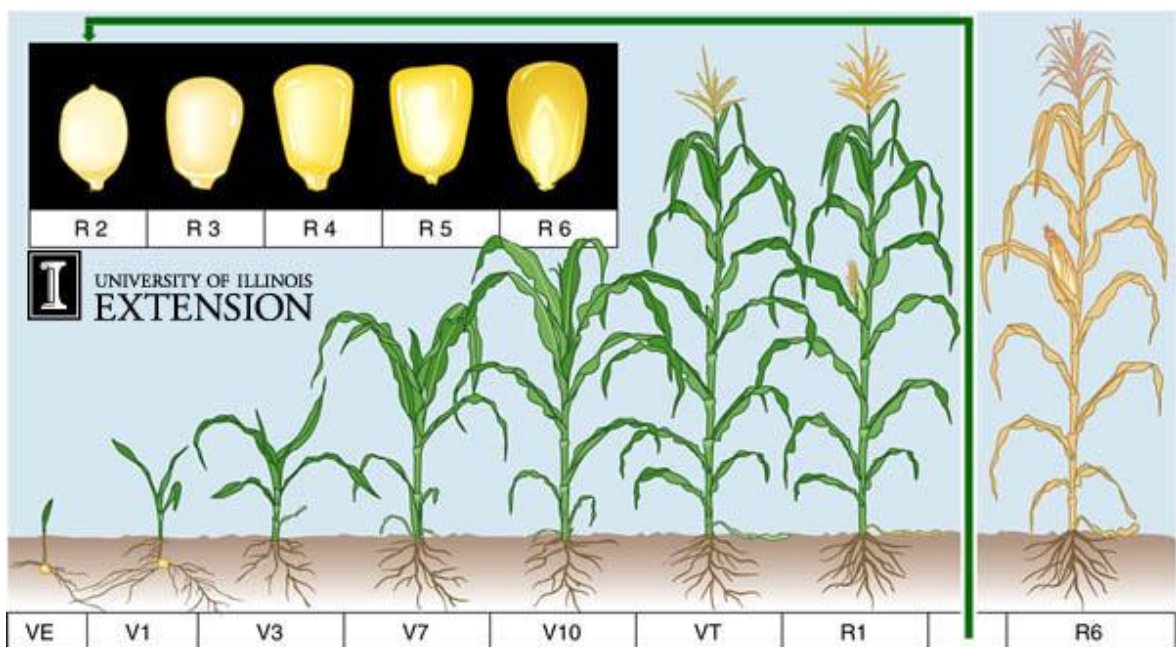


Figure 8.3. Life cycle of maize. Figure taken from Abendroth *et al.*, 2011

Maize is a monoecious plant, bearing male flowers (tassels) which produce pollen and female flowers (silks) which receive it (Kling and Edmeades, 1997). The plant has several developmental stages, which are summarised in Figure 8.3 and detailed below. It is worth noting that not all the plants in a field will reach development stages at the same time, therefore in general a development stage is designated to have occurred when 50% or more plants in a field have reached that point.

#### 8.2.1.1. Vegetative period (*Juvenile stage*):

This stage lasts from seedling emergence until tassel initiation and encompasses development stages VE to V1 in Figure 8.3. During this time, both the roots and leaves are initiated and stem elongation occurs. In short-day cultivars of maize, this period ends

when the plant becomes photo-sensitive. In cultivars insensitive to photoperiod, the vegetative phase ends with the initiation of the tassel, the male flower in maize. The length of the juvenile period is determined by temperature without any additional effect from photoperiod.

### **8.2.1.2. Photoperiod sensitive stage**

Short day cultivars of maize use photoperiod at the end of the vegetative stage to regulate the initiation of male flowers, or tassels. This happens between stages V3 and V6 in Figure 8.3 and is also known as the inductive vegetative stage (Kiniry *et al.*, 1983). Estimates of a critical day-length needed for flowering to occur in tropical maize range from 11hrs (Craufurd and Wheeler, 2009) to 12.5hrs (Kiniry *et al.*, 1983). Kiniry also suggests that the photoperiod sensitive stage should be a minimum of 4 days for the plant to switch to a reproductive state after the juvenile stage ends. It should be noted that, as shown in Figure 8.4, tropical maize cultivars can also be dependent on temperature during this development stage.

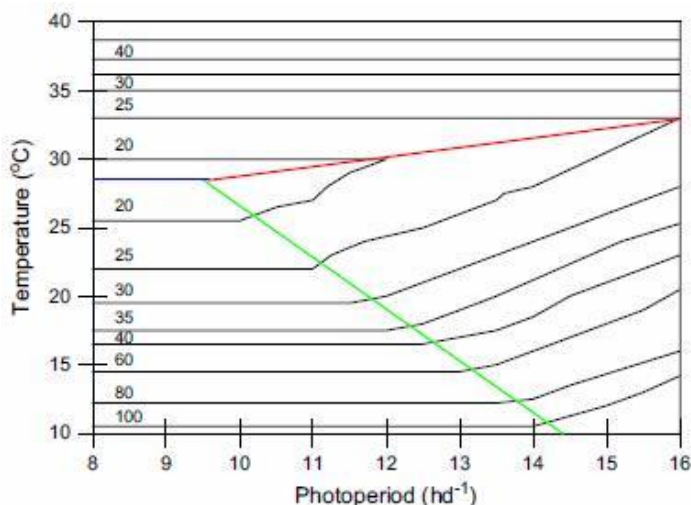


**Figure 8.4.** Relationship between temperature and photoperiod on the duration from sowing to tassel initiation for a lowland tropical maize cultivar, Tuxpeño. The blue line shows the minimum time to tassel initiation at the optimum temperature, the green line shows the critical photoperiod and the red line shows the upper temperature limit of the response to photoperiod. The area between the green and red line therefore shows where the rate of development is determined by photoperiod and temperature. Plot taken from Craufurd and Wheeler, 2009

Ethiopia is situated relatively near the Equator with day lengths consistently between 11.5 hrs and 12.5 hrs, therefore Figure 8.4 shows that daily mean temperatures between 20-25 °C could vary tassel initiation by 2-3 days.

### **8.2.1.3. Tassel Initiation to anthesis**

As shown in Figure 8.3, tassel initiation occurs when the plant is relatively small, thus although all the leaves have been initiated at this point, it still takes time for the stem to elongate, the leaves to develop and for the tassel to emerge from the leaf whorl. Photoperiod has no significant impact on the length of this stage (Ellis *et al.*, 1992). Instead, it is pre-determined by the number of leaves initiated and their expansion rate, with both processes controlled by thermal time. The stage ends when the tassel is fully formed and about to shed pollen (shown at stage VT in Figure 8.3). The female flower on the plant, or silk, is also developing during this time but at a slightly slower rate. Silk elongation starts approximately 10-14 days before it is fully developed (Nielsen, 2010). The point at which the silk is fully emerged and ready to receive pollen is called ‘silking’

### **8.2.1.4. Pollination and the Anthesis to Silking Interval (ASI)**

When the tassel has completely emerged it begins to shed pollen. Pollen shed, or anthesis, occurs during mid morning and one plant may produce pollen for up to 7 days, although the majority of pollen will be released on day 2-3 (Aldrich *et al.*, 1986). Due to in-field variability, a field of maize may take up to 14 days to complete pollen shed (Lauer, 1998). For each individual plant, the silk will finish developing and become receptive to pollen approximately 2-3 days after pollen shed starts. Silks are most receptive at 4-5 days after emergence and remain receptive to pollen for up to 10 days, but to an ever decreasing degree.

The period between pollen shed and pollination is highly susceptible to climatic stress. There are two possible reasons behind this. First, high temperature stress reduces the viability of pollen and so reduces pollen set, resulting in a lower yield. Schoper *et al* (1987) and Hussain *et al* (2006) report that if the temperature rises above 38°C, then pollen viability and silk receptivity is reduced, resulting in poor seed set and suppressed yield (Barnabas *et al.*, 2008). This effect is also reported in Wheeler *et al.* (2000) and Norman *et al.* (1995). It should be noted that this temperature must occur during the mid-morning when pollen is being released for any effect to be seen.

The second effect is on the development of the different flowering stages. As described in Campos *et al.* (2004), “water stress slows ear growth, and consequently silk emergence, more than it does tassel growth or anthesis, resulting in a widening interval between anthesis and silking, or ASI”. This is because water stress during this period will mean that the plant preferentially partitions biomass to the tassel instead of the silk (Vasilas, 2004 and Edmeades and Bolaños, 1998), thus silks take longer to develop and can emerge after pollen shed has finished. This results in increased barrenness and suppressed yields. A long ASI is commonly reported as a symptom of crop death or low yields.

This means that ASI length can be seen as a visual indicator of the underlying processes affecting reproductive success (Edmeades *et al.*, 2000). Bolaños and Edmeades (1996) mathematically linked the length of the ASI to yield as:

$$\text{Yield} = e^{2.45 - 1.16 \times \text{ASI}} \quad 8.2$$

The relationship holds for 6 different tropical maize cultivars, as shown in Figure 8.5. Hussain *et al.* (2006) reports that the ASI is also lengthened for temperatures above 30°C.

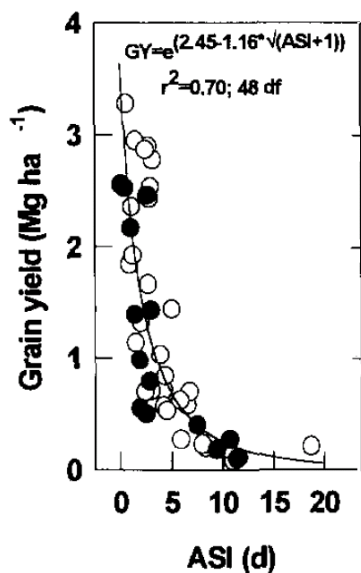


**Figure 8.5.** Grain yield as a function of mean anthesis-silking interval for 50 progeny trials from six tropical maize populations under a range of water regimes at Tlaltizapán, M6xico, 1986-1990. Each data point is the mean for the trial. Plot taken from Bolaños and Edmeades, 1996.

It should be noted that it can be difficult to specify the exact dates for pollen shed and silk emergence because they will vary from plant to plant within a field. The Corn Grower's guidebook (Nielsen, 2007) suggests that "from two weeks before silk emergence, the plant enters the period of grain yield determination most sensitive to drought stress. Nearly continual wilting of the plant due to drought stress at this stage can decrease yield 3-4% per day. During the silking and pollen shed period, severe stress may reduce yield up to 8% per day. During the 2 weeks following silking, severe stress may reduce yield up to 6% per day". This agrees in general with the results presented in Figure 8.5, although it should be noted that the article discusses temperate cultivars, which will probably react slightly differently than tropical maize. It also agrees with the results presented by Thelen (2007) who states that 4 days of drought stress experienced during pollen shed reduces yield by 40-50%. The result is also supported by Shaw (1988) and Rhoads and Bennett (1990). Unfortunately, there is little evidence from field trials to be able to quantitatively relate the exact level of physiological stress in maize to yield loss.

#### **8.2.1.5. Pod filling and pod-filling**

After silking, there is a lag phase of between 3 and 8 days, or approximately  $170^{\circ}\text{Cday}$  in thermal time units (Norman *et al.*, 1995; Jones and Kiniry, 1986) for the process of pollination. As the pollen has entered the female flower by this point, the impact of climate stresses is much less. The final stage of development is grain filling and drying. During this time, biomass is partitioned into the grain of the crop. Although it is sensitive to frost, the period is regarded as much less sensitive to water stress. For example, Brown (2009) reports that maize often benefits from drier conditions during this period. Leaf senescence occurs during the entire period.

#### **8.2.2. HARVEST INDEX**

Harvest index (H.I.) is defined as the economic (grain) yield of a crop expressed as a decimal fraction of total above ground biomass (Donald and Hamblin, 1976). The parameter has been observed to increase linearly over time for a number of crops (Moot *et al.*, 1996; Wheeler *et al.*, 1996; Bindi *et al.*, 1999), therefore:

$$\frac{dHI}{dt} = \text{Constant} \quad 8.3$$

For tropical maize, this rate was found to be stable at  $0.015 \text{ day}^{-1}$  (Muchow, 1990), although it should be noted that unlike temperate maize, the final harvest index of tropical maize “vary widely with environment, management and season” (Hay and Gilbert, 2001).

### 8.2.3. YIELD DEFINITIONS

Finally, it is important to define the word ‘yield’. Interpretations important to crop simulation modelling are described below and are discussed in more detail in Pasuquin and Witt (2007).

**Potential yield:** The maximum yield that can be produced by a crop genotype in a given climate. This yield is solely affected by radiation and temperature and is similar to many simulated yields in crop models.

**Attainable yield:** The yield attained under best farmer practice, thus the crop is limited by radiation, temperature and water and nutrient stress. You would expect to get this at an experimental crop station. If the crop is irrigated and kept supplied with nutrients then this is normally as close as you can realistically get to the potential yield.

**Farmer’s yield:** The yield is limited by radiation, temperature, water, nutrients, management practice, pests and anything else that might affect a crop. It's normally given as an average over a wide area so that all types of farmer practice are included. For example, the amount of wheat harvested in Ghana over 2007 would be a farmer’s yield.

In this thesis, the term ‘Yield Gap’ has been defined as the difference between farmer’s yield and potential yield.

### 8.3 CROP SIMULATION MODELLING

Van Ittersum and Donatelli (2003) describe crop simulation models as an attempt to condense assumptions about biological process interacting with the physical and chemical environment through mathematical equations. Specifically, the models attempt to quantitatively predict how a crop might respond to variations in factors such as climate, soil, management practice and genotype. There are several motivations behind this: one might wish to understand better the underlying mathematical relationships defining the growth and development of a crop, or more relevantly in this case, forecast yield for a given climate and management scenario. In general, crop simulation models can be described as one of two types:

**Empirical models** aim to capture statistically the relationship between yield and some input variables. The most simple of these in our case might be a basic regression between total seasonal rainfall and maize yield in Ethiopia. Empirical models can be designed to have few input parameters and so are easily applied to an African case study (where in general field level agronomic data will not be available). However, it should be noted that these models cannot be extrapolated beyond their calibration region. For example it might be inappropriate for a model calibrated using historical weather observations to be applied in a future climate. As seasonal means are often used as inputs, it is also often difficult for the models to capture the effect of intra-seasonal variability. This is because many poor crop yields are due to stress at specific points in the growing season, thus poor weather in just a few days of an otherwise good year could have a disproportionate effect on yields. Therefore, a model correlating total growing season rainfall and yield would not capture a poor yield caused by water stress during the anthesis-silking interval.

**Process based** or mechanistic crop simulation models are designed to dynamically capture the underlying physical and chemical processes which affect crop yield (Wheeler *et al.*, 2007). As these are underlying processes capturing crop behaviour, process based models can be applied outside the region of calibration, for example in a region with a different

climate or management strategy. However, care must be taken to understand the context in which a model has been applied in order to avoid systematic biases.

Crop simulation models vary greatly in complexity and scale and must be selected carefully depending on the end user's motivation, data availability and study area. As noted by Van Ittersum and Donatelli (2003), a crop model is adequate when it satisfies its objectives. In this case we wish to learn about the relationship between climate and crop yield over a large region with limited amounts of input data. Therefore complex process based crop simulation models such as APSIM (Wang *et al.*, 2002 Keating *et al.*, 2003) or DSSAT CERES-Maize (Jones and Kiniry, 1986) were deemed to require too many input variables to be useful in the project. At the other end of the scale, simple Crop Specific Water Balance models such as the FAO's CROPWAT have been found to behave poorly in The Gambia due to an inability to capture climate stresses on individual development stages (Teo, 2006). Therefore three 'intermediate complexity' crop simulation models have been chosen for further analysis. These generally contain processes relating large scale inputs to yield (e.g. water/yield processes), but exclude those pertaining to management (e.g. nitrogen use).

SARRA-H is a processed based crop simulation model designed to simulate attainable yield in the water limited regions of West Africa (Dingkuhn *et al.*, 2003). It is the updated or 'dressed' (habillé) version of the simple SARRA crop water balance model. SARRA-H includes processes for simple rainfall run-off/infiltration (using an empirical relationship calibrated for the Sahel), transpiration, water stress, carbon partitioning, leaf area index, thermal time based phenology, senescence and harvest index to define yield (Sultan *et al.*, 2005). The model has been applied both at a field scale (Marteau *et al.*, 2011) and for regional analysis (Samba *et al.*, 2001).

AQUACrop is a new model developed by the FAO as a more complex replacement for CROPWAT. This is a 'canopy-level and engineering type of model, mainly focused on simulating the attainable crop biomass and harvestable yield in response to the water

available' (Steduto *et al.*, 2009; Raes *et al.*, 2009; Hsiao *et al.*, 2009) . At the core of the model is the assumption that biomass,  $B$ , is linked to transpiration,  $T$ , by:

$$B = WP \times \frac{T}{ET_o} \quad 8.4$$

where  $WP$  is the 'water productivity' (Biomass per unit of transpired water) and  $ET_o$  is a reference transpiration calculated using the Penman-Monteith approach. The model contains a detailed water balance routine and separates evaporation from transpiration through the percentage of canopy cover (Todorovic *et al.*, 2009). Yield is calculated from biomass using harvest index. Water stress affects canopy growth, stomatal response, canopy senescence and harvest index although again there is no specific heat or water stress on sensitive development stages.

The final intermediate complexity model is the General Large Area Model for annual crops, GLAM, which is discussed further in the Section below (Challinor *et al.*, 2004). GLAM was chosen as the primary model for this work, due to its ability to include specific stresses on sensitive development stages and because it has been proven skill modelling crops in Africa (Teo, 2006).

## **8.4 THE GENERAL LARGE AREA MODEL FOR ANNUAL CROPS**

GLAM is a process based model designed to simulate tropical crop production in regions where there is an observed relationship between climate and crop yield (Challinor *et al.*, 2003). Therefore it is well suited for use in Ethiopia, where there is a documented link between climate and crop yield (World Bank, 2006), but the situation is too complex for simple statistical relationships between rainfall and yield to be effective.

GLAM is a one dimensional model with its spatial scale determined by the spatial scale of its inputs. However GLAM has been designed primarily to study the crop/weather relationship at large scales (> plot level), for example at the scale of a general circulation model or region. Therefore it only explicitly models yield determining processes; processes which are far removed from this level, such as photosynthesis, are parameterised

(Challinor *et al.*, 2004). GLAM also relies on limited input data so that is easily applicable over large areas e.g. it does not require detailed management information such as fertilizer applications. It can be set to model potential yield (though running the model in an ‘irrigated’ mode), attainable yield and farmers yield. As one cannot identify every non-climatic factor which might affect farmer’s yields each year and because we wish to know the average effect of climate on yield rather than model local variability, farmer’s yield is modelled through the use Yield Gap Parameter (YGP) which is calibrated against yield observations.

The relatively simple nature of the processes within GLAM means that it can be adapted to model most annual crops (Osborne, 2004). The original incarnation of the model was GLAMgroundnut, which has been extensively validated in India (Challinor *et al.*, 2004) and the Gambia (Teo, 2006). GLAMWinterwheat and GLAMspringwheat have also been created and tested in China (Li *et al.*, 2010). Finally GLAMSoybean and GLAMSorghum are currently in production. This Section discusses the general equations and processes used in GLAM, before the next Section goes on to present a new parameterisation of the model for maize.

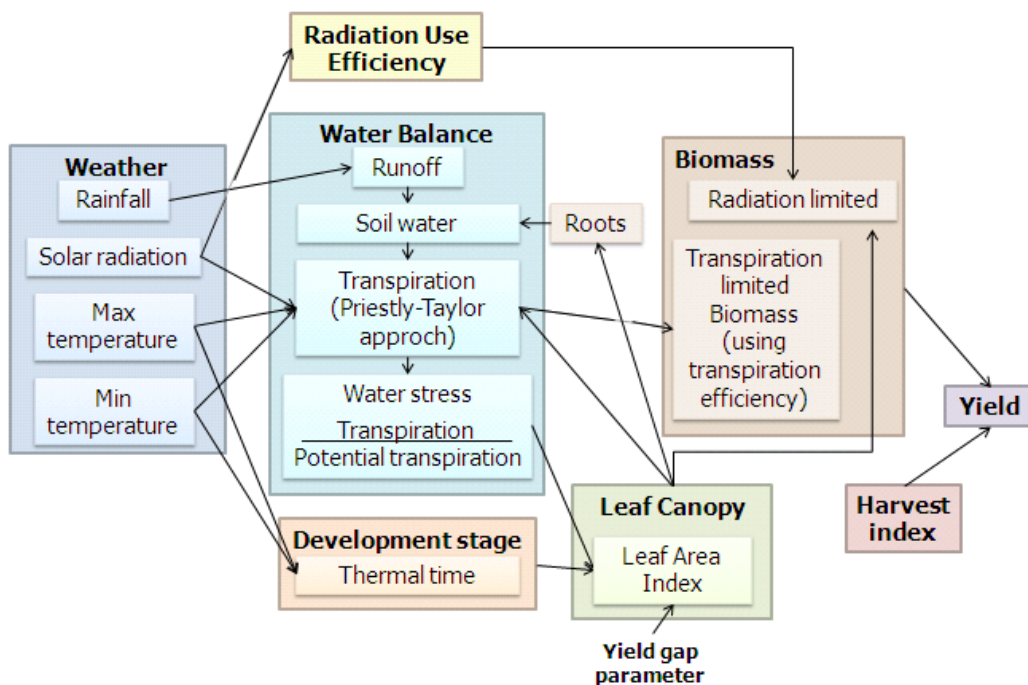


**Figure 8.6. Schematic of the processes contained within the GLAM crop model.**

The broad structure of GLAM can be seen in Figure 8.6 and a full description is given in Challinor *et al.* (2004). The model is one dimensional and runs on daily weather inputs. All equations are new apart from those cited from sources. For a given day,  $k$ , the following processes are run.

#### 8.4.1. INTELLIGENT PLANTING

As observed planting dates are generally provided at a coarse temporal resolution (i.e. month of the year) and in practice will vary from year to year, an intelligent planting routine has been adopted. The simulation starts on the 1<sup>st</sup> of the observed planting month, but the crop is only planted when the soil moisture exceeds a set threshold,  $C_{\text{sow}}$ .

#### 8.4.2. DEVELOPMENT AND LEAF AREA INDEX

Minimum and maximum temperatures are used to calculate the thermal time accumulated on day  $k$  according to Figure 8.1. Specifically, the thermal time elapsed within a specific development stage,  $t_{tt}$  can be expressed as:

$$t_{tt} = \int_{t_i}^{t_k} T_{\text{eff}} - T_b \ dt \quad 8.5$$

where  $t_i$  is the time at the beginning of development stage  $i$ ,  $T_b$  is the base temperature of the crop and  $T_{\text{eff}}$  is the effective temperature of the crop. This effective temperature is dependent on the value of the mean daily temperature  $\bar{T}$  and can be calculated as:

$$T_{\text{eff}} = \begin{cases} T_{\text{eff}} = \bar{T} & T_B \leq \bar{T} \leq T_o \\ T_o - T_o - T_B \left( \frac{\bar{T} - T_o}{T_M - T_o} \right) & T_o \leq \bar{T} \leq T_M \\ T_{\text{eff}} = T_B & \bar{T} < T_B \mid \bar{T} \geq T_M \end{cases} \quad 8.6$$

The length of each development stage is in general defined solely by thermal time accumulation. Leaf Area Index (LAI) can then be calculated according to development stage and is described further in the maize parameterisation in Section 8.5. In general, if

the LAI is increasing during a given development stage, then it can be expressed on day  $k$  as:

$$LAI_k = LAI_{k-1} + \left( \frac{dLAI}{dt} \right) \quad 8.7$$

where

$$\frac{dLAI}{dt} = \left( \frac{dLAI}{dt} \right)_{\max} \times \min \left( \frac{S}{S_{cr}}, 1 \right) \times YGP \quad 8.8$$

In this equation,  $\left( \frac{dLAI}{dt} \right)_{\max}$  is a prescribed maximum rate of leaf area increase and  $S$  is a stress factor which can be expanded as:

$$S = \frac{T_T}{T_{TPot}} \quad 8.9$$

Here  $T_T$  and  $T_{TPot}$  are the transpiration and potential transpiration respectively (described in the water balance section).  $YGP$  is the yield gap parameter, which is a dimensionless number from 0 to 1 which is locally calibrated to take into account any non-climatic effects on yield. If senescence occurs during a development stage, then LAI is represented as:

$$LAI_k = LAI_{k-1} - \left( \frac{dLAI}{dt} \right) \quad 8.10$$

### **Soil**

The soil in GLAM is defined to have a constant drained upper limit, lower limit and saturation limit ( $\theta_{dul}, \theta_{dl}, \theta_{sat}$ ) and has been split into  $N_{SL}$  layers at depths  $z = 1, \dots, z_{\max}$ . Each of these layers has a root length density  $l_v$  and on each day, roots are defined to grow as:

$$\frac{\delta l_v}{\delta LAI} \Big|_{z=0} = Constant \quad 8.11$$

where the extraction front velocity,  $V_{EF}$ , and the root length density at the extraction front,  $l_v \Big|_{z=z_{ef}}$  and are both prescribed constants.

#### 8.4.3. WATER BALANCE AND TRANSPiration

Daily precipitation is used to calculate run-off, which is input into a soil water balance model according to Suleiman (1999). This can then be used to calculate crop evapo-transpiration, which plays a key role in GLAM, as transpiration efficiency is used as a proxy for photosynthesis. Potential evaporation and transpiration are limited only by crop physiology and energy inputs, whilst standard evaporation and transpiration are also limited by water availability. Physiologically limited potential transpiration on day  $k$  can be modelled empirically as:

$$T_{T_{pot}}^p = \begin{cases} T_{T_{max}} \left( 1 - \frac{LAI_{Crit} - LAI_k}{LAI_{Crit}} \right) & LAI_k < LAI_{Crit} \\ T_{T_{max}} & LAI_k \geq LAI_{Crit} \end{cases} \quad 8.12$$

Where  $LAI_{Crit}$  is a prescribed constant. Energy limited evaporation, and transpiration ( $E^e$  and  $T_T^e$ ) were calculated using Priestly Taylor methodology as:

$$E_T^{pot} = E^e + T_T^e = \frac{\alpha \Delta (R_N - G)}{\lambda(\Delta + \gamma)} \quad 8.13$$

where  $R_N$  corresponds to net radiation,  $G$  is the soil heat flux,  $\lambda$  is the latent heat of vaporisation of water,  $\Delta = \frac{\delta e_{sat}}{\delta T}$  (Bolton, 1980) and  $\gamma$  is the ratio of the specific heat of air at constant pressure, to the latent heat of vaporisation of water. The Priestly-Taylor constant,  $\alpha$ , takes into account atmospheric vapour pressure deficit. The Beer-Bougart equation is then used to split this into evaporation and transpiration:

$$\begin{aligned} E^e &= 1 - C_G \cdot E_{\max}^T e^{-\kappa LAI} \\ T_T^e &= E_{\max}^T (1 - e^{-\kappa LAI}) \end{aligned} \quad 8.14$$

Here,  $\kappa$  is the extinction coefficient and  $E_{\max}^T$  is equal to  $E_{pot}^T$  when  $G = 0$ . So overall, the potential transpiration is:

$$T_{pot} = \min(T_{pot}^p, T_T^e) \quad 8.15$$

The water limited transpiration can then be calculated as:

$$\begin{aligned} T_T &= T_{pot} & \text{and } E &= E_{pot} & \text{for } \theta_{pe} \geq E_{pot}^T \\ T_T &= \theta_{pe} \frac{T_T^e}{T_T^e + E^e} & \text{and } E &= \theta_{pe} \frac{E^e}{T_T^e + E^e} & \text{for } \theta_{pe} < E_{pot}^T \end{aligned} \quad 8.16$$

where  $\theta_{pe}$  is the potentially extractable soil water calculated according to Passioura (1983).

#### 8.4.4. BIOMASS AND YIELD

Above ground biomass,  $W$ , is calculated as the minimum of transpiration efficiency and radiation use efficiency limited biomass:

$$W = \min(W_{TE}, W_{RUE}) \quad 8.17$$

where

$$\frac{dW_{TE}}{dt} = T_T \min\left(\frac{E_T}{V}, E_{T_{n,max}}\right) \quad 8.18$$

and

$$\frac{dW_{RUE}}{dt} = \min\left(RUE_{\max}, \frac{RUE}{V}\right) \times PAR \quad 8.19$$

In Equations 8.18 and 8.19,  $E_T$  is the normalised transpiration efficiency in Pa, RUE is the radiation use efficiency,  $E_{T_{n,\max}}$  is the maximum transpiration efficiency in  $\text{g kg}^{-1}$ , and V is the vapour pressure deficit which is modelled from vapour pressure,  $e$  as

$$V = e_{sat} \bar{T} - e \quad 8.20$$

PAR is the photosynthetically active radiation approximated as

$$\text{PAR} = \frac{\text{SRAD} \cdot f}{2} \quad 8.21$$

where  $f$  is the fractional interception of radiation.

In the latter stages of crop development, biomass is partitioned into yield using a constant rate of harvest index, as discussed in Section 8.2.2:

$$\text{Yield}_i = W_i \times \frac{dHI}{dt} \quad 8.22$$

Finally, the plant is harvested according to development stage.

## 8.5 A NEW PARAMETERISATION OF GLAM FOR MAIZE

The routines discussed in the previous Section are generic for any version of GLAM, therefore this Section presents a new parameterisation of GLAM for maize. Unsurprisingly, the main modifications have been within the crop phenology and LAI response, although there have also been parameterisations for water and heat stress. These are described in more detail below, within the framework of the crop's development stages. All numerical parameter values for GLAM<sub>MAIZE</sub> are given in Table 8.1.

### ***STAGE 0: Pre-emergence***

This represents the time from planting to development of the first leaf and is set to be 6 days independent of weather. This seems reasonable for tropical cultivars as emergence is unlikely to be delayed due to low temperatures.

### ***STAGE 1: Vegetative***

This stage commences at emergence and finishes when the crop becomes photo-sensitive. The length of this period is defined using thermal time only. The LAI response of the plant for day  $i$  during this stage is defined using Equations 8.7 and 8.8. Sobrado (1990) reports that drought stress in the vegetative stage reduces LAI and hence yields, supporting this approach.

### ***STAGE 2: Inductive***

The cultivar of maize chosen for this study is a short day variety, therefore a photosensitive period has been included to initiate tasselling. As this stage is short in Ethiopia, no developmental dependence on temperature has been included (discussed more in Section 8.2.1.2) and instead the approach of CERES-maize has been selected (Jones and Hoogenboom, 2007). The inductive development stage is completed when a cumulative factor  $PRATE$  reaches 1. This is dependent on photoperiod,  $PHOT$  as:

$$PRATE = \frac{1}{4 + PSEN \max(0, PHOT - CRITPP)} \quad 8.23$$

where  $CRITPP$  is the critical photoperiod for the effect to occur and  $PSEN$  is the plant's sensitivity to photoperiod. The relationship is designed so that even if the photoperiod is adequate to initiate flowering, the stage has a minimum length of 4 days (Kiniry *et al.*, 1983). LAI during this period is calculated in the same way as for the vegetative stage.

### ***STAGE 3: Tasselling Initiation – Silking***

Once tassel initiation has occurred, the leaves and tassel expand and grow, the speed of which can be measured using thermal time. This process is not dependent on photoperiod (Ellis *et al.*, 1992 and Kiniry *et al.*, 1983). However, as discussed in Section 8.2.1.4, it is

difficult to exactly define the dates of tassel emergence and pollen shed. A numerical relationship has been found between the total number of leaves and silking date, which has been applied to crop simulation modelling in CERES maize to calculate the length of this period. Here, the total leaf number can be described as a function of the total accumulated thermal time between emergence and tassel initiation,  $SUMDTT$ , and the thermal time for a leaf tip to emerge,  $PHINT$ :

$$TLNO = \frac{SUMDTT}{0.5PHINT + 5} \quad 8.24$$

The length of between tassel initiation and silking,  $P3$ , can then be expressed as:

$$P3 = PHINT \cdot TLNO + 0.5 - SUMDTT \quad 8.25$$

The CERES maize approach is described in more detail in Jones and Hoogenboom, 2007. It should be noted that this is the modelled time of silking for an unstressed plant.

#### ***STAGE 3B: Tassel emergence and pollen shed***

Although models of similar complexity to GLAM do not generally include specific climate stresses on flowering, the potential importance of the effect in tropical countries means that some effort must be taken to develop one for modelling Ethiopian maize. This parameterisation is also an issue for CERES maize, as discussed in detail in Edmeades and Bolaños (1998). It is particularly difficult to do this in GLAM as complexity far from yield determining processes have been removed. Therefore, a highly empirical approach is postulated in order to agree with the evidence reported in Section 8.2.1.4.

The CERES maize approach described in the previous Section gives the thermal time at which 50% of unstressed maize plants will have silked. As this is in general 3 days after tassel emergence, one might expect a significant amount of plants to have begun pollen shed 5 days before this date. This is supported by Worku *et al.* (2001) who states that an unstressed ASI length is 1-3 days for a range of Ethiopian cultivars. Preliminary runs for Ethiopia maize suggest that 5 days is approximately 10% of the length between tassel

initiation and silking described in Equation 8.25. This also agrees with the thermal time value of  $\sim 120^{\circ}\text{C}$  days postulated in Edmeades and Bolaños (1998) and the values stated in Birch *et al.* (2003). Therefore, maize has been defined to be sensitive to climate stress on flowering once 90% of P3 has elapsed. The potential stress period ends at the end of the P3 period. Although the impact of water stress is clearly to lengthen the length of the ASI, it can be envisioned that this would occur for individual plants within the flowering period defined above, rather than lengthening the entire period itself. It should be taken into account however, that this isn't an ideal situation and would be corrected if thermal time values between tassel initiation and pollen shed became available.

During the stress period, water stress is defined as when :

$$\frac{\text{Trans}}{P\text{Trans}} < \text{SWThreshold} \quad 8.26$$

where  $\text{SWThreshold}$  corresponds to the proportion of potential transpiration that transpiration can be reduced to before LAI is affected. At the end of the period of water stress, the rate of change of harvest index is then reduced by:

$$\frac{dHI}{dt} = \frac{dHI}{dt}_{\max} \frac{e^{2.45 - 1.16 * Dstress}}{6.333} \quad 8.27$$

where,  $Dstress$  corresponds to the number of days that the crop was stressed for. This follows the approach detailed in Figure 8.5 (Bolaños and Edmeades, 1996).

Independently a heat stress routine has also been incorporated to model the impact of reduced pollen set from high temperatures. This acts during the same time period as the ASI stress routine above. The routine is a simplified version (for computational efficiency) of the one described in Challinor *et al.*, 2005b. The rate of change of harvest index is reduced by the mean heat stress reduction factor,  $HS$ , during the days of flowering ( $j=1..n$ ):

$$\frac{dHI}{dt} = \frac{dHI}{dt}_{\max} \sum_{j=1}^n HS_j \quad 8.28$$

where the heat stress reduction factor is dependent on the temperature known to affect yields and the temperature known to reduce yields to zero.

$$HS = \begin{cases} 1 & \bar{T}_j < T_{SCrit} \\ 1 - \left( \frac{\bar{T}_j - T_{SCrit}}{T_{SZero} - T_{SCrit}} \right) & T_{SCrit} \geq \bar{T}_j < T_{SZero} \\ 0 & \bar{T}_j \geq T_{SZero} \end{cases} \quad 8.29$$

The inclusion of both types of climatic stress on flowering means that if there is an extended drought and a short period of high temperature, grain set (for which harvest index is a proxy for) and hence yield is drastically reduced. This agrees with the observations reported in Section 8.2.1.4.

#### ***STAGE 4: Pre-pod filling lag***

Pollination is assumed to occur during this stage, the length of which is defined by thermal time and as discussed in Section 8.2.1.5, appears to take a cultivar independent 170 °C days to complete. As described in Osaki (1995), leaf senescence starts rapidly after flowering, therefore LAI is reduced according to Equation 8.10.

#### ***STAGE 5: Pod-filling***

This is the grain development stage, thus yield is related to biomass as described in equations 8.17 and 8.22, where the length of the stage is determined by thermal time accumulation. The last 5% of the thermal time in this development stage is designated as a grain drying period, where yield/biomass does not increase.

## **8.6 CULTIVAR AND PARAMETER VALUES**

A wide variety of maize cultivars are grown in Ethiopia in order to match the diverse climatic conditions found in the country (Eiar, 2004). However, few have been studied with the aim of parameterisation in crop simulation models and there is little literature on East African maize cultivars. Adequate information was only found about one suitable cultivar, MH16. As described in Collis and Corbett (1998), “MH16 is a hybrid from

Malawi and is bred from SR52, which despite dating from the 1950s is still one of the better East African varieties. This is a fairly long-season variety, shorter stature, and capable of good yields". The cultivar choice is not ideal for use in Ethiopia as MH16 originated in Malawi and is generally grown in the lowlands of East Africa (Heisey and Smale, 1995; Thornton *et al.*, 1995), but was the only reasonable choice for this thesis.

The numerical parameters specific to GLAM<sub>MAIZE</sub> are listed in Table 8.1, all others can be found in Challinor *et al.*, 2004.

<b><i>Cardinal temperature stages</i></b>			
Base temperature	$T_B$	8°C	Goldsworthy and Fisher, 1984
Optimum temperature	$T_O$	30°C	
Maximum temperature	$T_M$	40°C	
<b><i>Development</i></b>			
Number of days from planting to emergence	IEMDAY	6	
Thermal time for Stage 1 (emergence – tassel initiation)	TLIMJUV	245°Cday	Collis and Corbett, 1998
Critical photoperiod for Stage 2	CRITPP	12.5hrs	
Photoperiod sensitivity for Stage 2	PPSEN	0.28	
Thermal time for a leaf to emerge (Stage 3)	PHINT	75°Cday	Collis and Corbett, 1998
Thermal time for Stage 4 (pre-pod filling)	TTPFL	170°Cday	
Thermal time for Stage 5 (Grain filling)	TTFGFL	843°Cday	
<b><i>Heat stress</i></b>			
Temperature at which pollen set starts to be affected	$T_{SCrit}$	37°C	Crafts-Brandner and Salvucci, 2002
Temperature at which pollen set is zero	$T_{SZero}$	45°C	

<b>Radiation use efficiency</b>			
Radiation use efficiency	RUE	2.3g/MJ (1.48-3.17)	Andrade <i>et al.</i> , 1993; Bolaños and Edmeades, 1993; Chapman and Edmeades, 1996; Birch <i>et al.</i> , 1999
Maximum radiation use efficiency	RUE_MAX	3 g/MJ	
<b>Transpiration</b>			
Maximum transpiration efficiency	$E_{T_{n,max}}$	5.6 g kg <sup>-1</sup>	Banziger and Edmeades, 1996; Ogola <i>et al.</i> , 2002; Zhong <i>et al.</i> , 2005; Suyker and Verma, 2009
Normalised transpiration efficiency	$E_T$	8 Pa	Walker, 1986; Ogola <i>et al.</i> , 2002
Maximum possible physiologically limited transpiration rate	$T_{T_{max}}$	0.63 cm/day	Bergamaschi <i>et al.</i> , 2001
<b>Water Balance</b>			
Extraction front velocity	$V_{EF}$	1.6cm/day	Ogindo and Walker, 2003
Root length density at the extraction front	$I_v \ z = Z_{eff}$	0.38cm <sup>-2</sup>	Qin <i>et al.</i> , 2006
Critical LAI (above which transpiration is not phonologically limited)	$LAI_{Crit}$	3	Smith <i>et al.</i> , 2004
Maximum rate of LAI increase	$\frac{dLAI}{dt}$	0.025	Birch <i>et al.</i> , 1999; Birch <i>et al.</i> , 2003
<b>Harvest Index</b>			
Maximum rate of change of harvest index with time	$\frac{dHI}{dt}_{max}$	0.011day <sup>-1</sup>	Birch <i>et al.</i> , 1999 (value selected from longest maturing tropical maize)
Maximum value of Harvest Index	$HI_{MAX}$	0.4	Birch <i>et al.</i> , 1999; Hay and Gilbert, 2001; Tittonell <i>et al.</i> , 2005

Table 8.1. Maize specific parameters for the GLAM crop model.

## 8.7 CONCLUSION TO CHAPTER EIGHT

The aim of Part 3 of this thesis is to link the satellite rainfall estimates discussed in earlier chapters to a crop simulation model in order to see how the uncertainty in weather inputs might be reflected in Ethiopian modelled maize yields. This chapter presented a study of the phenology and physiology of maize and a literature review of current crop simulation models, focusing in particular on the General Large Area Model for annual crops. The chapter then presented new research to parameterise GLAM for maize. This included a new routine to model specific water stress during the Anthesis-Silking Interval, a new phenology and a development response to photoperiod. Finally, GLAM<sub>MAIZE</sub> was then parameterised for an East African maize cultivar, MH16. It should be noted that there was very little tropical maize calibration data available to independently evaluate the model (i.e. a long time-series of weather and maize yields), thus future research will include a full evaluation for a less data-sparse region of the tropics. The lack of yield data also meant that it was not possible to evaluate the Yield Gap Parameter for Ethiopia, which traditionally requires at least 10 years of crop yield observations. The next chapter links GLAM<sub>MAIZE</sub> to the ensemble of rainfall estimates and evaluates both its sensitivity to climate and its regional response against the limited yield-dataset available.

# **CHAPTER NINE**

# **APPLICATION OF SATELLITE RAINFALL ENSEMBLES TO CROP YIELD MONITORING**

Until this point, this thesis has concentrated on creating the weather and crop model components needed to monitor observed maize yield in Ethiopia. This chapter now presents the results of running GLAM<sub>MAIZE</sub> using observed weather estimates for Ethiopia, which include both the TAMSAT rainfall ensembles and ERA<sub>\_INTERIM</sub> modelled rainfall. All aspects of this experiment are summarised in Section 9.1.

Section 9.2 then evaluates GLAM<sub>MAIZE</sub>'s sensitivity to different weather inputs in order to make sure that it is internally consistent and outputting realistic results. Section 9.3 then compares observed and modelled season lengths. As this is dependent mostly on temperature and ERA<sub>\_INTERIM</sub> temperatures were used throughout, it is relatively independent of which type of weather input was used.

Section 9.4 compares the results of running GLAM<sub>MAIZE</sub> with ERA<sub>\_INTERIM</sub> or using the TAMSAT ensemble mean, in order to see if the significant differences in rainfall inputs translate into differences in yield. The full ensemble of crop yields results from the TAMSAT ensembles is then analysed in Section 9.5 and Section 9.6, before being compared against observed yields in Section 9.7. The Chapter is concluded in Section 9.8.

## 9.1 EXPERIMENT SUMMARY

**Time period:** 1999-2005, chosen to match available yield data.

This is discussed more in Section 2.5.2.1.

**Season and crop:** Long season maize grown during the Meher (summer) season.

This crop was chosen because regions which plant long season maize are more likely to only have one maize crop a year, making observed yield data easier to interpret. The spring Belg season was excluded due to a lack of rainfall data for January and February, as discussed in Section 5.4.1. A long season East African maize cultivar, MH16, was selected for the GLAM<sub>MAIZE</sub> crop model, as it has previously been used in crop modelling studies in Ethiopia (Collis and Corbett, 1998). MH16 is described in full in Table 8.1.

**Yield data:** This was available at a regional and national level from 1997-2005. It is discussed in detail in Section 2.5.

**Planting dates and area planted:** Taken from the MoARD Livelihoods Integration Unit (LIU) "Livelihoods of Rural Ethiopia" database (MacAskill, 2006) at a resolution of 0.25°.

Meher maize planting dates can be seen in Figure 2.14. To ensure that only long season maize was modelled, any location with a planting date before March or after July was excluded from the study.

**Soil type:** This was obtained from the ISRIC-WISE global dataset of derived soil properties (Batjes, 2005) at a spatial scale of 1/12 degrees.

**Daily minimum temperature, maximum temperature and solar radiation data:** This was obtained from the corrected ERA-INTERIM model dataset described in Section 3.2.3. It is available at a spatial scale of 0.25°.

**Modelled rainfall data:** This was also taken from the ERA-INTERIM modelled dataset. It has been included in this study as a comparison for the satellite rainfall ensembles. From this point onwards, the system run with the ensembles is called GLAM\_ENSEMBLE and the system run with ERA-INTERIM has been named GLAM\_ERA.

**Satellite rainfall ensembles:** These are the focus of Chapters 4-7.

Sequential simulation was used to produce 200 ensemble members of TAMSAT satellite rainfall estimates from March-December at a resolution of  $0.125^\circ$ .

### ***The crop model***

The crop model selected for use in this study was the General Large Area Model for annual crops. This was selected over more complex models as it is specifically designed for a regional analysis, thus it requires only simple management data and parameterises any processes that are not directly related to yield. A simpler statistical analysis of the relationship between rainfall and crop yield was attempted for the four main maize growing regions in Ethiopia using the dense monthly rainfall dataset used to create Figure 3.1. This analysis is shown below in Figure 9.1. The results show that there is some relationship between rainfall and maize yield, especially in 2003-2005, however there is no clearly defined relationship. There is also some evidence to suggest that the some yield data is still shifted incorrectly by a year – for example in Oromiya increases/decreases in crop yield precede those of rainfall. Therefore, due to this and due to observed data availability GLAM was selected over more simple models. Adding weight to this argument is the work of Teo (2006) who showed that a simple water balance model (CROPWAT) underestimated interannual variability in a relatively homogenous case study of water limited groundnut in the Gambia.

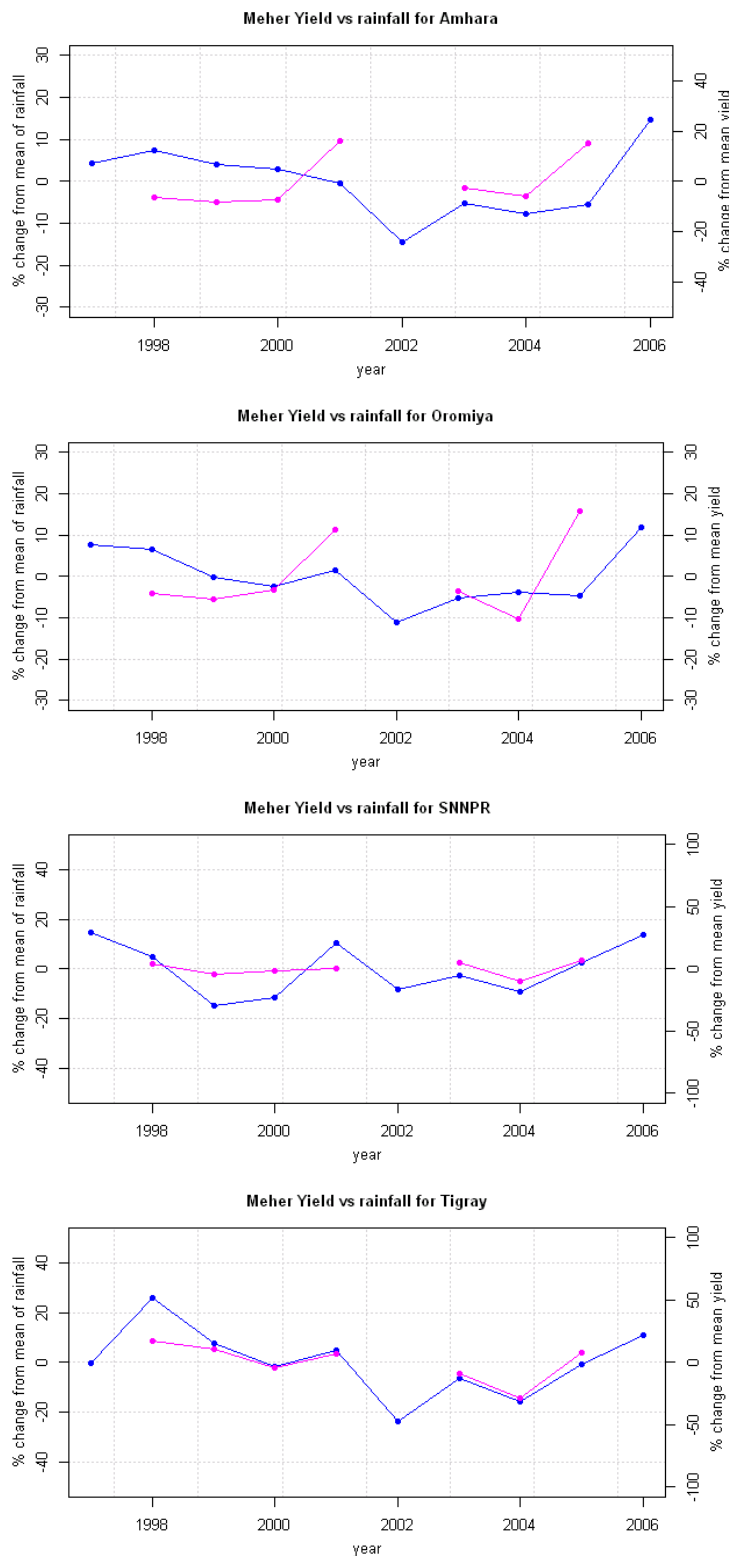


**Figure 9.1.** The percentage change from the annual rainfall mean (derived from gauges), plotted with the percentage change from the annual mean observed yield from the CSA.

### **Spatial scale**

As discussed in detail in Challinor *et al.* (2003), GLAM should be run at a spatial scale with a proven relationship between climate and crop yield, in order so that there is a ‘physical basis for productivity’. As shown above, there is some evidence for running GLAM at a regional scale. However Ethiopia’s climate and topography is so variable that a smaller spatial scale of  $0.25^\circ$  was selected in order to see if that improved the results. This was the most computationally simple option, as it is the grid size that agrees best with all of the input datasets. It is also the agreed spatial resolution for a larger crop model intercomparison study over Ethiopia, of which these results will form part (De Wit *et al.*, 2012). The time-limitations attached to this work meant that only one scale could be chosen, however a regional analysis is planned in future research. Therefore the model was run at a scale of  $0.25^\circ$  for 518 pixels located in 8 regions, as depicted in Figure 9.2.

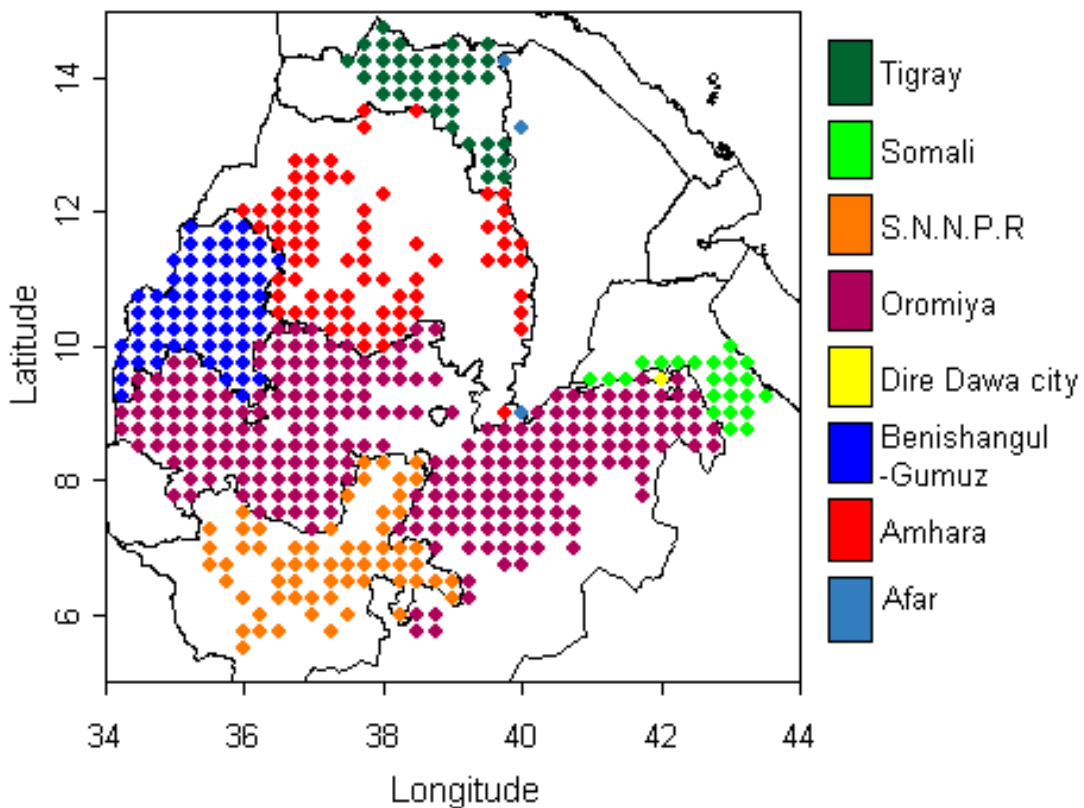


**Figure 9.2. The 518 pixels selected for analysis at  $0.25^\circ$  resolution.**

### **The Yield Gap Parameter**

Due to a lack of historical yield data needed to calibrate the Yield Gap Parameter, GLAM<sub>MAIZE</sub> was set to model attainable yield for all results presented in this Chapter, (i.e. YGP was set to 1). This is not ideal considering the overarching theme of this thesis is to create a set of tools for potential operational use in Africa, where farmers' yields are far from attainable ones. However, the Ethiopian authorities internally have access to a lot more observed data for calibration, therefore it is still feasible for an operational system to be able forecast farmers' yields.

## **9.2 ASSESSMENT OF INTERNAL CONSISTENCY & SENSITIVITIES**

As GLAM<sub>MAIZE</sub> is a new parameterisation, it is first important to check to test its sensitivities to climate in order to check it is internally consistent and exhibiting realistic behaviour. In order to test this, the model was run with a subset of 9 seasons representing different climates which might be experienced by the crop in Ethiopia. These seasons were selected independently of location, because the aim of this part of model assessment is simply to study GLAM<sub>MAIZE</sub>'s sensitivity to different climatic inputs (GLAM<sub>ERA</sub> was also used for simplicity). The envelope of potential climates experienced according to ERA-INTERIM can be seen in Figure 9.3, where the red points correspond to the runs selected for the sensitivity analysis.

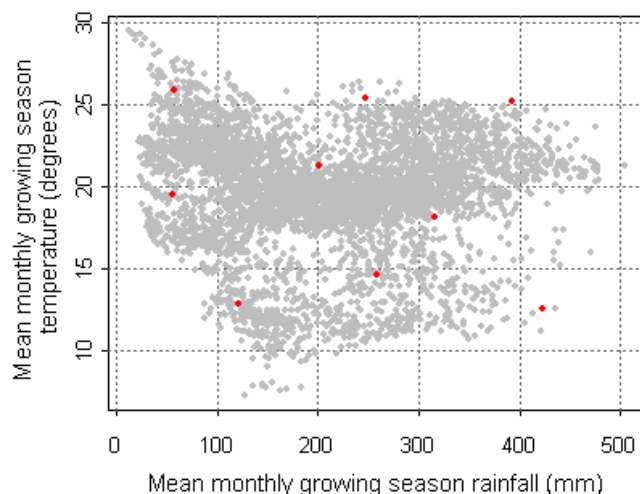


**Figure 9.3. Range of climates experienced by the Ethiopian maize crop from 1997-2005. Each point corresponds to one location and year. Nine points, marked in red were randomly selected from the dataset to use in the GLAM<sub>MAIZE</sub> sensitivity study.**

### 9.2.1. SEASONAL TIME-SERIES

Seasonal time-series of different model parameters have been plotted in Figure 9.4 in order to determine if the predicted values were realistic and exhibiting the correct sensitivities to climate. As the dominant climate variable affecting crops is temperature, the plots have been coloured with the mean monthly growing season temperature shown in Figure 9.3.

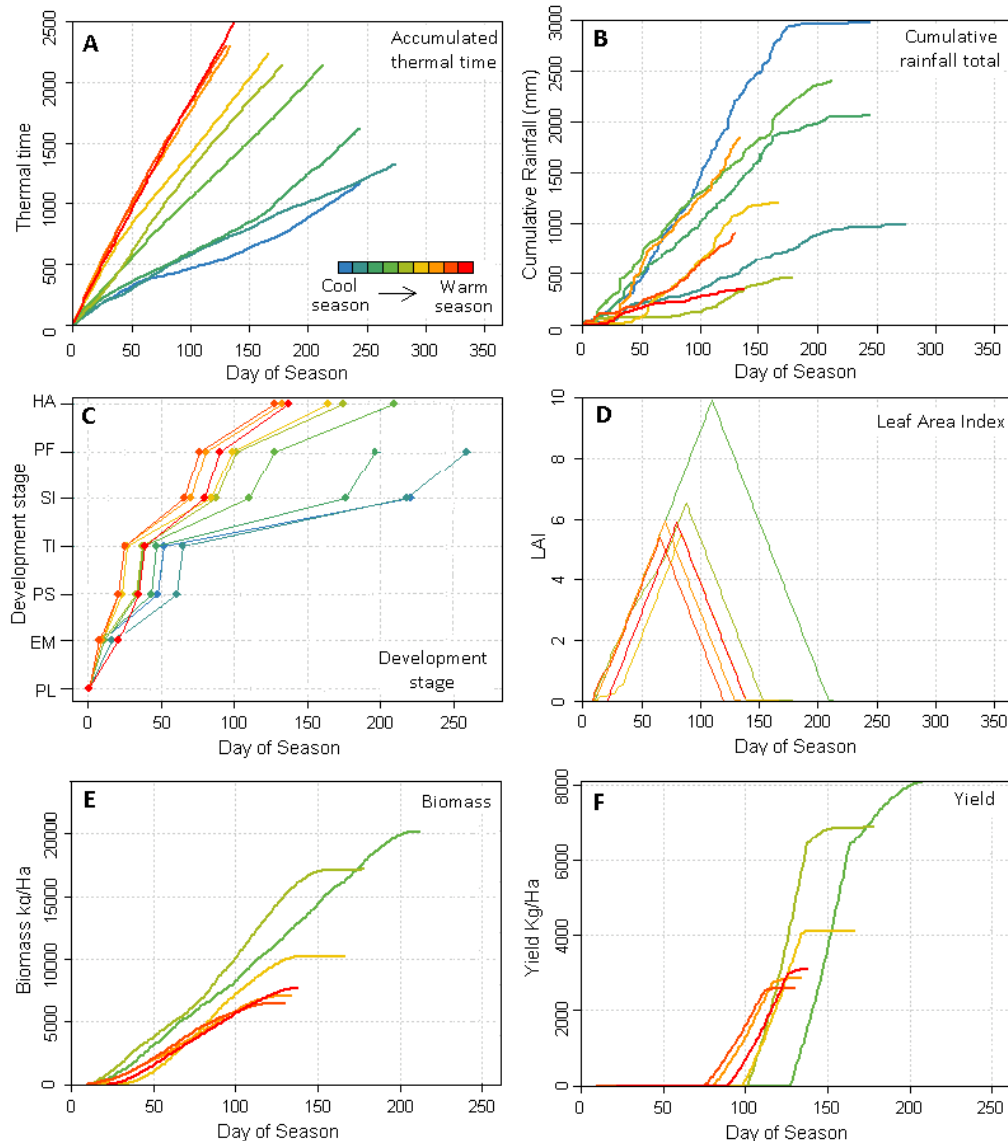


**Figure 9.4.** Time-series throughout the growing season of different modelled parameters where the colours in each plot correspond to the mean monthly temperature over the season.

The development stage plot's y-axis corresponds to the following stages:

**PL** = Start of Season, **EM** = Emergence, **PS** = Start of the Photo-sensitive stage, **TI** = Tassel Initiation, **SI** = Silking, **PF** = Start of Pod filling, **HA** = Harvest .

Sub-plot A shows the accumulated thermal time for the different seasons. Recorded temperatures rarely, if ever, were higher than the optimum temperature for development, so as expected, higher temperatures resulted in a faster developmental rate and a shorter season. Sub-plot B simply shows the recorded cumulative rainfall in each season so that the reader can determine which of the seasons was wet or dry. Sub-plot C shows development stage for the nine selected seasons. Again, as expected, the plots show that a higher temperature results in a faster progression through development stages. Excessively low temperatures also show a realistic relationship with development, as the three coolest seasons do not develop quickly enough to reach harvest (and so were excluded from the other diagnostic plots). Modelled season lengths appear to be reasonable compared to observations and are discussed in detail in Section 9.3 (EIAR, 2009). In addition, sub-plot C shows that there is very little effect of photoperiod on development. This is expected in the tropics for the simple photoperiod method employed within GLAM<sub>MAIZE</sub>. It should be noted that because the model uses intelligent planting (where planting is determined by soil moisture rather than calendar date), the first development stage in sub-plot C includes the pre-planting stage plus 6 calendar days from planting to emergence.

Leaf Area Index is depicted in sub-plot D. Although the shape of the distribution has been constrained to be more simplistic than the observed evolution of LAI, the maximum values of the parameter match observed maximums well. For example, Birch *et al.* (1999) measured LAI maxima of between 4-7 for a range of cultivars. The modelled LAI does appear to be too high in the coolest seasons in sub-plot D, but this might be explained by an inaccurate cultivar choice (discussed in Section 9.3). A reduction in LAI due to water stress can also be seen in the sub-plot; two seasons subject to water stress have been studied in more detail in Figure 9.5, which shows that the water stress is caused by a lack of rainfall and relatively high temperatures (as parameterised in the transpiration routines). Finally, biomass and yield are depicted in sub-plots E and F. These show a realistic values and progressions. In particular, the EIAR report on Maize Recommendations for Ethiopia (EIAR, 2009) notes research station yields of 5-12kg/Ha from field trials of 24 Ethiopian maize cultivars, which fits extremely well with the modelled range.

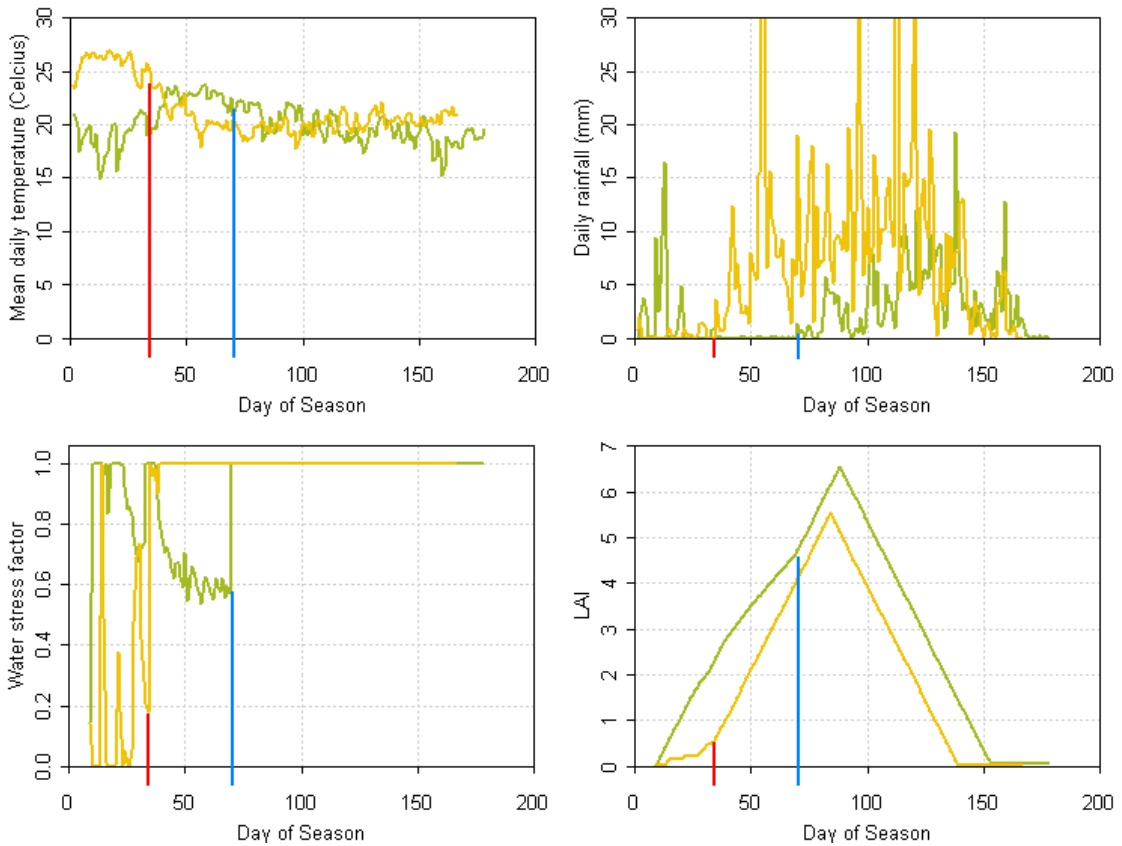


**Figure 9.5.** Two selected seasons which suffer from reduced LAI due to water stress. The sub-plots correspond to mean daily temperature, daily rainfall amount, water stress factor (transpiration/potential transpiration) and LAI. The red line in each sub-plot corresponds to the end of the stress period of the yellow season, and the blue line corresponds to the end of the stress period for the green season.

### 9.2.2. RELATIONSHIP BETWEEN CLIMATE AND YIELD

Another test of GLAM<sub>MAIZE</sub>'s sensitivity to climate is to examine directly the relationship between weather parameters and yield. The relationship between rainfall and yield can be seen in Figure 9.6. This plot includes four sub-plots, the first of which (sub-plot A) compares the total growing season rainfall with yield and the others (sub-plots B-D) look in more detail at specific development stages. The most striking feature of sub-plot A is the lack of correlation between total seasonal rainfall and yield, instead the plot is dominated by the response of the crop to temperature. This is expected in GLAM<sub>MAIZE</sub> because temperature dictates development stage and so the length of the growing season, whilst rainfall can only indirectly affect transpiration and LAI. The direct response of yield to temperature is depicted in Figure 9.7.

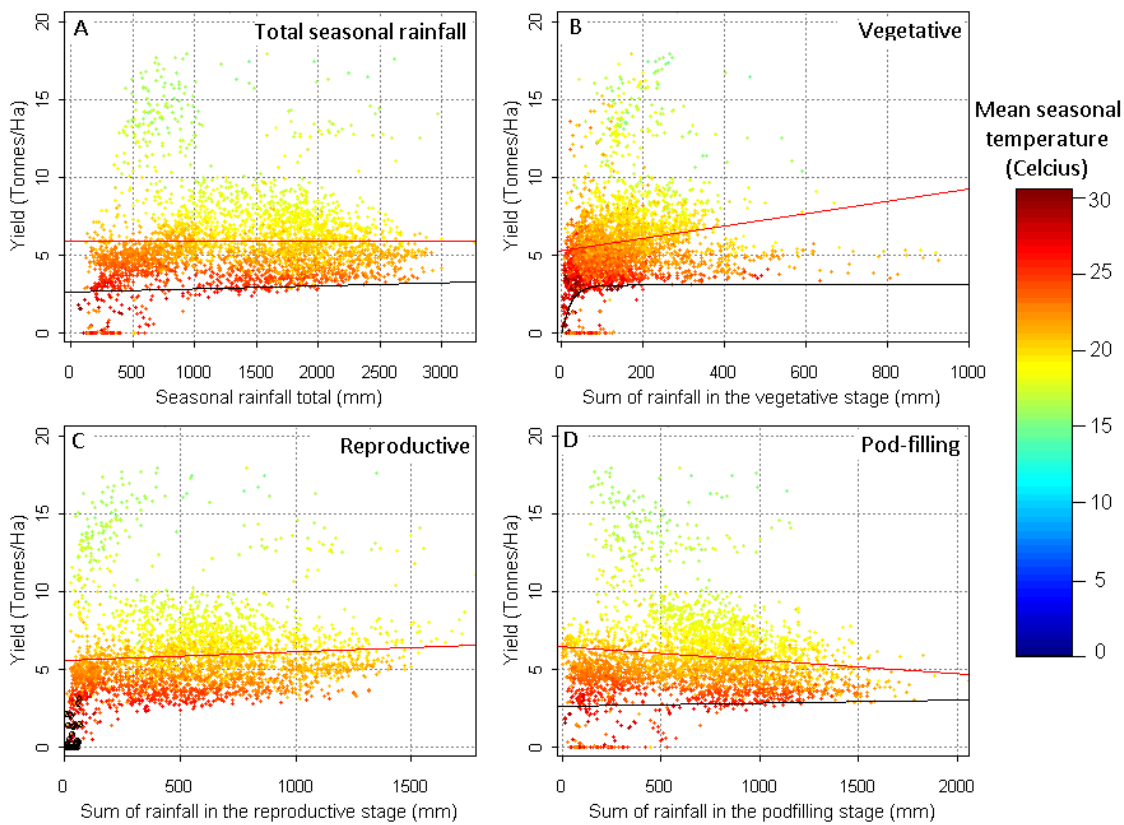


**Figure 9.6. Response of yield to rainfall in GLAM<sub>MAIZE</sub>.** Only pixels which reach harvest have been included and the plots are coloured according to mean growing season temperature. Linear relationships between rainfall and yield were calculated for each plot and are shown as red lines. The black lines show the relationship between rainfall and yield for temperatures above 25 °C. The black circles in plot C show the pixels which were subject to ASI stress. Plot A compares yield against total seasonal rainfall. Plot B compares yield against the total rainfall between planting and tassel initiation. Plot C compares yield against the total rainfall which fell between tassel initiation and silking. Finally, Plot D compares yield against the total rainfall which fell after silking.

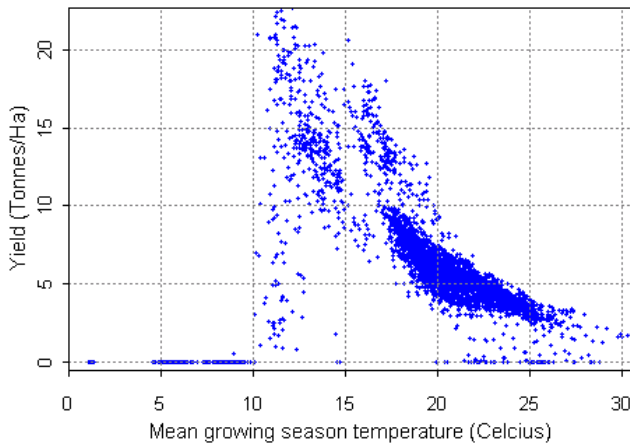


**Figure 9.7. Mean growing season temperature vs final yield.** In these GLAM<sub>MAIZE</sub> runs, the base temperature for development was 10°C and the optimum temperature for development was 34°C.

A subtly different picture can be seen in Figure 9.6, sub-plots B, C and D. These show that although temperature still dominates the yield determining processes within GLAM<sub>MAIZE</sub>, rainfall is having more of an impact than first appeared. In particular there is a positive relationship between yield and rainfall before silking, followed by a negative relationship after silking. This is realistic when compared to observations (Brown, 2009) and makes sense when one considers that rainfall primarily affects yield within GLAM<sub>MAIZE</sub> through influencing Leaf Area Index. As described in Equations 8.8 and 8.9, LAI increases at a constant rate for unstressed maize, but that rate can be reduced if the plant's transpiration falls below a fraction of its potential transpiration. This means that the relationship between rainfall and yield (for a constant temperature) in sub-plot B can be modelled as

$$yield = a \left[ 1 - e^{\left( \frac{Rain}{b} \right)} \right] \quad 9.1$$

where the parameters  $a$  and  $b$  were fitted using a least squares approach. Therefore, yield is only dependent on rainfall if there is not sufficient water for transpiration. In reality, a slightly different relationship might be seen because GLAM<sub>MAIZE</sub> does not consider soil water-logging or flooding. The situation is slightly complicated in sub-plot C because the reproductive development stage contains the anthesis-silking interval. This is highly sensitive to water stress as discussed in Section 8.2.1.4 and Section 9.5. Water stressed pixels are circled in black in sub-plot C. After silking in sub-plot D, LAI is set to decrease at a constant rate which is not dependent on transpiration. Therefore within a given temperature range, there is very little effect of rainfall on yield.

### **9.3 COMPARING MODELLED AND OBSERVED SEASON LENGTH**

Because simulated crop development is dependent on temperature and to a limited extent, photoperiod and so is relatively insensitive to rainfall, the observed growing season length can be compared against observations independently of whether GLAM\_ENSEMBLE or GLAM\_ERA was used as an input. Observations of season length were obtained from MoARD Livelihoods Integration Unit (LIU) "Livelihoods of Rural Ethiopia" database

(MacAskill, 2006), which has a high spatial resolution ( $0.125^\circ$ ) but a monthly temporal resolution. A comparison between modelled and observed season length is shown in Figure 9.8. Here, the left hand plots show observed season length spatially (top) and against elevation (bottom) at a monthly resolution. The centre set of plots show the modelled season lengths and the right hand column shows the anomaly (observed – modelled). In some locations, the temperature was too cool for the model to complete a season, therefore these pixels are shown as solid circles in the modelled spatial plot (pixels that reached harvest are outlined in black) and are excluded from the comparison of modelled season length with elevation. The pixels that did not reach harvest are excluded completely from the anomaly plots.

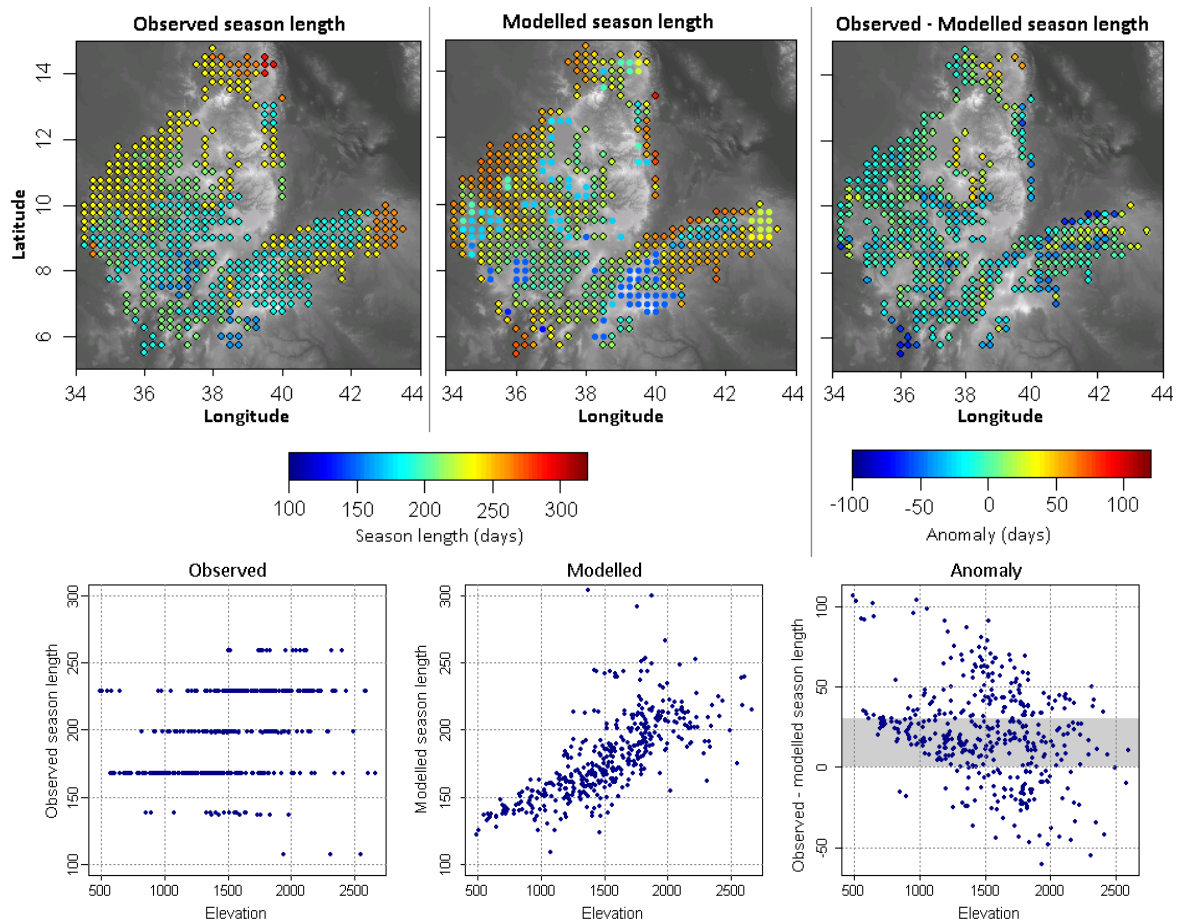


**Figure 9.8. Observed and modelled season lengths.** The left hand plots show observed season length spatially (top) and against observations (bottom) at a monthly resolution. The centre set of plots show the modelled season lengths and the right hand plots show the anomaly (observed – modelled). As the observations are at a monthly resolution, the anomaly plot with elevation has been shaded grey in areas where modelled season lengths fall within a month of observed in order to indicate where the fit is reasonable.

Because the observations are at a monthly resolution, it is difficult to draw detailed conclusions from these plots. The model appears to be capturing a realistic season length in most locations, but the plots clearly show some differences between observed and modelled season lengths at high and low elevations. The main conclusion that can be drawn from the plots is that there is a much stronger dependence on elevation than is seen in observations. The effect on yields of this feature is discussed in Section 9.5 and in the conclusion in Section 11.1.4.

One reason behind the differing results might be due to cultivar choice. In our modelled experiments, we have somewhat simplistically used one cultivar over the whole country. In reality, there are many tens of cultivars available and farmers are adept at choosing the correct cultivar for their location and conditions. Therefore, farmers will tend to choose a cultivar with the correct thermal time response to just fill the entire rainy season; most Ethiopian cultivars are chosen to make the season is 100-160 days in length (EIAR, 2004). There is also some discussion in literature about variations in other crop simulation parameters at higher elevations (e.g. optimum temperature for development), which might suggest that a less simplistic approach is needed that has been taken in this thesis (Edmeades and Bolaños, 1998). This slightly unrealistic response from just using one maize cultivar also explains the somewhat unrealistic values of LAI for cooler climates/higher elevations – in reality, the cultivar would be considered inappropriate.

There are perhaps two solutions to this issue. Ideally, the solution would be to select several maize cultivars and assign one to each location. This would be difficult to do in practice due to the scarcity of crop model coefficients for African maize cultivars, but might be possible if one worked in conjunction with an organisation such as the Ethiopian Institute for Agricultural Research. The second option would be to artificially change some crop parameter such as the amount of thermal time needed for different development stage, or limit LAI so that it does not rise above realistic levels.

## 9.4 COMPARING ERA-INTERIM AND THE TAMSAT ENSEMBLES

One of the main aims of this thesis is to investigate what effect the uncertainty on weather inputs might have on simulated crop yield estimates, therefore the main focus of the second half of this chapter is on the GLAM\_ENSEMBLE results. However, crop modelling studies are beginning to use rainfall outputs from numerical weather models, especially within climate change studies (Challinor *et al.*, 2005a; De Wit *et al.*, 2010). Consequently, it is interesting to compare the results of GLAM\_ERA with the mean of those from the GLAM\_ENSEMBLE. The total growing season rainfall is first compared in Figure 9.9.

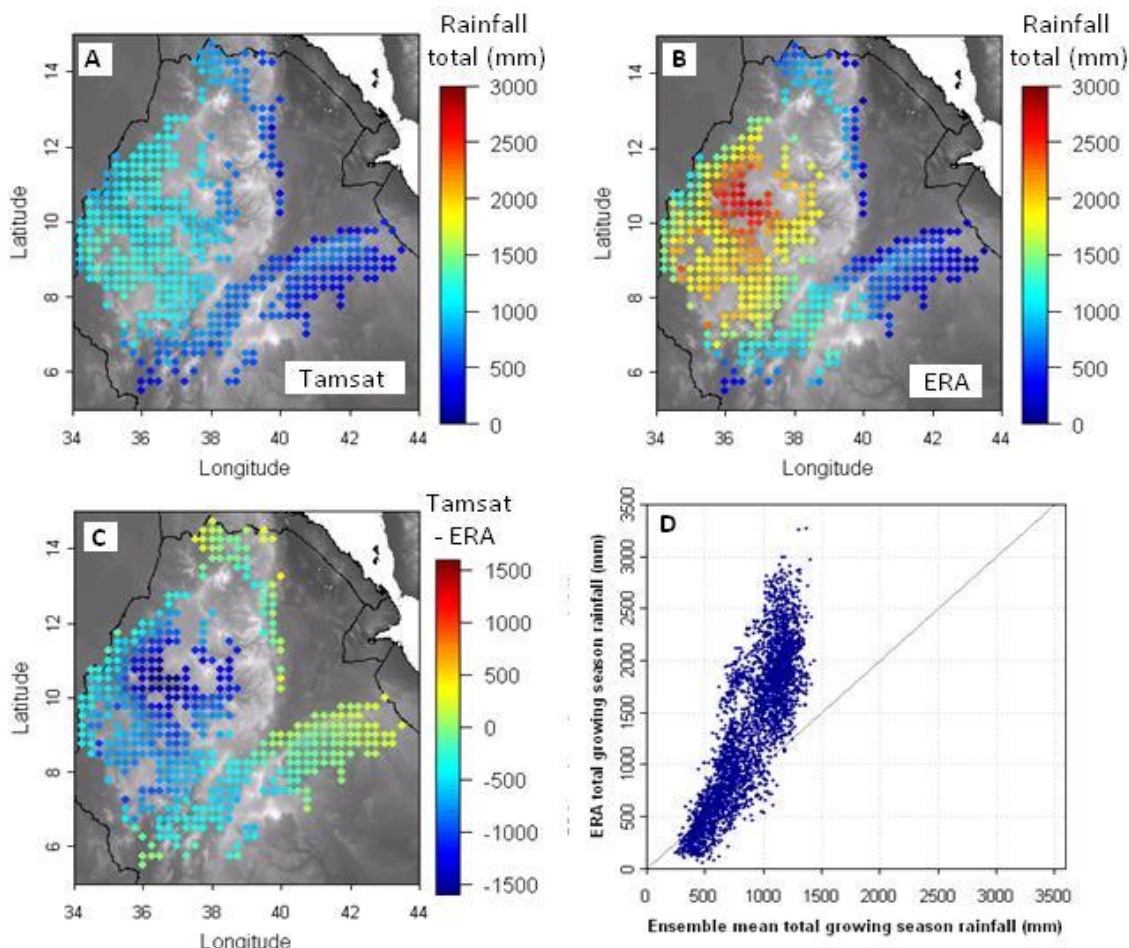


**Figure 9.9.** A comparison of growing season rainfall between the TAMSAT daily ensemble mean and ERA\_INTERIM. The top two sub-plots show the growing season rainfall for the two estimates, whilst the bottom two plots show a comparison of the two.

As discussed in Section 7.2, the TAMSAT rainfall ensembles seemed to capture observed rainfall well, especially in the Oromiya region where the ensembles were calibrated. Therefore it appears from Figure 9.9 that ERA\_INTERIM is overestimating rainfall in the wettest regions of Ethiopia, in some cases by over 1m during the season. This issue has been reported several times by ERA\_INTERIM literature and appears to be because the weather model is too sensitive to positive feedback once convection has been triggered (Dee *et al.*, 2011). Figure 9.9 also shows an apparent overestimation by TAMSAT in the driest regions of Ethiopia (in the North East of the country). There is a small amount of evidence in Dee *et al.* (2011) to say that ERA\_INTERIM may underestimate rainfall in dry regions. However this region is also least likely to have an accurate TAMSAT calibration, as it is geographically and climatically far from the calibration region. Unfortunately, there is no available gauge data in the region to say which estimate is more accurate.

The impact of using either TAMSAT or ERA rainfall in GLAM<sub>MAIZE</sub> simulations can be seen in Figure 9.10. The overriding message from these plots is that in the majority of cases, the overestimation of rainfall by ERA\_INTERIM seems to have little effect on crop development or growth. This is because unlike in the precursor to this study, which concentrated on The Gambia (Teo, 2006), most modelled maize in Ethiopia does not experience significant water stress, even in runs using the drier TAMSAT ensembles. As GLAM<sub>MAIZE</sub> does not take into account water logging or flooding, all excess water is simply removed as ‘run off’, thus for GLAM<sub>MAIZE</sub>, ERA and TAMSAT inputs appear to be similar for most pixels. This is clearly unrealistic and perhaps should be addressed before GLAM<sub>MAIZE</sub> is applied in wetter regions. There is more of a divergence between TAMSAT and ERA inputs for lower yields, but unfortunately as discussed above, this is for the drier region where little is known about the accuracy of the results.

The other factor affecting these results is cultivar choice and season length. As shown in Figure 9.7, temperature dominates the effect of climate on crop yield as it determines crop development and season length. However, both GLAM\_TAMSAT and GLAM\_ERA both used ERA\_INTERIM temperatures and solar radiation. This is somewhat unfair on the TAMSAT runs because there will be no correlation between rainfall and temperature (e.g.

more rainfall will generally mean cooler temperatures and less solar radiation). It should be noted that Figure 9.10 also shows that some of the modelled LAI, biomass and yields are unrealistically high. This feature is linked to the poor modelling of some season lengths and is discussed in more detail in Section 9.5 and in the conclusion in Section 11.1.4.

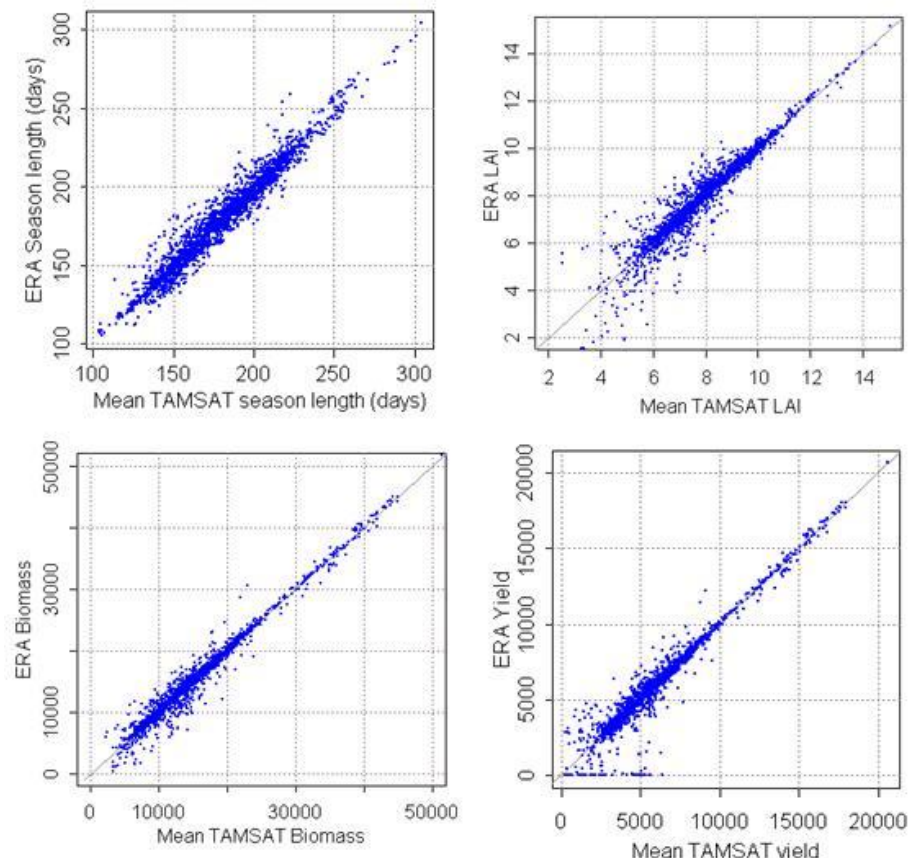


**Figure 9.10.** Comparison of simulated crop parameters using ERA and TAMSAT rainfall as an input. Each point corresponds to one location and season. The y-axis in each plot corresponds to either season length, LAI, Biomass and Yield for seasons run using ERA rainfall and the x-axis shows these parameters from the same season run with TAMSAT rainfall. Note, the TAMSAT values shown are the mean of the ensemble of crop yields, therefore there are very few zero values.

It should also be noted that there appear to be very few values of zero crop yield in the recorded TAMSAT yield in Figure 9.10. This is because the value used for comparison was the mean of each crop parameter from the 200 GLAM\_ENSEMBLE ensemble members for each season and location.

## 9.5 ENSEMBLE ANALYSIS

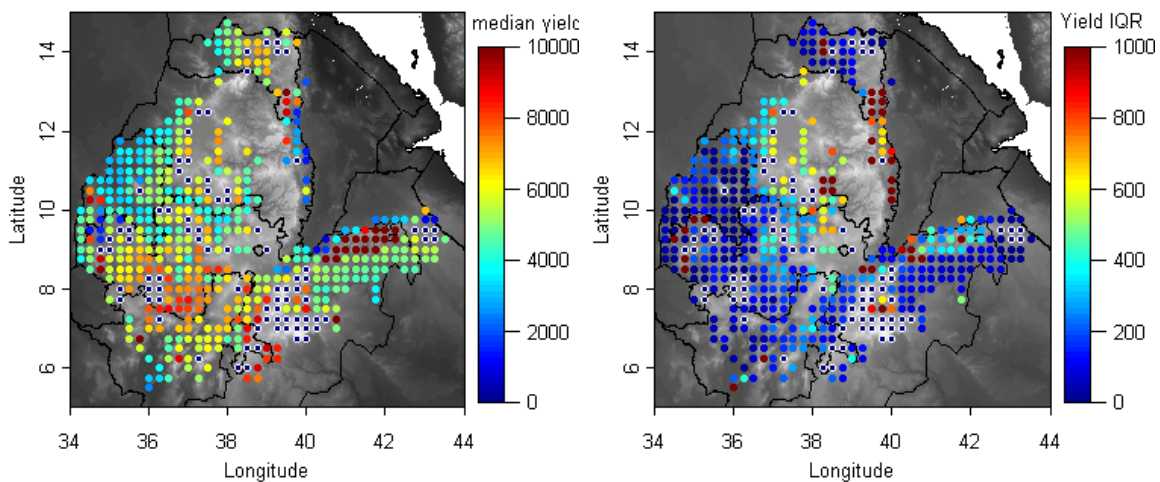


**Figure 9.11.** The median and Inter-Quartile Range (IQR) of the ensemble yield. The background to each plot corresponds to elevation and the regions are marked in black. Pixels outlined in white are ones where more than 90% did not complete the season (i.e. they reached the end of the calendar year before harvest and so were assigned zero yield).

Maps of the ensemble median and inter-quartile range (IQR) of yield at each pixel are depicted in Figure 9.11. These pixels can be split into three homogenous regions: Type 1 pixels are generally found in the west of the country and have a relatively high mean yield and a small variability. Type 2 pixels are normally found at high altitudes and are characterised by high mean yield and high variability (this regime also includes pixels where the season did not complete). Finally type 3 pixels have low mean yield and high variability and particularly found in the North East (region3).

Type 1 pixels have high mean yield and low variability because here, all ensemble members provide enough rainfall that the plant is never stressed and any extra rainfall ‘disappears’ as run-off. This leads to a very low range of modelled yields as each ensemble member is modelling yield potential. The variability in this area might be increased if water-logging routines were added into GLAM<sub>MAIZE</sub>.

When one looks more closely at pixels within this region, it can be seen that it is only rainfall before silking which is important, corroborating the results discussed in Figure 9.6.

This effect can also be seen in Figure 9.12, which shows histograms of the ensemble response of different crop parameters for one pixel at 10.75° latitude and 35.25° longitude during the years 1998 (left) and 1999 (right). The top pair of histograms show the modelled crop yield, followed by total seasonal rainfall, the proportion of rainfall which fell before silking and finally, the leaf area index (LAI).

It should be noted that none of the ensemble runs suffered water stress during the Anthesis-Silking Interval and all the ensemble members completed the season within 10 days of each other, thus temperature played a relatively small role in creating variability for this pixel.

The top pair of histograms show that there is a marked difference between the yield distribution in the two seasons; 1998 has a much broader distribution with a lower mean yield compared to 1999. This appeared unusual as the second set of histograms shows that the total seasonal rainfall was roughly equal in the two years and in fact had a slightly lower mean in 1999 where there were enhanced yields. However, when one looks at the intra-seasonal distribution of rainfall in the third pair of histograms, it is clear that the year with higher yields had much higher pre-silking rainfall. As discussed in Section 9.4, this is when the plant is more susceptible to water stress. This led to enhanced LAIs in 1999, as shown in the 4<sup>th</sup> pair of histograms, which led to a higher biomass and thus a higher yield.

Type 2 pixels have a high mean yield, a high ensemble variance and are generally found at high elevations. The natural cause of these symptoms is that the ensemble yield is being dominated by the model's response to temperature, hence type 2 pixels also includes those which didn't complete the season, or are surrounding pixels with a high variability. Figure 9.13a (left) shows the average proportion of ensembles which fail to complete the season. This is well correlated with yield, as shown in Figure 9.13b (right).

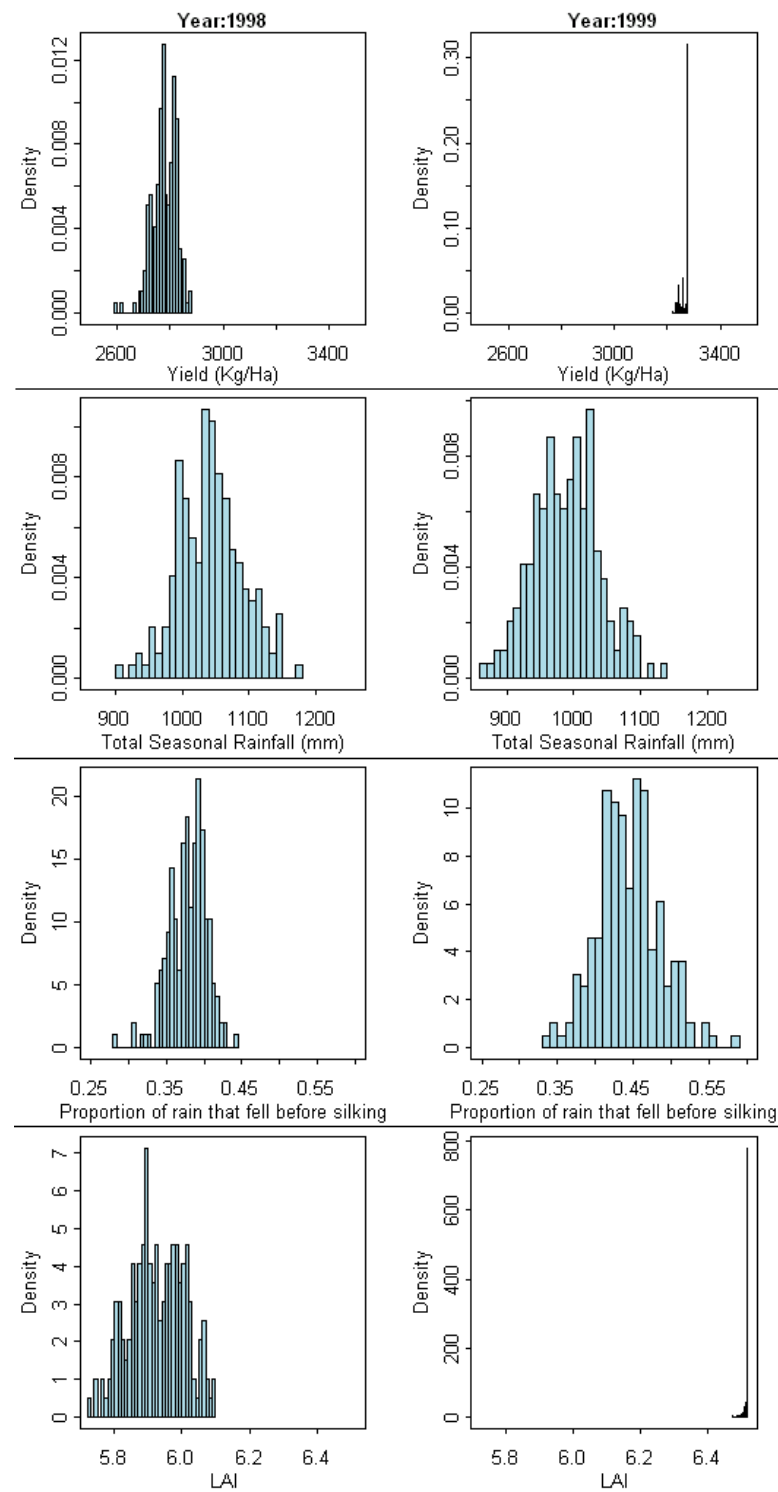


**Figure 9.12.** Ensemble histograms of crop yield, total seasonal rainfall, the proportion of rain before silking and LAI, for 1998 and 1999 at  $10.75^{\circ}$  latitude and  $35.25^{\circ}$  longitude. The two seasons show a marked response to pre-silking rainfall.

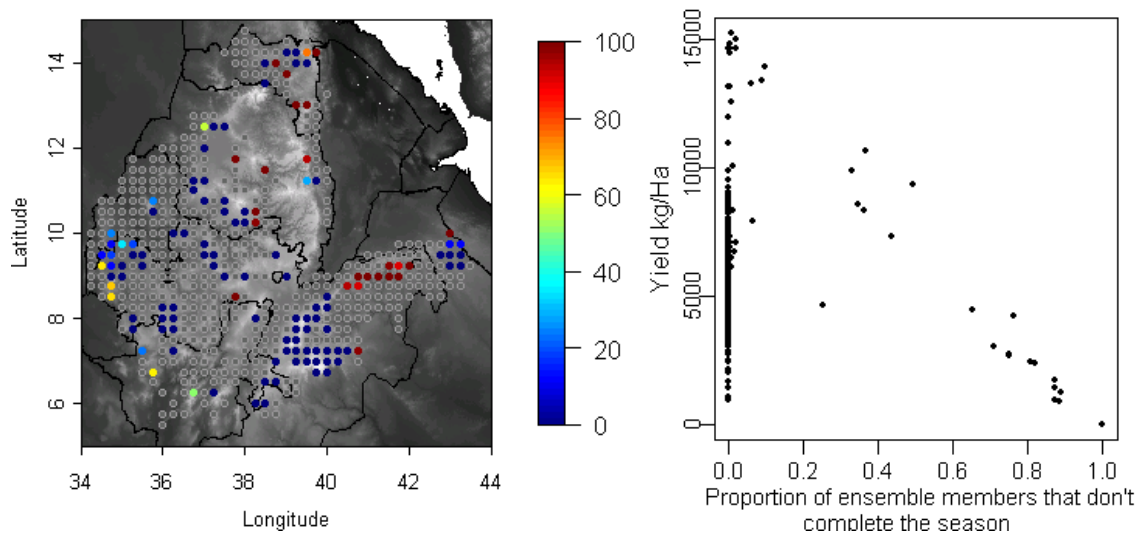


**Figure 9.13.a (left)** Proportion of ensemble members failing to complete the season, given that at least one ensemble member failed at that location. Pixels where all ensemble members completed the season in all years are marked in grey. **Figure b. (Right).** The proportion of ensemble members completing against mean yield. Each point corresponds to 1 pixel.

These pixels are ones for which the cultivar choice is unrealistic and modelled maize at these pixels has taken an improbably long time to develop. GLAM<sub>MAIZE</sub> ‘kills’ these plants if they reach the end of the calendar year without reaching harvest (The end of the calendar year was fixed as this cut off due to the lack of weather data in January and February). This means that as there was a poor cultivar choice for some high altitude pixels, there are some ensemble members which reach an improbably high yield and some which reach the end of the calendar year and so record zero yield; this leading to a high ensemble mean yield and a high variability. This is obviously unrealistic and suggests the crop model needs further development. As GLAM<sub>MAIZE</sub> is an intermediate complexity crop simulation model, there are currently no process-based routines which reduce yield if it is taking too long to develop (for example pests, nutrient deficiency or grain quality). The problem would also not arise in reality because farmers are careful to chose an adequate cultivar for their location. The problem is also exacerbated because the same temperature data is used for all ensemble members. As discussed in Section 9.3, two possible solutions to this would be to either select several maize cultivars and assign one to each location, or to artificially change limit some crop parameter so that that the modelled plant cannot develop unrealistically.

Finally, type 3 pixels are those affected by water stress during the anthesis-silking interval as described in Section 8.5. It should be noted that this is not the standard water stress which affects crops throughout the season and instead is the specific water stress which misaligns tasselling and silking resulting in massive yield loss.

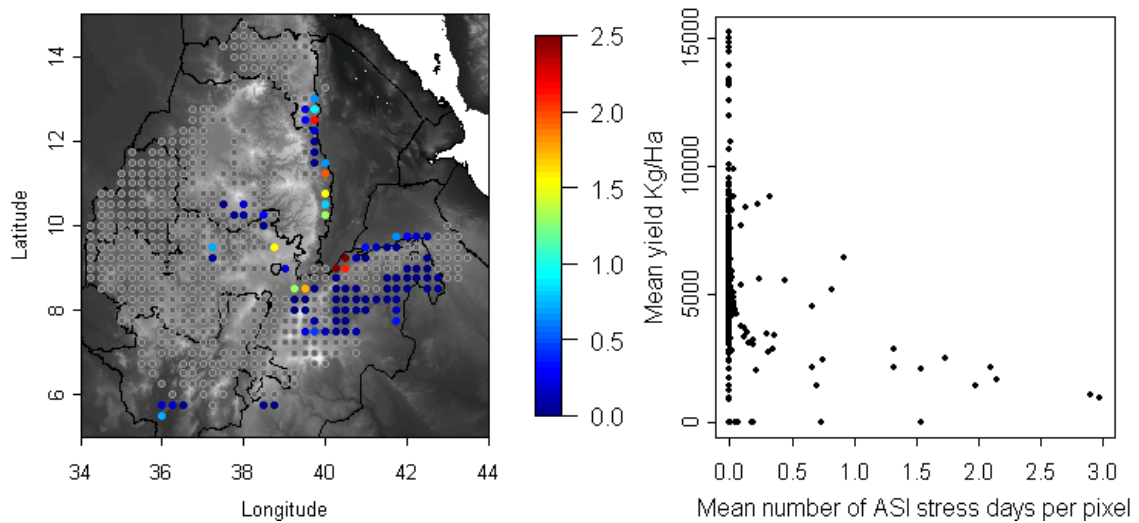


**Figure 9.14a (left).** Mean length of the specific water stress period at pixels affected by ASI stress. The right hand plot shows that yield is well correlated with ASI stress length.

These pixels are realistically located in the areas with the highest mean temperatures, along the edge of the Danakil and Somali deserts. The relationship between yield and the length of the ASI stress period also follows the prescribed exponential relationship described in Equation 8.27, confirming the internal consistency of the model. The effect of water stress on the ensemble at one specific location can clearly be seen in the example illustrated in Figure 9.15. For this location/year, two of the ensemble members were subject to water stress during the ASI interval, leading to drastic reductions in yield. The cumulative rainfall during the two seasons is similar to non-water-stress ensemble members and the seasonal rainfall totals fall closer to the ensemble mean than ‘drier’ seasons. The example clearly shows the benefit of using a process based model as the reduced yield in the water stress seasons would not have been captured using a simpler water balance or statistical weather/yield model, leading to reduced interannual variability. This effect was seen in the work of Teo (2006) who found that the FAO water balance model, CROPWAT failed to

capture interannual variability in Gambian groundnut yields due to the fact that it did not capture intra-seasonal rainfall events.

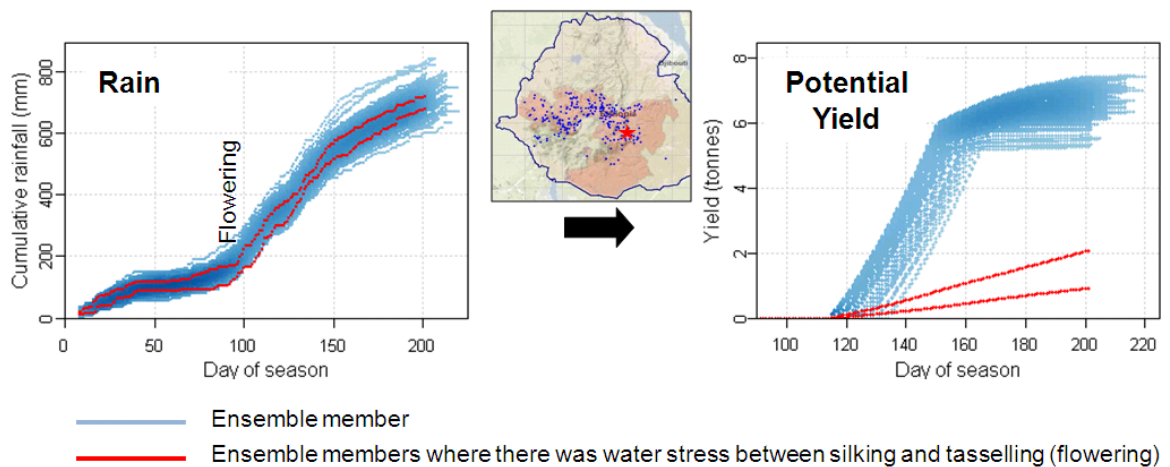


**Figure 9.15.** The effect of water stress on a pixel at 39.75° Longitude and 7.5° Latitude in the year 2000.

## 9.6 REGIONAL LEVEL STATISTICS

In this section, the model results have been split into time-series of regional level means in order to compare them against observed values. The pixels included in each region can be seen in Figure 9.2. Dire Dara and Harari were excluded from the analysis because the regions contained less than 2 pixels. The S.N.N.P.R region was also excluded because the Meher and Belg seasons merge in this region, making it different to compare to observations. In all of the plots in this section, the blue cloud corresponds to the ensemble values for that year (GLAM\_ENSEMBLE), the black lines show the GLAM\_ERA results and red lines correspond to observations.

First, it is prudent to see how the total seasonal rainfall varies across each region, as depicted in Figure 9.16. As discussed in Section 9.4, ERA\_INTERIM significantly overestimates rainfall in rainy areas in comparison to TAMSAT and observations, whilst slightly underestimating compared to TAMSAT in the drier Somali and Afar regions. It should be noted that it is difficult to verify rainfall amounts in the drier Somali and Afar regions due to a lack of observations, but the fact that the satellite was calibrated using data from a

much wetter Oromiya means that there is a greater chance Somali and Afar rainfall estimates aren't as accurate as in the wetter regions.

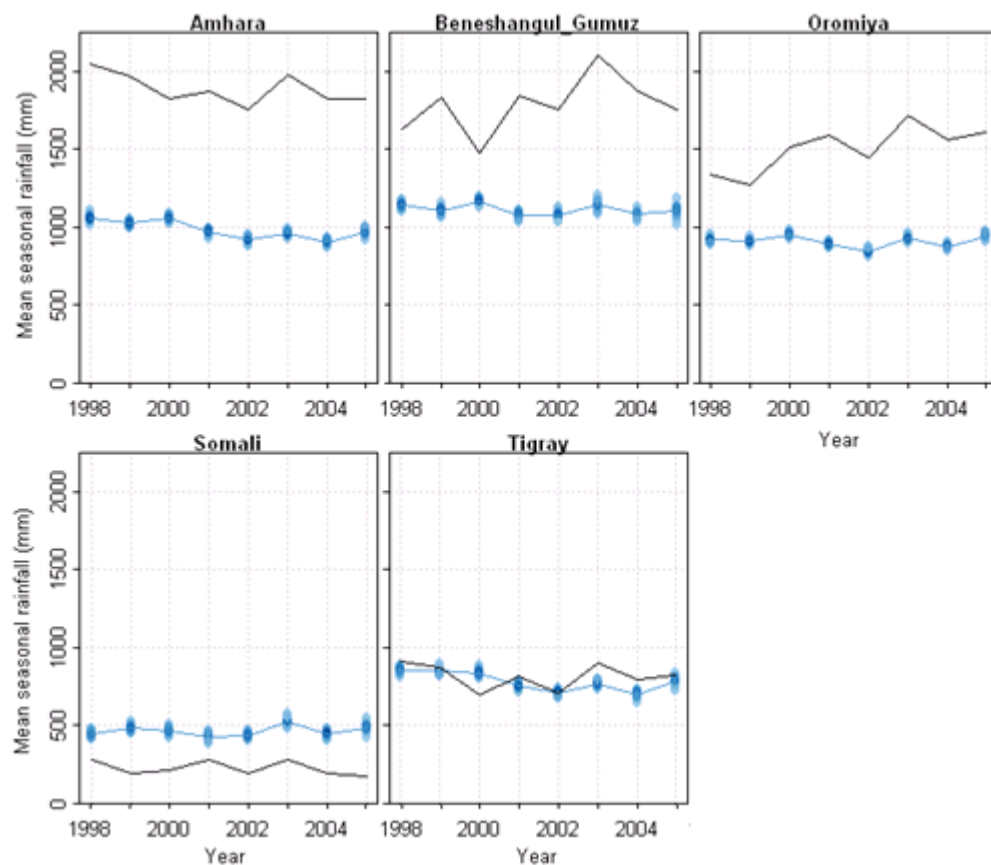


**Figure 9.16.** Time-series of mean total growing season rainfall for each of the regions. The TAMSAT ensemble is marked in blue and ERA\_INTERIM is marked in black. The y-axis is the same for all sub-plots.

Figure 9.17 and Figure 9.18 show time-series of the mean Leaf Area Index (LAI) and biomass over the season. As discussed in Section 9.4, in wet areas most excess rainfall is ignored as run-off, therefore GLAM\_ERA and GLAM\_ENSEMBLES are both modelling potential yield and so record very similar results. In the water stressed Somali region, ERA\_INTERIM recorded slightly lower rainfall than TAMSAT, which meant that it recorded slightly lower LAIs and biomasses, but with the same trend from year to year.

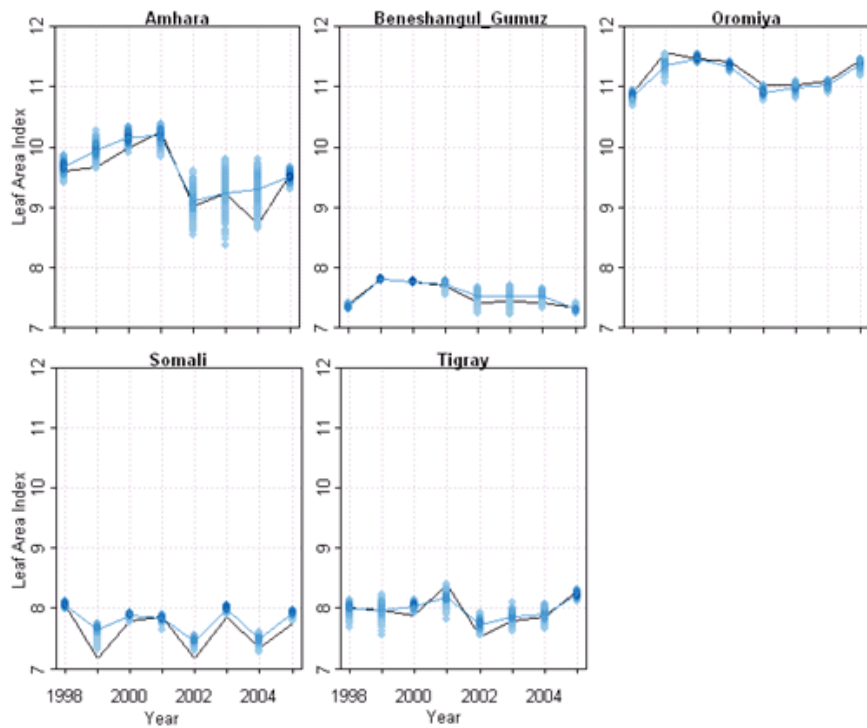


**Figure 9.17.** Time-series of leaf area index for each of the regions. The TAMSAT ensemble is marked in blue and ERA\_INTERIM is marked in black. The y-axis is the same for all sub-plots.

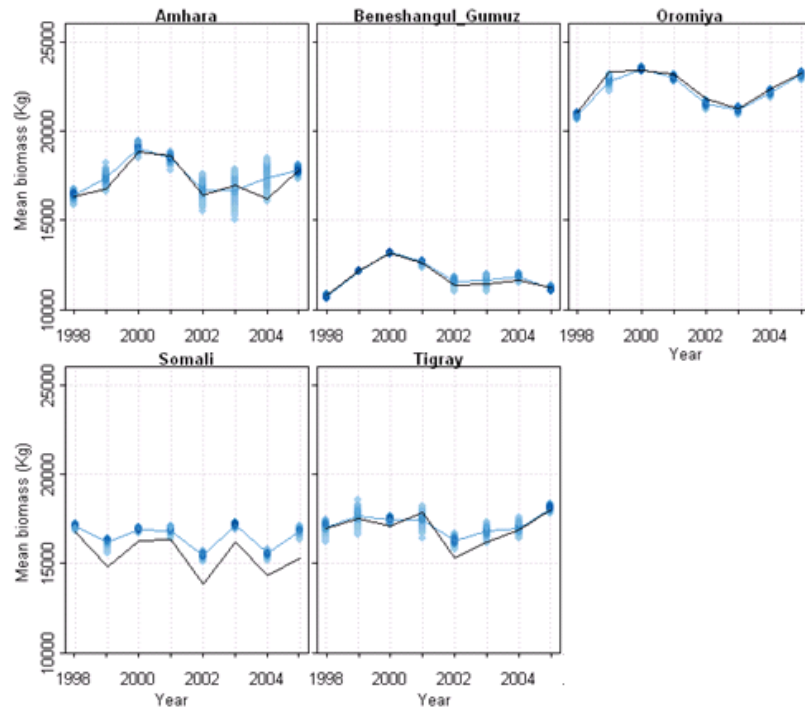


**Figure 9.18.** Time-series of mean biomass for each of the regions. The TAMSAT ensemble is marked in blue and ERA\_INTERIM is marked in black. The y-axis is the same for all sub-plots.

## **9.7 COMPARING MODELLED YIELDS WITH OBSERVATIONS**

The yield derived from these biomasses presented in the previous Section is shown in Figure 9.19, which also plots modelled yields against observed values. It should be noted that specific water-stress during the Anthesis-Silking Interval (ASI) affects crops in drier regions and acts to reduce harvest index, which directly impacts yield rather than biomass. Therefore, when one takes into account the stress at ASI, the results from GLAM\_ERA and TAMSAT diverge slightly, and even exhibit a different trend in the Somali region in 2002.

The observed yields depicted in Figure 9.19 are farmers yields and so are very much lower than the modelled values of attainable yields. There also appears to be very little correspondence between modelled and observed yields. GLAM<sub>MAIZE</sub> has a capability to model farmers yield through calibrating the Yield Gap Parameter, but this would have required more data for calibration. As the yield gap parameter acts on the plant's LAI rather than linearly on yield, it is difficult to predict modelled farmers yields from simple observation of attainable yield, as in some cases, even the trend from year to year might differ. This makes it difficult to compare the modelled values presented here against observed yield, especially as observed yields show very little variability and pre-2005 yields might be less well measured due to the FAO project mentioned in Section 2.5.1. There is also some controversy about whether CSA or FAO observed time-series is correct. This is discussed in detail in Section 2.5.2 and is depicted in the multiple observational time-series. .

Finally, the yield analysis is shown at a national level in Figure 9.20. This shows very little correlation between the modelled and observed yield trends, although it is difficult to make conclusive statements considering the uncertainty on the observations. One aspect that should be noted is that the 'dip' in modelled yields in 2002 is also reported in observations in Funk *et al.* (2003) and can be seen in Figure 2.10.

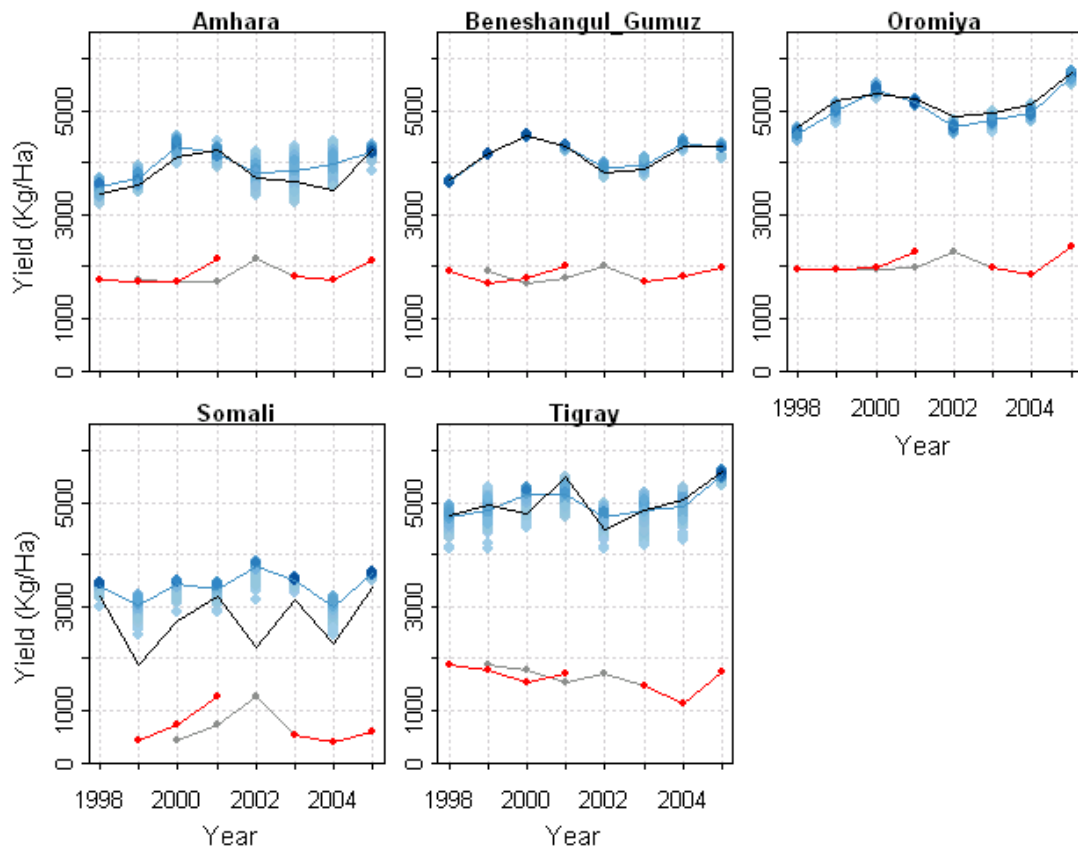


**Figure 9.19.** Time-series of mean yield for each of the regions. The TAMSAT ensemble is marked in blue and ERA\_INTERIM is marked in black. Observed regional yields from the original CSA dataset are shown in red and the time-series that was shifted to match the FAO in shown in grey (see Section 2.5.2 for details). The y-axis is the same for all sub-plots.

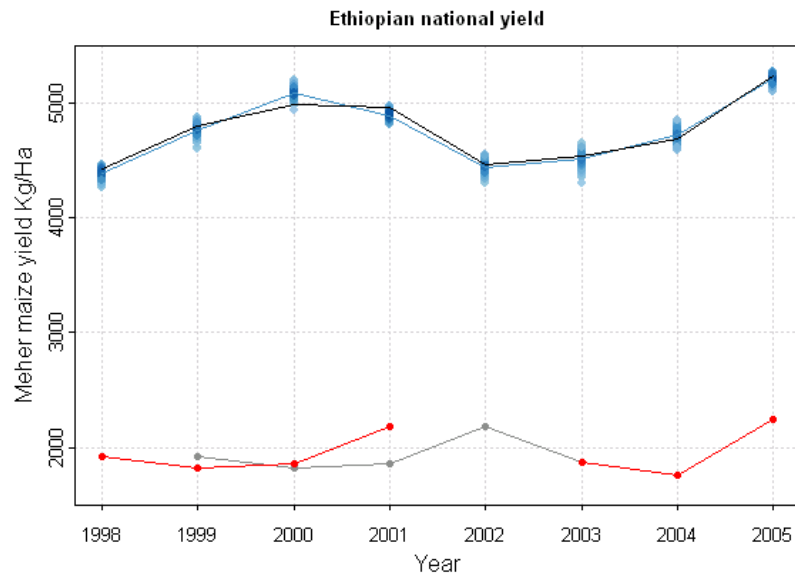


**Figure 9.20.** Time-series of national mean yield. The TAMSAT ensemble is marked in blue and ERA\_INTERIM is marked in black. Observed yields from the original CSA dataset are shown in red and the time-series that was shifted to match the FAO is shown in grey (see Section 2.5.2 for details).

## **9.8 CONCLUSION TO CHAPTER NINE**

This Chapter presented the results of linking GLAM<sub>MAIZE</sub> with satellite rainfall ensembles and ERA<sub>\_INTERIM</sub> modelled rainfall for 518 pixels over Ethiopia. The following results were found:

- ♦ The parameterisation of GLAM<sub>MAIZE</sub> for the MH16 cultivar generally resulted in realistic values of LAI, biomass and yield (Section 9.2)
- ♦ Maize yield is very sensitive to temperature, as this directly affects the length of the growing season. Therefore, the sharp variations in elevation/temperature over Ethiopia mean that the approach of using one Malawian maize cultivar over the entire country was too simplistic. The use of one cultivar over Ethiopia meant that growing season lengths at high elevations were unrealistically long and so yields were unrealistically high. The issue was compounded by the fact that there was no weather data available for January and February, therefore any plants which had not reached harvest by the 31<sup>st</sup> December were assumed to have died. This led to many pixels at high elevations that had an improbably high ensemble variability, because ensemble members either recorded a high yield or zero yield. The issue can be addressed in the future either by using a selection of cultivars which are more appropriate to their surroundings, or by artificially changing the crop model so that it is better able to kill the plant if the season becomes unrealistically long (Section 9.3). The issue might also have had less of an impact if observed temperatures could have been used rather than using those from ERA<sub>\_INTERIM</sub>.
- ♦ Only a few locations in Ethiopia experienced water stress, therefore the major determinant of crop yield was found to be temperature. In those pixels which were affected by water stress, a lack of water before flowering (silking) was found to have a negative impact on yield, whilst a lack of water after flowering was found to have a positive impact. This is because water stress acts on Leaf Area Index (LAI), which only increases before flowering. (Section 9.2.2)

- ♦ ERA\_INTERIM and the TAMSAT ensembles recorded very different values of rainfall over Ethiopia, with ERA\_INTERIM vastly overestimating rain with respect to TAMSAT in wet areas and underestimating in dry ones. In wet areas, both types of rainfall input were providing enough water to prevent water stress, therefore the extra ERA\_INTERIM rainfall flowed away as runoff and so similar yields were recorded. This suggests that GLAM<sub>MAIZE</sub> should include a water-logging or flooding routine to give more realistic results. In dry areas, there was a much bigger difference in yields between GLAM\_ENSEMBLE and GLAM\_ERA as water played a much more important role in determining yield.
- ♦ There were too few yield observations to calibrate GLAM<sub>MAIZE</sub>'s yield gap parameter, therefore the model recorded attainable yield rather than farmer's yields. This meant it was difficult to compare modelled and observed yields. Discrepancies between modelled and observed yields might have arisen because:
  - There were many pixels at high altitudes with unrealistic yields due to inadequate cultivar choice.
  - Pixels suffering from water stress tended to be found in the Somali and Afar regions. These regions also have very few rain-gauges, therefore it is reasonable to assume that the rainfall inputs, which were calibrated for the wetter Oromiya region might be less realistic in these areas, leading to variations in crop yield.
  - The yield gap parameter does not act linearly on crop yield, therefore modelled farmer's yields might show similar trends even if these are not reflected in the attainable yields shown here.
  - There might be issues with the observed yield dataset, for example the FAO and CSA time-series diverged pre-2003. This argument is somewhat supported because both modelled and observed time-series show an increase in 2005, when observed yield observations were at their most reliable.

Many of these experimental limitations can be overcome in an operational system because the Ethiopian authorities have access to a greater range of yield and climate observations.

## **9.9 CONCLUSION TO PART 3**

This Section of the thesis applied the satellite rainfall ensembles described in Part 2 and the synoptic and agronomic observations discussed in Part 1, to regional scale crop yield forecasts for Ethiopian maize.

In particular, the work presented in Part 3 concentrated on the design and sensitivity to climate of a new parameterisation of the GLAM crop simulation model for tropical maize. This work included modifying the phenology of the model, introducing a photo-sensitive phenological stage and designing a water stress routine for maize's anthesis-silking interval based on the research of Edmeades (1996). In Chapter Nine, GLAM<sub>MAIZE</sub> was then run for each individual TAMSAT rainfall ensemble member. The results showed that GLAM exhibited realistic responses and the correct sensitivity to climate, adding to the work of Teo (2006).

Many of the limitations of the work presented in this part of the thesis were due to a scarcity of calibration and validation data. In particular, GLAM could only be calibrated for one particular cultivar of maize which is generally grown in the East African lowlands. This led to high altitude pixels exhibiting unrealistically long modelling season lengths, which, when linked with a lack of 'plant death' routines in GLAM, led to unrealistically high values of modelled LAI, biomass and yield. A lack of robust yield observations also meant that only limited conclusions could be made regarding a validation of the model.

# PART 4

# SEASONAL FORECASTING

# & WEATHER GENERATORS

So far, this thesis has considered how to link weather observations and crop simulation models in order to produce an estimate of crop yield at the day of harvest. Part 4 explores the methodology needed to extend such system to be able forecast crop yield at the beginning of the season.

*Chapter Ten* (Seasonal crop yield forecasting) considers how to use output from a seasonal forecast as an input to a crop simulation model. In particular, the Chapter considers stochastic weather generators and introduces a new method, RainInt, to extend their output to a create spatially correlated rainfall fields.

# CHAPTER TEN

# SEASONAL CROP YIELD

# FORECASTING

## 10.1 INTRODUCTION

So far, this thesis has considered how to run a crop simulation model using different estimates of current weather conditions (from satellites and numerical models), in order to produce an estimate of crop yield at the day of harvest. This type of product is useful to decision makers as it can take some months after harvest to determine regional crop yield and production. However it would also be advantageous for decision makers to be able to translate seasonal weather forecasts into estimates of crop yield at the beginning of the growing season. This would enable a crop yield forecast to be made many months before the crop is harvested and could allow an earlier assessment of a country's food security needs.

This chapter explores the methodology needed to be able forecast crop yield at the beginning of the season. Section 10.2 provides a background to seasonal weather forecasting and Section 10.3 examines how a seasonal weather forecast and historical weather observations can be linked to form the updating crop yield forecast system discussed in the Introduction. Section 10.4 then discusses in more detail how a seasonal weather forecast might be linked to a crop simulation model.

As a seasonal weather forecast is probabilistic by nature, many of the approaches considered rely on the ability to create an ensemble of potential weather seasons which

agree with both the climatology of the region of interest and with the seasonal weather forecast itself. This is traditionally achieved using a weather generator, therefore Section 10.5 discusses the main concepts behind weather generators, before Section 10.6 introduces a new methodology for extending a weather generator to produce spatially correlated rainfall ensembles called RainInt. Preliminary outputs from this method are discussed in Sections 10.6.4 and extensions to the method are suggested in Section 10.6.5. Finally, future research questions and directions on the topic of seasonal crop yield forecasting are discussed in Section 10.7 before the chapter is concluded in Section 10.8.

It should be noted that time constraints meant that developing a fully functional crop yield forecasting system was beyond the scope of this thesis. Consequently, the seasonal forecasting sections of the chapter are conceptual in nature and focus on the methods which could be used to link any statistical seasonal weather forecast with a crop simulation model, rather than focusing on specific quantitative examples.

## **10.2 SEASONAL WEATHER FORECASTS**

A seasonal weather forecast is a statistical summary of expected weather over forthcoming months, derived from information both from the climatology of the region of interest and from slowly changing components of the Earth system e.g. sea surface temperature, snow cover or soil moisture. Forecasts are probabilistic in nature, that is they forecast the chance of a certain type of weather occurring during the season rather than deterministically forecasting specific weather conditions on particular days. Although the sparsity of weather observations in sub-Saharan Africa mean that short term weather forecasting is difficult beyond 24 hours, the fact that disruptions in sea surface temperatures are strongest in the tropics often mean that it is easier to predict the seasonal climate in Africa than in other parts of the globe (Hansen *et al.*, 2011). This is particularly apparent in regions with strong teleconnections to ENSO or the Indian Ocean Dipole, for example in Southern Africa during Boreal winter or the Sahel during Boreal summer. The large scale forcings and seasonal predictability of Ethiopian weather conditions are discussed Diro *et al.* (2008) and Diro *et al.* (2010a). These find that although Ethiopia's topography and placement

with respect to large scale weather systems make the situation complex, skill can be found in seasonal forecasts of both the Belg (spring) and Kiremt (summer) rains at a time-scale coincident with cropping seasons. It should be noted that although there are also many forecasts of temperature, this chapter has focused on rainfall because its intermittent and chaotic nature often makes it harder to predict.

A seasonal weather forecast can be considered ‘dynamical’, ‘statistical’ or as a hybrid between the two, in the same way that crop simulation models are classed as process based or empirical. Dynamical forecasts use coupled ocean-atmosphere models to solve the complex equations governing the evolution of the Earth system, whilst statistical seasonal forecasts generally exploit empirical relationships between rainfall and known sea surface temperature anomalies. Perhaps the most widely used seasonal weather forecasts in sub-Saharan Africa come from Regional Climate Outlook Forums (RCOFS). These are held in each region of Africa before the start of their rainy seasons. The forum for the Greater Horn of Africa is called GHACOF and is held every August and February. The aim of an outlook forum is to bring together national meteorological agencies, other climate experts and non-meteorological stakeholders to develop and distribute a weather forecast of the season ahead. The starting point for such a forecast is often a statistical approach with some input from regional climate experts. The final forecast is generally disseminated in rainfall tercile format where each tercile corresponds to the probability of ‘above normal rainfall’, ‘normal rainfall’ and ‘below normal rainfall’. An example forecast for September to December 2011 is shown in Figure 10.1. Initial attempts at quantitative verification show some skill but systematic bias towards the central ‘normal’ tercile due to the interpretation of the experts present at the RCOFs (Mason and Chidzambwa, 2008). The Ethiopian National Meteorological Agency also supplements these forecasts with their own similar products designed to fit in better with the Ethiopian cropping calendar (Aseffa, 2011).

Another seasonal weather forecast widely used by stake-holders in Africa is the one produced by the International Research Institute for Climate and Society (IRI) at the University of Columbia (Mason *et al.*, 1999). This takes a two-stage dynamical approach.

The first stage is to predict global sea surface temperatures. These are then used as boundary conditions for a suite of atmospheric models. The output is again presented as a tercile of rainfall amounts. Validations of the method show skill over the Southern half of Africa and limited skill in Ethiopia (Barnston *et al.*, 2009). An example is shown in Figure 10.2 for the same forecast time period as the GHACOF forecast. There are many other seasonal forecasts available that are less widely used by African decision makers and so have not been discussed here (e.g. the ECMWF dynamical seasonal forecast). In addition, this Chapter is designed to present a conceptual overview of how any seasonal weather forecast might be linked with a crop simulation model rather than recommending one forecast product in particular.

As illustrated in Figure 10.1 and Figure 10.2, seasonal forecasts have traditionally provided interpretation about average meteorological conditions over large regions. The plots also suggest that forecasts generated by different prediction centres can differ widely in their predictions for a given season. The non-linear impact of weather on crop yield makes it difficult to estimate how much these differences in forecast seasonal weather reflect in different agricultural seasons, therefore it is beneficial to link a seasonal weather forecast to a crop simulation model to provide more information to decision makers. The probabilistic and temporally aggregated nature of seasonal weather forecasts makes it difficult to input them directly into a crop simulation model, which (as discussed in Section 8.3) normally requires a daily or dekadal time-series of rainfall, temperature and solar radiation for a specified region or location. The large uncertainty on the daily output of a probabilistic seasonal weather forecast also means that it is important and non-trivial to be able to quantify the resulting uncertainty on a crop yield estimate.

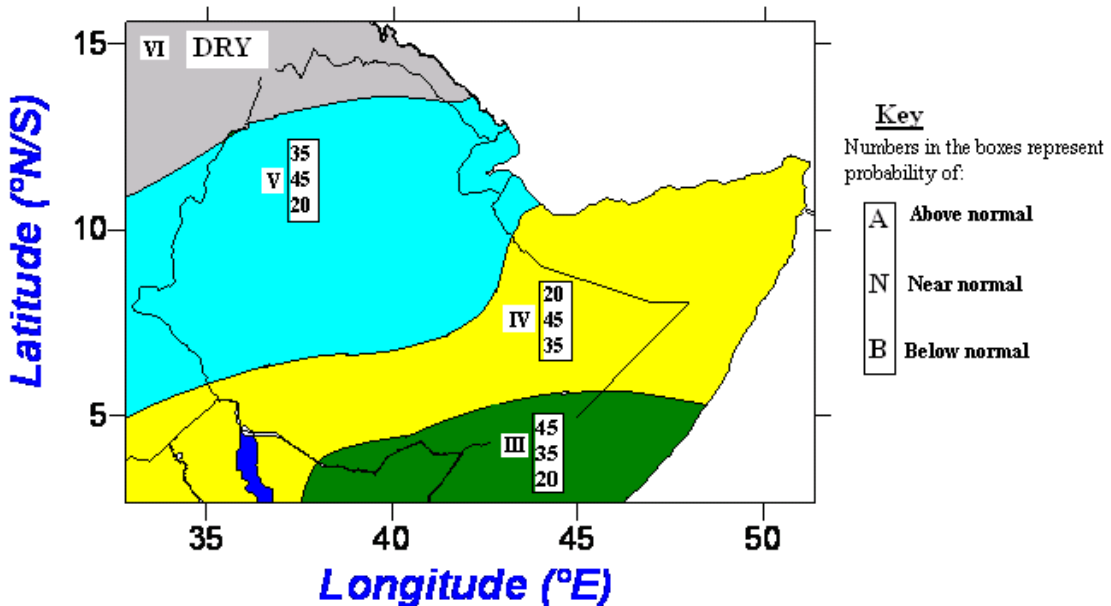


Figure 10.1. GHACOF seasonal forecast for September – December, 2011. The forecast covers the entire of East Africa but has been cropped to show Ethiopia in particular.

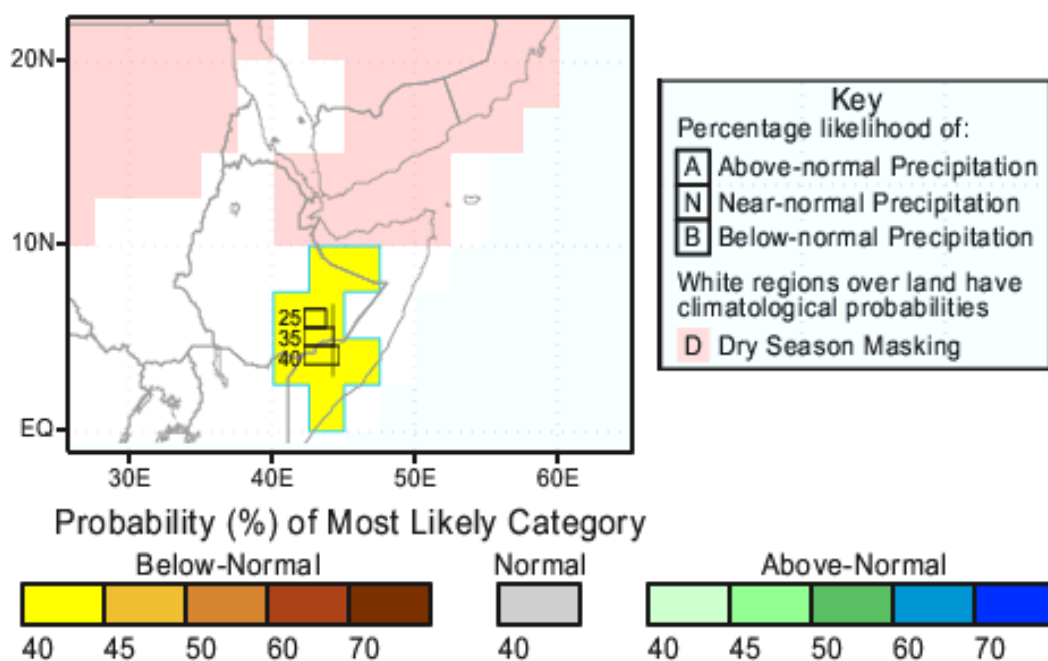


Figure 10.2. IRI seasonal forecast for October – December, 2011. The forecast covers the entire globe but has been cropped to show Ethiopia in particular.

### 10.3 AN UPDATING FORECAST SYSTEM

One method of providing a probabilistic assessment of the expected weather in the season ahead is to generate an ensemble of potential weather seasons which agree with the seasonal forecast. The crop model can then be run individually for each ensemble member, leading to an initial distribution of forecast crop yield. This is depicted schematically for one individual pixel in Figure 10.3A. The approach is useful for policy makers as it allows them to view the forecast uncertainty on the yield estimate thus allowing more informed decisions.

The process above will allow an initial estimate of crop yield at the start of the growing season. However, the inherent uncertainty in the seasonal forecast, weather generator and crop model means it is likely that there will be considerable uncertainty associated with the estimate, reducing its usefulness for decision makers. This uncertainty can be reduced as the season progresses through the use of weather observations. Parts 1 to 3 of this thesis discussed the lack of real-time rain gauge information in Africa and suggested that using ensembles of satellite rainfall estimates can provide a reliable and robust alternative. These satellite ensembles can be used to continuously update the forecast weather ensemble as the season progresses. This is shown for two time-slices in Figure 10.3B and Figure 10.3C. As one would expect the uncertainty on the satellite ensembles to be lower than the uncertainty on the seasonal forecast, it is reasonable to expect that the uncertainty on the final crop yield estimate will reduce as the season progresses. A similar updating system has been shown to generate realistic results in Hansen *et al* (2004) which used hind-casts of Queensland wheat yield to study different seasonal weather forecast inputs.

The shape and spread of the forecast yield distribution is also determined by the response of the crop to climate. Section 9.2.2 illustrates that GLAM is more sensitive to rainfall deficit before and during flowering, therefore one might expect the skill of the updating forecast system to increase significantly around the time of flowering, a feature indicated in the work of Teo (2006) for Gambian groundnuts.

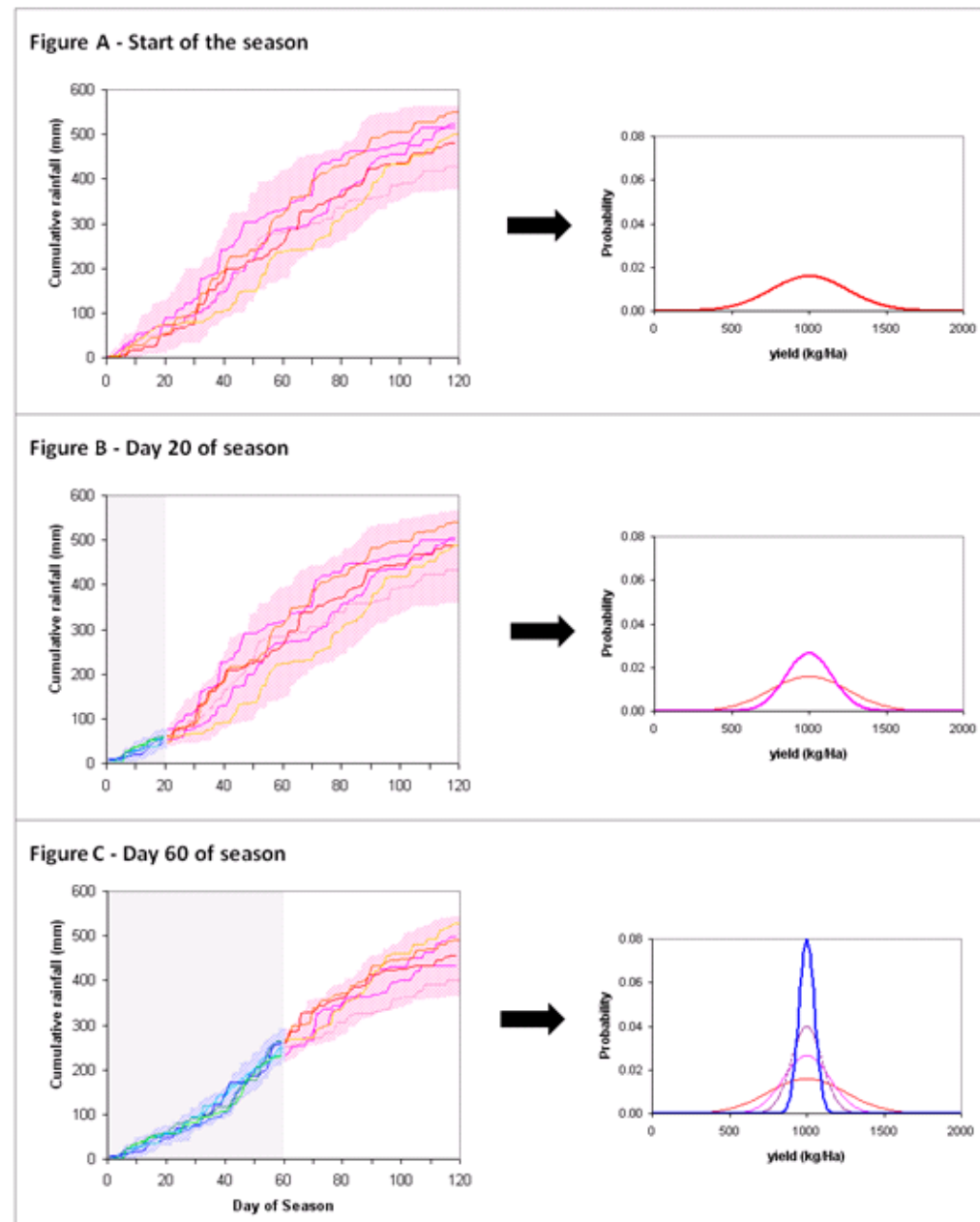


**Figure 10.3.** Schematic showing an updating forecast system for one location at three time-slices in the season. At the beginning of the season (subplot A), the crop model is driven using ensemble output purely from the seasonal forecast and weather generator. Each ensemble member is fed through the crop model to give an initial sample distribution of crop yield. As the season progresses (subplot B and C), the crop model is also driven using inputs from the satellite rainfall ensemble. As this has a lower uncertainty than the weather generator output, the resulting yield distribution should narrow as the season progresses.

## 10.4 LINKING A SEASONAL WEATHER FORECAST TO A CROP MODEL

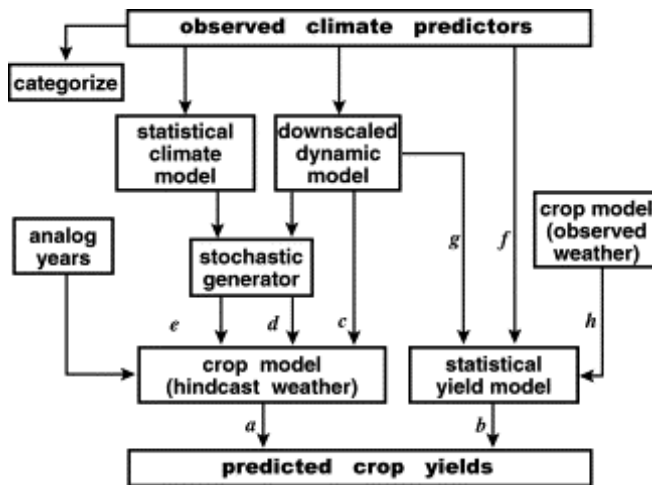


Figure 10.4. Potential information pathways from large-scale observed climatic predictors to simulation-based predicted crop yields. Figure reproduced from Hansen and Indeje, 2004

As depicted above, there are many different methods available to link a seasonal weather forecast to a crop simulation model. These methods are summarised in Figure 10.4 and reviewed in detail in Hansen and Indeje (2004). Only approaches suitable for linking with the Ethiopian case study are discussed further here, thus pathways including statistical yield models are not discussed because the process based GLAM crop model has already been selected for use. Many of the methods presented in Figure 10.3 involve the creation of an ensemble of potential weather seasons from the seasonal weather forecast which can then be individually run through a crop model as discussed in the previous section. An ensemble of potential seasons can be created for a dynamical seasonal weather forecast through the use of dynamic downscaling, which has been shown to generate realistic outputs in many studies both predicted weather (Sylla *et al.*, 2009) and crop yield (Baigorria *et al.*, 2008; Nicklin and Challinor, 2011).

A different approach must be taken for a statistical weather forecast using say a tercile output format, as the only information available is the chance of there being ‘more’ or ‘less’ rainfall than ‘normal’. Therefore one must determine first what climate statistics define ‘normal’ for the target location and then create an ensemble of daily time-series

which each look realistic but have mean statistics that agree with the climatology of the target location and the seasonal forecast. Different methods of achieving this are discussed in detail in the next section. For simplicity, this Section assumes that an ensemble of daily weather inputs can be created using a parametric weather generator at a specified spatial scale and resolution. It is then relatively simple to use a tercile format seasonal weather forecast to provide output suitable for a crop simulation model using the methodology described below. The entire process is also shown schematically in Figure 10.5.

***1) Categorise climate observations into groups corresponding to the seasonal forecast***

The first step is to choose a climate statistic which defines ‘normal’, ‘wet’ and ‘dry’. For example, in IRI’s seasonal forecast this was defined to be the total seasonal rainfall over a 3 month forecast period over a 2.5 degree grid square. One then needs access to a high spatio-temporal resolution dataset of weather observations. The resolution needs to be at least that of the final inputs for the crop simulation model e.g. in our case daily and a spatial resolution of  $0.25^\circ$ . If one is interested in forecasting crop yield at one specific location, then this dataset might consist of a long time-series of weather records for a single rain-gauge. If one is interested in regional crop yield analysis as in this thesis, then the dataset could either be comprised of a dense daily rain-gauge network kriged to the specified spatial resolution or from a long time-series of satellite rainfall estimates. Examples of these include the rain-gauge dataset available internally to the Ethiopian National Meteorological Agency or TAMSAT’s TARCAT 30-year satellite rainfall climatology.

***2) Use these groups to initialise a weather generator***

Assuming that an observational dataset has been obtained, each year can then be classified as ‘wet’, ‘normal’ or dry according to the forecast statistic. For example, if the forecast statistic was the total rainfall over September–December for a  $2.5^\circ$  grid, the observational data would first be scaled to a  $2.5^\circ$  grid, then sorted according to each year’s September–December rainfall totals. The wettest third of years would be classed as the ‘wet’ dataset, the driest third of years classed as the ‘dry’ dataset and the central third as the ‘normal’ dataset. Ideally, the observed dataset should have a long enough time-series

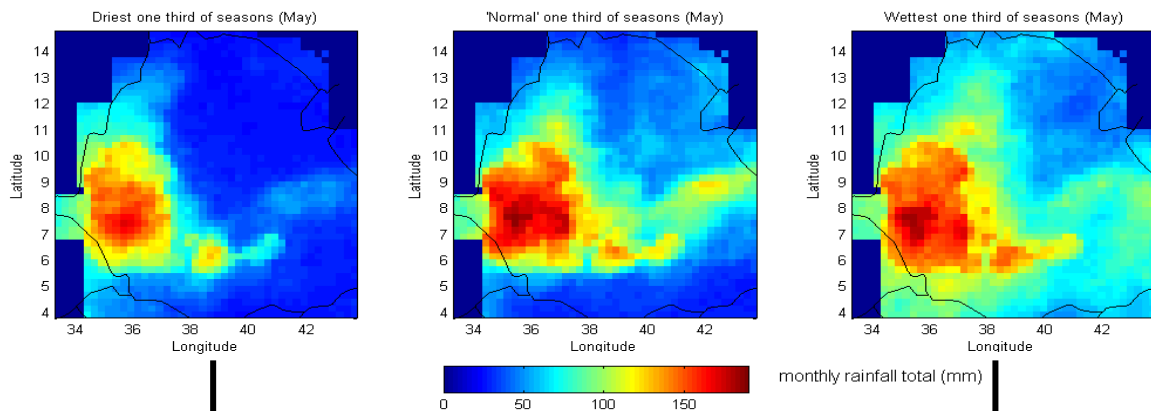
to capture the climate for wet years, dry years and normal years. Analysis of the wet, normal and dry datasets will then provide the climate statistics needed to run a weather generator in each type of year. When this is linked to a weather generator, one can create an set of ensembles of weather time-series corresponding each climate category. The methodology to do this is discussed in more detail in Sections 10.5 and 10.6.

**3) Selecting ensemble members to agree with the tercile forecast.**

The final step in the process is to choose an ensemble which agrees with the tercile weather forecast. For example if the final ensemble size is to be 100 and the tercile says that in this particular location the tercile is a 30% chance of above average rain, a 40% chance of average rain and a 30% chance of below average rainfall, 30 ensemble members would be selected from the ‘wet ensemble’, 40 from the ‘normal ensemble’ and 30 from the dry ensemble.

The method described above is often employed when linking a statistical seasonal forecast to a crop simulation model (Cantelaube and Terres, 2005; Moeller *et al.*, 2008) and the method has been used with a crop simulation model conditioned on ENSO phase rather than using a wet/normal/dry forecast (Podestá *et al.*, 2002; Stone and Meinke, 2005). It should be noted that all of these studies considered forecasting climate and crop yield at one specific location. It is relatively novel to extend the method to regional studies due to the lack of a regional weather generator or large scale crop simulation model. The rest of this chapter discusses how these issues might be overcome.

**STAGE 1:** Classify years according to some seasonal weather statistic. In this case, it was the monthly mean rainfall total in May on a pixel by pixel basis (i.e. the 'dry' sub-plot shows the mean monthly May rainfall for the driest three years for each individual pixel). Another example would be the case study above where the climate was classified over 3 months and 2.5 degree blocks.



**STAGE 2:** Use a weather generator to create an ensemble of time-series of rainfall using the input from the wet dry and normal classifications. In this case, a spatially correlated weather generator has been used (please see Section 10.5) to make an ensemble of spatially correlated time-series of rainfall maps.

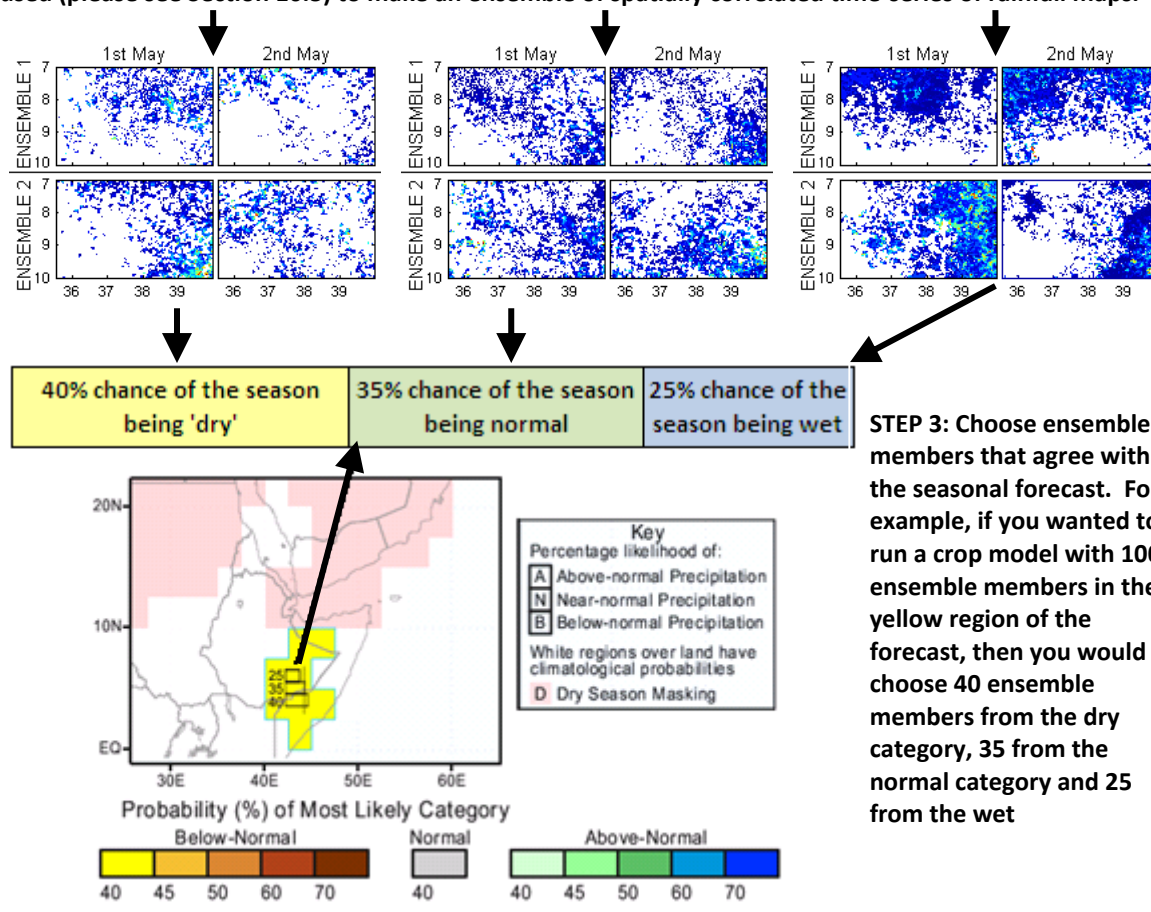


Figure 10.5. Schematic of the method used to use a tercile weather forecast to create a daily time-series of weather suitable for a crop simulation model

## 10.5 WEATHER GENERATORS

The previous Section provided an overview of the methods used to link a seasonal weather forecast and a crop simulation model. Many of these methods relied on the ability to create an ensemble of potential weather seasons which agree both with the seasonal forecast and the climate of the target location. To link to a crop model, these potential weather seasons need to include daily time-series of rainfall, solar radiation and temperature.

### 10.5.1. NON-PARAMETRIC TECHNIQUES

Various methods can be used to create this weather ensemble. One family of techniques can be labelled as non-parametric methods; these do not require pre-defined knowledge about which models should fit the data and are often based on resampling techniques (Rajagopalan *et al.*, 1997). Another non-parametric technique is that of ensemble re-ordering as presented in Ghile and Schulze (2009). In order to achieve a realistic level of interannual variability, these techniques require a large volume of data for calibration and so are not suitable for use in this particular project.

### 10.5.2. PARAMETRIC WEATHER GENERATORS

Parametric stochastic weather generators provide a different approach to the problem; these create an ensemble of artificial time-series of weather data based on modelling the statistical characteristics of observed weather (Wilks and Wilby, 1999). They generally rely on less data input than resampling techniques and have been linked in the past to both seasonal weather forecasts and crop simulation models (Wilks, 2001; Hansen and Indeje, 2004; Semenov and Doblas-Reyes, 2007; Apipattanavis *et al.*, 2010). .

A parametric weather generator is a stochastic model designed to produce long, realistic time-series of variables such as rainfall, temperature, solar radiation and relative humidity. These time-series can also be envisioned as an ensemble representing the uncertainty on one ‘general’ season. Weather generators are designed so that their overall statistics agree with climate statistics such as monthly means, the number and length of dry spells, the

number of days with extreme rainfall or interannual variability. A weather generator normally runs in two distinct stages to take into account the relative complexity of modelling rainfall. Rainfall occurrence and amount are first created, then the other variables of interest are modelled conditioned on rainfall. There are several good reviews on different weather generator approaches, in particular Wilks and Wilby (1999), Mavromatis and Hansen (2001) and C.I.C.S. (2004). This Section aims to briefly summarise the major concepts and products available.

There are two major schools of thought regarding parametric weather generation, Markov and Serial. The Markov approach was pioneered in Richardson (1981) and Richardson and Wright (1984). These papers presented the idea that rainfall occurrence could be modelled as a simple two-state first order Markov chain, dependent only on the probability of rain given that the day before was wet or dry. On rainy days, rainfall amount is sampled out of a locally calibrated gamma distribution. Finally, the other variables of interest are calculated from locally calibrated normal distributions conditioned on whether the day was wet or dry. The calibrations for these distributions change from location to location and from month to month. There are several drawbacks associated with the Richardson approach. First, the method requires a very long time-series of observed weather in order to calibrate the model correctly. One method of overcoming this was presented by the SIMMETO approach used within the WeatherMan weather generator, which estimates parameters from monthly summary data rather than raw daily values (Geng *et al.*, 1986; Geng *et al.*, 1988).

A second drawback to the Richardson approach is that the weather generator can only use information from the previous and current day to determine rainfall occurrence, which can result in an underrepresentation of persistent events such as dry or wet spells. More complex Markov chain weather generators were created to address this issue. For example, the MarkSim weather generator uses third order Markov chains which allow longer dry spells to be triggered (Jones and Thornton, 1993). Equally, WeatherMan2 incorporates a second-order hybrid Markov chain that simulates precipitation occurrence with a first-order chain if the previous day was wet or a second-order chain if the previous

day was dry (Hansen and Mavromatis, 2001). Serial weather generators were specifically developed by Racsko *et al* (1991) to overcome the underrepresentation of persistent events. In order to do this, serial weather generators first model a sequence of wet and dry spells from a semi-empirical distribution of spell length; this is normally a histogram created from observed spell lengths. During wet spells, rainfall amount is determined using another semi-empirical distribution. The remaining climate variables are then calculated based on their correlations with each other and on the wet and dry status of each day. LARS-WG is the most widely used example of a serial weather generator (Semenov *et al.*, 1998).

A final critique of the Richardson method is that it often underestimates interannual variability, both in rainfall means and in temperatures (Mavromatis and Hansen, 2001). Many weather generators have since attempted to correct this issue. For example, MarkSim resamples the baseline probit probability of rain each year to make interannual variability in monthly means agree with observations (Jones and Thornton, 1997). WeatherMan2 increases interannual variability by resampling monthly means from a contemporaneous, multivariate, first-order autoregressive Gaussian process. The model also introduces interannual variability into other synoptic variables by introducing an additive shift in the sequence of daily values for that month.

#### **10.5.3. INTER-COMPARISON STUDIES**

The advantage of a weather generator is that it can be designed to reproduce empirically the statistics which the user finds most important, even if the underlying physical processes behind them are complex. For instance a hydrologist might choose a weather generator designed to capture extreme rainfall events, whilst a crop modeller might be more interested in a model which is able to capture dry spells. This means there have been relatively few attempts to compare different weather generators over a range of locations or performance statistics, although there are more that validate a weather generator for a specific site. In terms of general intercomparisons studies, Mavromatis and Hansen (2001) compared the interannual variability of four weather generators (WeatherMan,

WeatherMan2, MarkSim and LARSWG) for 12 locations covering the USA, Central and South America and India. The paper showed that WeatherMan2 and MarkSim outperformed the others in terms of capturing interannual variability, although MarkSim did this at the expense of over predicting mean wet day frequencies. Hartkamp *et al* (2003) compared WGEN (the original Richardson weather generator), SIMMETO and MarkSim for 12 sites in central Mexico. In this case, no weather generator was ‘clearly superior’, although MarkSim again overestimated the length of wet spells. Semenov *et al.* (1998) compared the WGEN and LARS\_WG weather generators for 8 sites in ‘diverse climates’ across the US, Europe and Asia. This study found that LARS\_WG matched observed data more accurately than WGEN. To the author’s knowledge, there has been no intercomparisons of weather generators for locations in Africa, although there are papers validating weather generators against observations for specific African locations.

#### 10.5.4. INCORPORATING SPATIAL CORRELATION

One of the biggest challenges facing weather generator research is deciding how to best incorporate spatial correlation into the simulated time-series. The ability to do this would be of enormous benefit for applications such as modelling catchment rainfall, regional crop yield or the spread of weather influenced diseases such as malaria. A full catalogue and analysis of attempts to incorporate spatial correlations into weather generators is given in Baigorria and Jones (2010). The majority of methods are based on an approach devised in Wilks (1999) which proposes that spatially correlated random numbers are used to drive the weather generator across a grid of sites. This research has been taken forward by approaches such as Baigorria and Jones (2010), which uses a new orthogonal Markov chain algorithm to improve accuracy and computational speed. Non-parametric methods of defining the spatial correlation structure include Fowler *et al.* (2005), which uses sub-regional Neyman–Scott Rectangular Pulses (NSRP) rainfall models for spatial correlation and Apipattanavis *et al* (2007) which employs k-nearest neighbor bootstrap resampling to capture the distributional statistics of rainfall. One characteristic of all of these methods is that although they create spatially correlated rainfall statistics (i.e. if it dry in one area it is likely to be dry close by), they do not capture individual rainfall systems. As such, if one

was to employ one of these methods over a finely spaced grid, the resulting ‘map’ of rainfall for a given day would not necessarily look realistic. As rainfall is highly complex and intermittent, the ability to do this might provide a better product for end-users such as hydrologists and crop modellers. This issue has been addressed in part by Clark and Slater (2006), who presented a method for generating spatially coherent and correlated rainfall fields driven by information obtained from a network of rain-gauges. As described in the paper, the method uses locally weighted regression, where topographic attributes are used as explanatory variables to estimate spatial variations in precipitation occurrence and precipitation amounts. These are then used to define a conditional cumulative probability distribution function (CDF) of daily precipitation totals at each grid cell. Spatially coherent gridded ensembles are generated by using grids of correlated random numbers to sample from the CDFs at each grid cell. The next Section in this paper presents a similar method to address the spatial correlation issue, this time employing the geostatistical approach of sequential simulation.

## **10.6 RAININT**

### **10.6.1. INTRODUCTION**

It should first be noted that the method presented here is not a weather generator in itself. Rather it is a method of linking together ensembles produced by any existing site-specific weather generator at different locations, thus it has been labelled a ‘rainfall interpolation method’ rather than a regional weather generator. For easy reference, this label has been shortened to RainInt. The end product of the method is an ensemble of time-series of rainfall maps with the following characteristics:

- 1) Each map should have a realistic spatial correlation derived from observations.
- 2) The rainfall statistics at any pixel within the field (e.g. mean rainfall or the probability of rain) should agree with observed rainfall statistics at that location. The simulation method should also take into account the non-Gaussian nature of rainfall. This agreement should occur for a ‘reasonable ensemble size’ as defined by end-users

(normally 100-200 ensemble members); the system would be less useful if several thousand ensemble members were needed to ensure the mean field was reproduced.

- 3) Each ensemble member should provide an equally probable and realistic estimate of rainfall over the region.
- 4) The temporal statistics input from the site specific weather generator should be propagated throughout the field for each ensemble member, thus any one pixel should have realistic temporal statistics.

The methodology behind RainInt is described in Section 10.6.2 and Section 10.6.3. It is supported using a case study modelling April rainfall for the Oromiya region of Ethiopia, as shown in Figure 10.6. This region was chosen as it has a high density of rain-gauges, thus the system could be tested without the complication of using uncertain satellite rainfall estimates as a climatology.

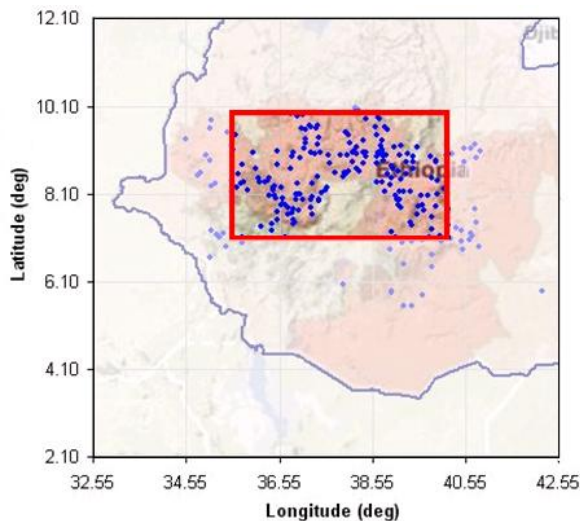


**Figure 10.6. Test region for the weather generator.** The Oromiya region is depicted as red shading and the Oromiya rain-gauge datasets are shown as blue dots.

Before the methodology is discussed further, is important to note two factors. The first is that the current state of research on RainInt is that it has been designed, created using the Matlab programming language and tested for internal consistency. The case study included in this Chapter is there simply to illustrate the method and highlight features; it

has not yet been comprehensively validated against observations. Future research planned to develop the system to an operational state is discussed in Section 10.6.5. The second factor to be noted is that the geostatistical process of sequential simulation underlies much of the methodology presented below. This was formally described in Chapter Six, thus a full mathematical description of the technique has not been presented here.

## 10.6.2. INPUT PARAMETERS

### 10.6.2.1. *Spatial statistics fields*

The basic concept behind RainInt is that a site-specific weather generator can be run at a selection of seed pixels. If these pixels are far enough apart to be spatially independent, then sequential simulation can be used to ‘fill in the gaps’, thus ensuring appropriate spatial correlation, a realistic underlying mean field and temporal correlation as defined by the statistics at the seed pixels. The following inputs are needed for sequential simulation for each month of the target region.

- A map of the probability of rain on a given day in the target month, the daily mean rainfall if raining, and the variance of rainfall if raining. The resolution of these images will determine the resolution of the final rainfall maps. The rainfall amount statistics could also be represented as the shape and scale parameters of the gamma distribution.
- An indicator residual variogram and a normalised rainfall amount residual variogram for the region of interest. The creation of these is discussed more in Section 6.4.3.

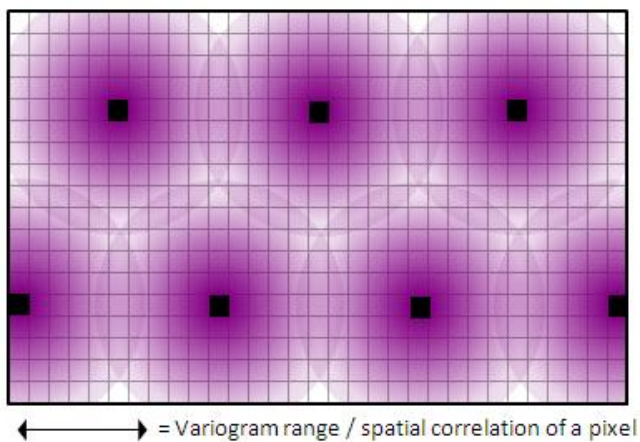
The maps and variograms described above need to be robust and unchanging within the region and time-scale of interest, in this case these monthly maps for the case study region. A monthly time-step was recommended for Ethiopia because the complexity of its climate. Less rapidly changing climatologies might only need these inputs for longer time-scales such as ‘the wet season’ or ‘summer’.

Figure 10.8 shows these inputs for the Oromiya case study. All of the inputs were created through kriging the Oromiya daily rainfall dataset discussed in Section 3.2.1.1. The rain-gauges making up this dataset are depicted as crosses in Figure 10.8 and dots in Figure

10.6. The dataset is not ideal for use in a weather generator as it is only based on 5 years of observations and so cannot be expected to be a true representation of the climate statistics. This is exacerbated by the fact that the indicator and rainfall amount variograms (Figure 10.8D and Figure 10.8E) have a relatively small range. Consequently even the high density of gauges used here is not enough to capture the complexity of the underlying climate. The result of this is that the maps in Figure 10.8A-C appear ‘patchy’, as a large proportion of the area is only being influenced by one rain-gauge or derived from the mean rainfall (because no gauge has any significant correlation with the target pixel). Clear examples of this can be seen in the high mean rainfall patch around the gauge positioned at 39.5° longitude, 8.75° latitude. Also, the region between 37-39° longitude, 7-8.5° latitude is outside the Oromiya region and so contains no gauges. Therefore, the statistics in this area are derived from the mean climatology. This suggests that the patch of high probability of rain at 37.5° longitude and 8.75° latitude is isolated even though in reality it might be expected to link with the wetter area in the South. However, as the motivation for the case study was simply to illustrate the method, the inputs provide a good test of RainInt’s ability to capture a spatially complex situation. A full discussion on the best methods for creating the rainfall maps is included in Section 10.6.5.

#### **10.6.2.2. Seed pixels**

One of the central components of RainInt is the selection of seed pixel inputs, thus it can be envisioned that the choice of site-specific weather generator and the location of the seed pixels will have a large effect on the final ensemble of rainfall fields. The seed pixel location selection method is based on the concept that the range of a variogram represents the radial distance over which rainfall is correlated. Therefore, a set of seed pixels can be selected in the target region which are close enough together that the temporal statistics of all pixels in the region are influenced by a seed pixel, but far enough apart that each seed is spatially independent. This is depicted schematically in Figure 10.7 and should allow the temporal correlations present in the site specific weather generator to propagate across the target region.



**Figure 10.7. The envisioned influence of the seed pixels (black pixels) on the other pixels in the target region.**

It is not trivial to answer the question ‘over what distance does a seed pixel have influence?’, but one that might be potentially important as it is the seed pixels propagating temporal statistics across the field. A first attempt might be to say that this is defined as the range of the variogram. However, in the Oromiya case study, Figure 10.8D-E both show that a nested variogram is appropriate for the dataset. In this case, it is expected that over 80% of the spatial correlation occurs within 30km of the seed pixel, but that there will still be some correlation up until ~500km away. Therefore, does one chose the separation distance at 50km or 500km?

Another factor that must be considered is the need for an adequately long time-series of observations at a seed pixel to calibrate the site-specific weather generator. This was more of a deciding factor in the Oromiya case study as there were very few locations where there was access to a long time-series of weather data. So in this case, four seed pixels were chosen at locations far enough apart that the semi-variance of the climatological variogram was greater than or equal to 1, but that there was a long time-series of data available. The chosen seed pixels are depicted as red squares in Figure 10.8A-C.

Once the seed pixels have been selected, one can then choose a site specific weather generator which best captures the input climate statistics. Ideally, the simulated probability of rain rainfall amount and rainfall variance should match the input fields. The weather

generator is then run for each of the seed pixels, to produce an ensemble of time-series for each location. LARS-WG was selected as the weather generator for this case study due to easy availability and reasonable performance in the weather generator intercomparisons studies discussed in Section 10.5.3. Again, it should be noted that as the aim of the case study is to demonstrate that the interpolation method works and is internally consistent rather than to validate its results against observations, so other weather generators were not tested in this case.

### 10.6.3. RAININT METHODOLOGY

Section 10.6.2 states all the ingredients needed for the sequential simulation process described in Chapter Six, albeit they come from a site specific weather generator and kriged observations rather than from satellite statistics. Consequently, the ‘standard’ sequential simulation methodology can be used to create the rainfall fields. This was formally described in Section 6.3 and schematically described in Section 6.5, so the description has not been repeated here. The only difference between the two methods is that in this case, the rainfall values at the seed pixels are not randomly taken from the underlying distribution, rather they are provided by the site-specific weather generator. One improvement to the method has been made in that nested variograms are now used. This should produce more realistic results, especially as the observed variograms in Figure 10.8 are best modelled using nested models.

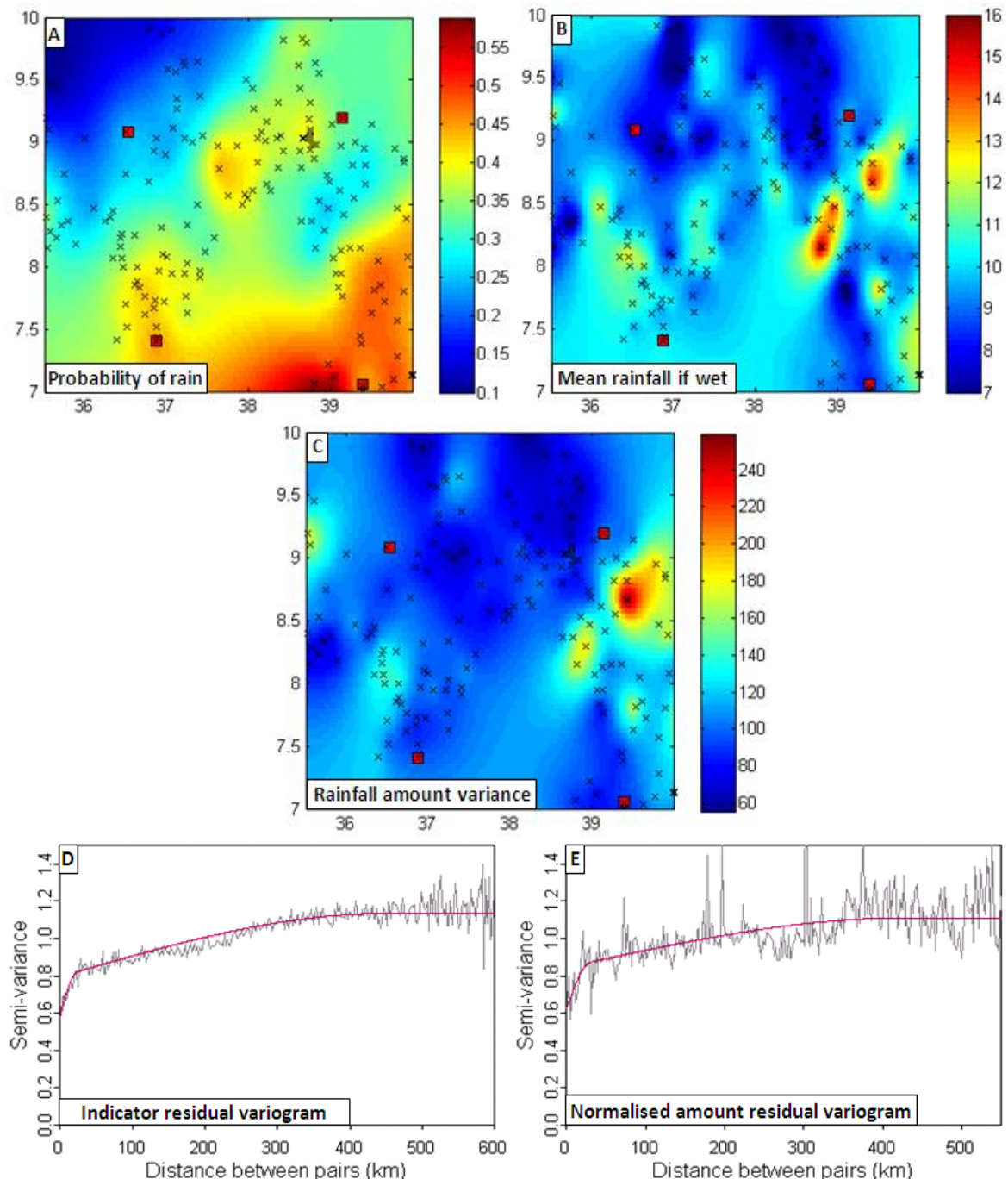


**Figure 10.8. Rain-gauge derived spatial inputs for the Ethiopian RainInt case-study.** Plot A depicts the probability of rain on a given day in April, plot B shows the mean rainfall amount if raining, plot C shows the rainfall variance if raining, plot D shows the indicator residual variogram and plot E shows the normalised rainfall amount residual variogram. In plots A-C, the crosses represent input rain-gauges and the red squares the selected seed pixels.

Plots A-C were made by calculating the appropriate statistics for the Oromiya gauges, then kriging these values. Therefore they are based on subtly different variogram than those shown here, but these variograms can be used to give a general idea about the spatial complexity of the field.

#### 10.6.4. INTERNAL CONSISTENCY

The system was run for 200 ensemble members for the Ethiopian case study. Four random ensemble members were pulled from the results and are depicted in Figure 10.9.

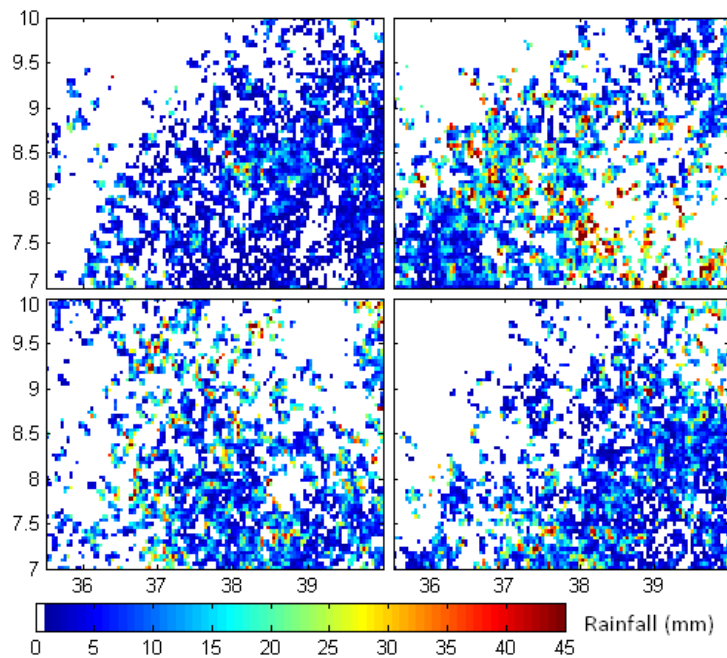


**Figure 10.9. Four random ensemble members from the Oromiya case study.**

With a large enough ensemble, the model is constrained to reproduce the ensemble mean in either the mean rainfall amount (if raining), or the probability of rain. In the satellite rainfall sequential simulation described in Chapter Six, the seed pixels were selected out of the prescribed input rainfall occurrence and amount distributions, thus ensuring the ensemble mean is reproduced was simply a check of internal consistency.

The matter is slightly more complex for RainInt. In this case, the seed pixels were generated by an independent weather generator. As the aim of the system is to propagate information from the seed pixels, if the statistics at the seed pixels differ greatly from the background fields shown in Figure 10.8, then one might expect the RainInt to struggle to capture the input fields in the ensemble mean. This can be seen in the ‘internal consistency’ plots in Figure 10.10 and Figure 10.11. Figure 10.10 shows how the ensemble mean rainfall occurrence compares to the input probability of rain.

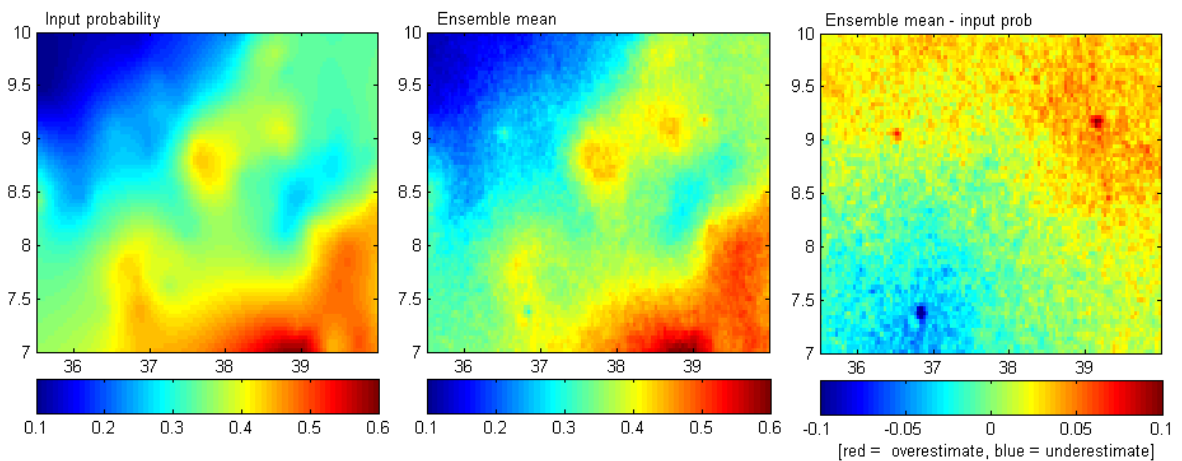


**Figure 10.10.** Comparison of input probability of rain (left) and the ensemble mean rainfall occurrence (centre). The plot on the right shows the ensemble mean minus the input probability, thus red colours mean that the system is overestimating rainfall occurrence and blue colours mean it is underestimating.

Although the pattern is clearly reproduced, the effect of the seed pixels can easily be seen in the residual plot on the right. On a positive note, this means that information is being propagated away from the seed pixels.

Capturing rainfall amount is more complex because the seed input time-series created by the weather generator contain days with zero rainfall whilst the rainfall amount process of sequential simulation considers rainfall amount if raining. This makes it difficult to integrate the seed pixels in to the model. As there were four seeds in the case-study, seed pixels recording zero rainfall could not simply be excluded on a given day. Instead two simple methods were tested to begin exploring how to address the issue.

Method 1: Seed pixels recording zero rainfall were set to 0.1mm so that it can be included in the gamma distribution. The concept behind this is that there should be low rainfall in the area around a dry seed pixel. It should be noted that this goes against the assumption of independence between rainfall amount and occurrence underpinning the sequential simulation method, but was the simplest method computationally.

Method 2: Seed pixels recording zero rainfall were replaced by the mean rainfall (if raining) for that particular month and ensemble member. If the weather generator had produced an entirely dry month for a given ensemble number, then the general mean

rainfall if raining for that pixel was used instead (i.e. April rainfall at that seed over all ensemble members).

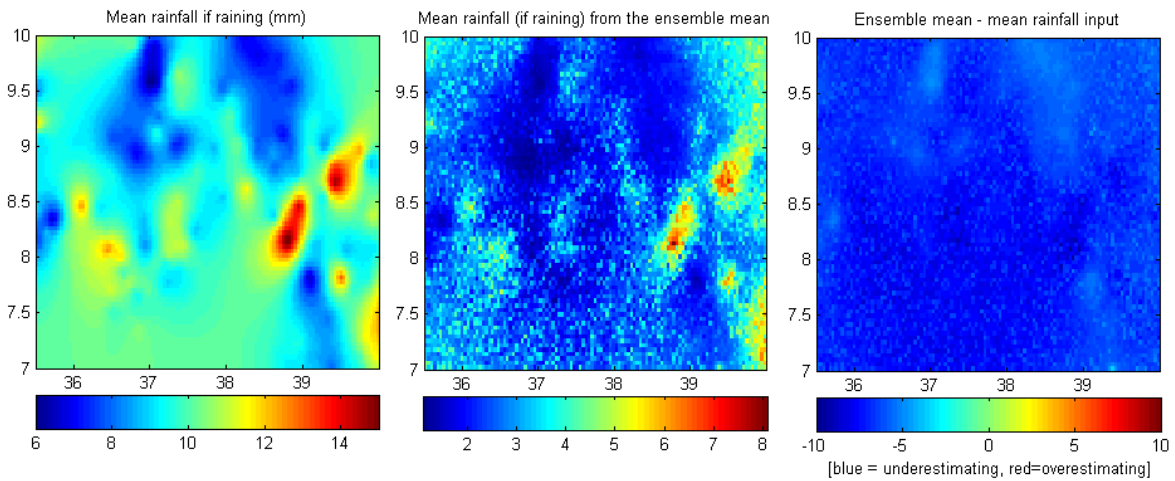


**Figure 10.11.** Comparison of input mean rainfall if raining (left) and the ensemble mean rainfall if raining (centre), using method 1 to replace zero rainfall values in the seed pixels. Note the different colour scales in each plot. The plot on the right shows the ensemble mean minus the input mean, thus red colours mean that the system is overestimating mean rainfall and blue colours mean it is underestimating.

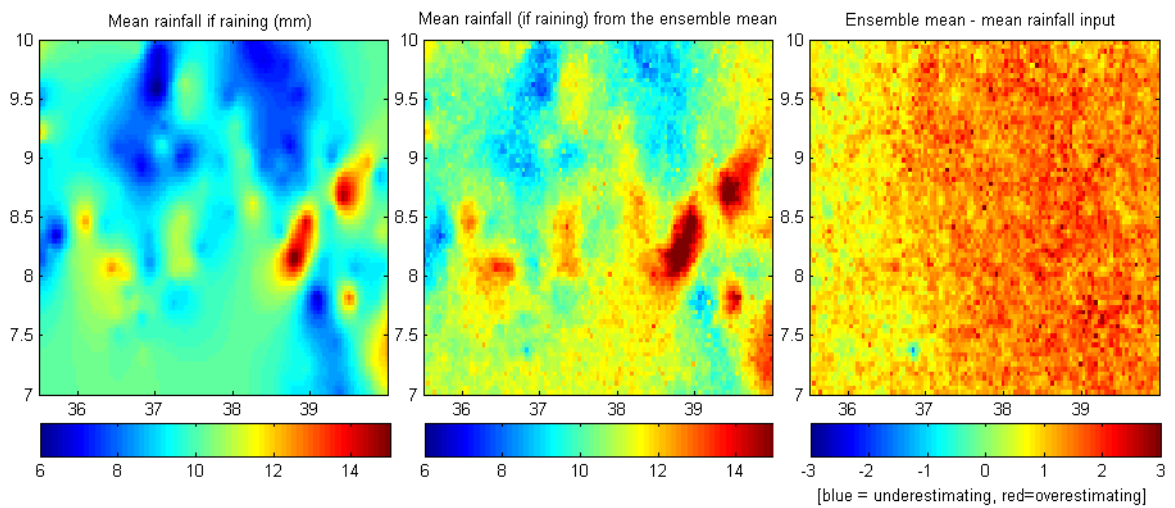


**Figure 10.12.** Comparison of input mean rainfall if raining (left) and the ensemble mean rainfall if raining (centre), using method 2 to replace zero rainfall values in the seed pixels. The plot on the right shows the ensemble mean minus the input mean, thus red colours mean that the system is overestimating mean rainfall and blue colours mean it is underestimating.

Figure 10.11 and Figure 10.12 show the results of using these methods for an ensemble of 200 members. As expected the impact of using Method 1 is large; each time there is zero

rainfall, the low seed value is forcing the system to select a rainfall amount value at the lower limit of the gamma distribution. Therefore the entire field severely underestimates rainfall amount. This impact is particularly severe in locations where the input mean rainfall if raining is high, because it is even more unlikely in those cases to randomly select a rainfall value of 0.1mm from the input gamma distribution thus repeatedly forcing this to happen has a larger effect.

The impact of Method 2 in Figure 10.12 is less severe, but it is still apparent that the mean rainfall field is not being reproduced. In this case it is overestimating, probably because filling in the zero rainfall gaps with the mean rainfall if raining has skewed the statistics of the seed pixels further away from the input mean field. The plots show that the situation is clearly more complex than expected, especially as it also relies on the spatial scale of the variogram (and so is very case specific). Extensive further investigation will be needed to formally test and solve the issue, or a new approach could be taken as discussed in Section 10.6.5. The variograms for the model are shown in Figure 10.13.

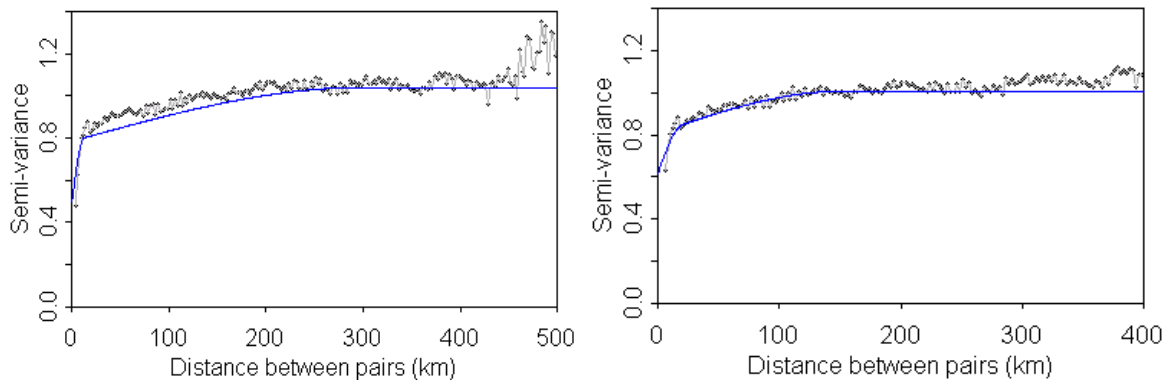


**Figure 10.13. Residual variograms input into the RainInt model for April (smooth blue lines) compared against experimental variograms created using individual ensemble members. The indicator residual variogram is on the left and the normalised residual amount variogram on the right.**

These show extremely good correspondence with the input variogram, showing that the methodology is internally consistent in that the RainInt code working as it has been defined. The results also show the advantage of adding the ability to create nested variograms into the sequential code as the ensemble variograms presented here agree much

better with their input model than the ensemble variograms creating using the sequential simulation code presented in Section 7.4.2.

#### 10.6.5. CHARACTERISTICS AND FEATURES

The general conclusion from the results presented above is that the method has been shown to work and be internally consistent. It is particularly encouraging that the spatial correlation has been preserved in the ensembles and that information is being propagated from the seed pixels to the rest of the field, which should ensure that temporal statistics are preserved. However, there are some issues which must be addressed as the system is developed further.

- ♦ *Creating realistic spatial input fields:* To produce realistic output, it is first important to adequately define the spatial input fields depicted in Figure 10.8. As discussed throughout this work, it can be difficult to obtain enough daily ground based observations to create such a field.
- ♦ *Linking seed pixels and the spatial input fields:* A problem highlighted in the case study above was that if the point based weather generator used to create the seeds fails to capture the spatial statistics provided by the input fields, then the resulting mismatch can have a large impact on the resulting ensemble.
- ♦ *A lack of interannual variability:* As discussed earlier in this Chapter and in detail in Mavromatis and Hansen, 2001, capturing interannual variability is something most weather generators find difficult to do. The RainInt system suffers particularly from this issue as the same input fields are used for a ‘general’ month (i.e. any given April), thus the interannual variability is suppressed still further.

To address these topics, the following extensions to the basic RainInt method have been proposed. These are still very much in their infancy and will be investigated in future work.

***Forcing the weather generator to agree with the mean field***

The simplest option to address the seed pixel/spatial field mis-match is by manipulating the point based weather generator output so that it is forced to match the spatial fields at the seed locations. However, this option would not address the issue of interannual variability or the source of the spatial fields.

***Using time-series at seed pixels which are directly generated from the mean field***

A second option is to ensure that the seed pixels come from the same source as the input spatial distributions. This would allow the use of a similar sequential simulation method to the one described in Chapter Six, where seeds are simply selected from distributions created from the spatial input fields. One method of fully integrating the seed pixel time-series and the spatial fields is to use the MarkSim weather generator. The main feature of MarkSim is that although it is still a point specific model, it can be used in any location in the tropics rather than relying on a rain-gauge being present. This is achieved by selecting from weather distributions derived from spatial fields of climate statistics, which are themselves generated from over 17,000 African weather stations. Therefore, the RainInt technique could take its inputs from MarkSim spatial fields and the MarkSim point based time-series derived from it. This would also allow a method of addressing interannual variability as MarkSim resamples the baseline probit probability of rain each year to make interannual variability in monthly means agree with observations.

***Using satellite estimates as inputs***

A natural response to the lack of rainfall information from ground based weather data might be to turn to the large amount of remotely sensed information now available. For instance the TAMSAT project has access to Meteosat data for 28 years (from 1983) and Chapter Six demonstrated that the sequential simulation process is able to realistically capture the uncertainty on a satellite rainfall estimate. In this case, two methods could be employed:

The first method would be to use the satellite estimates in exactly the same way as described in the original RainInt method. For example, satellite rainfall estimates would

be used instead of gauge information to make the mean spatial input fields. A Markov approach could then be employed to create pixel based time-series at the seed locations. This would reduce the computational burden of the system as there would be no reliance on an external weather generator. However, one could not be sure that the Markov method employed would be any better at linking the seed pixels to the spatial fields as in the original RainInt technique.

The second method of generating synthetic weather time-series from the satellite differs subtly from the RainInt system. Instead the method relies on two assumptions:

- 1) That sequential simulation can be used to generate a field of ensembles which agrees with a CCD field.
- 2) That the CCD field itself has temporal statistics which relate to the temporal statistics of rainfall.

If these assumptions are correct, then one has a large time-series of CCD fields with realistic spatio-temporal correlations which could be directly used to generate ensembles of spatially correlated rainfall time-series. This process could be envisioned as follows: First, a non-parametric resampling technique could be used to select CCD images from the Meteosat archive which preserve observe temporal correlations. Sequential simulation could then be used to create ensembles of rainfall fields based on the methods and calibrations described in Chapter Six. The result of this would be an ensemble of time-series of spatially correlated maps with a realistic interannual variability (as the method would preserve the interannual variability in the CCD fields).

A challenge associated with this technique would be to select an appropriate re-sampling approach that takes into account spatial correlation, or to define a single statistic that could be used with a standard resampling technique to select a series of CCD images. One would also need to consider the size of image which would be re-sampled e.g. would the entire image for the region of interest get resampled, or would it be split into large ‘meta pixels’?

## 10.7 FUTURE RESEARCH DIRECTIONS FOR SEASONAL FORECASTING AND WEATHER GENERATORS

Much of the work presented in this chapter is still in development, thus there is a rich selection of topics which could be investigated in future research.

### ***How to link the seasonal forecast and the satellite ensembles in the updating forecast system:***

On any day during the growing season, there will be  $n$  ensemble members of observed weather from the satellite from the beginning of the season and  $n$  ensemble members from the weather generator/seasonal forecast until the end of the season. These need to be paired so that each time-series from the satellite links to one from the weather generator. As the weather generator data from the beginning part of the season would still be available (it is simply being overwritten by the satellite data), an initial approach might be to match the two datasets according to cumulative rainfall amount. Another subtlety which must be addressed is how to deal with an ensemble member from the weather generator that clearly becomes unrealistic as the season goes on. Therefore another option might be to re-run the weather generator at each forecast date, but initialise it using the observed rainfall from the satellite. This means that the weather generator will be forced to react to the ‘observed’ rainfall amounts as the season progresses.

### ***What output format should the data be released in***

One of the underlying themes in this work has been an attempt to relate the research to an operational product for decision makers. It is relatively simple to view how yield is changing at one location if one uses the format presented in Figure 10.3 or through the use of a format such as a shifted probability of exceedance graph used in Hansen *et al.* (2011) and Cooper *et al* (2009). However, careful consideration must be paid to how to visualise the results at a regional scale. This also links with research questions about whether one should run the entire system at a regional scale (scaling up weather inputs) or to run the system at a fine scale and then scale the final crop yield estimates.

***What impact does critical moments in crop development and different seasonal forecasts have on the system***

One of the most important topics for future work is a general exploration of the system and the impact of uncertainty at different points in the crop cycle. This in itself will undoubtedly raise further topics for research.

## **10.8 CONCLUSION OF CHAPTER 10/PART 4**

This chapter explored the subject of seasonal crop yield forecasting. This first included a brief background on seasonal weather forecasting (Section 10.2) and a discussion of the structure of an operational crop yield forecasting system (Section 10.3). An important component of this system is the ability to link a probabilistic seasonal forecast with a crop simulation model. Traditionally, parametric and non-parametric weather generators have been used in this role as these create an ensemble of potential weather seasons which can be conditioned on the seasonal weather forecast.

A widespread feature of weather generators is their point based nature, thus to allow it to link with the regional crop yield forecasting system, the work in this chapter concentrated on efforts to incorporate spatial correlation into a weather generator. Section 10.6 described a new method of achieving this through the use of sequential simulation and presented preliminary results. Extensions to the method were discussed in Section 10.6.5. Finally, future research questions and directions on the topic of seasonal crop yield forecasting were discussed in Section 10.7.

# CHAPTER ELEVEN

# CONCLUSION

This Chapter draws together the main results from the thesis and attempts to examine them in light of the objectives discussed in the Introduction. Section 11.1 provides a brief summary of major results and limitations, before Section 11.2 discusses future directions of research.

## 11.1 SUMMARY OF MAIN RESULTS

Many countries in sub-Saharan Africa are highly dependent on rain-fed agriculture. When combined with a lack of coping mechanisms and crop management options, climate shocks can have a disproportionate effect on food security. This is particularly apparent in Ethiopia, which has an economy strongly linked to rain-fed agriculture and where it can be difficult to forecast, monitor or measure crop yield in time for regional food security assessments. It would be extremely useful for policy makers to be able to forecast regional crop yield either at the time of harvest or at the beginning of the season, as it would allow advance planning in the event of crop surplus or failure. Of equal importance is to be able to assign a measure of uncertainty to the forecast.

This thesis aimed to explore these issues, in particular focusing on two overarching themes:

- 1) *Quantifying the uncertainty in rainfall estimates for a complex African climate, focusing in particular on satellite rainfall estimation and seasonal weather forecasts*
- 2) *Researching how the uncertainty in estimated rainfall propagates through to uncertainty in modelled crop yield.*

These themes were investigated using a case study based on forecasting and hindcasting Ethiopian maize and aimed to answer the following specific questions:

- 1) How might satellite rainfall estimates be used as a substitute for sparse ground based weather observations in crop yield forecasting?
- 2) How can the uncertainty on satellite rainfall estimates be quantified and propagated through to an uncertainty in modelled crop yield?
- 3) How can the GLAM crop simulation model be modified to forecast maize?
- 4) How can a spatially correlated weather generator be created that is suitable for input into a regional scale crop simulation model?
- 5) How can the questions above be answered in the context of an operational crop yield forecast system for African policy makers?

The work in this thesis has fully addressed Questions 1-4 and a lot of headway has been made into addressing Question 5. The following sub-sections present a discussion of the specific work done to answer these questions and summarises the limitations and successes of the methods employed.

### **11.1.1. AN OPERATIONAL CROP YIELD FORECAST SYSTEM**

#### ***Main Results***

- ♦ In this work, a framework for an updating crop yield forecast system has been designed and put into the context of operational seasonal weather and crop yield forecasts for Africa.

#### ***Details***

In designing the structure of the system presented in Chapter Ten, a lot of thought was given to the requirements of African policy makers and other end-users. For such a product to be useful for food security decisions, it must be able to provide regional scale assessments of crop yield along with a measure of uncertainty. As estimates of crop yield are of interest to decision makers throughout the growing season, this work proposed an updating crop yield forecast system, described fully in the Introduction and in Section 10.3.

In brief, a crop simulation model can be driven at the beginning of the growing season using individual members of an ensemble of potential weather seasons conditioned on a seasonal weather forecast. As the season progresses, the initial forecast distribution of crop yield can be constantly renewed by updating the forecast weather ensemble with an ensemble of real-time/historical weather observations. This approach means that the uncertainty in estimating climate is sampled using the weather ensembles, then incorporated with the inherent & unquantifiable uncertainty present in a crop simulation model. Therefore the final system should capturing the complex non-linear relationship between climate and crop yield.

### **11.1.2. SATELLITE RAINFALL ESTIMATION FOR AFRICA**

#### ***Main results***

- ◆ An ensemble of daily rainfall estimates were designed, calibrated and validated for Ethiopia using a daily TAMSAT calibration.
- ◆ The methodology to do this was designed in a previous study (Teo and Grimes, 2007). This work added new features to the calibration, including multiple gamma generalised linear regression and a new method of selecting homogeneous calibration zones.
- ◆ The ensemble mean was evaluated as a daily deterministic rainfall product and were found to be as good as or better than other daily rainfall products, especially with respect to bias. This is particularly encouraging because the TAMSAT ensembles were evaluated at a finer scale than the other products (which also all use additional sources of microwave or gauge information in addition to infra-red inputs).

#### ***Details***

A well-documented feature of African climate studies is a lack of real-time ground-based weather observations. This provided a challenge for this thesis, as real-time rainfall information is a vital component of the operational crop yield system described above. As discussed in Chapter Four, this work chose to concentrate on satellite rainfall estimation as a replacement for rain gauges, due to full spatial coverage and real-time availability. In

particular, the Meteosat-derived TAMSAT rainfall algorithm were selected as the most appropriate estimation technique due to good performance in inter-comparison studies and because of previous work linking them to crop simulation models (Teo, 2006).

Daily TAMSAT rainfall estimates were first introduced in Teo and Grimes (2007) for a case study modelling Gambian rainfall. The complexity of Ethiopia's climate and the large region over which the estimates were required meant that a large part of the work in this thesis (presented in Section 4.3 and Chapter Five) was to extend the calibration method to include multiple, non-rectangular monthly calibration zones, gamma generalised linear models and multiple CCD temperature thresholds. The work was complicated by the fact that the calibration dataset was only available for the Oromiya region of Ethiopia, but that the areas where rainfall affects maize yield the most are found in the drier regions to the North and East.

A novel aspect of this work was to compare calibration zones derived using different input information, in particular comparing a calibration made using one zone, mean monthly rainfall isohyets, elevation contours, the 10-day TAMSAT calibration and zones drawn manually by eye. The results of this comparison are discussed in Section 5.4.2 and showed that the most appropriate zonation method was strongly linked with the seasonal rainfall cycle. During the main rainy season, rainfall isohyets outperformed the other zone methods. At the beginning and end of the rains, the more complex 'dekadal' hypothesis had the best fit, suggesting that the situation was complicated enough to need the extra information included in the dekadal fit (which was calibrated using much more historical rain gauge data than available for this study). Finally, in the dry season, there was less consistency in the zone choice apart from a general wet West/dry East divide, which again follows the main rainfall progression but is perhaps indicative of a lack of information from the limited calibration dataset.

Another interesting result was that many of the calibration months required multiple CCD temperature threshold information (discussed in Section 5.4). In particular, the optimum calibration for many of the drier months required one warm and one cold temperature

threshold. This might be because in these months, rainfall is more likely to come from less organised convection, therefore including information from colder temperature thresholds may indicate a method of removing cirrus contamination. Although this result is theoretically sound, it is relatively unexpected because previous TAMSAT studies have concluded that although multiple thresholds do provide additional information, they do not provide enough to warrant the additional complexity of a multiple linear model (Grimes *et al.*, 2003).

A validation of the daily calibration was presented in Section 7.2. Although there is a relatively large uncertainty at a pixel scale, the method was found to have a very low bias and compare comparably or better than other daily satellite estimates presented in similar validation studies for Ethiopia (Dinku *et al.*, 2008). It should be noted that the estimates cannot be used in their present form as a deterministic daily rainfall assessment. This is because the estimates were defined as the product of the probability of rain and the rainfall amount if raining, thus if they were used directly as a product, it would mean that rainfall occurrence would be vastly over-estimated. As the validation of the mean rainfall amount of the daily estimates showed some skill, a potential avenue of research would be to investigate how a daily deterministic TAMSAT estimate could be created.

It would be relatively simple to further improve the TAMSAT calibration because in this study all of the calibration data was situated in the relatively wet Oromiya region of Ethiopia. This made it difficult to extend the calibration or validation to the drier regions in the North or to the Somali and Danakil deserts, areas important for food security. However, National Meteorological Agencies internally have access to a lot more rain-gauge data, so the ensembles piloted in this thesis can be improved through future collaborations and research.

One limitation to the approach is that one of the assumptions behind the TAMSAT method is that rainfall comes from convective clouds. In Ethiopia's dry season from November to February, rainfall instead often comes from 'warm rain' processes. There are also so few rainfall events that the calibration data set from 2002-2006 included very little information

about the relationship between dry season rainfall and Cold Cloud Duration. The result of this was that the calibrations performed less well in the validation study for November and December and it decided that there was too little data to provide a calibration in January and February. Again, additional calibration data is likely to improve this situation.

### **11.1.3. CAPTURING UNCERTAINTY IN SATELLITE RAINFALL ESTIMATES**

#### ***Main results***

- ◆ Spatial correlation was incorporated into the TAMSAT calibration using the geostatistical process of sequential simulation using methodology derived in Teo, 2006.
- ◆ The work had to overcome the computational challenge of applying this process over a much larger geographic region than in the previous study.
- ◆ This study also included a validation of the ensembles for Ethiopia, which showed that they produced realistic estimates of Ethiopian rainfall fields which agreed both with an observed spatial correlation and the input mean fields of the probability of rain and the mean rainfall if raining.

#### ***Details***

One of the aims of the thesis was to research how to capture the uncertainty associated with the daily satellite estimates. The calibration discussed above and in Chapter Four and Five derived rainfall amount as the product of the probability of rain and the mean rainfall amount if raining. The calibration also included the variance of rainfall amount if raining, therefore it was natural to turn to a stochastic approach to sample from the rainfall occurrence and amount distributions at a given pixel. As the thesis has concentrated on regional climate and yield estimates, it was also important to incorporate spatial correlation into the estimates.

The geostatistical method of sequential simulation is discussed in Chapter Six and was employed to generate ensembles of daily rainfall maps, where the rainfall amount and occurrence were randomly sampled from the calibrated distribution at each pixel, but each

rainfall map had a realistic spatial correlation derived from observations. This ensemble approach was shown to work well in the validation study presented in Chapter Seven. One somewhat unrealistic feature of the ensembles was that they slightly overestimated the occurrence of low rainfall amounts. This could potentially lead to an overestimation of modelled maize yields if used in a crop simulation model, thus some thought was given as to the causes behind and how to remove excess low rainfall as discussed in Section 7.5. The modified ensemble then performed much better in the validation study.

#### **11.1.4. CROP SIMULATION MODELLING AND GLAM<sub>MAIZE</sub>**

##### ***Main results***

- ◆ In this body of work, a new parameterisation of the GLAM crop model was designed for tropical maize including a novel approach to addressing water stress during the anthesis silking interval.
- ◆ GLAM<sub>MAIZE</sub> was then driven using individual members of the satellite ensemble and modelled rainfall. Extensive investigation went into quality controlling any observations used in the model, especially as it was difficult to assess observed crop yields.
- ◆ GLAM<sub>MAIZE</sub> was shown to exhibit the correct sensitivities to climate inputs and performed reasonably well when compared against crop yield observations.

##### ***Discussion***

As discussed in Section 11.1.1, an operational crop yield forecasting system needs to be able to work at a regional scale if it is to be of use to policy makers. This presented an interesting challenge for this work because the growth and development of a plant is determined by its local environment and microclimate, thus some thought was given as to the best method for determining the regional response of a crop to weather. The matter was also complicated in the case study by the high spatial variability of Ethiopia's agronomy, which occurs due to the complexity of the country's topography and climate (described in Chapter Two and Chapter Three). Figure 2.1 clearly shows that there is a

relationship between Ethiopia's climate and crop yield, thus the crop simulation model chosen for this work was the General Large Area Model for annual crops, GLAM. This was because GLAM is a process based model designed to simulate tropical crop production in regions where there is an observed relationship between climate and crop yield and has been shown in previous studies to capture the crop/weather relationship at large scales (>> plot level) (Challinor *et al.*, 2004).

One of the main results of the thesis was the design of a new parameterisation of GLAM for tropical maize. This included modifying the phenology of the model, introducing a photo-sensitive phenological stage and designing a water stress routine for maize's anthesis-silking interval based on the research of Edmeades (1996). GLAM<sub>MAIZE</sub> was then run for each individual TAMSAT rainfall ensemble member and the results presented in Chapter Nine. The model was shown to exhibit the correct sensitivity to climate and to perform reasonably when compared with observed crop yields. The limitations of the approach with the current calibration dataset are discussed in more detail below:

#### *High altitude outputs*

One of the limitations of the GLAM<sub>MAIZE</sub> calibration arose from the scarcity of African maize cultivar parameters. GLAM requires several cultivar specific parameters to correctly calibrate it for a given region. As there are very few East African maize cultivars that are described in sufficient detail in literature, the model could only be calibrated for the Malawian MH16 cultivar of maize. Ethiopian agriculture is extremely complex with many different varieties of maize used by farmers to adapt to their climate, thus the use of a single cultivar in GLAM<sub>MAIZE</sub> led to unrealistic results in some high altitude locations as described below.

To reduce data input and make it appropriate for regional use, GLAM is designed to only include parameterisations that directly affect yield. For example, instead of modelling processes such as photosynthesis and individual leaf growth, GLAM uses parameterisations of transpiration efficiency and LAI. This means it is difficult to include parameterisations in GLAM of yield reduction or 'plant death' processes such as disease or

grain quality, which might naturally reduce the yield of a plant taking a long time to develop.

The time a plant takes to develop to maturity is one of the most important determinants of final yield and strongly dependent on growing season temperature. In turn, temperature is highly dependent on altitude, thus maize grown at a high altitudes will experience lower growing season temperatures, resulting in longer development times and higher yields. In this study, GLAM<sub>MAIZE</sub> was run using a single lowland maize cultivar that needs relatively high temperatures in order to develop. This means that for high altitude, low temperature pixels, GLAM<sub>MAIZE</sub> took an excessively and unrealistically long time to develop. The lack of plant death parameterisations meant that this resulted in improbably high values of LAI, biomass and yield, or, if the season took longer than an arbitrary ‘end of year’ cut off, recorded zero yield. The overall result was an unrealistic pattern of extremely high yields merged mixed with zero yields at high altitudes.

There are several methods of addressing this issue in future work. The first is to use a number of cultivars of maize which correspond to different regions and micro-climates. This would allow a more realistic approach to be taken in the study, especially as farmers in Ethiopia select from a large range of maize cultivars to ensure that they reduce the risk and maximise gains from their crops. This could also be achieved by working more closely with organisations such as the Ethiopian Institute for Agricultural Research. An alternative would be to build into the GLAM<sub>MAIZE</sub> code subroutines that reduce the yield of a plant that takes too long to develop.

#### *The influence of modelled synoptic weather observations*

A second limitation on this work was the lack of synoptic observations such as temperature and solar radiation. This meant that numerical model output from ERA-Interim had to be employed as a crop model input for non-rainfall variables. In reality, temperature and solar radiation are strongly linked to rainfall occurrence, thus the disconnect between the model derived synoptic data and satellite rainfall data might have introduced some unrealistic results. In addition, there has not been a validation study of ERA-Interim’s temperature

and solar radiation data over East Africa, although this study (in Section 9.4) and other literature (Maidment *et al.*, In press) found that the model strongly overestimated rainfall amounts. Finally, ERA-Interim is a reanalysis product and so is not available in real-time for use in an operational system.

A different approach in future work might be to use a stochastic weather generator to fill in the missing temperature data using a program such as WeatherMan (Pickering *et al.*, 1994). This approach was used successfully in Thornton *et al.* (1997) and would allow observed synoptic data to be added into the system as it becomes available. It should be noted that as for rainfall, care would have to be taken to incorporate spatial correlation into the output.

#### *Comparison with yield observations*

Although rain-fed agriculture is one of the primary drivers of the Ethiopian economy, robust and reliable records of crop yield have only become available since 2003. Before that date, this work found differences between different Ethiopian crop yield datasets which proved difficult to resolve (discussed in Section 2.5.2), consequently the yield data was of limited use for calibration or validation. The crop yield data available to this study (1997-2005) also showed very little interannual variability. One reason behind this might be because the majority of Ethiopian maize is grown in relatively wet regions by risk adverse farmers, therefore one might expect a similar value of yield in all but the most extreme years, of which the period 1997-2005 contained none.

The scarcity and uncertainty of Ethiopian yield observations meant that it was considered inappropriate to calibrate the Yield Gap Parameter of GLAM<sub>MAIZE</sub>, thus only attainable yield was modelled in this study. The data scarcity also made it difficult to verify the yield ensembles as discussed in Section 9.7. It should be noted that it was encouraging that the modelled trend for 2003-2005 matched that seen in observations, although as one is comparing three data points, this result might easily have occurred by chance. The Ethiopian authorities have access internally to a lot more observed yield data for calibration, therefore it is still feasible for an operational system to be able forecast

farmers' yields and for more extensive validation to be carried out. In addition, a concerted effort has gone into improving Ethiopian crop yield measurements since 2003 (discussed in Section 2.5.2), hence it is reasonable to assume that future work would be able to validate modelled crop yields in Ethiopia.

### 11.1.5. WEATHER GENERATORS

#### ***Main results***

- ◆ A novel method was designed in this study to spatially interpolate time-series output from a point specific weather generator. This employed the process of sequential simulation to create ensembles of time-series of spatially correlated rainfall maps.
- ◆ The method was then run for a case study modelling April rainfall to show internal consistency and a detailed discussion was included about future development plans.

#### ***Discussion***

As discussed in Section 10.4, seasonal weather forecasts rarely provide output in the correct format to input directly into a crop simulation model. Traditionally, parametric and non-parametric weather generators have been used to bridge this gap; these create an ensemble of potential weather seasons which can be conditioned on the seasonal weather forecast. A widespread feature of weather generators is their point based nature, thus there have been several attempts in research literature to incorporate spatial correlation into weather generator output (discussed in Section 10.5.4).

As the aim of this work was to study how a seasonal forecast can be linked to a crop simulation model at a regional scale, a significant part of this thesis focussed on the feasibility of applying a weather generator at a regional scale. The result of this research is discussed in Section 10.6, which introduced a new 'rainfall interpolation method', RainInt, based on the process of sequential simulation. The input to this system was a set of rainfall climatology maps, variograms of observed rainfall correlation and ensembles produced by a point based weather generator at a selection of seed pixels. The output of the system is an ensemble of spatially correlated rainfall maps, conditioned on the climatology but

incorporating the temporal statistics produced by the weather generator at the seeds. The method is still very much in development, but initial results show that individual ensemble members have a realistic spatial correlation and that rainfall occurrence ensemble statistics match the input observed climatology. RainInt needs to undergo significant development before it can be tested and employed as a viable method of creating spatially correlated rainfall ensembles. Such development was beyond the scope of this thesis, however the appropriate steps were discussed in detail in Section 10.6.5 and include a better method of linking the seed pixels to the climatology and creating interannual variability. The use of sequential simulation in RainInt provided an elegant link between the satellite and seasonal forecast weather ensembles, which should make it easier to incorporate them into a single crop yield forecast system in future research.

## **11.2 FUTURE RESEARCH DIRECTIONS**

There is much scope for future research into the themes presented in this thesis, both to overcome some of the limitations discussed above and to let the work evolve and grow in new directions.

### ***Overcoming data sparsity***

The scarcity of observed data had a large impact on many of the results presented above. However, the Ethiopian authorities have access to considerably more data than was used in this thesis, thus there is a strong case for collaboration to ensure that future research is both includes more data and is designed in collaboration with end-users.

### ***Weather generators***

One of the most promising avenues of future research is to extend the introductory work done on the RainInt regional weather generator. As discussed in Section 10.6.5 and 10.7, the aim of this work will be to overcome the limitations found in the current system. In particular, these include introducing a realistic level of interannual variability into the system and studying the optimum methodology of linking the input climatologies and seed pixels. Some thought will also be given to the ‘new satellite based approach’ proposed in

Section 10.6.5. If this could be developed into a working technique, it would provide an elegant component to the operational crop yield forecasting system. In particular, it would mean that rain-gauges would only have to be used to calibrate the satellite at the beginning of the process (which means the system would not have rely on a long time-series of gauge data being available). There are 30 years of satellite data currently available from TAMSAT's TARCAT archive, which is relatively short time-period on which to calibrate a weather generator but is still much more information than available in many regions of Africa. It should be noted however that this work found that satellite rainfall estimates also underestimated interannual variability (discussed in Section 7.4.3), thus this issue will also need to be addressed in a satellite based weather generator.

#### ***Seasonal forecasts and an updating forecast system***

Once the regional weather generator has been improved and validated, it can be used as a link between a seasonal weather forecast and the crop simulation. A proposed method of achieving this is discussed in Section 10.3. Once this has been accomplished, there are several directions future research might take. These include testing the sensitivity of the crop simulation model to different seasonal forecasts, validating the system using historical seasonal weather forecasts and comparing against different systems (for example those based on dynamical forecasts) and determining output formats which best communicate uncertainty to non-scientists. It would also be interesting to apply the system in new regions of Africa, especially those where maize is subject to water stress.

#### ***A question of scale***

A large part of this thesis was concerned about how to integrate the spatiotemporal scales of crop simulation models and their weather inputs. For example, a regional scale crop simulation model was used and the satellite and weather generator ensembles could be applied at any resolution. These now provide the tools to answer many new research questions. These include

- Would running the system at a high resolution, then scaling the results to a regional scale give the same results as running the system at a regional resolution.

- What characteristics of weather are the most important for a regional crop simulation model? E.g. dry spells, extreme rainfall events, mean rainfall amount. How do these characteristics change at different spatial scales and in different stages of crop development.

### ***GLAM<sub>MAIZE</sub>***

There are two potential improvements for GLAM<sub>MAIZE</sub>. One would be to include ‘plant death’ routines to stop pixels recording unrealistically high yields. A second would be to add a water-logging routine so that excess rainfall can have a negative effect rather than disappearing as run-off.

### ***Including temperatures and improving synoptic inputs***

This thesis concentrated primarily on the uncertainty in rainfall amounts, therefore it would be extremely interesting to apply some of the research ideas to temperature and solar radiation estimates, especially as the results presented in Chapter Nine showed that temperature had a large impact on modelled crop yield. In the event that synoptic data could not be obtained, it would also be interesting to replace the ERA-Interim with the output from a synoptic weather generator as in Thornton *et al.* (1997).

### ***Deterministic daily rainfall estimates***

Finally, one of the successes of this thesis was in creating daily satellite rainfall estimates which performed well in validation studies. It would be interesting to continue this work to create and test a deterministic daily rainfall estimate using some of the ideas discussed in Section 11.1.2.

### **11.3 FINAL COMMENTS**

The aim of this thesis was to investigate how to quantify the uncertainty in rainfall estimates for a complex African climate and to see how this uncertainty propagates through to estimates in crop yield. This was achieved through the development of satellite based rainfall ensembles, a regional scale weather generator and a new parameterisation for the GLAM crop simulation model. This thesis also allowed communication between the UK climate research community and Ethiopian decision makers. This provided valuable information about how the research presented in this thesis might be used in an operational system and just as importantly, allowed the author to experience working in a new and interesting culture.

# APPENDIX ONE

## TAMSAT CALIBRATION

## PARAMETERS

This appendix contains a full set of calibration parameters and plots for the ensembles calibration discussed in Chapter Five. To recap, the equations needed for the calibration for each zone are:

$$P(Z > 0 | CCD = D_T) = p = \begin{cases} \frac{1}{e^{-b_0 + b_1 D_T}} & D_T > 0 \\ p_0 & D_T = 0 \end{cases} \quad A1.1$$

$$f(Z | Z > 0, CCD = D_T) = g(\mu | D_T, \sigma | \mu) \quad A1.2$$

$$\mu = a_0 + a_1 D_{30} + a_2 D_{40} + a_3 D_{50} + a_4 D_{60} \quad A1.3$$

$$\sigma^2 = \begin{cases} \kappa_c \mu^{\theta_c} - \kappa_G \mu^{\theta_G} + \bar{\sigma}_l^2 & \kappa_c \mu^{\theta_c} \leq \kappa_G \mu^{\theta_G} \\ \bar{\sigma}_l^2 & \kappa_c \mu^{\theta_c} > \kappa_G \mu^{\theta_G} \end{cases} \quad A1.4$$

Please note these are equivalent to equations 4.3, 4.4, 4.7 and 4.11; they are simply included here for easy reference. In all cases,  $\sigma_l^2$  is set to 2.5 mm as discussed in Section 4.3.2.3. This Section summarises the zone and parameter choice for each month.

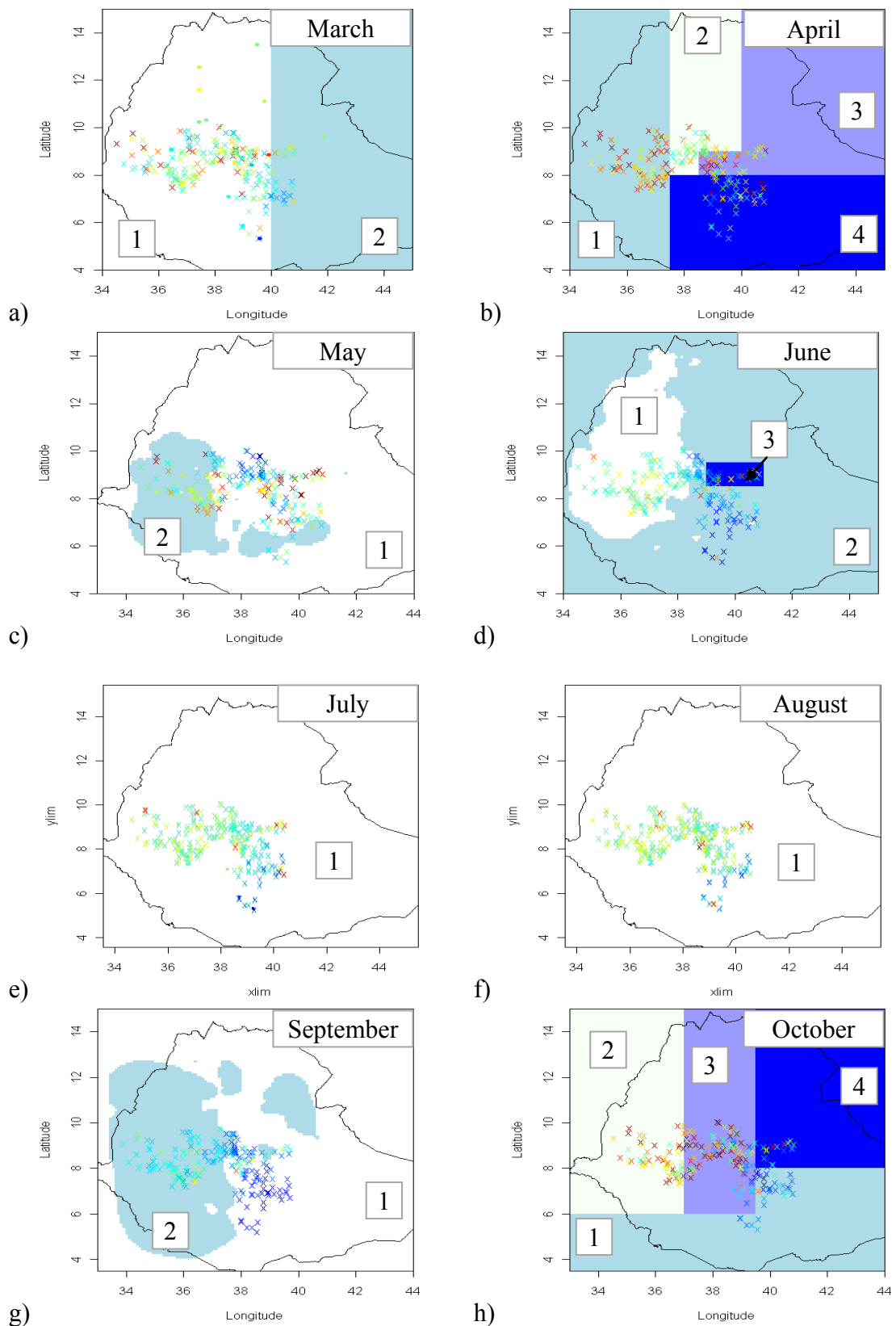
### A1.1. ZONE CHOICE

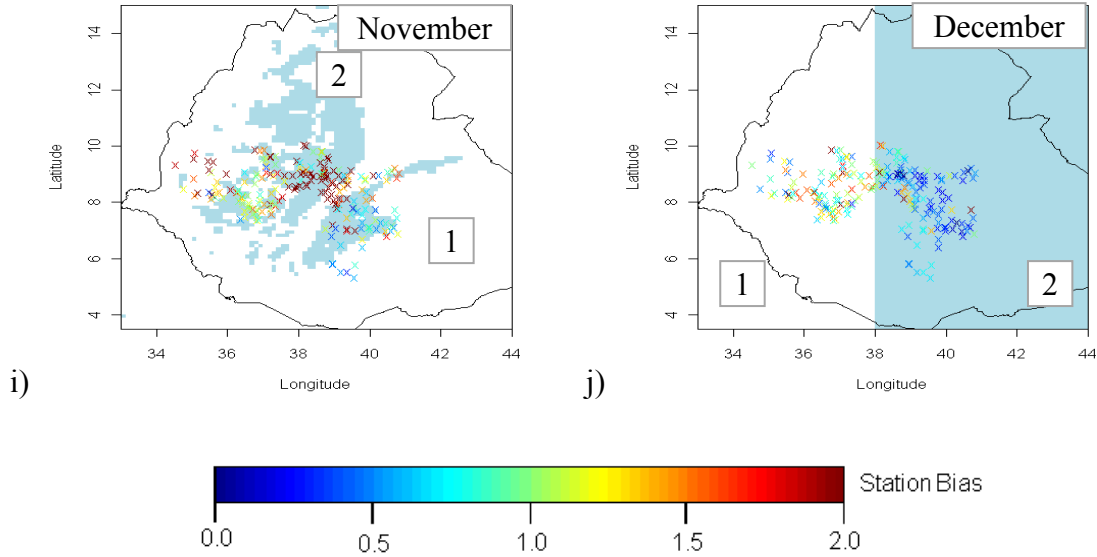
These plots show the zonal divisions for each month. Superimposed on each plot are the rain/no rain bias for CCD threshold 30 for each rain-gauge during that month.

---

## Appendix Two Statistical definitions and tests

---





## A1.2. CALIBRATION PARAMETERS

This Section contains all the calibration parameters for each month. The probability of rain and the error parameters are portrayed graphically in latter sections of the appendix. Note, there are no plots for the linear regression of rainfall amount. This is because a multiple regression has been performed, thus the plots would be too complex to elicit useful information. The residual indicator variograms and the normalized residual variograms are portrayed graphically in Section 7.4.2.

### A1.2.1 March.

Zone	Probability			Rainfall amount				Error analysis				
	$p_0$	$b_0$	$b_1$	$a_0$	$a_1$	$a_2$	$a_3$	$a_4$	$\kappa_C$	$\theta_C$	$\kappa_G$	$\theta_G$
1	0.21	-0.0012	0.058	6.24	0.33	-	0.21	-	0.75	0.77	3.72	0.34
2	0.17	-0.308	0.086	7.64	0.37	-	-	-	0.88	0.54	2.67	0.42

**Indicator variogram:** Type: Exponential, Nugget: 0.77, Range: 178 km, Sill: 0.44

**Residual variogram:** Type: Exponential, Nugget: 0.62, Range: 26 km, Sill: 0.39

### A1.2.2 April

Zone	Probability			Rainfall amount					Error analysis			
	$p_0$	$b_0$	$b_1$	$a_0$	$a_1$	$a_2$	$a_3$	$a_4$	$\kappa_C$	$\theta_C$	$\kappa_G$	$\theta_G$
1	0.15	-0.539	0.068	7.98	0.19	-	-	0.24	0.27	0.95	10.32	0.13
2	0.20	-0.156	0.07	7.24	0.26	-	0.34	-	0.44	0.79	7.02	0.21
3	0.15	-0.290	0.07	8.13	0.30	-	-	-	0.70	0.89	4.59	0.33
4	0.23	-0.267	0.04	8.32	0.23	-	-	0.27	0.36	0.88	4.37	0.34

**Indicator variogram:** Type: Exponential, Nugget: 0.74, Range: 328 km, Sill: 0.544

**Residual variogram:** Type: Exponential, Nugget: 0.64, Range: 31 km, Sill: 0.349

### A1.2.3 May

Zone	Probability			Rainfall amount					Error analysis			
	$p_0$	$b_0$	$b_1$	$a_0$	$a_1$	$a_2$	$a_3$	$a_4$	$\kappa_C$	$\theta_C$	$\kappa_G$	$\theta_G$
1	0.12	-0.778	0.093	6.72	0.20	-	-	0.20	0.79	0.45	4.42	0.32
2	0.20	-0.218	0.071	8.12	0.13	-	-	0.17	0.89	0.37	2.79	0.40

**Indicator variogram:** Type: Exponential, Nugget: 0.60, Range: 580 km, Sill: 1.259

**Residual variogram:** Type: Exponential, Nugget: 0.457, Range: 31.7 km, Sill: 0.497

### A1.2.4 June

Zone	Probability			Rainfall amount					Error analysis			
	$p_0$	$b_0$	$b_1$	$a_0$	$a_1$	$a_2$	$a_3$	$a_4$	$\kappa_C$	$\theta_C$	$\kappa_G$	$\theta_G$
1	0.31	0.3752	0.052	6.74	0.27	-	-	-	0.98	0.32	17.28	0.01
2	0.54	1.0058	0.046	8.86	0.16	0.14	0.13	-	0.78	0.94	4.51	0.30
3	0.27	-0.611	0.093	7.87	0.16	-	-	-	1.20	0.14	19.57	0.00

**Indicator variogram:** Type: Exponential, Nugget: 0.0 , Range: 51 km, Sill: 1.0

**Residual variogram:** Type: Exponential, Nugget: 0.23, Range: 8.9 km, Sill: 0.73

---

*Appendix Two Statistical definitions and tests*

---

### A1.2.5 July

Zone	Probability			Rainfall amount					Error analysis			
	$p_0$	$b_0$	$b_1$	$a_0$	$a_1$	$a_2$	$a_3$	$a_4$	$\kappa_C$	$\theta_C$	$\kappa_G$	$\theta_G$
I	0.47	1.01	0.053	9.34	0.247	-	-	-	0.87	0.39	9.46	0.19

**Indicator variogram:** Type: Spherical, Nugget: 0.65 , Range: 53.74 km, Sill: 1.0

**Residual variogram:** Type: Exponential, Nugget: 0.46 , Range: 24.85 km, Sill: 1.0

### A1.2.6 August

Zone	Probability			Rainfall amount					Error analysis			
	$p_0$	$b_0$	$b_1$	$a_0$	$a_1$	$a_2$	$a_3$	$a_4$	$\kappa_C$	$\theta_C$	$\kappa_G$	$\theta_G$
I	0.48	0.783	0.0578	9.16	0.22	-	-	-	0.22	0.98	7.08	0.26

**Indicator variogram:** Type: Spherical, Nugget: 0, Range: 57 km, Sill: 1.0

**Residual variogram:** Type: Exponential, Nugget: 0, Range: 32 km, Sill: 1.0

### A1.2.7 September

Zone	Probability			Rainfall amount					Error analysis			
	$p_0$	$b_0$	$b_1$	$a_0$	$a_1$	$a_2$	$a_3$	$a_4$	$\kappa_C$	$\theta_C$	$\kappa_G$	$\theta_G$
I	0.4	0.3928	0.0673	7.83	0.293	-	-	-	0.92	0.19	16.5	0.01
2	0.46	0.6558	0.0643	8.45	0.203	-	-	0.138	0.91	0.24	7.79	0.19

**Indicator variogram:** Type: Exponential, Nugget: 0.6, Range: 70 km, Sill: 1.0

**Residual variogram:** Type: Spherical, Nugget: 0.6, Range: 27 km, Sill: 1.0

---

*Appendix Two Statistical definitions and tests*

---

### A1.2.8 October

Zone	Probability			Rainfall amount					Error analysis			
	$p_0$	$b_0$	$b_1$	$a_0$	$a_1$	$a_2$	$a_3$	$a_4$	$\kappa_C$	$\theta_C$	$\kappa_G$	$\theta_G$
1	0.385	0.519	0.068	7.73	0.20	-	-	-	1.23	0.04	1.89	0.45
2	0.179	-0.096	0.046	7.23	0.16	-	-	0.13	1.04	0.95	1.17	0.56
3	0.173	-0.802	0.167	7.18	0.25	-	-	-	0.79	0.24	1.30	0.57
4	0.089	-0.850	0.071	7.65	0.17	-	-	-	1.25	0.04	1.53	0.53

**Indicator variogram:** Type: Exponential, Nugget: 0.44, Range: 50 km, Sill: 1.0

**Residual variogram:** Type: Exponential, Nugget: 0.53, Range: 13 km, Sill: 1.0

### A1.2.9 November

Zone	Probability			Rainfall amount					Error analysis			
	$p_0$	$b_0$	$b_1$	$a_0$	$a_1$	$a_2$	$a_3$	$a_4$	$\kappa_C$	$\theta_C$	$\kappa_G$	$\theta_G$
1	0.098	-0.906	0.010	6.49	-	0.11	-	-	0.93	0.33	12.50	0.00
2	0.064	-1.662	0.180	6.06	-	0.13	0.32	-	0.74	0.66	9.49	0.05

**Indicator variogram:** Type: Spherical, Nugget: 0.22, Range: 400 km, Sill: 1.0

**Residual variogram:** Type: Spherical, Nugget: 0.70, Range: 108 km, Sill: 1.0

### A1.2.10 December

Zone	Probability			Rainfall amount					Error analysis			
	$p_0$	$b_0$	$b_1$	$a_0$	$a_1$	$a_2$	$a_3$	$a_4$	$\kappa_C$	$\theta_C$	$\kappa_G$	$\theta_G$
1	0.106	-0.405	0.087	6.01	0.41	-	-0.28	-	0.78	0.78	1.78	0.54
2	0.125	0.345	0.060	6.28	0.57	-	-	-				

**Indicator variogram:** Type: Exponential, Nugget: 0.40, Range: 123km, Sill: 1.0

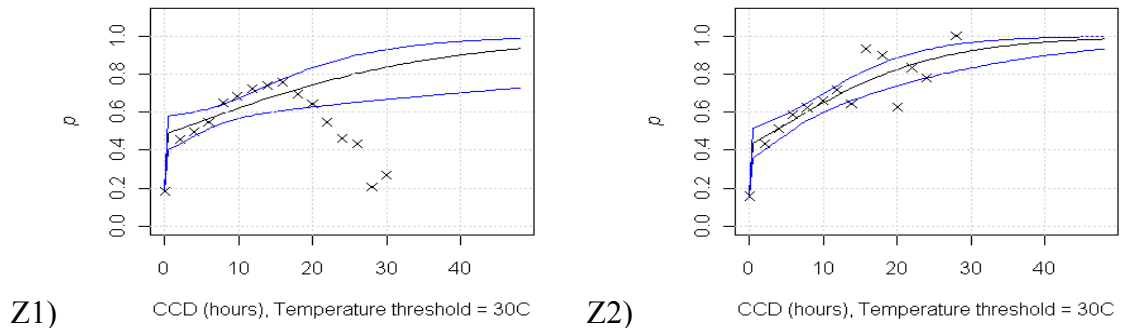
**Residual variogram:** Type: Exponential, Nugget: 0.77, Range: 5km, Sill: 1.0

Note, the entire region was treated as one zone in December for the error parameters because the iterative least squares calibration approach failed to converge to a solution when the two zones were treated independently.

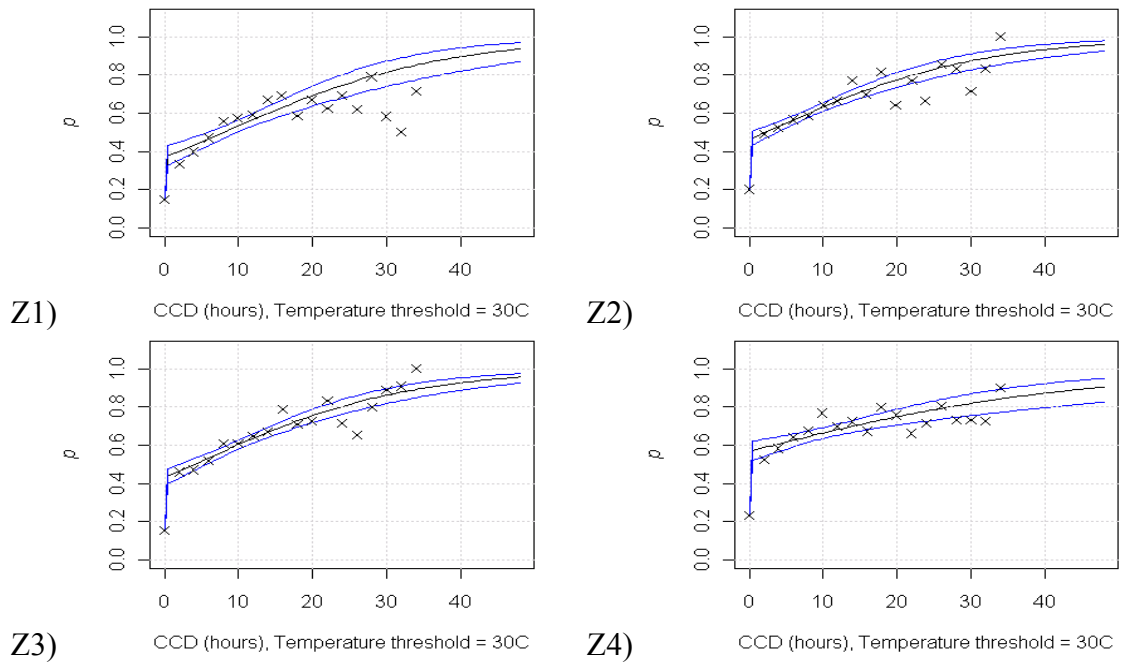
### A1.3. PROBABILITY OF RAIN

This collection of plots shows the probability of rain (from the calibration kriged rain-gauge dataset) against CCD for each month and zone. They also shows the weighted logistic regression fit (black solid line) plus 90% Confidence intervals (blue lines)

#### A1.3.1 March



#### A1.3.2 April

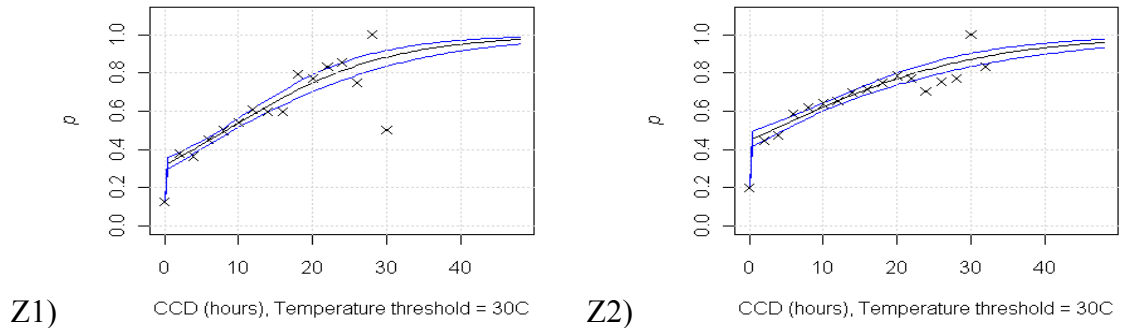


---

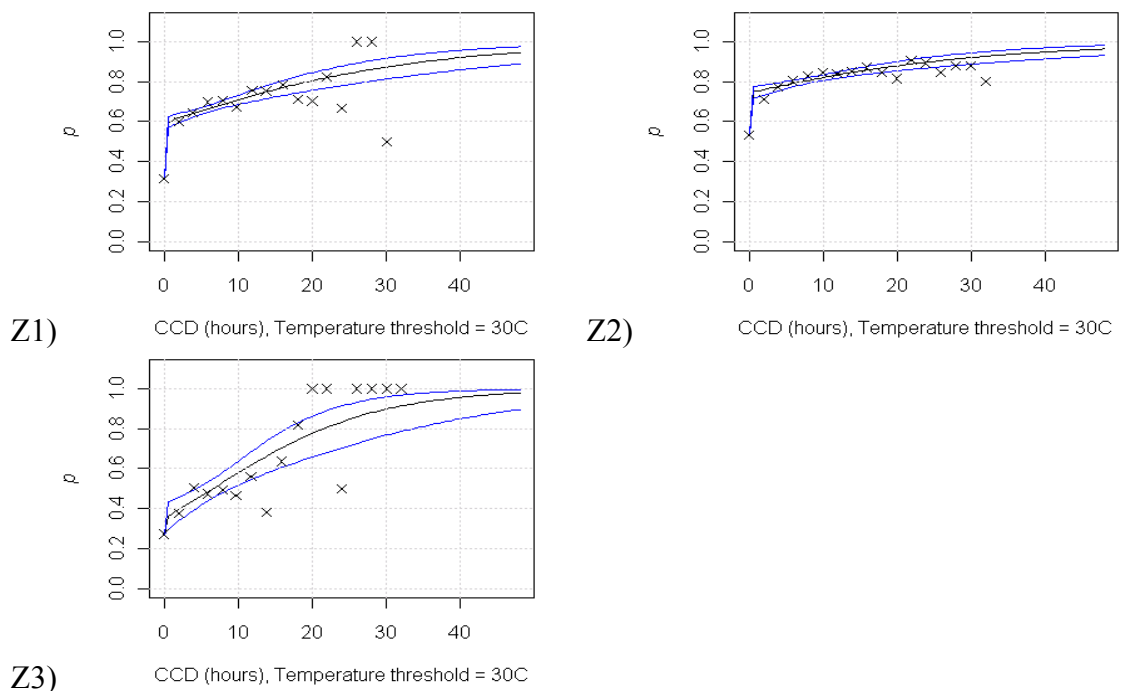
## Appendix Two Statistical definitions and tests

---

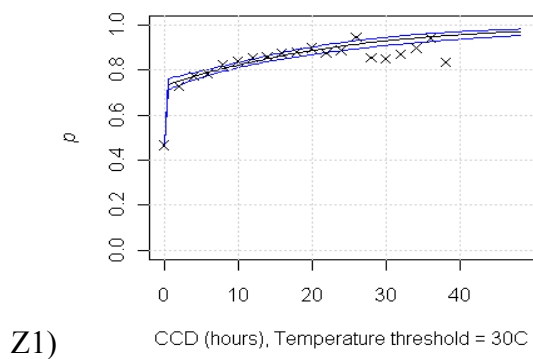
### A1.3.3 May



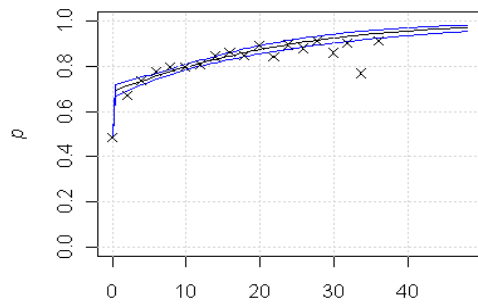
### A1.3.4 June



### A1.3.5 July

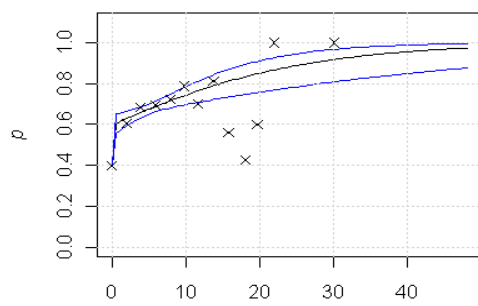


**A1.3.6 August**

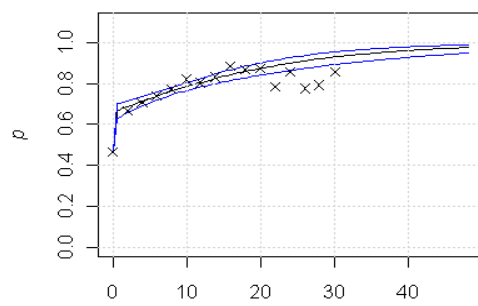


Z1) CCD (hours), Temperature threshold = 30C

**A1.3.7 September**

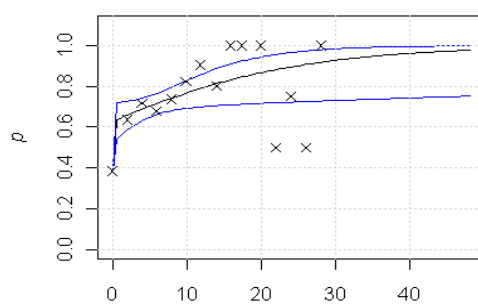


Z1) CCD (hours), Temperature threshold = 30C

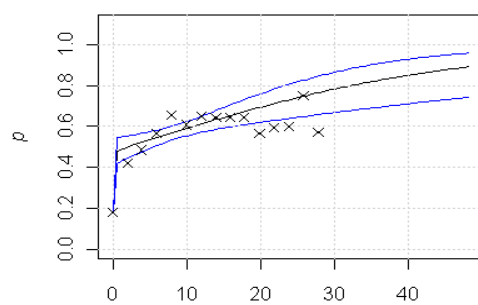


Z2) CCD (hours), Temperature threshold = 30C

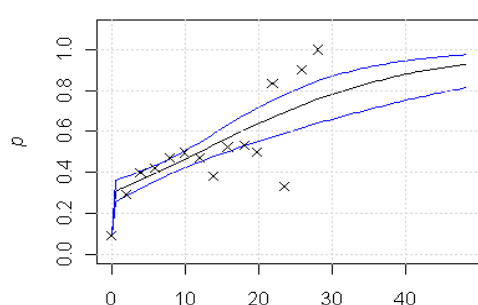
**A1.3.8 October**



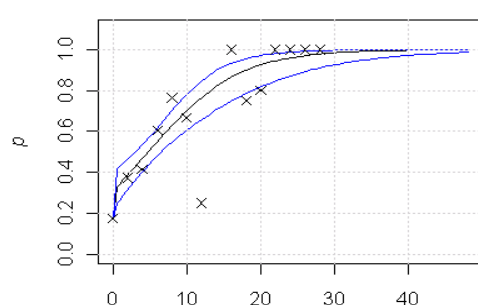
Z1) CCD (hours), Temperature threshold = 30C



Z2) CCD (hours), Temperature threshold = 30C

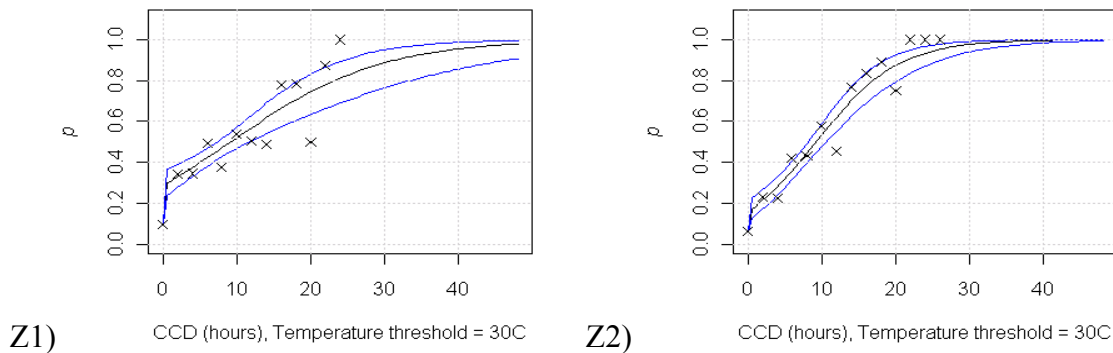


Z3) CCD (hours), Temperature threshold = 30C

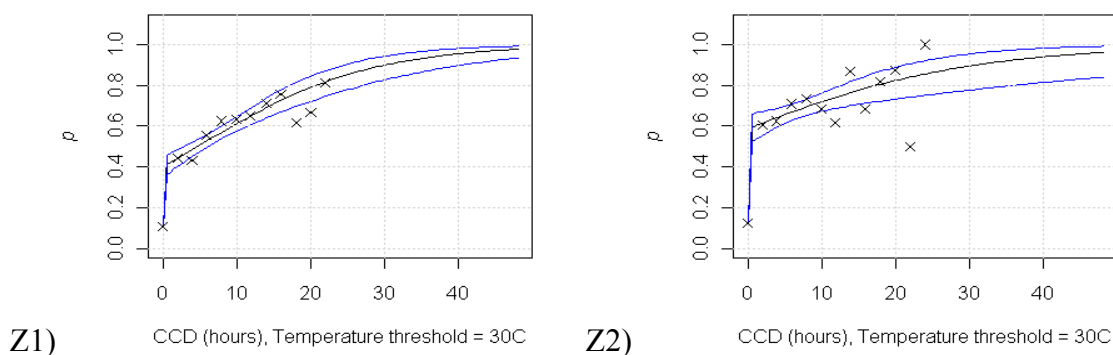


Z4) CCD (hours), Temperature threshold = 30C

### A1.3.9 November



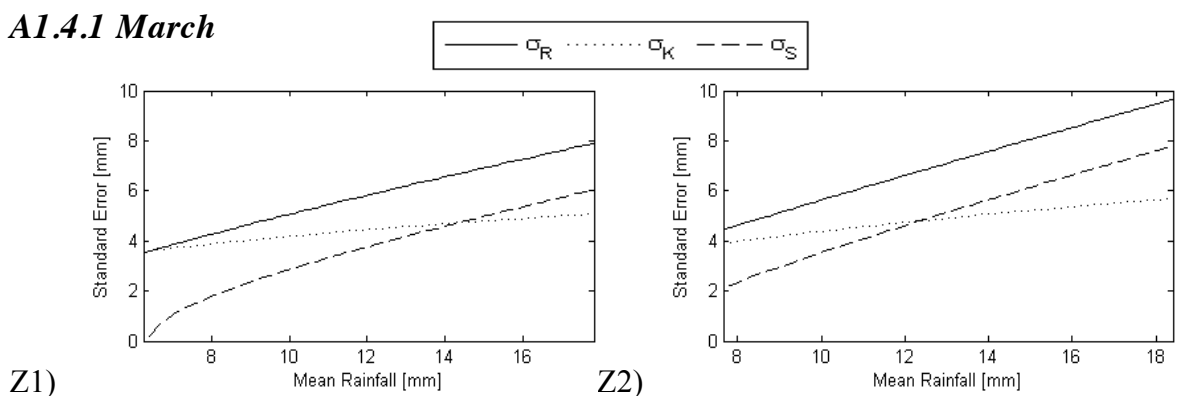
### A1.3.10 December



## A1.4. ERROR REGRESSIONS

These plots show the error regressions from equation A1.4 for each month and zone. In each plot the regression for the kriged gauge variance is denoted by  $\sigma_K$ , the regression variance by  $\sigma_R$  and the difference by  $\sigma_S$ . Note that in all cases, a minimum variance of 2.5 has been applied, as discussed in Section 4.3.2.3.

### A1.4.1 March

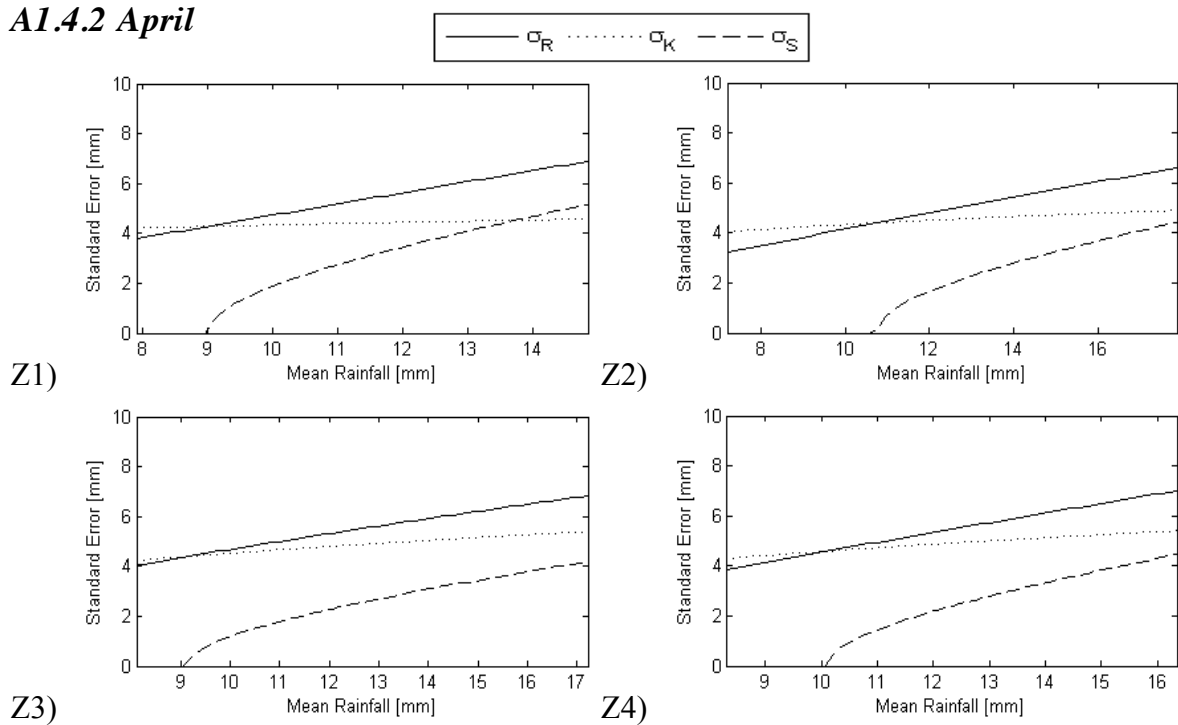


---

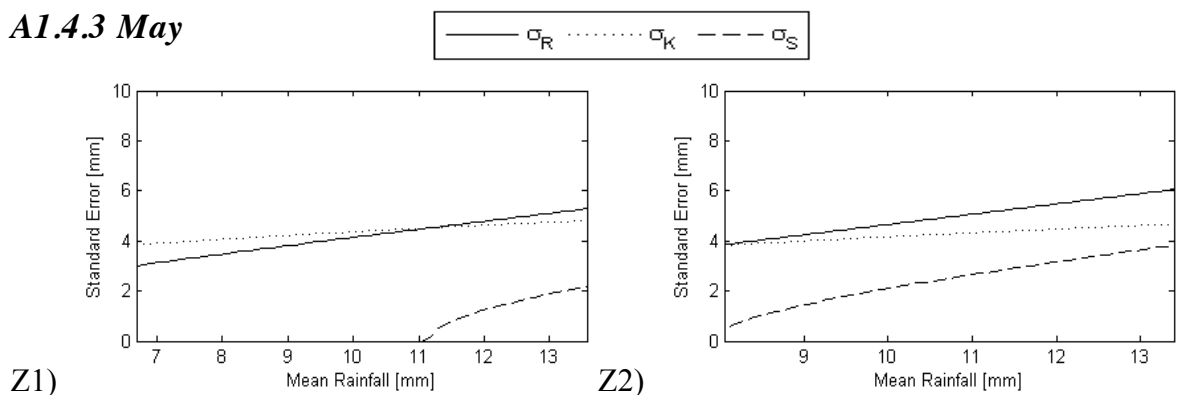
*Appendix Two Statistical definitions and tests*

---

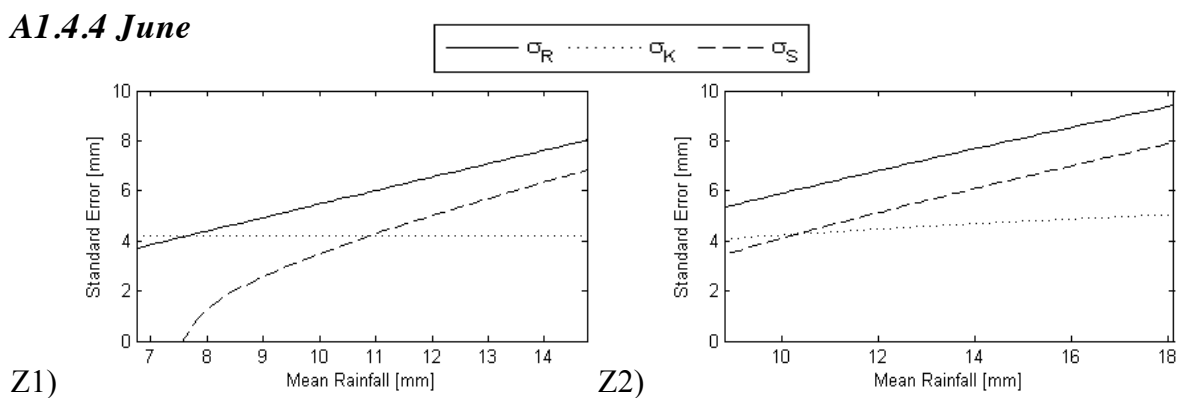
**A1.4.2 April**

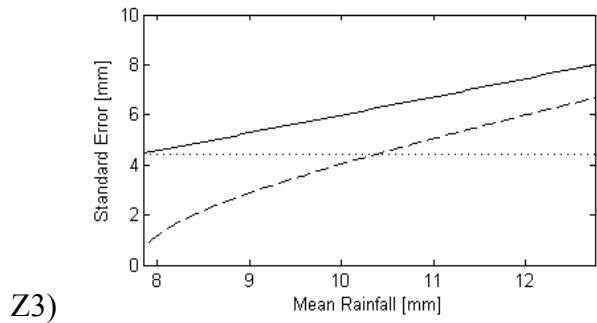


**A1.4.3 May**

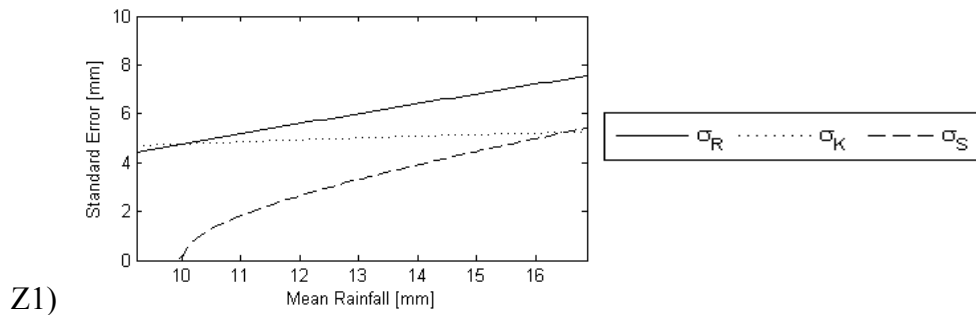


**A1.4.4 June**

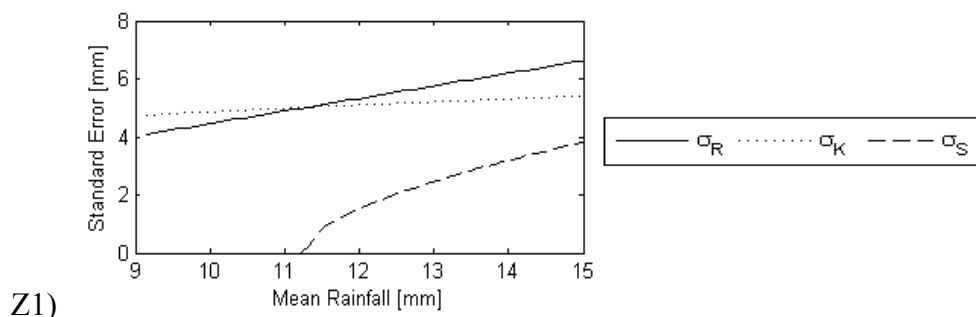




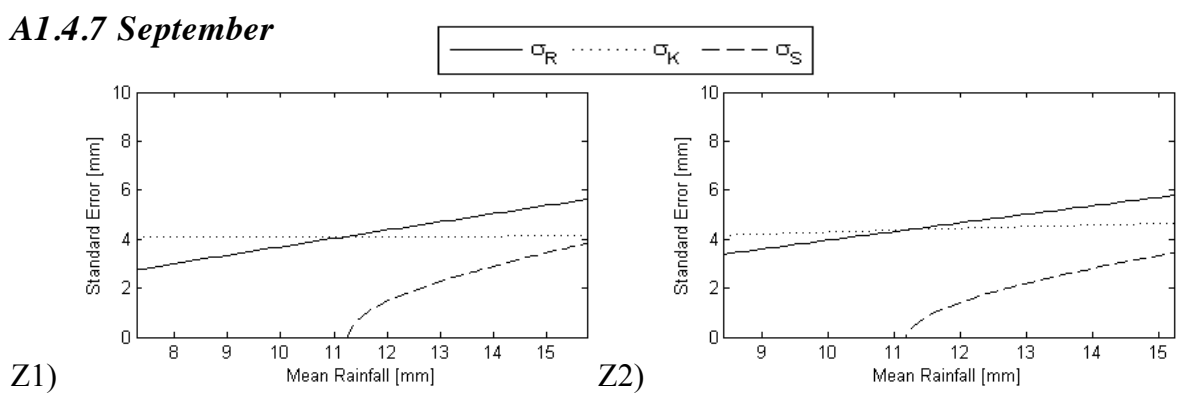
#### *A1.4.5 July*



#### *A1.4.6 August*



#### *A1.4.7 September*

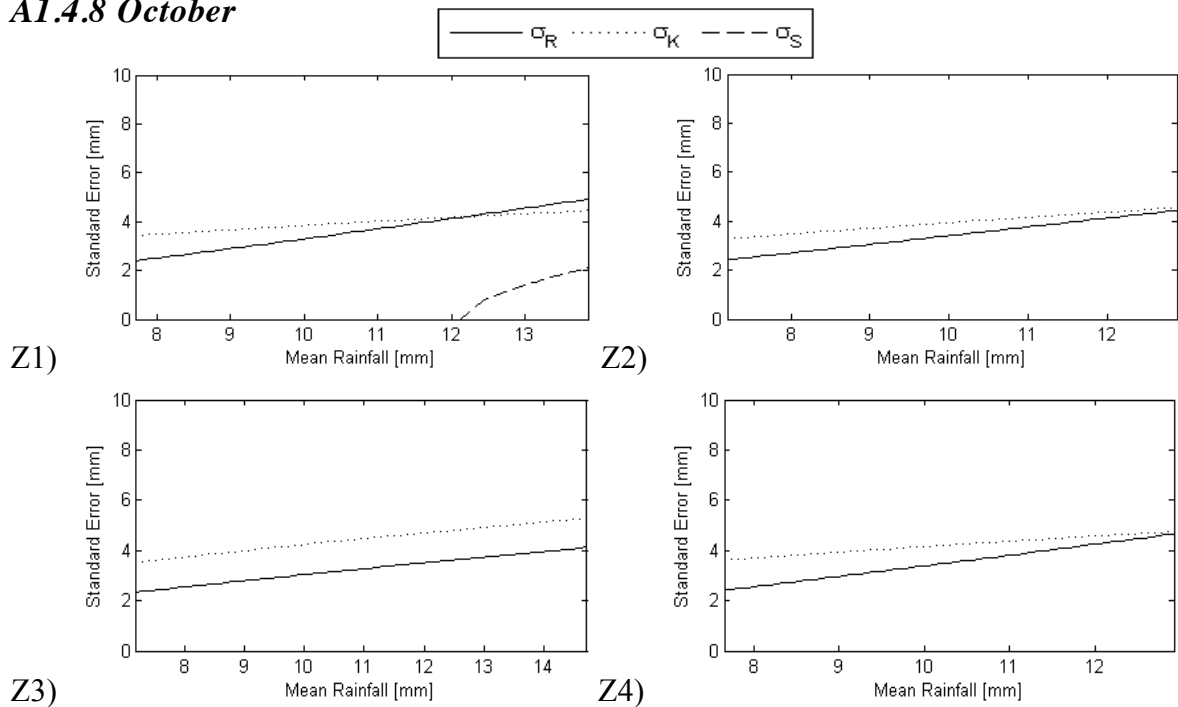


---

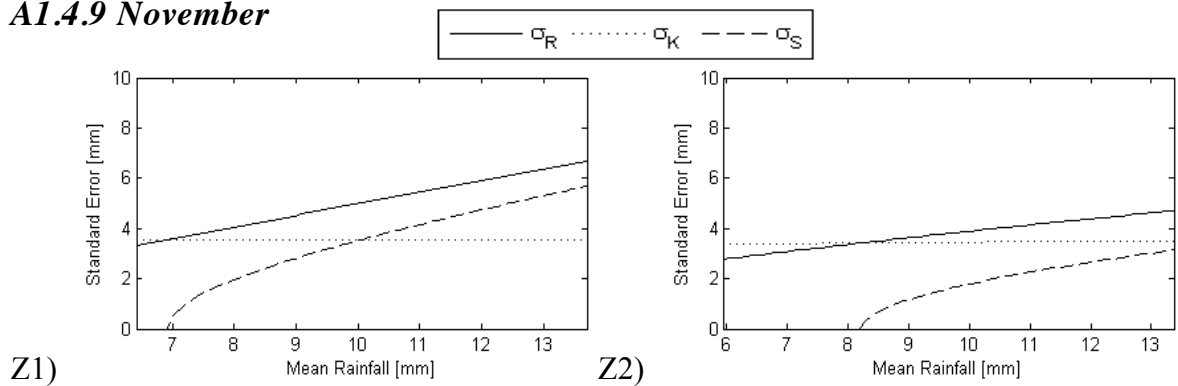
## Appendix Two Statistical definitions and tests

---

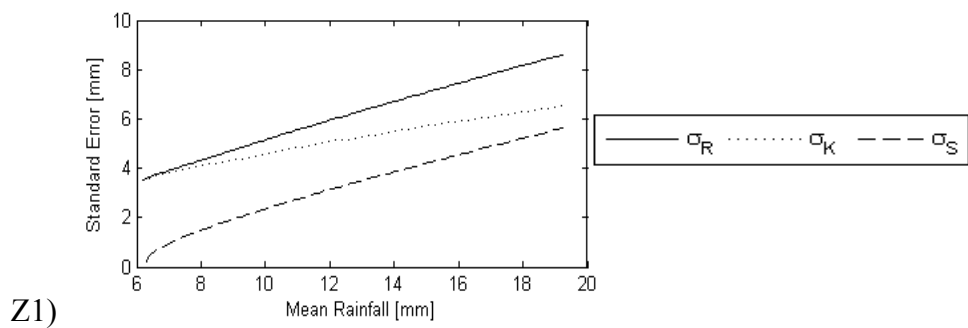
### A1.4.8 October



### A1.4.9 November



### A1.4.10 December



---

*Appendix Two Statistical definitions and tests*

---

As mentioned in Section A1.2.10, the entire region was treated as one zone in December for the error parameters because the iterative least squares calibration approach failed to converge to a solution when the two zones were treated independently.

## **APPENDIX TWO**

# **STATISTICAL DEFINITIONS AND TESTS**

The following statistical tests are used in the calibration. This appendix relies heavily on the excellent definitions provided by WCRP, (2012).

### **A2.1. SKILL SCORES FOR DICHOTOMOUS FORECASTS**

Dichotomous forecasts predict binary or yes/no events. Most ways to measure the skill of these forecasts are based on a contingency table (used in the basic TAMSAT calibration). An example table can be seen below for rainfall:

		<b>Observed</b>		<b>Total</b>
		Rain	Dry	
<b>Forecast</b>	Rain	Hits	False alarms	Forecast rainy pixels
	Dry	Misses	Correct negatives	Forecast dry pixels
Total		Observed rainy pixels	Observed dry pixels	Total

If the forecast was perfect, the table would contain only hits and correct negatives, with zero misses and false alarms. A good forecast might also be expected to contain roughly even amounts of false alarms and misses, a quantity which can be measured by the Bias.

#### **A2.1.1 Bias**

This calculates the frequency of wet events in comparison to dry ones. It can be calculated as shown below, where a perfect score is 1 (so the contingency table above is balanced):

$$Bias = \frac{hits + false\ alarms}{hits + misses} \quad A2.1$$

A score of  $> 1$  indicates an overestimate and a score of  $< 1$  an underestimate (with a range of  $-\infty$  to  $+\infty$ ). The score does not measure forecast accuracy.

#### **A2.1.2 Probability of detection (P.O.D.)**

This measures how well the forecast frequency of rain events compares to observed. It does not consider false alarms:

$$P.O.D. = \frac{hits}{hits + misses} \quad A2.2$$

A perfect score is 1 and the score has a range from 0 to 1. The score is sensitive to climatology and should be used in conjunction with the false alarm ratio below.

#### **A2.1.3 False alarm ratio (F.A.R.)**

This measures the fraction of false alarms, but does not consider hits.

$$F.A.R = \frac{false\ alarms}{false\ alarms + hits} \quad A2.3$$

A perfect score is 0 and the score has a range from 0 to 1. The score is sensitive to climatology.

#### **A2.1.4 Probability of false alarm (P.O.F.D.)**

This measures the proportion of dry events which were inaccurately forecast as rainy.

$$P.O.F.D. = \frac{false\ alarms}{false\ alarms + correct\ neg} \quad A2.4$$

It ranges from 0 to 1 with a perfect score equal to 0

### A2.1.5 Peirce's Skill Score (P.S.S)

This is a measure of the ‘true skill’ of the forecast – e.g. how did the forecast separate rain events from dry ones. It has a range from -1 to 1 with 0 indicating no skill and is written as

$$PSS = \frac{\text{hits}}{\text{hits} + \text{misses}} - \frac{\text{false alarms}}{\text{false alarms} + \text{correct neg}} = POD - POFD \quad \text{A2.5}$$

### A2.1.6 Critical Success Index (CSI) or Threat Index

This is a measure of the fraction of correctly predicted rainfall events, however it is sensitive to climatologies i.e. there will be a penalty for rarer events. The score ranges from 0-1 where 0 indicates no skill and 1 a perfect forecast.

$$CSI = \frac{\text{hits}}{\text{hits} + \text{misses} + \text{false alarms}} \quad \text{A2.6}$$

## A2.2. OTHER SKILL SCORES

### A2.2.1 The sum of squares

This is useful in linear regression and its components are used widely in the statistical tests discussed below. In the context of comparing pixel rainfall observations,  $z_i$ , against their estimated values,  $\hat{z}_i$ , the total sum of squares (TSS) can be written as:

$$TSS = \sum_{i=1}^N (z_i - \bar{z})^2 = \sum_{i=1}^N (\hat{z}_i - \bar{z})^2 + \sum_{i=1}^N (z_i - \hat{z})^2 \quad \text{A2.7}$$

where  $\bar{z}_i$  is the mean value from the linear fit. This equation can also be written as:

$$TSS = MSS + RSS \quad \text{A2.8}$$

In this equation, the mean sum of squares, MSS, shows the proportion of variability explained by the model and the residual sum of squares, RSS, shows the variability of unexplained residuals. In a perfect fit, the residual sum of squares would be zero. The residual sum of squares is also often written as:

$$RSS = \sum_{i=1}^N \hat{\varepsilon}_i^2 \quad \text{A2.9}$$

Therefore for the case study of comparing satellite rainfall estimates,  $x$  against  $N$  gauge observations,  $g$ , the root mean squared error can be written as:

$$RSS = \sum_{i=1}^N \hat{\varepsilon}_i^2 = \sum_{i=1}^N |x_i - g_i|^2 \quad \text{A2.10}$$

### **A2.2.2 Mean squared error (MSE) and Root mean squared error (RMSE)**

This estimates the quality of a prediction in terms of its bias and variation from a fit. For an estimator,  $\hat{\theta}$ :

$$MSE \hat{\theta} = \frac{RSS \hat{\theta}}{N} = \frac{\sum_{i=1}^N \hat{\varepsilon}_i^2}{N} = Var \hat{\theta} - Bias \hat{\theta}, \theta^2 \quad \text{A2.11}$$

The mean squared error can range from 0 to  $\infty$  and a perfect score would be 0. The RMSE is simply the square root of the MSE and gives a measure of a model's precision. Therefore, for the case study of comparing satellite rainfall estimates,  $x$  against  $N$  gauge observations,  $g$ , the root mean squared error can be written as:

$$RMSE = \sqrt{\frac{\sum_{i=1}^N \hat{\varepsilon}_i^2}{N}} = \sqrt{\frac{\sum_{i=1}^N |x_i - g_i|^2}{N}} \quad \text{A2.12}$$

This ranges from 0 to  $\infty$  and a perfect score would be 0. A variant of this is the relative root mean squared error (RMS):

$$RMS = \frac{\sqrt{\frac{1}{N} \sum_{i=1}^N |x_i - g_i|^2}}{\bar{g}} \quad \text{A2.13}$$

### A2.2.3 The coefficient of determination, $R^2$

This is the proportion of variability in a dataset explained by the model:

$$R^2 = \frac{RSS}{TSS} = \frac{\sum_{i=1}^N (\varepsilon_i)^2}{\sum_{i=1}^N (z_i - \bar{z})^2} \quad \text{A2.14}$$

As this measure of goodness of fit does not contain the amount of parameters used to fit the model, it cannot distinguish if a model has been over-fitted.

### A2.2.4 Multiplicative Bias (Bias2)

Note this is different to the dichotomous bias described in Section A2.1.1 and has thus been denoted Bias2. This unit less statistic gives a measure of whether a predicted model is underestimating or overestimating the magnitude of its estimate, when compared to a measured value. For example, in the case of rainfall predicted by a satellite estimate,  $z$ , compared to an observed gauge,  $g$ , the bias would be:

$$\text{Bias2} = \frac{\sum_{i=1}^N (z_i)}{\sum_{i=1}^N (g_i)} \quad \text{A2.15}$$

where N is the number of observations. Bias2 can range from  $-\infty$  to  $\infty$  and a perfect score is 1.

### A2.2.5 Efficiency (EFF)

This is a measure of the optimisation and stability of a fit. In our case study, it would be written as:

$$EFF = \frac{\sum_{i=1}^N (z_i - g_i)^2}{\sum_{i=1}^N (g_i - \bar{g})^2} \quad \text{A2.16}$$

### **A2.2.6 Akaike's information criterion (AIC)**

This is one of the most important calibration statistics as it measures accuracy but offsets it against model complexity. Therefore the model with the lowest RSS will not necessarily have the best score. The AIC is written formally as:

$$AIC = 2k + n \left[ \ln \left( \sum_{i=1}^n \hat{\varepsilon}_i^2 \right) \right] \quad \text{A2.17}$$

where k is the number of model parameters and  $\sum_{i=1}^n \hat{\varepsilon}_i^2$  the residual sum of squares (RSS).

# GLOSSARY

<b>AIC</b>	Akaike's Information Criterion skill score (See Appendix 2)
<b>AQUA-CROP</b>	An FAO process based crop model
<b>ASI</b>	Anthesis -Silking Interval, The time between tasselling and silking in maize. Susceptible to water stress
<b>Bega</b>	The dry spell running from October to January over most of Ethiopia
<b>Belg</b>	This is the Feb-May rainfall and agricultural season in Ethiopia
<b>Bernoulli trial</b>	A statistical trial with a fixed probability and only 2 outcomes, for example tossing a coin is a Bernoulli trial with a probability of 0.5
<b>CCD</b>	Cold Cloud Duration (See section 4.3)
<b>CERES</b>	Crop Environment Resource Synthesis : A group of crop simulation models within the DSSAT system
<b>CERES-Maize</b>	CERES-Maize (Crop Environment Resource Synthesis) model is a predictive, deterministic model designed to simulate corn growth, soil, water and temperature and soil nitrogen dynamics at a field scale for one growing season
<b>CIMMYT</b>	International maize and wheat improvement centre
<b>CMORPH</b>	The NOAA-CPC morphing technique
<b>CPSZ</b>	The JRC/MARS-OP Crop Production System Zones database
<b>CROPWAT</b>	An FAO water balance model
<b>CSA</b>	The Ethiopian Central Statistical Agency
<b>CSFAM</b>	Crop and Food Security Assessment Mission - In Ethiopia this is done in conjunction between the FAO and MoARD using farmer surveys
<b>CSWB</b>	Crop Specific Water Balance model

---

## Glossary

---

<b>CYMFS</b>	Crop Yield Monitoring and Forecasting System - run by the Ethiopian NMA and MARS-OP
<b>Dekad / Dekadal</b>	10 days/10 daily
<b>Deyr</b>	The second rainy season in the Somalian region of Ethiopia (Sept-Nov)
<b>DSSAT</b>	The Decision Support System for Agrotechnology Transfer (DSSAT) is a software application program that comprises crop simulation models for over 28 crops
<b>ECMWF</b>	European Centre for Medium-Range Weather Forecasts
<b>ENSO</b>	El Niño/La Niña-Southern Oscillation
<b>ERA_INTERIM</b>	A numerical climate reanalysis of the period 1989-present produced by ECMWF
<b>EUMETSAT</b>	The European Organisation for the Exploitation of Meteorological Satellites
<b>FAO</b>	The UN Food and Agriculture Organisation
<b>FEWS-NET</b>	US-AID Famine Early Warning NETwork
<b>GCM</b>	Global Climate Model
<b>GHACOF</b>	Regional Outlook Forum for the Greater Horn of Africa - produces seasonal weather forecasts
<b>GIS</b>	Geographical Information system
<b>GLAM</b>	The General Large Area Model for annual crops is a regional scale crop model developed at the University of Reading
<b>GLM</b>	Generalized Linear Model
<b>GOS</b>	Global Observing System
<b>Gu</b>	The first rainy season in the Somalian region of Ethiopian (April-May)

---

---

## Glossary

---

<b>HI</b>	Harvest Index
<b>IRI</b>	The International Research Institute for climate and society
<b>IGAD</b>	Intergovernmental Authority on Development. Organisation of six eastern African countries focused on drought control and development initiatives
<b>IR</b>	Infrared
<b>Isohyet</b>	A contour joining points of equal precipitation
<b>ITCZ</b>	The Intertropical Convergence Zone
<b>JRC</b>	The EU Joint Research Council
<b>Kiremt</b>	This is the May-September rainy season in Ethiopia
<b>LAI</b>	Leaf Area Index
<b>LARS_WG</b>	A weather generator
<b>LIU</b>	The Ethiopian MoARD Livelihoods assessment unit
<b>MARKSIM</b>	A weather generator
<b>MARS-OP</b>	The Monitoring Agricultural ResourceS project is an EU project designed to monitor and forecast the current agricultural season
<b>MCYFS</b>	MARS Crop Yield Forecasting System
<b>Meher</b>	This is the main agricultural season in Ethiopia
<b>MeteoSat</b>	The Meteosat series of satellites are geostationary meteorological satellites operated by EUMETSAT
<b>MoARD</b>	The Ethiopian Ministry of Agriculture and Rural Development
<b>NDVI</b>	Normalised Difference Vegetation Index
<b>NGO</b>	Non-governmental organisation, normally a charitable organisation

---

---

## Glossary

---

<b>NMA</b>	The Ethiopian National Meteorological Agency
<b>NWP</b>	Numerical Weather Prediction Model
<b>Oz-Wheat</b>	A regional-scale crop yield simulation model for Australian wheat
<b>PERSIANN</b>	Precipitation Estimation from Remotely Sensed Information using Neural Networks
<b>PM</b>	Passive Microwave
<b>RCOF</b>	Regional Outlook Forum - produces seasonal weather forecasts
<b>RFE2</b>	The NOAA Climate Prediction Centre (NOAA-CPC) African rainfall estimation algorithm
<b>RUE</b>	Radiation Use Efficiency
<b>SARRA-H</b>	Processed based crop simulation model
<b>SIMMETO</b>	A weather generator
<b>SPOT VEGETATION</b>	A European remotely sensed NDVI product
<b>SRFE</b>	Satellite RainFall Estimate
<b>TAMSAT</b>	Tropical Applicaitons of Meteorology from Satellites
<b>TARCAT</b>	The TAMSAT 30-year rainfall climatology
<b>TRMM</b>	Tropical Rainfall Measuring Mission. Name of a satellite and several satellite derived rainfall products
<b>UN</b>	United nations
<b>WGEN</b>	The original Richardson weather generator
<b>WMO</b>	World Meteorological Organistaion
<b>WMO GTS</b>	Global Telecommnication System. How GOS data is distributed. Normally refers to a rain gauge dataset

---

---

## Glossary

---

<b>WMO WWW</b>	The WMO world weather watch program
<b>WOFOST</b>	WOrld FOod STudies is a simulation model for the quantitative analysis of the growth and production of annual field crops
<b>YGP</b>	The Yield Gap Parameter in a crop simulation model

---

## References

- Abendroth, L., E. R.W., M. J. Boyer, and S. K. Marlay (2011), Corn growth and development, *Rep.*, Iowa State University, Iowa City.
- Admass, S. (2004), Rainfall variation and its effect on crop production in ethiopia, PhD Thesis, Addis Ababa University Addis Ababa.
- Aldrich, S. R., W. O. Scott, and R. G. Hoeft (1986), How the corn plant grows, in *Modern corn production*, edited, Ohio State University Extension, A&L Publications
- Ali, A., T. Lebel, and A. Amani (2005), Rainfall estimation in the sahel. Part i: Error function, *Journal of Applied Meteorology*, 44(11), 1691-1706.
- Andrade, F. H., S. A. Uhart, and A. Cirilo (1993), Temperature affects radiation use efficiency in maize, *Field Crops Research*, 32(1-2), 17-25.
- Apipattanavis, S., G. Podestá, B. Rajagopalan, and R. W. Katz (2007), A semiparametric multivariate and multisite weather generator, *Water Resour. Res*, 43(11).
- Apipattanavis, S., F. Bert, G. Podestá, and B. Rajagopalan (2010), Linking weather generators and crop models for assessment of climate forecast outcomes, *Agricultural and Forest Meteorology*, 150(2), 166-174.
- Araya, A., and L. Stroosnijder (2011), Assessing drought risk and irrigation need in northern Ethiopia, *Agricultural and Forest Meteorology*, 151(4), 425-436.
- Araya, A., S. D. Keesstra, and L. Stroosnijder (2010), Simulating yield response to water of teff (eragrostis tef) with the FAO AquaCrop model, *Field Crops Research*, 116(1-2), 196-204.
- Aseffa, K. (2011), Seasonal forecasts for Ethiopia, edited, Ethiopian National Meteorlogical Agency.

---

## References

---

- Baigorria, G. A. (2007), Assessing the use of seasonal climate forecasts to support farmers in the andean highlands, in *Climate prediction and agriculture: Advances and challenges*, edited by M. V. K. Sivakumar, J. Hansen and World Meteorological Organization, pp. 99-110, Springer Verlag, Berlin.
- Baigorria, G. A., and J. W. Jones (2010), GIST, a stochastic model for generating spatially and temporally correlated daily rainfall data, *Bulletin of the American Meteorological Society*.
- Baigorria, G. A., J. W. Jones, and J. J. O'Brien (2008), Potential predictability of crop yield using an ensemble climate forecast by a regional circulation model, *Agricultural and Forest Meteorology*, 148(8-9), 1353-1361.
- Banziger, M., and G. O. Edmeades (1996), Genetic variation for transpiration efficiency in a lowland maize population, paper presented at Developing drought and low N-tolerant maize: proceedings of a symposium, International Maize and Wheat Improvement Center, El Batán, Mexico, March 25-29, 1996.
- Barancourt, C., J. D. Creutin, and J. Rivoirard (1992), A method for delineating and estimating rainfall fields, *Water Resour. Res.*, 28(4), 1133-1144.
- Barnabas, B., K. Jager, and A. Feher (2008), The effect of drought and heat stress on reproductive processes in cereals, *Plant Cell and Environment*, 31(1), 11-38.
- Barnston, A. G., S. Li, S. J. Mason, D. G. DeWitt, L. Goddard, and X. Gong (2009), Verification of the first 11 years of IRI's seasonal climate forecasts, *Journal of Applied Meteorology and Climatology*, 49(3), 493-520.
- Baron, C., B. Sultan, M. Balme, B. Sarr, S. Traore, T. Lebel, S. Janicot, and M. Dingkuhn (2005), From GCM grid cell to agricultural plot: Scale issues affecting modelling of climate impact, *Phil. Trans. R. Soc. B*, 360, 2095-2108.
- Batjes, N. H. (2005), ISRIC wise global data set of derived soil properties on a 5 by 5 arc minutes global grid (version 3.0)Rep., ISRIC – World Soil Information, Wageningen.

---

## References

---

- Bekele, F. (1997), Ethiopian use of ENSO information in its seasonal forecasts, *International Journal of African Studies*, 2.
- Bellerby, T. J., and J. Sun (2005), Probabilistic and ensemble representations of the uncertainty in an ir/microwave satellite precipitation product, *Journal of Hydrometeorology*, 6(6), 1032-1044.
- Bergamaschi, H., B. Radin, L. M. G. Rosa, J. I. Bergonci, R. Aragones, A. O. Santos, and S. Franca (2001), Estimating maize water requirements using agrometeorological data, *Revisita Argentina de Agrometeorologia*, 1(1), 23-27.
- Berrisford, P., D. Dee, K. Fielding, M. Fuentes, P. Kallberg, S. Kobayashi, and S. Uppala (2009), The era-interim archive, *ERA report series*(1), 1-16.
- Bert, F. E., E. H. Satorre, F. R. Toranzo, and G. P. Podestá (2006), Climatic information and decision-making in maize crop production systems of the argentinean pampas, *Agricultural Systems*, 88(2-3), 180-204.
- Bettio, M., and G. Genovese (2004), Vol. 4: Statistical data collection processing and analysisRep. *Methodology of the MARS Crop Yield Forecasting System*.
- Beyene, E. G., and B. Meissner (2010), Spatio-temporal analyses of correlation between noaa satellite RFE and weather stations' rainfall record in Ethiopia, *International Journal of Applied Earth Observation and Geoinformation*, 12(Supplement 1), S69-S75.
- Beyene, H. (2009), Personal communication, edited by H. Greatrex, Central Statistical Agency of Ethiopia, Addis Ababa, Ethiopia.
- Bindi, M., T. R. Sinclair, and J. Harrison (1999), Analysis of seed growth by linear increase in harvest index, *Crop Science*, 39(2), 486-493.
- Birch, C., G. Hammer, and K. Rickert (1999), Dry matter accumulation and distribution in five cultivars of maize (*zea mays*): Relationships and procedures for use in crop modelling, *Australian journal of agricultural research*, 50, 513-528.

---

## References

---

- Birch, C. J., J. Vos, and P. E. L. van der Putten (2003), Plant development and leaf area production in contrasting cultivars of maize grown in a cool temperate environment in the field, *European Journal of Agronomy*, 19(2), 173-188.
- Birhanu, S., and T. Alamirew (2008), Rainfall intensity-duration-frequency analysis for selected parts of eastern Oromia, paper presented at Regional Workshop on hydrology and ecology of the Nile River basin under extreme conditions, Addis Ababa, Ethiopia.
- Bohling, G. (2005), Kriging, in *Course notes for Data Analysis in Engineering and Natural Science*, edited, Kansas Geological Survey, Kansas.
- Bolaños, J., and G. O. Edmeades (1993), Eight cycles of selection for drought tolerance in lowland tropical maize. I. Responses in grain yield, biomass, and radiation utilization, *Field Crops Research*, 31(3-4), 233-252.
- Bolaños, J., and G. O. Edmeades (1996), The importance of the anthesis-silking interval in breeding for drought tolerance in tropical maize, *Field Crops Research*, 48(1), 65-80.
- Bolton, D. (1980), The computation of equivalent potential temperature, *Monthly Weather Review*, 108(7), 1046-1053.
- Borgman, L., M. , Taheri, and R. Hagan (1984), Three-dimensional frequency-domain simulations of geological variables., in *Geostatistics for natural resources characterization, proceedings of the 1983 south lake tahoe nato asi*,, edited by M. D. G. Verly, A. Journel, and A. M. Dordrecht, Netherlands.
- Bouvier, C., L. Cisneros, R. Dominguez, J.-P. Laborde, and T. Lebel (2003), Generating rainfall fields using principal components (pc) decomposition of the covariance matrix: A case study in Mexico City, *Journal of Hydrology*, 278(1-4), 107-120.
- British Broadcasting Corporation (2006), Hundreds lost in Ethiopia flood, date accessed, 12/06/2011, last edited, Monday, 7 August 2006, London, url: <http://news.bbc.co.uk/1/hi/world/africa/5251768.stm>

---

## References

---

- Brown (2009), Agronomy guide for field crops *Rep.*, Ontario Ministry for Agriculture and Rural Affairs, Ontario, Canada.
- Brown, M. (2008), *Famine early warning systems and remote sensing data*, Springer.
- C.I.C.S. (2004), Weather generators, edited, The Canadian Institute for Climate Studies, Victoria, Last edited, 18/02/2004,  
url [http://www.cics.uvic.ca/scenarios/index.cgi?More\\_Info-Weather\\_Generators](http://www.cics.uvic.ca/scenarios/index.cgi?More_Info-Weather_Generators)
- Campos, H., M. Cooper, J. E. Habben, G. O. Edmeades, and J. R. Schussler (2004), Improving drought tolerance in maize: A view from industry, *Field Crops Research*, 90(1), 19-34.
- Cannon, A. J. (2008), Probabilistic multisite precipitation downscaling by an expanded bernoulli-gamma density network, *Journal of Hydrometeorology*, 9(6), 1284-1300.
- Cantelaube, P., and J. M. Terres (2005), Seasonal weather forecasts for crop yield modelling in Europe, *Tellus Series a-Dynamic Meteorology and Oceanography*, 57(3), 476-487.
- Chadwick (2010), Multi-spectral satellite rainfall estimation over Africa using METEOSAT second generation data, 197 pp, PhD Thesis, University of Reading, Reading, UK.
- Chadwick, R. S., D. I. F. Grimes, R. W. Saunders, P. N. Francis, and T. A. Blackmore (2010), The TAMORA algorithm: Satellite rainfall estimates over West Africa using multi-spectral seviri data, *Advances in Geosciences*, 25, 3-9.
- Challinor, A. J., T. R. Wheeler, J. M. Slingo, and D. Hemming (2005a), Quantification of physical and biological uncertainty in the simulation of the yield of a tropical crop using present-day and doubled CO<sub>2</sub> climates, *Philosophical Transactions of the Royal Society B-Biological Sciences*, 360(1463), 2085-2094.

---

## References

---

- Challinor, A. J., T. R. Wheeler, P. Q. Craufurd, and J. M. Slingo (2005b), Simulation of the impact of high temperature stress on annual crop yields, *Agricultural and Forest Meteorology*, 135(1-4), 180-189.
- Challinor, A. J., J. M. Slingo, T. R. Wheeler, P. Q. Craufurd, and D. I. F. Grimes (2003), Toward a combined seasonal weather and crop productivity forecasting system: Determination of the working spatial scale, *Journal of Applied Meteorology*, 42(2), 175-192.
- Challinor, A. J., T. R. Wheeler, P. Q. Craufurd, J. M. Slingo, and D. I. F. Grimes (2004), Design and optimisation of a large-area process-based model for annual crops, *Agricultural and Forest Meteorology*, 124(1-2), 99-120.
- Chapman, S. C., and G. O. Edmeades (1996), Differences in radiation use efficiency among lines in a tropical maize population, paper presented at 8th Australian Agronomy Conference; Agronomy - Science with its sleeves rolled up, Toowoomba, Queensland.
- CIMMYT (2010), MAIZE - global alliance for improving food security and the livelihoods of the resource-poor in the developing world, edited. CYMMIT, Proposal submitted by CIMMYT and IITA to the CGIAR Consortium Board
- Clark, I. (1979), *Practical geostatistics*, Applied Science Publishers Barking, Essex, UK.
- Clark, M. P., and A. G. Slater (2006), Probabilistic quantitative precipitation estimation in complex terrain, *Journal of Hydrometeorology*, 7(1), 3-22.
- Collis, S. N., and J. D. Corbett (1998), A methodology for linking spatially interpolated climate surfaces with crop growth simulation models, paper presented at Directions in modeling wheat and maize for developing countries, CIMMYT, Batan, Mexico.
- Cooper, P., K. Rao, P. Singh, J. Dimes, P. Traore, K. Rao, P. Dixit, and S. Twomlow (2009), Farming with current and future climate risk: Advancing a ‘hypothesis of hope’ for rainfed agriculture in the semi-arid tropics, *Experimental Agriculture*

---

## References

---

- Cooper, P. J. M., J. Dimes, K. P. C. Rao, B. Shapiro, B. Shiferaw, and S. Twomlow (2008), Coping better with current climatic variability in the rain-fed farming systems of sub-saharan Africa: An essential first step in adapting to future climate change?, *Agriculture Ecosystems & Environment*, 126(1-2), 24-35.
- Coppola, E., D. I. F. Grimes, M. Verdecchia, and G. Visconti (2006), Validation of improved TAMMAN neural network for operational satellite-derived rainfall estimation in Africa, *Journal of Applied Meteorology and Climatology*, 45(11), 1557-1572.
- Crafts-Brandner, S. J., and M. E. Salvucci (2002), Sensitivity of photosynthesis in a C4 plant, maize, to heat stress, *Plant physiology*, 129(4), 1773.
- Craufurd, P., and T. Wheeler (2009), Climate change and the flowering time of annual crops, *Journal of experimental botany*, 60(9), 2529.
- Davis, M. (1987), Production of conditional simulations via the lu triangular decomposition of the covariance matrix, *Mathematical Geology*, 19(2), 91-98.
- De Michele, C., and P. Bernardara (2004), Spectral analysis and modeling of space-time rainfall fields, *Atmospheric Research*, 77(1-4), 124-136.
- de Wit, A. (2007), Regional crop yield forecasting using probabilistic crop growth modelling and remote sensing data assimilation, Wageningen University
- de Wit, A., and S. de Bruin (2006), Simulating space-time uncertainty in continental-scale gridded precipitation fields for agrometeorological modelling, paper presented at 7th International Symposium on Spatial Accuracy Assessment in Natural Resources and Environmental Sciences. , Lisbon, Portugal.
- de Wit, A., K. van Diepen, and H. Boogaard (2009), Regional crop yield forecasting: A probabilistic approach, paper presented at European General Union General Assembly, Vienna.

---

## References

---

- De Wit, A., H. Greatrex, and D. Grimes (2012), A comparison of several crop simulation models for ethiopia, *in prep.*
- de Wit, A., B. Baruth, H. Boogaard, K. van Diepen, D. van Kraalingen, F. Micale, J. te Roller, I. Supit, and R. van den Wijngaart (2010), Using ERA-INTERIM for regional crop yield forecasting in Europe, *Climate Research*, 44(1), 41-53.
- Dee, D. P., et al. (2011), The ERA-INTERIM reanalysis: Configuration and performance of the data assimilation system, *Quarterly Journal of the Royal Meteorological Society*, 137(656), 553-597.
- Dercon, S. (2004), Growth and shocks: Evidence from rural Ethiopia, *Journal of Development Economics*, 74(2), 309-329.
- Deressa, T. T. (2006), Measuring the economic impact of climate change on Ethiopian agriculture: a Ricardian approach *Rep.*, Centre for environmental policy and economics in Africa.
- Deutsch, C. V., and A. G. Journel (1998), *Gslib. Geostatistical software library and user's guide*, 2nd ed., Oxford University Press, New York.
- Devereux, S. (2000), Food insecurity in ethiopia: A discussion paper for DFID *Rep.*, Institute for Development Studies & DFID, London.
- Dilley, M. (2002), The use of climate information and seasonal prediction to prevent disasters, *WMO Bulletin*, 51, 42-48.
- Dingkuhn, M., C. Baron, V. Bonnal, F. Maraix, B. Sarr, B. Sultan, A. Clopes, F. Forest, T. Struif Bontkes, and M. Wopereis (2003), Decision support tools for rainfed crops in the sahel at the plot and regional scales, *Decision Support Tools for Smallholder Agriculture in Sub-Saharan Africa: A Practical Guide*.

---

## References

---

- Dinku, T., S. Chidzambwa, P. Ceccato, S. Connor, and C. Ropelewski (2008), Validation of high-resolution satellite rainfall products over complex terrain, *International Journal of Remote Sensing*, 29(14), 4097-4110.
- Dinku, T., P. Ceccato, E. Grover-Kopec, M. Lemma, S. Connor, and C. Ropelewski (2007), Validation of satellite rainfall products over East Africa's complex topography, *International Journal of Remote Sensing*, 28(7), 1503-1526.
- Diro, E. Black, and D. I. F. Grimes (2008), Seasonal forecasting of Ethiopian spring rains, *Meteorological Applications*, 15(1), 73-83.
- Diro, D. Grimes, and E. Black (2010a), Teleconnections between Ethiopian summer rainfall and sea surface temperature: Part ii. Seasonal forecasting, *Climate Dynamics*, 1-11.
- Diro, D. Grimes, and E. Black (2010b), Teleconnections between Ethiopian summer rainfall and sea surface temperature: Part i—observation and modelling, *Climate Dynamics*, 1-17.
- Diro, D. I. F. Grimes, E. Black, A. O'Neill, and E. Pardo-Iguzquiza (2009), Evaluation of reanalysis rainfall estimates over Ethiopia, *Int. J. Climatol.*, 29(1), 67-78.
- Donald, C. M., and J. Hamblin (1976), The biological yield and harvest index of cereals as agronomic and plant breeding criteria, *Advances in Agronomy*, 28, 361-405.
- DPPC (2003), Impact of the belg harvest and rains in pastoral areas on food availability Rep., Disaster Prevention and Preparedness Commission,
- Dugdale, G., V. D. McDougall, and J. R. Milford (1991), Potential and limitations of rainfall estimates of Africa derived from cold cloud statistics, in *Eighth Meteosat Scientific Users' Conference*, edited, pp. 211–220, Norrkoping, Sweden.
- Dunn, P. K. (2004), Occurrence and quantity of precipitation can be modelled simultaneously, *Int. J. Climatol.*, 24(10), 1231-1239.

---

## *References*

---

- Edmeades, G. O. (1996), *Developing drought and low n-tolerant maize: Proceedings of a symposium, march 25-29, 1996, cimmyt, el batán, mexico*, International Maize and Wheat Improvement Center.
- Edmeades, G. O., and J. Bolaños (1998), Issues arising from the use of cereals for tropical maize, paper presented at Directions in modeling wheat and maize for developing countries, CIMMYT, Batán, Mexico.
- Edmeades, G. O., J. Bolanos, A. Elings, J. M. Ribaut, M. Banziger, and M. E. Westgate (2000), The role and regulation of the anthesis-silking interval in maize, paper presented at Symposium on Physiology and Modeling Kernel Set in Maize, Crop Science Society America Baltimore, US.
- Ehleringer, J., and T. Cerling (2002), C<sub>3</sub> and C<sub>4</sub> photosynthesis, in *Encyclopedia of global environmental change*, edited by H. Mooney and J. Cerdadell, Wiley, Chichester.
- EIAR (2004), Directory of maize crop varieties Rep., Ethiopian Institute for Agricultural Research Addis Ababa.
- EIAR (2009), Research recommendations for maize production in ethiopia, edited, Ethiopian Institute for Agricultural Research, Addis Ababa.
- Ellis, R. H., R. J. Summerfield, G. O. Edmeades, and E. H. Roberts (1992), Photoperiod, temperature, and the interval from sowing to tassel initiation in diverse cultivars of maize, *Crop Sci.*, 32(5), 1225-1232.
- Endalew, G. (2007), Changes in the frequency and intensity of extremes over north east Africa Rep., 46 pp, Royal Netherlands Meteorological Institute, Amsterdam.
- FEWS-NET (2011), Famine in southern Somalia - main page news article, edited by FEWS-NET, US-AID, publisher US-AID, access date 01/09/2011,  
url <http://www.fews.net/Pages/default.aspx>

---

## References

---

- Fowler, H. J., C. G. Kilsby, P. E. O'Connell, and A. Burton (2005), A weather-type conditioned multi-site stochastic rainfall model for the generation of scenarios of climatic variability and change, *Journal of Hydrology*, 308(1-4), 50-66.
- Funk, C., A. Asfaw, P. Steffen, S. G., J. Rowland, and J. Verdin (2003), Estimating meher crop production using rainfall in the 'long cycle' region of Ethiopia *Rep.*, United States Geographical Survey.
- Funk, C., G. Senay, A. Asfaw, J. Verdin, J. Rowland, D. Korecha, G. Eilerts, J. Michaelsen, S. Amer, and R. Choularton (2005), Recent drought tendencies in Ethiopia and equatorial subtropical Eastern Africa *Rep.*, FEWS NET.
- Gebrehiwot, T., A. van der Veen, and B. Maathuis (2011), Spatial and temporal assessment of drought in the northern highlands of Ethiopia, *International Journal of Applied Earth Observation and Geoinformation*, 13(3), 309-321.
- Geng, S., F. W. T. Penning de Vries, and I. Supit (1986), A simple method for generating daily rainfall data, *Agricultural and Forest Meteorology*, 36(4), 363-376.
- Geng, S., J. Auburn, E. Brandstetter, and B. Li (1988), A program to simulate meteorological variables: Documentation for SIMMETO, *Agronomy progress rep./Univ. of California, Davis, Agr. exp. station*.
- Germann, U., M. Berenguer, D. Sempere-Torres, and M. Zappa (2006), Ensemble radar precipitation estimation — a new topic on the radar horizon, paper presented at Proc. 4th European Conf. on Radar in Meteorology and Hydrology, Barcelona, Spain, 18–22 September 2006.
- Germann, U., M. Berenguer, D. Sempere-Torres, and M. Zappa (2009), Real—ensemble radar precipitation estimation for hydrology in a mountainous region, *Quarterly Journal of the Royal Meteorological Society*, 135(639), 445-456.
- Getahun, A. (1978), Agricultural systems in Ethiopia, *Agricultural Systems*, 3(4), 281-293.

---

## References

---

- Ghile, Y., and R. Schulze (2009), Use of an ensemble re-ordering method for disaggregation of seasonal categorical rainfall forecasts into conditioned ensembles of daily rainfall for hydrological forecasting, *Journal of Hydrology*, 371(1-4), 85-97.
- Goldsworthy, P., and N. Fisher (1984), *The physiology of tropical field crops*, Wiley, New York.
- Goovaerts, P. (1997), *Geostatistics for natural resources evaluation*, 496 pp., Oxford University Press.
- Grimes, D. I. F. (2006), TAMSAT rainfall monitoring, paper presented at Precip-AMMA workshop, Niamey, Niger, 12/12/2006.
- Grimes, D. I. F., and E. Pardo Igúzquiza (2010), Geostatistical analysis of rainfall, *Geographical Analysis*, 42(2), 136-160.
- Grimes, D. I. F., E. Pardo-Igúzquiza, and R. Bonifacio (1999), Optimal areal rainfall estimation using raingauges and satellite data, *Journal of Hydrology*, 222(1-4), 93-108.
- Grimes, D. I. F., E. Coppola, M. Verdecchia, and G. Visconti (2003), A neural network approach to real-time rainfall estimation for Africa using satellite data, *Journal of Hydrometeorology*, 4(6), 1119-1133.
- Haberlandt, U., and C. Gattke (2004), Spatial interpolation v. Simulation of precipitation for rainfall-runoff modelling – a case study in the Lippe river basin, paper presented at British Hydrological Society Conference, Imperial College London, 12-16 July.
- Habtegebrial, K., B. R. Singh, and M. Haile (2007), Impact of tillage and nitrogen fertilization on yield, nitrogen use efficiency of Tef (eragrostis tef (zucc.) trotter) and soil properties, *Soil and Tillage Research*, 94(1), 55-63.
- Haile, M. (2005), Weather patterns, food security and humanitarian response in sub-saharan Africa, *Philosophical Transactions of the Royal Society B-Biological Sciences*, 360(1463), 2169-2182.

---

## References

---

- Hansen, J. W., and T. Mavromatis (2001), Correcting low-frequency variability bias in stochastic weather generators, *Agricultural and Forest Meteorology*, 109(4), 297-310.
- Hansen, J. W., and M. Indeje (2004), Linking dynamic seasonal climate forecasts with crop simulation for maize yield prediction in semi-arid Kenya, *Agricultural and Forest Meteorology*, 125(1-2), 143-157.
- Hansen, J. W., A. Potgieter, and M. K. Tippett (2004), Using a general circulation model to forecast regional wheat yields in northeast Australia, *Agricultural and Forest Meteorology*, 127(1-2), 77-92.
- Hansen, J. W., S. J. Mason, L. Q. Sun, and A. Tall (2011), Review of seasonal climate forecasting for agriculture in sub-saharan Africa, *Experimental Agriculture*, 47(2), 205-240.
- Hartkamp, A. D., J. W. White, and G. Hoogenboom (2003), Comparison of three weather generators for crop modeling: A case study for subtropical environments, *Agricultural Systems*, 76(2), PII S0308-0521X(0301)00108-00101.
- Hay, and R. A. Gilbert (2001), Variation in the harvest index of tropical maize: Evaluation of recent evidence from Mexico and Malawi, *Annals of Applied Biology*, 138(1), 103-109.
- Hay, K. M., and J. Porter (2006), *The physiology of crop yield*, 2nd ed., 328 pp., Wiley-Blackwell, London.
- Heisey, P. W., and M. Smale (1995), *Maize technology in malawi: A green revolution in the making?*, International Maize and Wheat Improvement Center.
- Hellmuth, M., D. Osgood, U. Hess, A. Moorhead, and H. Bhojwani (2010), *Climate and society no. 2: Index insurance and climate risk: Prospects for development and disaster management*, International Research Institute for Climate and Society New York.

---

## References

---

- Hsiao, T. C., L. Heng, P. Steduto, B. Rojas-Lara, D. Raes, and E. Fereres (2009), AquaCrop—the FAO crop model to simulate yield response to water: III. Parameterization and testing for maize, *Agron. J.*, 101(3), 448-459.
- Hsu, K., H. Gupta, X. Gao, and S. Sorooshian (1999), Estimation of physical variables from multichannel remotely sensed imagery using a neural network: Application to rainfall estimation, *Water Resources Research*, 35(5), 1605-1618.
- Huffman, G., R. Adler, D. Bolvin, and E. Nelkin (2009), The trmm multi-satellite precipitation analysis (tmpa). Chapter in satellite applications for surface hydrology, f. Hossain and m. Gebremichael, eds, edited, Springer Verlag, accepted. PDF available at [ftp://meso.gsfc.nasa.gov/agnes/huffman/papers/TMPA\\_hydro\\_rev.pdf](ftp://meso.gsfc.nasa.gov/agnes/huffman/papers/TMPA_hydro_rev.pdf).
- Hussain, T., A. K. Khan, M. A. Malik, and Z. Ali (2006), Breeding potential for high temperature tolerance in corn (*zea mays*), *Pakistan Journal of Botany*, 38(4), 1185-1195.
- I.R.I. (2011), A warning to the world, in *Newsletter of the Earth Institute*, edited, Columbia University, New York.
- Jobard, I., F. Chopin, J. C. Berges, and R. Roca (2011), An intercomparison of 10-day satellite precipitation products during the west African monsoon, *Int. J. Remote Sens.*, 32(9), 2353-2376.
- Jones, C. A., and J. R. Kiniry (1986), Ceres-maize: A simulation model of maize growth and development.
- Jones, J. W., and G. Hoogenboom (2007), Simulating basic growth and development processes: CERES maize, sorghum and millet, *Computer Simulation of Crop Growth and Management Responses (ABE6933)*, (31/08/2011).
- Jones, P. G., and P. K. Thornton (1993), A rainfall generator for agricultural applications in the tropics, *Agricultural and Forest Meteorology*, 63(1-2), 1-19.

---

## References

---

- Jones, P. G., and P. K. Thornton (1997), Spatial and temporal variability of rainfall related to a third-order markov model, *Agricultural and Forest Meteorology*, 86(1-2), 127-138.
- Journel, A. G., and C. J. Huijbregts (1978), *Mining geostatistics*, Academic Press, London.
- Joyce, R., J. Janowiak, P. Arkin, and P. Xie (2004), Cmorph: A method that produces global precipitation estimates from passive microwave and infrared data at high spatial and temporal resolution, *Journal of Hydrometeorology*, 5(3), 487-503.
- Juglea, S., Y. Kerr, A. Mialon, E. Lopez-Baeza, D. Braithwaite, and K. Hsu (2010), Evaluation of persiann database in the framework of SMOS calibration/validation activities over valencia anchor station, *Evaluation*, 7, 1143-1166.
- Kaluski, D. N., E. Ophir, and T. Amede (2002), Food security and nutrition - the Ethiopian case for action, *Public Health Nutrition*, 5(3), 373-381.
- Kassahun, B. (1987), Weather systems over Ethiopia, paper presented at Proceedings of the First Tech Conf on Meteorological Research in Eastern and Southern Africa, Kenya Meteorological Department, Nairobi, Kenya.
- Keating, B. A., et al. (2003), An overview of APSIM, a model designed for farming systems simulation, *European Journal of Agronomy*, 18(3-4), 267-288.
- Kerdiles, H. (2011), Era-interim discussion, edited by H. Greatrex.
- Kiniry, J. R., J. T. Ritchie, R. L. Musser, E. P. Flint, and W. C. Iwig (1983), The photosensitive interval in maize, *Agronomy Journal*, 75(4), 687-690.
- Kling, J., and G. O. Edmeades (1997), Morphology and growth of maize *Rep.*, International Institute of Tropical Agriculture (IITA).
- Korecha, D., and A. G. Barnston (2007), Predictability of June–September rainfall in Ethiopia, *Monthly Weather Review*, 135(2), 628-650.

---

## References

---

- Lauer, J. (1998), Successful corn pollination: One key to high yield, in *Wisconsin Crop Manager Newsletter* edited, UW-Madison Plant Sciences, Madison.
- Laurence, M. (2010), An atlas of Ethiopia livelihoodsRep.
- Lazar, C., and G. Genovese (2004), Vol. 2: Agro-meteorological modelling, processing and analysisRep., ISBN 92-894-8181-1-EUR 21291/EN/2.
- Lebel, T., G. Bastin, C. Obled, and J. Creutin (1987), On the accuracy of areal rainfall estimation: A case study, *Water Resources Research*, 23(11), 2123-2134.
- Li, S., T. Wheeler, A. Challinor, E. Lin, H. Ju, and Y. Xu (2010), The observed relationships between wheat and climate in China, *Agricultural and Forest Meteorology*, 150(11), 1412-1419.
- Liu, J., S. Fritz, C. F. A. van Wesenbeeck, M. Fuchs, L. You, M. Obersteiner, and H. Yang (2008), A spatially explicit assessment of current and future hotspots of hunger in sub-saharan Africa in the context of global change, *Global and Planetary Change*, 64(3-4), 222-235.
- Lobell, D. B., W. Schlenker, and J. Costa-Roberts (2011), Climate trends and global crop production since 1980, *Science*.
- Loewenberg, S. (2011), Global food crisis takes heavy toll on east Africa, *The Lancet*, 378(9785), 17-18.
- Lumsden, T. G., and R. E. Schulze (2007), Application of seasonal climate forecasts to predict regional scale crop yields in South Africa, in *Climate prediction and agriculture: Advances and challenges*, edited by M. V. K. Sivakumar, J. Hansen and World Meteorological Organization, pp. 213-224, Springer Verlag, Berlin.
- MacAskill, J. (2006), Livelihoods of rural Ethiopia database edited by E. Livelyhood Integration Unit of the Ministry of Agriculture and Rural Development.

---

## References

---

- Maidment, R. I., D. I. F. Grimes, and E. Tarnesky (2012), TARCAT: The TAMSAT 30-year rainfall climatology, *In prep.*
- Maidment, R. I., D. I. F. Grimes, R. P. Allan, H. Greatrex, O. Rojas, and O. Leo (In press), Evaluation of satellite-based and model re-analysis rainfall estimates for Uganda, *Meteorological Applications*.
- Maplecroft (2011), Somalia, dr congo top maplecroft's food security risk ranking – Horn of Africa food crisis heightened by man-made factor, in *News Article*, edited, p. News Article, Maplecroft.
- Mariam, D. (2002), Maize export possibility from Ethiopia to some potentially importing neighbouring countriesRep., Ethiopian Development Research Institute and International Food Policy Research Institute, Washington D.C.
- Marteau, R., B. Sultan, V. Moron, A. Alhassane, C. Baron, and S. B. Traoré (2011), The onset of the rainy season and farmers' sowing strategy for pearl millet cultivation in southwest Niger, *Agricultural and Forest Meteorology*, 151(10), 1356-1369.
- Mason, S., and S. Chidzambwa (2008), Position paper: Verification of African rcof forecastsRep., International Research Institute, New York.
- Mason, S. J., L. Goddard, N. E. Graham, E. Yulaeva, L. Sun, and A. P.A. (1999), The IRI seasonal climate prediction system and the 1997/98 el niño event, *Bulletin of the American Meteorological Society*(80), 1853–1873.
- Matheron, G. (1968), Krigeage d'un panneau rectangulaire par sa périphérieRep., CG, Ecole des Mines de Paris, Paris.
- Mavromatis, T., and J. W. Hansen (2001), Interannual variability characteristics and simulated crop response of four stochastic weather generators, *Agricultural and Forest Meteorology*, 109(4), 283-296.

---

## References

---

- Meze-Hausken, E. (2004), Contrasting climate variability and meteorological drought with perceived drought and climate change in northern Ethiopia, *Climate Research*, 27(1), 19-31.
- Micale, F., and G. Genovese (2004), Vol. 1: Meteorological data collection, processing and analysisRep.
- Moeller, C., I. Smith, S. Asseng, F. Ludwig, and N. Telcik (2008), The potential value of seasonal forecasts of rainfall categories—case studies from the wheatbelt in western Australia's mediterranean region, *Agricultural and Forest Meteorology*, 148(4), 606-618.
- Moot, D., P. Jamieson, A. Henderson, M. Ford, and J. Porter (1996), Rate of change in harvest index during grain-filling of wheat, *Journal of agricultural science,-Cambridge-*, 126, 387-396.
- Mottram, A., D. P. James, W. I. Robinson, and S. Zekaria (2005), The Ethiopian agricultural sample enumeration (ease), paper presented at The Ethiopian Agricultural Sample: Enumeration In-depth Analysis:, Centre for Arid Zone Studies (CAZS), Addis Ababa, Ethiopia.
- Muchow, R. C. (1990), Effect of high temperature on grain-growth in field-grown maize, *Field Crops Research*, 23(2), 145-158.
- Nicklin, K., and A. J. Challinor (2011), Ensemble crop yield prediction using dynamical seasonal forecasts and observations. , *Agricultural and Forest Meteorology*, *In press*.
- Nielsen, R. L. (2007), Drought and heat stress effects on corn pollination, in *The Corn Grower's Guidebook*, edited by P. U. Agronomy Department.
- Nielsen, R. L. (2010), Silk development and emergence in cornRep., Agronomy Dept., Purdue Univ, Purdue, IN.

---

## References

---

- Nikolopoulos, E. I., E. N. Anagnostou, F. Hossain, M. Gebremichael, and M. Borga (2010), Understanding the scale relationships of uncertainty propagation of satellite rainfall through a distributed hydrologic model, *Journal of Hydrometeorology*, 11(2), 520-532.
- NOAA (2010), The noaa climate prediction center African rainfall estimation algorithm. Version 2., edited.
- Norman, M., C. Pearson, and P. Searle (1995), *The ecology of tropical food crops*, Cambridge Univ Pr.
- Ogindo, H. O., and S. Walker (2003), The estimation of soil water extraction by maize-bean intercrop and its sole crop components in a semi-arid region, paper presented at African Crop Science Conference Kampala, Uganda.
- Ogola, J. B. O., T. R. Wheeler, and P. M. Harris (2002), Effects of nitrogen and irrigation on water use of maize crops, *Field Crops Research*, 78(2-3), 105-117.
- Osaki, M. (1995), Comparison of productivity between tropical and temperate maize: I. Leaf senescence and productivity in relation to nitrogen nutrition, *Soil science and plant nutrition*, 41(3), 439-450.
- Osborne, T. (2004), Towards an integrated approach to simulating crop-climate interactions, 193 pp, University of Reading, Reading.
- Pardo-Igúzquiza, E. (1998), Optimal selection of number and location of rainfall gauges for areal rainfall estimation using geostatistics and simulated annealing, *Journal of Hydrology*, 210(1-4), 206-220.
- Passioura, J. (1983), Roots and drought resistance, *Agricultural Water Management*, 7(1-3), 265-280.
- Pasuquin, J. M. C. A., and C. Witt (2007), Yield potential and yield gaps of maize in southeast Asia, in *Electronic International Fertilizer Correspondent (e-ifc)*. edited by I. P. Institute, International Potash Institute.

---

## References

---

- Petitgas, P., J. Massé, P. Beillois, E. Lebarbier, and A. Le Cann (2003), Sampling variance of species identification in fisheries acoustic surveys based on automated procedures associating acoustic images and trawl hauls, *ICES Journal of Marine Science: Journal du Conseil*, 60(3), 437-445.
- Pickering, N., J. Hansen, J. Jones, C. Wells, V. Chan, and D. Godwin (1994), WEATHERMAN: A utility for managing and generating daily weather data, *Agronomy Journal*, 86(2), 332-337.
- Podestá, G., D. Letson, C. Messina, F. Royce, R. A. Ferreyra, J. Jones, J. Hansen, I. Llovet, M. Grondona, and J. J. O'Brien (2002), Use of ENSO-related climate information in agricultural decision making in argentina: A pilot experience, *Agricultural Systems*, 74(3), 371-392.
- Potgieter, A. (2011), Seasonal wheat outlook for Queensland, edited by Q. G. D. o. P. I. a. Fisheries.
- Potgieter, A., G. L. Hammer, and A. Doherty (2006), Oz-wheat: A regional-scale crop yield simulation model for australian wheat Australia: Qld dept of primary industries & fisheries Rep., 1-15 pp, Qld Dept of Primary Industries & Fisheries.
- Prasad, P., P. Craufurd, R. Summerfield, and T. Wheeler (2000), Effects of short episodes of heat stress on flower production and fruit-set of groundnut (*arachis hypogaea* l.), *Journal of experimental botany*, 51, 777-784.
- Qin, R., P. Stamp, and W. Richner (2006), Impact of tillage on maize rooting in a cambisol and luvisol in Switzerland, *Soil and Tillage Research*, 85(1-2), 50-61.
- Racsko, P., L. Szeidl, and M. Semenov (1991), A serial approach to local stochastic weather models, *Ecological modelling*, 57(1-2), 27-41.
- Raes, D., P. Steduto, T. C. Hsiao, and E. Fereres (2009), AquaCrop the FAO crop model to simulate yield response to water: II. Main algorithms and software description, *Agron. J.*, 101(3), 438-447.

---

## *References*

---

- Rajagopalan, B., U. Lall, D. Tarboton, and D. Bowles (1997), Multivariate nonparametric resampling scheme for generation of daily weather variables, *Stochastic Hydrology and Hydraulics*, 11(1), 65-93.
- Regassa, S., C. Givey, G. E. Castillo, J. Magrath, and K. Pfeifer (2010), The rain doesn't come on time any more; poverty, vulnerability, and climate variability in Ethiopia *Rep.*, Oxfam International.
- Rhoads, F. M., and J. M. Bennett (1990), Corn, in *Irrigation of agricultural crops*, edited by B. A. Stewart and D. R. Nielsen, pp. 569-596, ASA-CSSA-SSSA, Madison, WI.
- Richardson, C. W. (1981), Stochastic simulation of daily precipitation, temperature, and solar radiation, *Water Resources Research*, 17(1), 182-190.
- Richardson, C. W., and D. A. Wright (1984), Wgen: A model for generating daily weather variables, *ARS*, 8, 83.
- Riddle, J. (2005), Bumper harvest in Ethiopia, but more than 2 million people need food aid, edited by F. a. A. O. N. Room.
- Roberts, E., and R. Summerfield (1987), Measurement and prediction of flowering in annual crops. In 'manipulation of flowering'.(ed. Jg atherton) pp. 17–50, edited, Butterworths: London.
- Rojas, O., F. Rembold, A. Royer, and T. Negre (2005), Real-time agrometeorological crop yield monitoring in eastern Africa, *Agron. Sustain. Dev.*, 25(1), 63-77.
- Romaguera, M., A. Hoekstra, Z. Su, M. Krol, and M. Salama (2010), Potential of using remote sensing techniques for global assessment of water footprint of crops, *Remote Sensing*, 2(4), 1177-1196.
- Rosell, S. (2011), Regional perspective on rainfall change and variability in the central highlands of Ethiopia, 1978-2007, *Applied Geography*, 31(1), 329-338.

---

## References

---

- Royer, A., and G. Genovese (2004), Vol. 3: Remote sensing information, data processing and analysisRep.
- Samba, A., B. Sarr, C. Baron, E. Gozé, F. Maraux, B. Clerget, and M. Dingkuhn (2001), La prévision agricole à l'échelle du sahel, in *Modélisation des agro-écosystèmes et aide à la décision*, edited by E. Malézieux, G. Trébuil and M. Jaege, pp. 243–262, CIRAD and INRA, Montpellier, France
- Samson, J., D. Berteaux, B. J. McGill, and M. M. Humphries (2011), Geographic disparities and moral hazards in the predicted impacts of climate change on human populations, *Global Ecology and Biogeography*, 20(4), 532-544.
- Schoper, J. B., R. J. Lambert, B. L. Vasilas, and M. E. Westgate (1987), Plant factors controlling seed set in maize: The influence of silk, pollen, and ear-leaf water status and tassel heat treatment at pollination, *Plant physiology*, 83(1), 121.
- Segele, Z. T., P. J. Lamb, and L. M. Leslie (2009), Large-scale atmospheric circulation and global sea surface temperature associations with horn of Africa June–September rainfall, *Int. J. Climatol.*, 29(8), 1075-1100.
- Semenov, M. A., and F. J. Doblas-Reyes (2007), Utility of dynamical seasonal forecasts in predicting crop yield, *Climate Research*, 34(1), 71-81.
- Semenov, M. A., R. J. Brooks, E. M. Barrow, and C. W. Richardson (1998), Comparison of the WGEN and LARS-WG stochastic weather generators for diverse climates, *Climate Research*, 10, 95-107.
- Sen, A. (1983), *Poverty and famines: An essay on entitlement and deprivation*, Clarendon Press.
- Setvak, M. (2006), Weather radar composite (zmax), 14:00 utc, png, 292 kb, czech hydrological institute, edited. url.  
[http://oiswww.eumetsat.org/WEBOPS/iotm/iotm/20060625\\_convection/2006\\_06\\_25\\_1400\\_czrad\\_zmax.png](http://oiswww.eumetsat.org/WEBOPS/iotm/iotm/20060625_convection/2006_06_25_1400_czrad_zmax.png)

---

## References

---

- Shaw, R. H. (1988), Climate requirement, in *Corn and corn improvement*, edited by G. F. Sprague and J. W. Dudley, pp. 609-638, American Society of Agronomy, Madison, WI.
- Shepard, D. (1968), A two-dimensional interpolation function for irregularly-spaced data, in *Proceedings of the 1968 23rd ACM national conference*, edited, pp. 517-524, ACM.
- Sinclair, S., and G. Pegram (2009), A comparison of ascat and modelled soil moisture over south Africa, using topkapi in land surface mode, *Hydrology and Earth System Sciences Discussions*, 6, 7439-7482.
- Smith, C., J. Betrán, and E. Runge (2004), *Corn: Origin, history, technology, and production*, John Wiley & Sons Inc.
- Sobrado, M. (1990), Drought responses of tropical corn. 1. Leaf area and yield components in the field, *Maydica*, 35(3), 221-226.
- Steduto, P., T. C. Hsiao, D. Raes, and E. Fereres (2009), AquaCrop—the FAO crop model to simulate yield response to water: I. Concepts and underlying principles, *Agron. J.*, 101(3), 426-437.
- Stone, R. C., and H. Meinke (2005), Operational seasonal forecasting of crop performance, *Philosophical Transactions of the Royal Society B: Biological Sciences*, 360(1463), 2109-2124.
- Suleiman, A. A. (1999), Assessing and modeling the spatial variability of soil water redistribution and wheat yield along a sloping landscape, Michigan State University.
- Sultan, B., C. Baron, M. Dingkuhn, B. Sarr, and S. Janicot (2005), Agricultural impacts of large-scale variability of the west African monsoon, *Agricultural and Forest Meteorology*, 128(1-2), 93-110.
- Suyker, A. E., and S. B. Verma (2009), Evapotranspiration of irrigated and rainfed maize-soybean cropping systems, *Agricultural and Forest Meteorology*, 149(3-4), 443-452.

---

## References

---

- Sylla, M. B., A. T. Gaye, J. S. Pal, G. S. Jenkins, and X. Q. Bi (2009), High-resolution simulations of west African climate using regional climate model (regcm3) with different lateral boundary conditions, *Theoretical and Applied Climatology*, 98(3), 293-314.
- Tadesse, A., and E. Anagnostou (2009), The effect of storm life cycle on satellite rainfall estimation error, *Journal of Atmospheric and Oceanic Technology*, 26(4), 769-777.
- Taffesse, A. S., P. Dorosh, and S. Asrat (2011), Crop production in Ethiopia: Regional patterns and trends *Rep.*, IFPRI.
- Teo, C. K. (2006), Application of satellite-based rainfall estimates to crop yield forecasting in Africa, 242 pp, University of Reading.
- Teo, C. K., and D. I. F. Grimes (2007), Stochastic modelling of rainfall from satellite data, *Journal of Hydrology*, 346(1-2), 33-50.
- Thelen, K. (2007), Assessing drought stress on corn yield, in *Field Crop News*, edited, Integrated Pest Management.
- Thorne, V., P. Coakeley, D. Grimes, and G. Dugdale (2001), Comparison of TAMSAT and CPC rainfall estimates with raingauges, for southern Africa, *International Journal of Remote Sensing*, 22(10), 1951 - 1974.
- Thornton, P. K., P. G. Jones, G. Alagarswamy, and J. Andresen (2009), Spatial variation of crop yield response to climate change in east Africa, *Global Environmental Change*, 19(1), 54-65.
- Thornton, P. K., A. R. Saka, U. Singh, J. D. T. Kumwenda, J. E. Brink, and J. B. Dent (1995), Application of a maize crop simulation model in the central region of Malawi, *Experimental Agriculture*, 31(02), 213-226.
- Thornton, P. K., W. T. Bowen, A. C. Ravelo, P. W. Wilkens, G. Farmer, J. Brock, and J. E. Brink (1997), Estimating millet production for famine early warning: An application of

---

## References

---

- crop simulation modelling using satellite and ground-based data in Burkina Faso, *Agricultural and Forest Meteorology*, 83(1-2), 95-112.
- Thow, A., M. de Blois, and CARE International (2010), Climate change and human vulnerability: Mapping emerging trends and risk hotspots for humanitarian actors *Rep.*, UN Office for Coordination of Humanitarian Affairs, Geneva, Switzerland.
- Tilahun, A. (1995), Yield gain and risk minimization in maize (*zea mays*) through cultivar mixtures in semi-arid zones of the rift valley in Ethiopia, *Experimental Agriculture*, 31(02), 161-168.
- Tittonell, P., B. Vanlauwe, P. A. Leffelaar, and K. E. Giller (2005), Estimating yields of tropical maize genotypes from non-destructive, on-farm plant morphological measurements, *Agriculture, Ecosystems & Environment*, 105(1-2), 213-220.
- Todorovic, M., R. Albrizio, L. Zivotic, M.-T. A. Saab, C. Stöckle, and P. Steduto (2009), Assessment of AquaCrop, CROPSYST, and WOFOST models in the simulation of sunflower growth under different water regimes, *Agron. J.*, 101(3), 509-521.
- Tompson, A. F. B., R. Ababou, and L. W. Gelhar (1989), Implementation of the three-dimensional turning bands random field generator, *Water Resour. Res.*, 25(10), 2227-2243.
- Tsintikidis, D., K. P. Georgakakos, G. A. Artan, and A. A. Tsonis (1999), A feasibility study on mean areal rainfall estimation and hydrologic response in the blue nile region using meteosat images, *Journal of Hydrology*, 221(3-4), 97-116.
- Tsonis, A. A., G. N. Triantafyllou, and K. P. Georgakakos (1996), Hydrological applications of satellite data 1. Rainfall estimation, *J. Geophys. Res.*, 101(D21), 26517-26525.
- USAID (2003), Maize market assessment and baseline study for Ethiopia *Rep.*, Regional Agricultural Trade Expansion Support, RATES, USAID.

---

## References

---

- van Ittersum, M. K., and M. Donatelli (2003), Modelling cropping systems--highlights of the symposium and preface to the special issues, *European Journal of Agronomy*, 18(3-4), 187-197.
- Vasilas, B. L. (2004), Corn pollination & drought stressRep., Delaware Cooperative Extension.
- W.M.O. (2010), Status of current and planned cgms members satellites; current low earth orbit (LEO) satellites contributing to the gos, edited.
- Walker, G. K. (1986), Transporatation efficiency of field-grown maize, *Field Crops Research*, 14, 29-38.
- Wang, E., M. J. Robertson, G. L. Hammer, P. S. Carberry, D. Holzworth, H. Meinke, S. C. Chapman, J. N. G. Hargreaves, N. I. Huth, and G. McLean (2002), Development of a generic crop model template in the cropping system model apsim, *European Journal of Agronomy*, 18(1-2), 121-140.
- Washington, R., M. Harrison, D. Conway, and E. Black (2004), *African climate report: A report commissioned by the uk government to review African climate science, policy and options for action*, Department for Environment, Food and Rural Affairs.
- Washington, R., M. Harrison, D. Conway, E. Black, A. Challinor, D. Grimes, R. Jones, A. Morse, G. Kay, and M. Todd (2006), African climate change - taking the shorter route, *Bulletin of the American Meteorological Society*, 87(10), 1355-+.
- WCRP (2012), Verification methods for dichotomous (yes/no) forecasts, in *Forecast Verification: Issues, Methods and FAQ*, edited by W.W.R.P./W.G.N.E. Joint Working Group on Forecast Verification Research, Australian Bureau of Meteorology, Sydney.
- Webster, R., and M. A. Oliver (2007), *Geostatistics for environmental scientists*, Wiley, Chichester

---

## References

---

- Wheeler, T. R., A. Challinor, T. Osborne, and J. M. Slingo (2007), Development of a combined crop and climate forecasting system for seasonal to decadal predictions, in *Climate prediction and agriculture, advances and challenges*, edited by M. Sivakumar and J. W. Hansen, Springer, New York.
- Wheeler, T. R., P. Q. Craufurd, R. H. Ellis, J. R. Porter, and P. V. Vara Prasad (2000), Temperature variability and the yield of annual crops, *Agriculture, Ecosystems & Environment*, 82(1-3), 159-167.
- Wheeler, T. R., T. D. Hong, R. H. Ellis, G. R. Batts, J. I. L. Morison, and P. Hadley (1996), The duration and rate of grain growth, and harvest index, of wheat (*triticum aestivum l.*) in response to temperature and co<sub>2</sub>, *Journal of experimental botany*, 47(5), 623-630.
- White, J. W., G. Hoogenboom, P. W. Stackhouse Jr, and J. M. Hoell (2008), Evaluation of nasa satellite- and assimilation model-derived long-term daily temperature data over the continental us, *Agricultural and Forest Meteorology*, 148(10), 1574-1584.
- Wiebe, K. (2003), Land quality, agricultural productivity, and food security at local, regional, and global scales, in *American Agricultural Economics Association Annual Meeting*, edited, Montreal, Canada.
- Wilks, D. S. (1999), Multisite downscaling of daily precipitation with a stochastic weather generator, *Climate Research*, 11, 125-136.
- Wilks, D. S. (2001), Space-time downscaling of probabilistic seasonal forecasts with a "Weather generator", paper presented at The 26th Annual Climate Diagnostics and Prediction Workshop, La Jolla, California.
- Wilks, D. S., and R. L. Wilby (1999), The weather generation game: A review of stochastic weather models, *Progress in Physical Geography*, 23(3), 329-357.
- WMO (2010), Status of current and planned cgms members satellites; current low earth orbit (LEO) satellites contributing to the GOS, edited.

---

## *References*

---

- Worku, M., H. Tuna, W. Abera, L. Wolde, A. Diallo, T. Afriyie, and A. Guta (2001), Developing low-n tolerant maize varieties for mid-altitude sub-humid agro-ecology of Ethiopia, paper presented at Seventh Eastern and Southern Africa Regional Maize Conference, Nairobi, Kenya.
- World Bank (2006), Managing water resources to maximize sustainable growth: A world bank water resources assistance strategy for Ethiopia *Rep.*, World Bank, Washington, DC.
- World Bank (2010), *Wdr 2010 : Development and climate change*, World Bank.
- Zekaria, S., W. Mandefro, and R. Favre (2009), Harmonising agricultural statistic programs & small area estimators *Rep.*, FAO, CSA, JRC, MoARD.
- Zelleke, G., G. Agegnehu, D. Abera, and S. Rashid (2010), Fertilizer and soil fertility potential in Ethiopia *Rep.*, 42 pp, International Food Policy Research Institute (IFPRI)
- Zhong, Q., Y. Qiang, X. Shouhua, H. Bingmin, S. Xiaomin, L. Enmin, W. Jishun, Y. Guirui, and Z. Zhilin (2005), Water, heat fluxes and water use efficiency measurement and modeling above a farmland in the north china plain, *Science in China Ser. D Earth Sciences*, 48(S1), 207-217.